ISBN 978-82-471-2361-4 (printed ver.)
ISBN 978-82-471-2362-1 (electronic ver.)
ISSN 1503-8181

NTNU
Norwegian University of
Science and Technology

Anette Mathisen

Doctoral theses at NTNU, 2010:192

NTNU

Doctoral Thesis

NTNU
Norwegian University of
Science and Technology
Thesis for the degree of
doktor ingeniør
Telemark University College
Department of Technology

Doctoral theses at NTNU, 2010:192

Anette Mathisen

An Experimental and Computational Investigation of Gas/Particle Flow in a Vertical Lifter

NTNU
Norwegian University of
Science and Technology

Anette Mathisen

An Experimental and Computational Investigation of Gas/Particle Flow in a Vertical Lifter

Thesis for the degree of doktor ingeniør

Trondheim, October 2010

Norwegian University of
Science and Technology
Telemark University College
Department of Technology

NTNU
Norwegian University of
Science and Technology

Høgskolen i Telemark

NTNU
Norwegian University of Science and Technology

Thesis for the degree of doktor ingeniør

Telemark University College
Department of Technology

ISBN 978-82-471-2361-4 (printed ver.)
ISBN 978-82-471-2362-1 (electronic ver.)
ISSN 1503-8181

Doctoral Theses at NTNU, 2010:192

Printed by Tapir Uttrykk

ABSTRACT

Experimental and computational investigations of dilute gas/particle flow in a vertical lifter are performed. The effect of superficial gas velocity, particle density, particle size distribution and particle loading on particle velocities, particle fluctuations and particle cross-moment have been studied experimentally using laser Doppler anemometry (LDA) and particle image velocimetry (PIV). The results from the experimental investigation is compared with the computational investigation using Fluent®.

The experimental measurements are performed on a lab-scale vertical lifter, consisting of a fluidizing silo and a receiving tank with a glass pipe in which the solids phase is transported. The particles are placed in the fluidization tank and transport air enters at the bottom of the silo. The transport pipe is suspended above the inlet and as the transport air passes the opening, the particles are dragged into the air flow and transported upwards to the receiving tank. Fluidizing air is used to control the particle loading in the system and supplied through a distribution plate. The test section of the transport pipe is made of glass to enable the use of the optical laser based investigation techniques, LDA and PIV. Two types of powders are used, ZrO_2 and glass, each with two different particle size distributions, average diameter of 260 and 530 micron and 120 and 518 micron, respectively.

The experimental techniques LDA and PIV are used to investigate a dilute gas/particle vertical flow. The two techniques are also evaluated for use on this type of flow. LDA is a single point measurement technique, which means that one point is measured at a time. The acquisition stops when a pre-set criteria is reached, this can either be based on sample number or time. A measurement spanning over the whole cross-section of the pipe consists of several points. These points makes up a cross-sectional profile. PIV on the other hand is a whole field technique and consequently the whole cross-section of the pipe is measured simultaneously. Within a given time interval two laser pulses light up the flow and the reflection of the particles is captured by a camera.

Satisfactory measurements of all the particle types are performed using LDA. The mean axial and normal particle velocities and fluctuations as well as the cross-moment, are measured at varying particle volume fraction and superficial gas velocity. The value of the measured quantities will vary depending on the particle size, particle density, particle volume fraction and superficial gas velocity. A comparison between the particle types show that the mean axial particle velocity is highest for the lighter and smaller particles, but the fluctuations are greatest for the larger and heavier particles. For smaller particles LDA is a very efficient measurement tool. For the largest particles the acquisition can be time consuming due to relatively few particles in the system.

PIV measurements are generally performed satisfactory on all of the particle types. The exception is measurements performed on the smaller particles at the higher particle volume fractions. The mean axial and normal particle velocities and fluctuations including the cross-moments are measured at varying particle volume fraction and superficial gas velocity. The results from the measurements show that the measured quantities will vary depending on the particle size, particle density, particle volume fraction and superficial gas velocity. When comparing the particle types, it is observed that the mean axial particle velocity is highest for the smaller and lighter particles while the fluctuations are lower than for the larger and heavier ones. The combination of particles larger than commonly used tracer particles and higher particle volume fractions is challenging, but overall the PIV technique works well.

Comparison between LDA and PIV results show generally a good agreement for the mean axial particle velocity. The mean axial and normal particle fluctuations and the particle cross-moment are generally measured lower when using PIV.

Simulations are performed using Fluent® and the model Euler-Euler, where both phases are regarded as being continua. The kinetic theory of granular flow (KTGF) is included for the solids phase. Initially only the single transport pipe is simulated in 2d and 3d. The flow in this pipe is dilute and therefore the simulations which included KTGF and the Gidaspow drag model are compared to simulations enabling the constant viscosity model (CVM) and the Schiller-Naumann drag model. The results from the simulations show very little difference between the two simulations. Euler-Euler with KTGF 2d and 3d simulations are performed for all of the particle types. Little difference between 2d and 3d simulations are observed. A comparison between simulations and experimental results, LDA and PIV, showed good agreement for axial particle velocity for all of the particle types. The upward transport of particles in a vertical pipe is also simulated using Euler-Lagrange. Here a number of particles are tracked and compared to the experiments with good agreement.

Simulations of the vertical lifter, a silo containing the particles and a transport pipe, show that simulations using Euler-Euler including KTGF and the Gidaspow drag model over-predicted the particle volume fraction in the pipe compared to the experiments. The reason for this discrepancy is that the experimental set-up is modified to give low particle volume fractions in the transport pipe to enable the use of lasers to investigate the flow.

AKNOWLEGEMENTS

This work has been carried out at Telemark Technological Research and Development Centre, Tel-Tek, and Telemark University College, Dep. of Technology. The work has been sponsored by the Norwegian Research Council (NFR).

First and foremost I would like to thank my supervisor Morten C. Melaaen whose encouragement, guidance and support was invaluable during my work. Secondly I would like to express my sincere gratitude to my co-supervisor Britt Halvorsen for useful discussions and support.

Several people helped with the experimental set-up, Talleiv Skredtveit and Eivind Fjelddalen. A special thanks goes to Talleiv for always being willing to help with the glass pipe.

I am grateful to my employers at Tel-Tek, Managing Director Marit Larsen and Department Leader Hans Aksel Haugen. Thanks also to my co-workers and the rest of the people at the Technology Centre.

Finally, a very special thanks goes to my family for their continued support.

May, 2010 Anette Mathisen

CONTENTS

1. INTRODUCTION

At the beginning of this chapter a short introduction to pneumatic conveying is given to place this study in a context. An overview of previous work is presented with a focus on dilute pneumatic transport. Finally, the aim and scope of this study is given as well as the outline of the thesis.

1.1 Pneumatic conveying

Pneumatic conveying is the transportation of powders (bulk of particulate materials) through pipelines with the help of a compressed gas, usually air. The transportation is driven either by a positive or a negative pressure. When the particles reach their destination they are separated from the transport gas.

Pneumatic conveying of solids is common and is an important part of numerous manufacturing industries like the chemical, food processing, pharmaceutical and mining industry among others. Due to the variation in types of industry the size and complexity of the pneumatic conveying system varies. A general transport length limit for pneumatic systems are around 300 m. Longer transportation can be achieved by connecting several systems in a series. The need for transport air in pneumatic conveying makes the process energy demanding. In order to minimize the frictional pressure loss, reduce erosion and energy cost it is desirable that the pneumatic conveying system operates at the lowest possible velocity, Rhodes (2001).

An example of a pneumatic conveying system can be seen in Figure 1.1. Both horizontal and vertical transportation of particulate materials are common in pneumatic conveying systems and both are found in the figure. Inclined transport pipes can also be found in pneumatic conveying but this is not displayed in the figure.

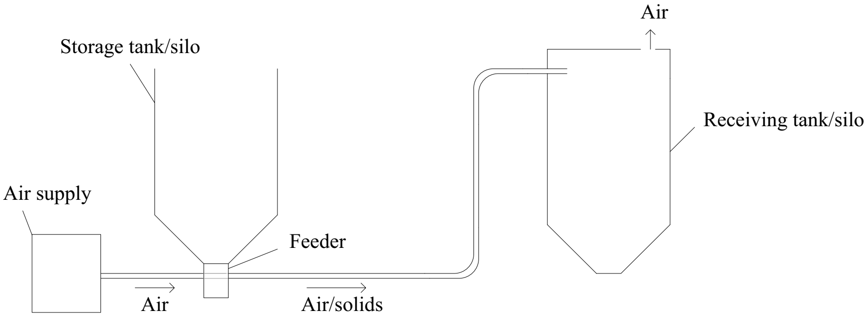

Figure 1.1: An example of a pneumatic conveying system.

The flow in horizontal and vertical transport of solids can either be classified as dilute or dense depending on the degree of particle solid loading. The forces that define the flow depend on the type of flow. Particle-particle and wall-particle interactions dominate in dense flow systems. In dilute flow the particles behave as individuals and they are fully suspended in the gas/air. Fluid-particle interactions like drag forces dominate the flow together with gravity. The solids loading ratio, the ratio between the mass flow rate of the dispersed phase and the mass flow rate of the transport air, is usually less than 10 in a dilute flow.

The solids phase

There are several factors associated with powders which need to be addressed when pneumatic conveying is considered. The most important factors are found in the characteristics of the solids phase. A powder's fluidizing ability is taken into account when the optimal form of pneumatic conveying for the powder is to be decided. As mentioned above there are two main types of pneumatic conveying of solids, these are dense and dilute phase transport. Geldart (1973) developed a classification method for particles depending on their fluidizing ability. This is called Geldart's classification and can be seen in Figure 1.2. Here the particles are divided into groups depending on the particle diameter and density.

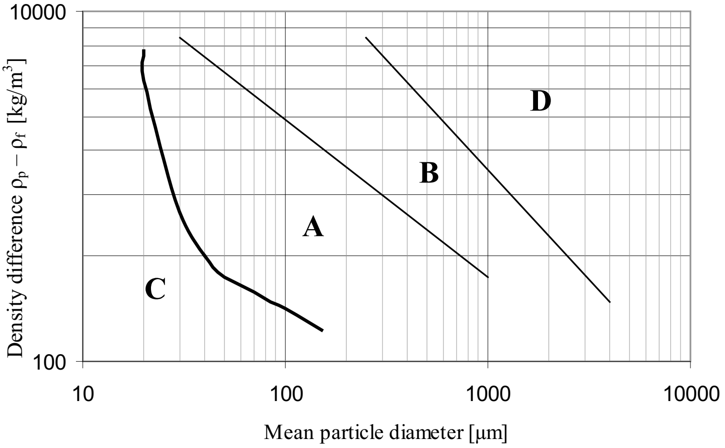

Figure 1.2: Geldart's classification (Geldart (1973)).

Group A

In this group powders with small diameters and/or low densities can be found. A bed will expand considerably before bubbling occurs. The powders in this group are best transported in dense phase conveying.

Group B

This group includes powders that can be found in the mean size and mean density range. The expansion of the bed is small and bubbles begin to form when the minimum fluidizing velocity is reached. When air is turned off the bed collapses quickly. Powders in this group are generally transported in dilute phase.

Group C

The powders in this group have a small particle size. This leads to high interparticle forces which make them difficult to fluidize. Because of the powders cohesiveness they are not suitable for dense phase transportation.

Group D

Powders with a large particle size and/or high density make up this group. They have similar fluidizing characteristics to that of particles in group B. The transportation can be done in dense phase but dilute phase transport is more common.

The above classifications are only guidelines and there are many other factors that will influence the transportation of powders. It is important to remember that a powder generally consists of particles with a wide size distribution. This means that it is not always easy to place the powder in a specific group in the diagram shown in Figure 1.2. There are also several other factors other than the particles size and density that will influence pneumatic conveying of powders. The most important factors are presented by de Silva & Datta (2004) and Woodcock & Maison (1987), particle shape, particle surface texture, powder bulk density, moisture content, electrostatic charging, particle hardness, particle cohesiveness.

1.2 Previous work

A short overview of previous work on dilute pneumatic vertical transport of particles is given in this section. This includes both experimental and numerical investigations. The focus will be on laser based studies, laser Doppler anemometry (LDA) and particle image velocimetry (PIV), experimental techniques and Euler-Euler modeling of the gas/particle flow.

1.2.1 Experimental work

Laser Doppler anemometry (LDA) has become one of the most important experimental techniques for use in velocity measurements. The LDA technique has several advantages. Some of the most important ones are that it is a non-invasive optical technique, and will therefore not disturb the flow. Another is that it has a high spatial resolution with fast dynamic response and range.

Laser-based measurements by LDA also called laser Doppler velocimetry (LDV), have previously been applied to investigate dilute gas/solid flow in vertical transport. The focus in these investigations has been on how the presence of particles affects the gas phase turbulence intensity. Particle size, particle density and particle loading are factors that can influence the turbulence in gas/particle flows. Maeda et al. (1980) investigated the effect of mass fraction of 93 µm copper particles and glass particles with a diameter of 45 and 136 µm on the velocity profiles and turbulence in the pipe. They found that the turbulence intensity increases for all the investigated cases. Lee & Durst (1982) used glass particles with the diameters 100, 200, 400 and 800 µm and investigated velocity and fluctuation profiles. It is shown through experiments with 800 µm particles that the turbulence in the flow increases. They also reported that the other particle sizes reduce the turbulence. Tsuji et al. (1984) used polystyrene particles with several different diameters ranging from 200 µm to 3 mm. The mean and fluctuating velocities in the axial direction were measured for both the gas and the solids phase for several Reynolds numbers and solid loadings. They found that the presence of the smaller particles reduce the gas turbulence intensity while the presence of larger particles increase the gas turbulence. For the smaller particles an increase in the particle loading led to a further decrease in turbulence. An increase in the solid loading for the larger particles led to an increase in the turbulence. Mierka & Timar (1997) used polymethylmethacrylate (PMMA) particles with a diameter of 1000 µm to investigate the effect of solid mass flow rate, at constant Reynolds and Archimedes number. Further they used glass particles with different diameters, 290, 521 and 1096 µm, to investigate the effect of Archimedes number while the Reynolds number was kept constant. Lastly, they varied the Reynolds number while keeping the particle mass flow rate and the particle diameter constant. For these experiments the smallest glass particles were used. In the above mentioned studies middle and fluctuating velocity profiles for both the gas and particle phase have been presented. Tracer particles were used to measure the gas phase. Most of the focus has been on how the presence of particles influences the gas phase turbulence. Depending on the particle size and particle density the presence of particles can either dampen or heighten the turbulence in the flow.

Mathiesen & Solberg (2004) performed their experiments on the same vertical lifter used in the current study. Pneumatic transport of zirconium oxide (ZrO_2) particles with a mean size distribution of 260 and 530 µm was investigated. Different air velocities and air inlet configurations are applied to investigate the influence on the particle flow. Several review articles have been published where available data has been gathered and compared. Gore & Crowe (1989) tries to explain the increase and decrease in turbulent intensity that occurs with the addition of particles through a physical model. The ratio between particle diameter and turbulent length scale, d_p/l_e, is introduced as a critical parameter, while the Reynolds number is held constant. They concluded that when the ratio is greater than 0.1, the addition of particles will increase the turbulence level, while they observed a decrease when the ratio is less than 0.1. In Hetsroni (1989) it is claimed that the available data support the theory that particles with a low Reynolds number, less than 400, reduce the turbulence while particles with a high Reynolds number, above 400, will increase the turbulence due to wake shredding. The tendency in the studies is that the turbulence increases with increasing particle size. Hadinoto et al. (2005) used two-component laser Doppler velocimetry/phase Doppler particle analyser (LDV/PDPA) to investigate the downward flow of particles in a vertical pipe. Two different particle sizes were measured at different Reynolds numbers while the solid loading was held constant. For the lowest Re-number (8300), the presence of the smallest particles reduces the gas-phase turbulence, while measurements at higher Re-number increase the turbulence. An increase was also the effect for the larger particles for all Re-numbers except the lowest (6400) where the gas-phase turbulence was no different from the turbulence observed in the single phase measurements. Ayranci et al. (2006) used LDA to measured the particle concentration of a vertical air jet. The particle arrival rate is utilized to retrieve the particle number density.

Kussin & Sommerfeld (2001) performed LDA experiments on gas/particle flow in a horizontal channel. Velocity profiles on both phases are presented. The effect of particle size, particle loading and wall roughness is investigated. Caraman et al. (2003), Boree et al. (2005) and Boree & Caraman (2005) investigated vertical downward flow using LDA. They measured particle fluctuations in a fully developed pipe flow. Kulick et al. (1994) investigated the interactions between particles and fluid turbulence in a channel by LDA. The flow was fully developed downward. They investigated how turbulence is modified by particles and how small particles respond to turbulence in shear flow. Kuan et al. (2007) used LDA to study a dilute gas/particle flow through a curved 90° duct. Both phases were measured and the results were compared with numerical simulations and a good agreement was found. A downward gas/dispersed turbulent gas flow was studied using LDA and compared to numerical simulations by Pakhomov et al. (2007). The influence of the particles on the turbulence was studied in moderate particle concentrations. Several studies using LDA have also been performed on liquid/particle flow, an example of this is Alajbegović et al. (1993). The measurements were performed on two different particle types with a diameter of 2 mm and different density. The flow was an upward flow.

An early investigation on the PIV technique was performed by Keane & Adrian (1990). PIV has been used to investigate the flow in fluidized beds by among others Ibsen et al. (2003) and Deen et al. (2006). Jakobsen et al. (1996) presented a method for simultaneously measuring the gas and particle phase in pneumatic conveying by isolating the measurements of each phase. Kiger & Pan (2000) developed a PIV technique for a turbulent liquid/particle flow where both phases can be measured simultaneously. Lueptow et al. (2000) reported that PIV measurements of particle velocities through clear walls were relatively easy. They investigated the displacement of particles in a shaker box and concluded that the method is a useful tool in investigations of quasi-two dimensional granular flows. Scarano (2002) performed a review of image processing methods for PIV. The focus of this work is mainly on the PIV method and the experiments are performed on liquid/particle flow in a backward facing step. Grüner et al. (2004) investigated the solids phase in a highly turbulent gas flow in a vertical channel with the help of PIV. They added obstacles in the flow and studied the behaviour of the particles around these. Tartan & Gidaspow (2004) used a particle imaging technique on a riser flow to verify CFD models for multiphase flows. Tartan et al. (2004) performed PIV experiments on 530 μm glass particles. Martin et al. (2005) measured both the gas and particle velocity simultaneously in a model two dimensional (2d) gas fluidized bed. The flow in a gas cyclone was studied by stereoscopic PIV (3d-PIV) by Liu et al. (2006). Yao et al. (2006) used PIV to measure granular velocities in a study on electrostatic equilibrium in granular flow. They used polypropylene granules with a diameter of 2.8 mm. PIV was used to investigate granular silo flow by Slominski et al. (2006). An investigation of a vibrating granular bed was studied using PIV by Zeilstra et al. (2007). They found that PIV with some modification can be used, but problem areas were at the walls and on top of the bed. Flow patterns in a 2d spouted bed was investigated using PIV by Zhao et al. (2008). Recktenwald et al. (2009) used PIV to analyse a channel flow rotating about the streamwise axis.

Tanaka et al. (2002) studied a liquid/solid two-phase flow. The flow in stirred tanks has been studied with the help of the PIV technique. Fan et al. (2005) investigated a laminar flow of solid/liquid suspension and a single-phase laminar liquid flow. In the two-phase flow, the liquid was seeded with polyurethane fluoresced particles in order to distinguish these from the solid phase. Deen et al. (2005) have also used PIV in the investigation of a gas/liquid stirred tank. The flow was seeded with fluorescent tracer particles. Shah et al. (2007) studied the effect of PIV interrogation area on turbulent statistics.

1.2.2 Numerical modelling

Numerical modelling of gas/particle transport has been widely documented in literature. In most cases the authors have developed or expanded an existing code. The computational fluid dynamics (CFD) codes are usually compared and evaluated against experimental investigations. Rizk & Elghobashi (1989) developed a two-equation model for low Reynolds number turbulence for dispersed dilute gas/particle confined flow. The conservation of turbulence kinetic energy and dissipation rate of that energy for the gas phase are described by the two equations. They compare their model to the experimental findings of Tsuji et al. (1984) and Maeda et al. (1980). The experimental investigation performed by Tsuji et al. (1984) was used to evaluate the numerical model developed by Louge et al. (1991). They used balance equations for rapid granular flow modified to include the drag force from the gas. Collisional exchanges of momentum and energy at the wall are included as boundary conditions.

Littman et al. (1993) performed both experimental and numerical investigation on decelerating and non-accelerating turbulent dilute phase flow. Bolio & Sinclaire (1995) used the experimental findings of Maeda et al. (1980), Lee & Durst (1982) and Tsuji et al. (1984). The mean and fluctuating velocity profiles of the particles were simulated. They concluded that the model based on kinetic theory for granular material described the particle flow satisfactory. Mierka et al. (1994) use a model to simulate the transport of gas/particle flow in vertical direction. The results are compared with experiments. Lun (2000) developed a numerical model which were compared with Tsuji et al. (1984) and found that they had a generally good agreement. Haim et al. (2003) compared their model with the experimental findings of Lee & Durst (1982), Tsuji et al. (1984) and Littman et al. (1995). The turbulent flow pattern in vertical dilute gas/particle was investigated with the help of the Eulerian-Lagrangian approximation by using the k-ε model. Cao & Ahmadi (1995) compared their work with the experimental findings of Tsuji et al. (1984) and found that their model predictions agree reasonably well. Ranade (1999) used the CFD code Fluent® to simulate gas/solid flows in a vertical riser. The two fluid model with the theory of granular flow was used and compared with experimental results.

Triesch & Bohnet (2000) also used Fluent® and employed the Lagrangian approach for calculating the dispersed phase. The authors added subroutines to the standard model successfully and compared the results to experimental findings. The Eulerian-Lagrangian approach was also used by Li & Tomita (2001) to simulate the dilute swirling flow in vertical pneumatic conveying.

Eskin et al. (2004) used kinetic theory of granular flow to model horizontal dilute pneumatic conveying. A model introduced by Bolio et al (1995) was expanded by Hadinoto & Curtis (2004). A kinetic theory of granular flow that includes the effect that the interstitial fluid has on the random motions of particles was added. Chan et al. (2005) developed a mathematical model which included turbulence modelling for use on the gas/particle flow in vertical direction. A modified k- ε turbulence model was developed to describe the gas phase flow. Benyahia et al. (2005) used the MFIX CFD code to model turbulent dilute gas/solid flows in a pipe at different solids loadings. The results were compared to experimental data. Hildayat & Rasmuson (2005) used Fluent® to simulate gas/particle flow in a vertical section and the following bend. The findings were evaluated against experimental data. Benyahia et al. (2000) simulated the riser section of a circulating fluidized bed with the kinetic theory approach in Fluent®. The results were compared with experimental findings. Grüner et al. (2004) investigated the particle behaviour in an upward flow with added obstacles using their own CFD software package. A high-resolution three-dimensional numerical simulation of a fluidized bed was performed by Zang & VanderHeyden (2001). They successfully used a simple average equation model and concluded that this can be used if the resolution of the grid is high enough. Their findings are compared with experimental results. Patil et al. (2004) used both the constant viscosity of the solids phase model (CVM) and a model based on the kinetic theory of granular flow (KTGF) to simulate gas/solids fluidized beds.

The numerical code Flotracs was used by Mathiesen et al. (2000) to simulate a dilute riser flow. Hjertager et al. (2005) simulated a circulating fluidized bed using the same code and implemented the kinetic theory of granular flow. The effectiveness of the model was tested and compared with experimental results. Jiradilock et al. (2006) considers both the dense and the dilute regions in a circulating fluidized bed. The standard kinetic theory is used together with a modified drag model. A numerical study of the pneumatic transport of particles in both vertical and horizontal direction was performed by Lim et al. (2006). Here the discrete element method (DEM) is used to model the individual particles CFD is used to model the continuous phase. The results are compared with previous experimental findings. Hartge et al. (2009) used Fluent® to study a circulating fluidized bed riser. Several combinations of granular temperature formulation, turbulence models, approaches to solids phase turbulence, drag correlations and solid/solid restitution coefficients were tested.

1.3 Objective of the thesis

Since each type of powder has its own properties depending on the size distribution, density, shape etc. and different transport conditions like geometry of transport pipe and inlet velocity of the transport air, gas/particle flows are difficult to understand. Because of this a lot of work still has to be done on this type of flow before it is fully understood. The work in this thesis contributes towards this goal.

The scope of this study is to use experimental techniques and numerical simulations to obtain a better understanding of the gas/particle multiphase upward flow. All experiments are performed on a lab scale vertical lifter. The lifter has a total height of approximately 4 m and consists of a fluidizing silo at the bottom and a receiving silo at the top with a transport pipe connecting the two. This transport pipe is made of glass to enable the use the optical experimental techniques. The experimental techniques used are laser Doppler anemometry (LDA) and particle image velocimetry (PIV). These laser based techniques are used to measure the mean and fluctuating particle velocity profiles in both axial and normal direction as well as cross-moments in dilute vertical pneumatic flow. The process is simulated numerically in the commercially available computational fluid dynamics code Fluent®. The results from the simulations are compared and evaluated against the experimental findings.

Several types of particles are investigated so that the effect of both the particle size and density can be investigated closer. Another important parameter is the particle volume fraction which can also influence the turbulence in the gas/particle flow.

Gas/particle flows are a crucial part of several industrial process, from coal fired power plants to pharmaceutical. Optimal transport of particles is key. If it is not optimal the efficiency of the power plant may be reduced and the quality of the product can be affected. This thesis is contributing to an increased understanding of optimal transport through an experimental and numerical investigation.

LDA has long been a well known and tested method for investigating a wide range of gas/particle flows. In recent years the use of PIV has become more common. The current work contributes to establishing PIV as a method that can be used for gas/particle flow investigations. An extensive comparison between LDA and PIV has been performed. The comparison shows that PIV is just as good as LDA for the current flow conditions, but some limitations were observed.

The end goal of numerical investigations is that it will be able to perfectly simulate actual processes reducing the need for expensive and time consuming experiments. This thesis contributes towards this end.

1.4 Outline of the thesis

In the current chapter a short introduction to pneumatic conveying of particles is presented. A literature review of previous experimental and numerical investigations of pneumatic conveying can be found in this chapter.

In Chapter 2 the experimental set-up, particles and important factors in particle transportation are offered.

The theory of the experimental techniques laser Doppler anemometry (LDA) and particle image velocimetry (PIV) is found in Chapters 3 and 4, respectively.

In Chapter 5 the governing equations of gas/particle flow systems are described.

The results from the experimental investigation with LDA are presented in Chapter 6. In Chapter 7 the findings from the PIV investigation is presented. A comparison between the experimental findings from the LDA and PIV investigations can be found in Chapter 8, as well as a discussion on the difference between LDA and PIV.

In Chapter 9 the results from the 2d and 3d numerical investigations are presented. The results from this investigation are compared with the results from the experimental investigation.

In Chapter 10 the thesis is finalized with conclusion and recommendations for further work.

2. THE VERTICAL LIFTER AND PARTICULATE MATERIALS

2.1 Vertical lifter

The vertical lifter is designed as a lab-scale. A schematic sketch of the lifter is shown in Figure 2.1. It has three main parts, a fluidized silo at the bottom, a vertical transport pipe, and a receiving tank at the top.

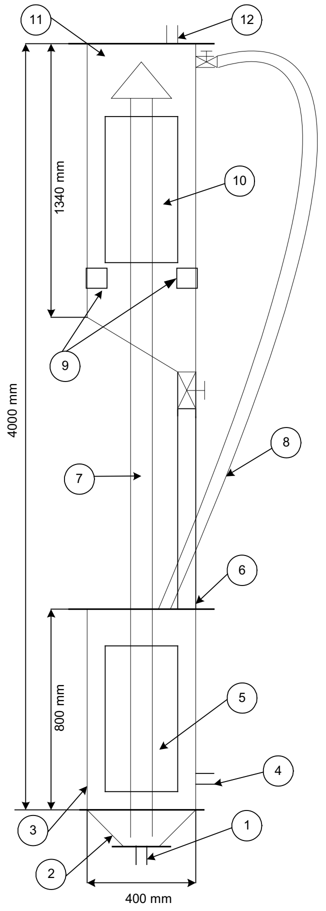

1. Transport air inlet
2. Fluidized cone
3. Fluidized silo
4. Pressure transmitter
5. Inspection glass
6. Return line
7. Transport pipe
8. Bleed line
9. Weigh cells
10. Inspection glass
11. Receiving tank
12. Exhaust (to filter)

Figure 2.1: Schematic sketch of the vertical lifter.

The particulate phase in the bottom silo is transported with the help of air through the transport pipe and up to the top silo. The vertical lifter is close to 4 m high. The transport pipe has an internal diameter of 42 mm and is made of clear glass to enable the use of optical measurement techniques (LDA and PIV). Air which is used for transport enters the bottom silo through a cylindrical nozzle with an internal diameter of 15 mm. The penetration dept of the nozzle into the transport pipe can be varied. In this thesis this nozzle is at level with the bottom plate of the fluidizing silo and the transport pipe is suspended 15 mm above this inlet. The nozzle position will have a strong influence on the amount of transported particles. When the particles have been transported to the top silo, they are returned to the bottom silo via a return pipe.

When ZrO_2 and glass particles flow through a glass pipe, static electricity can be generated. This will influence the flow and it may no longer be uniform. To reduce this effect a steel pipe can be used. Steel is a neutral material in the triboelectric series, Besançon (1985). Since optical laser based techniques are used in this study, one cannot simply replace the glass pipe with a steel pipe. The solution is to use a glass pipe for the part of the pipe that is critical for the investigation and a steel pipe where it will not influence the investigation.

The flow condition is classified as dilute phase pneumatic transport. To help the transportation of the particulate phase, fluidization air is used. In Figure 2.2 the bottom of the fluidizing tank is shown in more detail. Fluidizing air enters a ceramic air distribution plate through four air inlets to provide uniform fluidization. Four additional fluidizing inlets are placed uniformly around the transportation pipe on the bottom plate. The amount of fluidization air can be regulated and this will make it possible to obtain the desired particle concentration in the transportation pipe. The function of the bleed line is to ensure equal pressure in the bottom and receiving tank. To prevent pressure build up in the system, the top tank has an exhaust to atmosphere.

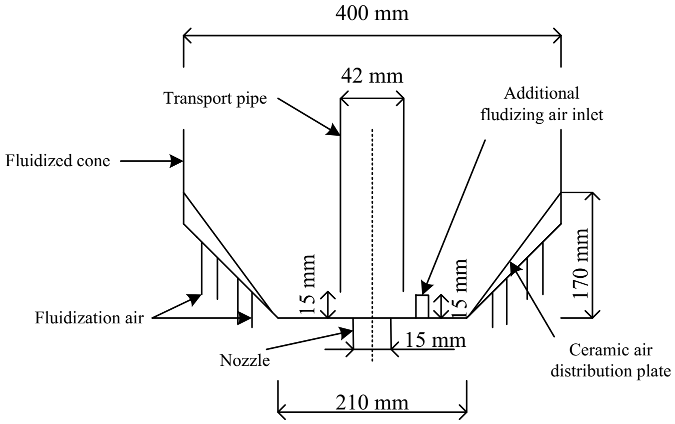

Figure 2.2: The bottom of the fluidizing silo.

In order monitor the solid volume fraction in the transport pipe, it is necessary to know the amount of particles which are transported over a certain time period. One way of doing this is to use weighing cells. Three cells are mounted on the receiving tank. The valve on the return line can be closed so that the particles stay in the receiving tank. The increase in mass is registered by the weighing cells and logged on a computer by using the program LabView. The values are logged over a period of time, between 120 and 240 s. After, the valve is opened and if the desired particle volume fraction is reached, the LDA and PIV measurements can begin.

During the experiments there are a few things that need to be remembered. The pressurised air that is feed to the vertical lifter passes through a pressure valve before it is split into the feed line for the transport air and the secondary air feed which is the fluidizing air. The fluidizing air is again split into air going into the distribution plate and air going into the additional fluidizing inlets.

The ideal gas law is written,

$$\rho = {}^{p}\!/\!_{RT} \tag{2.1}$$

From Eq. 2.1 it can be seen that a reduction in pressure will lead to a reduction of the density and an increase in the gas velocity for a given mass flow. On the other hand a reduction in gas temperature will lead to an increase in the density and therefore a reduction in the gas velocity. The pressure valve ensures that the pressurised air has the same pressure for all measurements. There are no differences in the temperature so this is not assumed to have any influence on the air velocity. The pressure valve is set to operate at 4.2 bar which will give enough pressure so that a superficial gas velocity of 9 m/s in the transport pipe can be reached. The value of 4.2 bar is kept for all of the measurements to ensure that the air properties are as similar as possible throughout the study.

2.2 Particles

General information about particles/powders can be found in Section 1.1. The particles used in this thesis are so-called model particles. In the different processes in industry where particle transport is common, all types of particles can be found. They vary in size, shape, density and colour. As seen in Section 1.1 the type of transport which is suitable for the different particle groups given by Geldart (1973) vary. The particles chosen in this thesis are all particles which are best transported in dilute phase. When laser based techniques are used to investigate a particulate flow it is necessary for the flow to be dilute. The reason for this is because the individual particles need to be seen to be measured correctly. Other important restrictions which needs to be taken into account when using laser techniques are that the particles need to reflect light, they have to have a close to spherical shape and they need to be durable so that they do not degrade over the duration of the experiments. To ensure this, the model particles chosen fulfil these criteria. In this study, spherical zirconium oxide (ZrO_2) and spherical glass particles are used. The size distribution and particle density together with their placement in Geldart's classification, Figure 1.2, can be seen in Table 2.1.

Table 2.1: Properties of the particles used in this thesis.

Name	Size distribution (μm)	Mean particle size (μm)	Density (kg/m^3)	Group in Geldart classification
Zirconium oxide (ZrO_2)	100 – 300	260	3800	B
Zirconium oxide (ZrO_2)	400 – 600	530	3800	The border between B and D
Glass	100 – 200	120	2500	B
Glass	400 – 600	518	2500	B

2.3 Factors and forces in pneumatic conveying

A multiphase flow is a flow that consists of two or more distinct phases. Pneumatic conveying is a two-phase flow, where the continuous phase is air and the dispersed phase is particles. The components in a multiphase flow are assumed mixed, not on a molecular level but on the much larger macroscopic length scale. The two phases in pneumatic conveying interact with each other and the different factors and forces that are important are presented below. The forces due to particle-fluid, particle-particle and particle-wall interactions will vary in importance depending on the nature of the flow studied.

Stokes number
The Stokes number is a dimensionless number. The equation for the Stokes number presented in Crow et al. (1998) is presented. It gives an indication of the expected particle response to changes in the flow field.

$$\mathrm{St}_V = \frac{\tau_V}{\tau_F} \tag{2.2}$$

where τ_V is a time characteristic of the particle and τ_F is a time characteristic of the flow field.

If $\mathrm{St}_V << 1$ the characteristic time associated with the flow field is much higher than the particles response time. The particles will follow the flow.
If $\mathrm{St}_V >> 1$ the characteristic time associated with the flow field is lower than the particles response time. The particles will not be affected by changes in the flow field.

Heavier particles are less likely to follow the flow faithfully.

When laser based techniques are used to study a gas or liquid flow, it is often necessary to add tracer particles. These particles are chosen because of their ability to follow the flow faithfully flow. In pneumatic transport the particulate phase is a part of the flow. Particles/powders ability to follow the flow depends on their shape, size and weight.

Slip velocity
The slip velocity is the velocity difference between the fluid velocity and the particle velocity,

$$U_{Slip} = U_g - U_s \tag{2.3}$$

The slip velocity depends on the density difference and the holdup difference, the relative volumes of the two phases.

$$U_g = \frac{\dot{m}_g}{\rho_g \alpha_g A}, U_s = \frac{\dot{m}_s}{\rho_s (1-\alpha_g) A} \tag{2.4}$$

Here $\dot{m}$ is the mass flow rate, ρ is the density, α_g is the gas volume fraction and A is the cross-section of the pipe.

Particle-fluid interaction
The coupling between the phases is due to the exchange of forces between them. Drag and lift are the reason for momentum transfer between the phases. The individual motions of phases in a flow are mainly influenced by drag and gravity. Drag is a friction and pressure force between the phases, due to the relative movement between the particles and the surrounding fluid. It is a force that resists the movement of a particle in a fluid, Troshko & Mohan (2005). The drag coefficient will depend on the particle and flow parameters, like the particle shape and size as well as the Reynolds number, Mach number, turbulence level etc. of the flow. Several drag models are developed for use in a gas/particle flow. The most common are the Shiller-

Naumann, Wen and Yu, Ergun Gidaspow, and Syamlal and O'Brien.

- Shiller-Naumann: Two drag coefficients are used in this model. They depend on the Reynolds number, one coefficient for Re > 1000 and one for Re < 1000. This model can be used for dilute flow and spherical particles, Shiller and Naumann (1935).
- Wen and Yu: This model is a modification of the Shiller-Naumann model, and was developed for use in sedimentation of solid particles in liquid columns. The model is also applicable for gas/particle flows with a low particle volume fraction, Wen and Yu (1966).
- Ergun: This model was developed for use in fixed beds, Ergun (1952).
- Gidaspow: The model is a combination of the Wen and Yu model when the particle volume fraction is low and the Ergun model when the particle volume fraction is high. The Gidaspow model should be used when both low and high particle volume fraction is present in the flow, Gidaspow (1994).
- Syamlal and O'Brien: This model takes an increase in particle volume fraction into account through the use of drag coefficients that depend on particle volume fraction-dependent terminal velocities, Syamlal and O'Brien (1989).

For more information on the different drag models the reader is referred to the respective references and Crowe et al. (1998).

Lift forces are forces on particles due to rotation and pressure variations. Rotation of a particle may be caused by a velocity gradient, from contact with other particles or contact with a wall, Crowe et al. (1998).

The virtual mass effect and the Basset force are due to the acceleration of the relative velocity. Here the virtual mass effect is the force needed to accelerate the surrounding fluid. The force due to the lagging boundary layer development with changing relative velocity is called the Basset force. Crow et al. (1998) have more information on these forces. These forces together with the lift force are usually negligible compared to the drag force in gas/particle flow.

Gravity is the most common body force. It will have a large influence on the transport of particles in an upward flow, where gravity will work in the opposite direction of the flow. The force of gravity will depend on the weight of the particle and the acceleration due to gravity.

The main forces acting on particles in vertical pneumatic conveying are gravity and drag forces. In order to achieve an effective transport of particles vertically the drag force needs to be larger than the gravitational force.

Particle-particle interactions

It can be assumed that in most pneumatic transport systems there will be some degree of particle-particle interactions, Woodcock & Mason (1987) and Crowe et al. (1998). The motion of the particles will be influenced by other particles. In dense particle flow the motion is controlled by the particle-particle interactions. It will also most likely be a factor in dilute systems, but in extremely dilute systems it may be negligible. When particles collide, particle kinetic energy is lost. The restitution coefficient is defined as the ratio between the velocity of the particle before and after the collision.

Adhesion of a particle to a wall or another particle is due to inter-particle forces caused by particle moisture, electrostatic charges and van der Waals forces. Molecular interaction between solid surfaces causes van der Waals forces, which is a cohesive force.

Particle-wall interaction

The particle/wall interaction is important in both dense and dilute flow, Crowe et al. (1998). Particle energy is lost due to particle/wall collisions. The result of this type of interaction depends on the inertia of the particle. Inertia is a property of the particle which resists changes in velocity unless it is acted upon by an outside force. The inertia of the particle depends on the mass and velocity. Friction and inelasticity effects lead to loss of kinetic energy when particles collide with the wall. For very small particles the molecular forces dominate over the inertial forces when they approach the wall. In these cases there is no rebounding or sliding along the wall because the particles sticks to the wall due to a cohesive van der Waals force.

Electrostatic charging of particles

Electrostatic charging of particles often occurs in pneumatic transport and can greatly affect the particle flow, Besançon (1985). Collisions between the particles and the pipe wall generate electrostatic charges during pneumatic conveying. The main negative aspect of this is the safety hazard this can cause, but can also influence the nature of the flow. Contact and the following separation between two materials generate a charge. This charging mechanism is known as contact electrification or triboelectrification, Yang (1999). Particle/wall adhesion, inter particle cohesion, and electrostatic discharges are examples of electrostatic effects. Electrostatic cohesion is the mutual attraction of oppositely charged particles and will generally make powder handling more challenging. It is difficult to predict the triboelectric behaviour of powders. Particle shape, prior mechanical contacts, material purity and moisture content are examples of factors that influence this. The triboelectric series is a list of materials where the materials at the top become positively charged when rubbed against a material lower in the series. According to Cross (1987) pneumatic conveying creates the highest triboelectric charging for dry particulates. All types of particles become charged, but only highly insulating powders retain the high charge levels. The charge will not build up for less or non insulating particles if a conductive path to ground exists. The electrostatic charge is naturally delayed for many types of particles.

Too high moisture content in the air used for pneumatic conveying may lead to agglomeration of particles. This may influence the efficiency of the transport negatively. In order to combat the problem of static charging of particles it is often desirable to have a certain degree of moisture content in the transport air. This will keep the process from being too dry and therefore reduce static charging of the particles. According to a study on electrostatic equilibrium in granular flow by Yao et al. (2006) the highest electrostatic field strength is found near the pipe wall. The strength of the field will be reduced from the pipe wall to the pipe centre. They also report that granules stick to the wall at low airflow rates due to electrostatic force. The granular concentration is generally increased near the pipe wall in vertical pneumatic conveying systems with low airflow rates. This implies that the particles are drawn to the pipe wall because of the electrostatic charge. To reduce the effect of electrostatic charging it is important to choose the right pipe wall material. The optimal material depends on the type of particles that are to be transported in the pipe. In the industry, the pipe is usually made of metal. It is often necessary to use either glass or plexiglass pipes in research when the flow is to be investigated in detail.

3. LASER DOPPLER ANEMOMETRY

3.1 Introduction

Laser Doppler anemometry (LDA) is one of several local measurement techniques. These techniques are used to determine the properties of two-phase flows with relative high spatial resolution depending on the applied method. This group of techniques can again be divided into three subgroups according to Crow et al. (1998);

- Probing methods (e.g. isokinetic sampling)
- Field imaging techniques (e.g. particle image velocimetry (PIV))
- Single particle counting methods (e.g. light scattering, laser Doppler and phase Doppler anemometry (LDA/PDA))

Probing methods are intrusive methods, while field imaging techniques and single particle counting methods are not. Intrusive methods may disturb the flow considerably depending on the application, but in despite of this they are widely used in industry for process control because of their robustness. In this chapter the single particle counting method, laser Doppler anemometry or LDA for short, will be presented and in the following chapter the field imaging technique, PIV will be presented.

3.2 Principle

A LDA system is a non intrusive optical measurement technique, and is an important investigation technique for fluid flow structures in gases and liquids. A general laser Doppler anemometer layout is displayed in Figure 3.1.

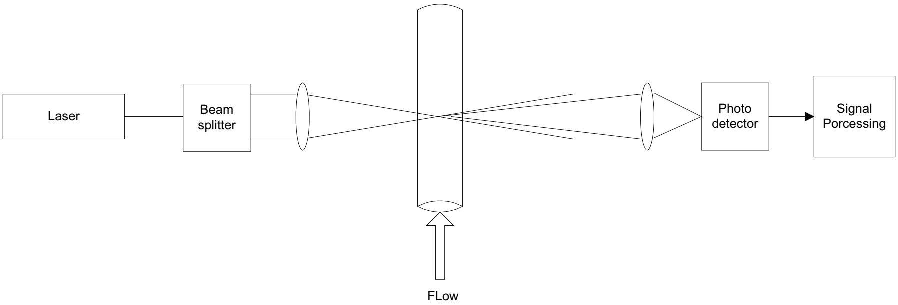

Figure 3.1: Schematic representation of a laser Doppler anemometer [Durst et al. (1981)].

3.2.1 Laser beam

The intensity has a Gaussian distribution at all cross-sections of the laser beam. The laser beam is described by the size and position of the beam waist, which is located where the cross-section is at its narrowest. This can be seen in Figure 3.2. The width of the beam can be defined by the edge-intensity equal to $1/e^2 = 13.5\ \%$ of the core intensity.

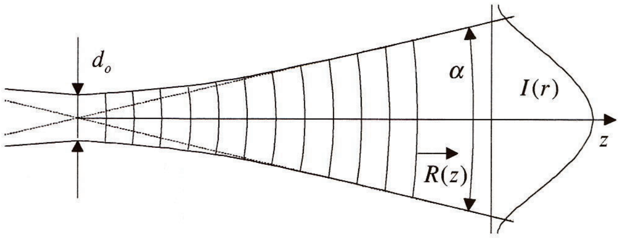

Figure 3.2: Laser beam with Gaussian intensity distribution [Dantec reference guide (2000)].

3.2.2 Doppler shift

The LDA technique is based on the fact that the moving particles in a flow scatter light. Light is emitted from the laser source, the Doppler shift (frequency shift) in wavelengths of reflections from particles moving with the flow is measured. There are two ways of registering this effect, either by a moving source and a stationary receiver, or by a moving receiver and a stationary source. When particles pass through the laser light, the light is scattered. This scattered light is detected by a light detector/receiver. In cases like these the scattering particles will act as both moving receivers and moving sources. They will be moving receivers for the laser source and moving sources for the receiver. For more theory on the Doppler-effect caused by a moving source and stationary receiver, and stationary source and moving receiver see Shao (1996). In the present work only scattering particles as moving receivers and moving sources will be considered.

The Lorenz-Mie scattering theory states that light reflected from a particle is scattered in all directions. This theory is also known as Mie's scattering theory. According to van de Hulst (1981) this theory states that the average intensity of the light scattered by a particle is roughly proportional to the square of its diameter. This theory can be applied for spherical particles with diameters larger than the wavelength of the incident light. The light scattered in the direction of the receiver and subsequently registered are used in the calculations.

Doppler effect caused by a scattering particle
In Figure 3.3 the laser source is a stationary source and the light detector is a stationary receiver. The scattering particle moves with velocity, $\vec{V}$, and is therefore both a moving receiver and a moving source.

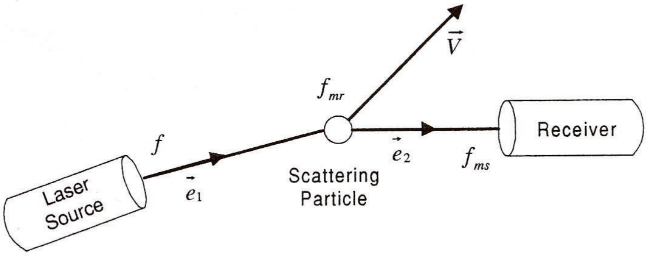

Figure 3.3: Doppler effect caused by a moving scattering particle [Shao (1996), Elseth (2001)].

The frequency of a wave emitted from a stationary receiver is,

$$f = \frac{c}{\lambda} \tag{3.1}$$

where c is the propagating speed of the wave and λ is the wavelength. When the particle is a moving receiver (mr), it records waves with a frequency of:

$$f_{mr} = f\left(1 - \frac{\vec{V}\cdot\vec{e}_1}{c}\right) \tag{3.2}$$

Since the particle also acts as a moving source (ms), the stationary receiver records waves with a frequency of:

$$f_{ms} = f_{mr}\left(\frac{1}{1 - \frac{\vec{V}\cdot\vec{e}_2}{c}}\right) = f\left(\frac{1 - \frac{\vec{V}\cdot\vec{e}_1}{c}}{1 - \frac{\vec{V}\cdot\vec{e}_2}{c}}\right) \tag{3.3}$$

where $\vec{e_1}$ and $\vec{e_2}$ are the unit vectors in the direction from the laser source to the scattering particle and in the direction from the scattering particle to the receiver, respectively. The total frequency shift is,

$$\Delta f_D = f_{ms} - f = f\left(\frac{\frac{\vec{V}\cdot\left(\vec{e}_2 - \vec{e}_1\right)}{c}}{1 - \frac{\vec{V}\cdot\vec{e}_2}{c}}\right) \tag{3.4}$$

The denominator in Eq. 3.4 is often close to unity because $\left|\vec{V}\right| \ll c$, and the equation can be simplified to,

$$\Delta f_D = \frac{\vec{V}\cdot\left(\vec{e}_2 - \vec{e}_1\right)}{\lambda} \tag{3.5}$$

Doppler shift for the dual beam (differential) mode

Two laser beams of equal light intensity are used in the dual beam mode. The beams are emitted from the laser at two different points, and they therefore have an angle difference, α. At the point where these two beams meet, the measurements are performed. Here particles scatter the light, which is then received by a light detector. Instead of one beam as shown in Figure 3.3, there are now two beams, Figure 3.4, but the principle is the same.

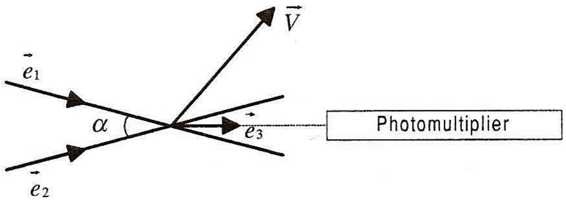

Figure 3.4: Dual beam LDA [Shao (1996), Elseth (2001)].

The detector registers the scattered light from the two beams simultaneously. Because there are two scattering angles, a beat with a frequency equal to the difference in Doppler shifts which corresponds to the two angles of scattering is obtained. Eq. 3.5 is rewritten to give the Doppler shift from the two beams,

$$\Delta f_{D1} = \frac{\vec{V}\cdot\left(\vec{e}_3 - \vec{e}_1\right)}{\lambda} \tag{3.6}$$

$$\Delta f_{D2} = \frac{\vec{V}\cdot\left(\vec{e}_3 - \vec{e}_2\right)}{\lambda} \tag{3.7}$$

The detector registers a beat frequency of,

$$f_D = \Delta f_{D2} - \Delta f_{D1} = \frac{\vec{V}\cdot\left(\vec{e}_1 - \vec{e}_2\right)}{\lambda} \tag{3.8}$$

By decomposing the vectors perpendicular to the point where the two laser beams intersect, and use $\vec{n} = \vec{e_1} - \vec{e_2}$, Eq. 3.8 becomes,

$$f_D = \frac{\vec{V}\cdot\vec{n}}{\lambda} = \frac{2\sin\left(\alpha/2\right)}{\lambda}\left(\vec{V}\cdot\vec{n}_0\right) = \frac{2V_v \sin\left(\alpha/2\right)}{\lambda} \tag{3.9}$$

here V_v is the projection of $\vec{V}$ and $\vec{n_0}$ is the unit vector in the given direction. The vectors in a dual beam LDA is illustrated in Figure 3.5.

From Eq. 3.8 it is clear that the Doppler signal frequency is independent of the receiving directions. This means that all light contribute usefully to the signal, since scattered light can be collected over a wide aperture.

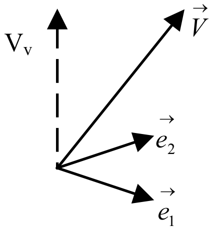

Figure 3.5: Vectors in dual beam LDA [Shao (1996), Elseth (2001)].

3.2.3 The fringe model

The fringe model is a theoretical model proposed by Rudd (1969) for the interpretation of LDA signals based on the interference or the fringe pattern. The wave fronts of the two beams are approximately plane if the beams intersect in their beam waist. As shown in Figure 3.6, this interference produces light and dark parallel planes.

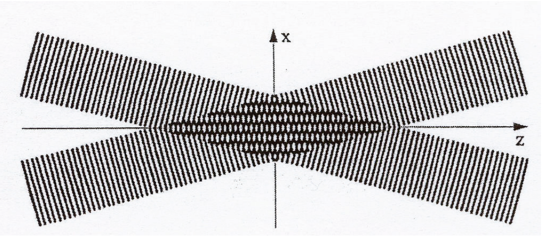

Figure 3.6: The fringe pattern which is formed where the two laser beams intersect [Dantec reference guide (2000)].

The fringe spacing, d_f, in a dual-beam LDA system is determined by the angle α between the beams and the wavelength, λ, of the light,

$$d_f = \frac{\lambda}{2\sin\left(\alpha/2\right)} \tag{3.10}$$

The light scattered by a particle moving through the interference area will vary in intensity depending on light intensity variations in this area. A photo detector records the intensity variation of the scattered light.

$$f_D = \frac{\vec{V}.\overrightarrow{n_0}}{d_f} = \frac{2V_v \sin\left(\alpha/2\right)}{\lambda} \tag{3.11}$$

When the Doppler frequency shift is known, the relation between the Doppler frequency shift and the velocity of the particle can be applied to find the perpendicular velocity component. By using the fringe model the end equation is equal to Eq. 3.9.

3.2.4 Control volume

The control volume is where the measurements take place and is situated in the intersection between the two incident laser beams. This intersection is found in the beam waist. The measuring volume has an ellipsoid shape, see Figure 3.7, because of the Gaussian intensity distribution in the beams. The volume where the modulation depth is higher than $1/e^2$ times the peak core is defined as the measuring volume. The ellipsoid has the following height, width and length,

$$\text{Height} = \frac{d_0}{\cos\left(\alpha/2\right)}, \qquad \text{Width} = d_0, \quad \text{Length} = \frac{d_0}{\sin\left(\alpha/2\right)} \tag{3.12}$$

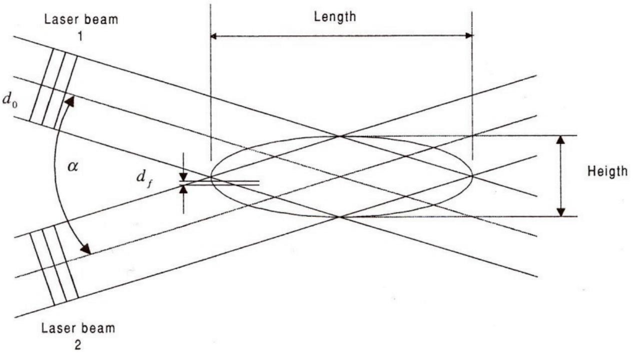

Figure 3.7: The measuring volume [Dantec reference guide (2000), Elseth (2001)].

The number of fringes can be calculated from Eq. 3.13, where d_f is the fringe spacing,

$$N_f = \frac{\text{Height}}{d_f} = \frac{2d_0}{\lambda}\tan\left(\alpha/2\right) \tag{3.13}$$

This equation will give the number of fringes which a (tracer-) particle will pass when following the x-axis through the centre of the control volume, Eq. 3.6 and 3.7. A particle will pass fewer fringes if it follows any other path through the control volume. If this is the case, then the Doppler frequency will be estimated from fewer periods in the recorded signal. The control volume should have a sufficiently high number of fringes to ensure good LDA results. It is possible to obtain good results with less, but the LDA set-up should produce between 10 and 100 fringes [Dantec reference guide (2000)].

The number of fringes passed by a particle can be decreased or increased when a frequency shift causes the fringe pattern to roll through the control volume. The number of fringes passed will increase if the fringes move toward the movement of the particle, and decrease if the fringes move away from the particle [Dantec reference guide (2000)].

3.2.5 Frequency shift

One negative aspect with the LDA technique is that the receiver is not able to distinguish between positive and negative frequencies. This may lead to directional ambiguity in the measured velocities. If the velocity in Eq. 3.9 is negative, the frequency will become negative. Figure 3.8 shows this directional ambiguity without frequency shift.

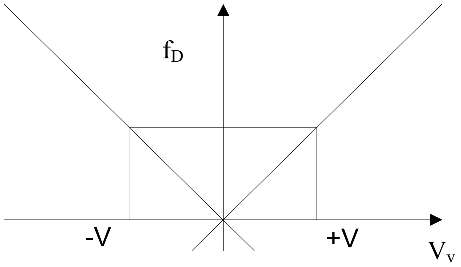

Figure 3.8: Directional ambiguity without frequency shift [Dantec reference guide (2000)].

To solve this problem, a Bragg cell, which is a piece of glass, is placed in the path of one of the laser beams (http://www.sew-lexicon.com). An oscillator drives an electro-mechanical transducer. This transducer is excited by a microwave signal to create a wave in the glass. This wave has the frequency of the microwave and changes the optical index of refraction of the glass. A portion of the incident laser light which enters the Bragg cell is diffracted by this change. The result of this is that two beams exits the cell. One which is not diffracted and exits at the angle of entry. The second beam is the diffracted beam, which exits at an angle proportional to the frequency of the sound wave. The principle of the Bragg cell is illustrated in Figure 3.9.

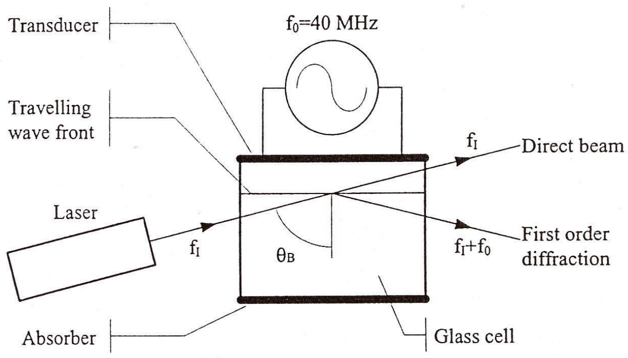

Figure 3.9: Bragg cell [Dantec reference guide (2000)].

A series of travelling wave fronts acts as a thick diffraction grating when they are hit by the incident light beam. The intensity maxima is emitted in a series of directions because of interference of the light scattered by each acoustic wave front. The intensity balance between the direct beam and the first order of diffraction can be adjusted by adjusting the acoustic signal intensity and the tilt angle θ_B (seen in Figure 3.9) of the Bragg cell.

A fixed frequency shift, f_0, is added to the diffracted beam,

$$f_D \cong f_0 + \frac{2\sin\left(\alpha/2\right)}{\lambda} V_v \qquad (3.14)$$

As long as the particle velocity does not produce a negative last term larger than f_0, a positive Doppler frequency, f_D, is ensured.

3.2.6 Forward and backscatter LDA

When the particles are illuminated by the laser light, light is scattered in all directions, but the majority is scattered in the direction away from the transmitting optics. Because of this, forward scatter LDA used to be the most common. Here the receiving optics is placed on the opposite side of the transmitting optics. Over the years the progress in technology has made it possible to detect even a small amount of scattered light, and this has made the detection of backscattered light possible. This has also made LDA a more accessible and easier technique.

In addition to forward and backscatter LDA there is a third option, off-axis scattering. Here the receiver is situated at an angle relative to the measuring volume. A negative aspect with the off-axis mode, as with forward mode, is the need for a separate receiver and careful alignment is needed.

As shown in Figure 3.10, the effective size of the measuring volume is reduced when off-axis scattering is used.

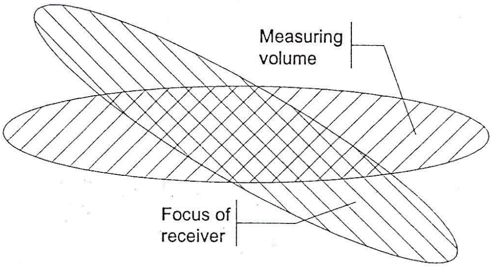

Figure 3.10: Off-axis scattering [Dantec reference guide (2000)].

Particles that are out of focus, usually those particles which pass the measuring volume at either end, are omitted. This is illustrated in Figure 3.10. These can contribute to the background noise and not to the actual signal. This means that the sensitivity to velocity gradients within the measuring volume is reduced.

3.2.7 Tracer particles

In all LDA experiments particles must be present in the flow and in cases where particles are not naturally present, tracer particles must be added. For more information on tracer particles see Chapter 4 and Durst et al. (1981).

3.3 Data analysis

In LDA measurements the signal processor receives analogue signals directly from the photo detectors. For each detected and validated Doppler-burst the corresponding particle velocity is calculated and then transferred to a computer for further analysis.

3.4 Moments

Moments can be calculated for a data set and are the simplest form of statistics. During calculation the possible relation between samples and the timing are ignored because it is based on individual samples. Since the samples are treated one at a time moments are also called one-time statistics.

The raw data of axial or (U) and normal or (V) velocities are the basis for the statistical analysis. There is no need for co-ordinate transformation because the green (U) and the blue (V) beam pair is positioned in planes perpendicular to each other. The axial and normal mean velocities,

$$\overline{U} = \eta \sum_{i=1}^{N} U_i \qquad \overline{V} = \eta \sum_{i=1}^{N} V_i \tag{3.15}$$

The root mean square, rms, velocities or the velocity fluctuations,

$$U_{rms} = \eta \sqrt{\sum_{i=1}^{N} (U_i - \overline{U})^2} \qquad V_{rms} = \eta \sqrt{\sum_{i=1}^{N} (V_i - \overline{V})^2} \tag{3.16}$$

The cross-moments are proportional to the Reynolds stresses,

$$\overline{U'V'} = \overline{UV} - \overline{U}\,\overline{V} = \eta \sum_{i=1}^{N} (U_i - \overline{U})(V_i - \overline{V}) \tag{3.17}$$

In Equations 3.15 to 3.17 a weighting factor η is included. The expression is,

$$\eta = \frac{1}{N} \tag{3.18}$$

Here N is the number of instantaneous velocity samples.

3.5 The LDA system

Local velocities and velocity fluctuations are measured with LDA on a part of the test section which is transparent. The LDA set-up is a two-colour off-axis backscatter system that enables simultaneous measurements of axial (horizontal) and normal (vertical) velocity components. The LDA set-up is displayed in Figure 3.11.

The laser is a water-cooled 3 W Lexel 80 argon-ion laser. The coherent beam is split into two parts by two prisms in a beam splitter. Following this the beams enter the Bragg cell where one of the beams is frequency shifted. The laser system at Telemark University College was originally a one-dimensional LDA. Later it was extended to two dimensions through an extension unit called the Four Beam Module. This is basically a colour beam splitter. In this module the two beams, both the shifted and the non-shifted beam, are split into two green and two blue beams. A beam pair is made up of one frequency shifted beam and one non-shifted. Each pair has the same colour, either green with a wavelength of 514.5 nm or blue with a wavelength of 488 nm. From here the four beams are transferred to the transmitting probe with the help of transmitting fibre optical cords. The transmitting lens focuses the beams at a focal point. The scattered light from the particles is received by receiving lens which is placed next to the transmitting lens because of the off-axis backscattering mode. The backscattered light is focused into receiving optical fibres by special lenses and transported to a colour separator. Here the green and the blue components are separated and re-collimated before they are sent to the two detectors, PM1 and PM2. These detectors are photo multiplier type detectors. Here the light is converted into electrical signals. From here the signals continues on to the signal processor.

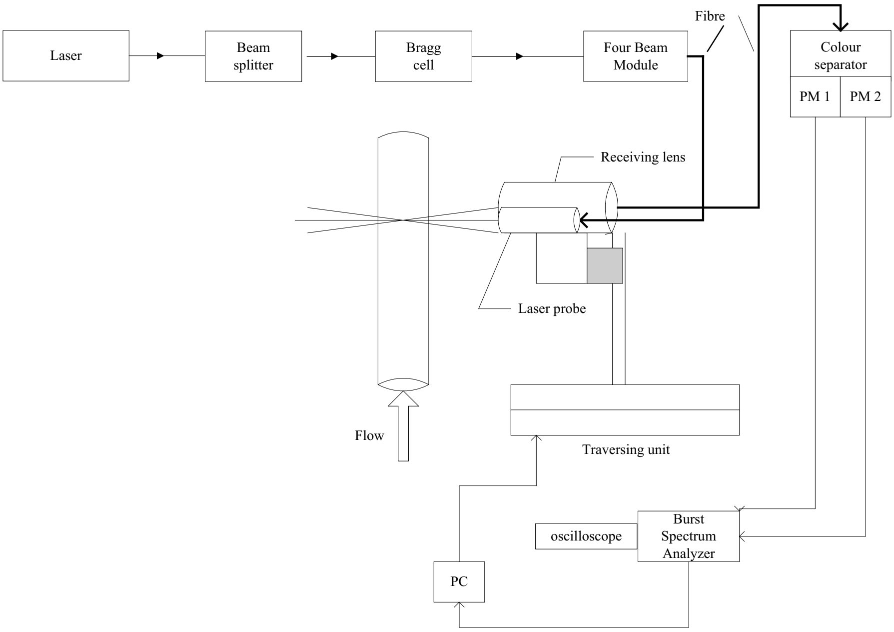

Figure 3.11: The LDA set-up.

The signal processor, a burst spectrum analyser (BSA), is connected to an oscilloscope and a PC. The electrical signals can be viewed on the oscilloscope and they are converted into velocity data by the BSA, which are monitored online by a PC. With the help of special software from Dantec, the raw-data is processed into statistical values like mean velocities, rms values and turbulent quantities.

The traversing unit is a Dantec Dynamics lightweight system. It is operated from a computer and enables three-dimensional movement.

In the LDA experiments performed in this thesis the samples were assumed to be statistically independent due to the size of the particles and the number of particles in the flow. The particles used in this investigation are not seeding particles.

4. PARTICLE IMAGE VELOCIMETRY

4.1 Introduction

As already mentioned in Chapter 3, particle image velocimetry (PIV) is a field imaging technique. It is a non-intrusive method just like LDA. This means that it will not have any effect on the flow beyond the need for it to be optically accessible. The main difference between LDA and PIV is that LDA performs measurements in a single point with a high temporal resolution. It is necessary to combine the results from several points to get an understanding of the flow. These points are very small volumes and their size depends on the lens used, as explained in Chapter 3. PIV is a whole field method where it is possible to obtain all the information of the cross-section at once. The technical restrictions limit the temporal resolution. The difference between the two measuring techniques is illustrated in Figure 4.1, indicating several point measurements with LDA and a whole field is analysed by PIV.

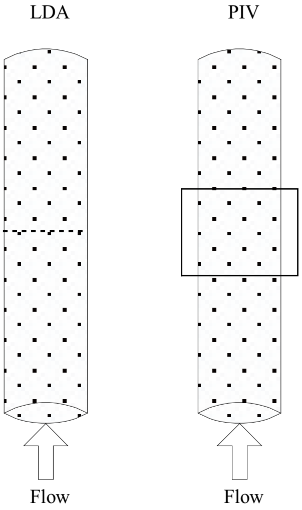

Figure 4.1: Difference in how the measurements are performed when using LDA and PIV.

4.2 Principle

PIV is one of the methods that can be used to measure the velocity of fluid flow without disturbing the flow. Figure 4.2 displays a typical PIV set-up.

In order to measure the velocity, particles have to be present in the flow. Gas or liquid flows can in many instances naturally contain enough particles. If this is not the case it is necessary to seed the flow with tracer particles. This means that the velocity in cases like these is measured indirectly, it is therefore necessary to chose tracer particles that are good representatives of the actual flow. Another use for PIV is to measure the velocity of a particulate phase. In this case the velocity is measured directly.

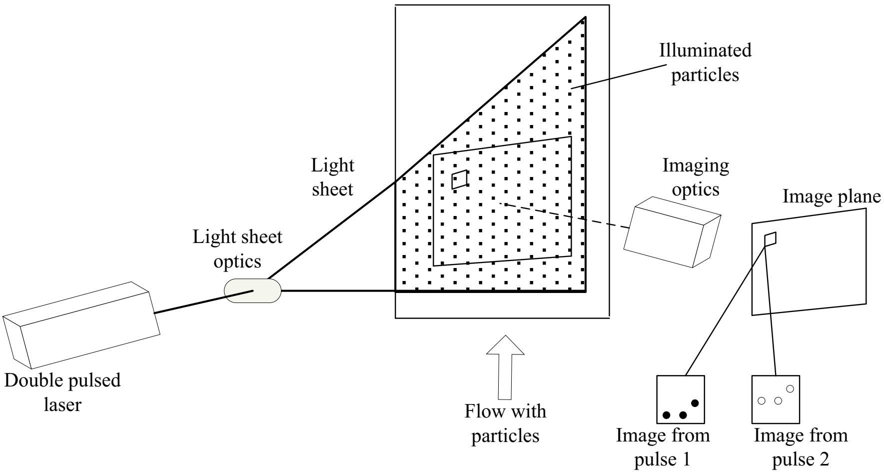

Figure 4.2: An example for a PIV set-up.

4.2.1 Main principle

The principle of PIV is that within a short time interval, particles are illuminated in a plane of the flow. The illumination is usually provided by a laser. The mean flow velocity and the magnification at imaging decide the optimal time delay between the pulses. The delay between the pulses needs to be long enough so that the movement of the particles can be registered. Particles will have moved too far if the delay is too long. Magnification at imaging is an important factor which will vary with each set-up. It is a length scale needed so that the distance the particles have moved can be given in mm, cm, etc. An illustration of how this can be done can be seen in Figure 4.3.

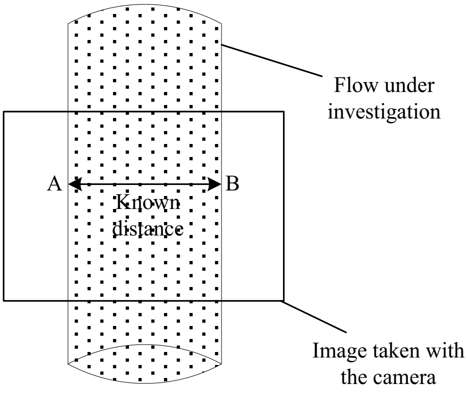

Figure 4.3: Illustration of how the magnification at imaging is calculated.

The length scale is usually calculated in the program by post-processing and feeding it with a known distance. In Figure 4.3 the diameter of the pipe is known and used to calculate the length scale. Points A and B are marked on the picture and then the diameter of the pipe (the distance between A and B) is used to calculate the length scale.

The particles will scatter the light and this light is recorded on a sequence of frames by a camera. The recordings from the camera are divided into smaller sub areas called interrogation areas (IAs) for evaluation. This is illustrated in Figure 4.4.

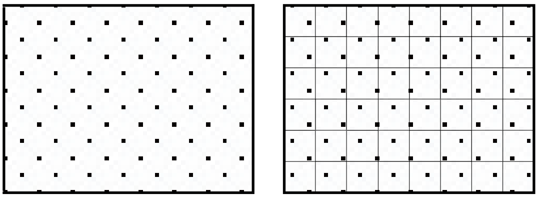

Figure 4.4: An illustration of a PIV recording and the same recording divided into IAs.

By evaluation of the resulting PIV recordings the displacement of the particle images between the light pulses can be determined. Statistical methods are used to determine the local displacement vectors for the images of the particles between the first and second illumination for each interrogation area. An example of this is shown in Figure 4.5. Cross-correlation and adaptive correlation are typical statistical methods. Adaptive correlation is an expansion of cross-correlation. The vector of the local flow velocity is calculated by using the time delay between the two illuminations and the magnification at imaging (length scale).

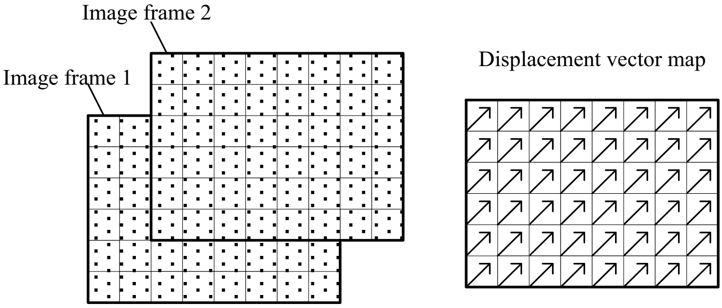

Figure 4.5: IAs from image frames 1 and 2 and the resulting displacement vector map.

4.2.2 Light source

A laser is a common light source used in PIV experiments. Light emitted from a laser, the laser beam, is distinguished by the fact that it has a high intensity, emitted in a distinct direction, monochromatic and coherent, which means that there is a fixed phase proportion between the light quanta emitted. The laser light can be bundled into thin light sheets for illumination. In many cases it is necessary to use two light sources to be able to produce two pulses within a short time interval. A laser system that consists of two light sources can be seen in Figure 4.6. The lasers are Nd:YAG lasers and are often used in PIV.

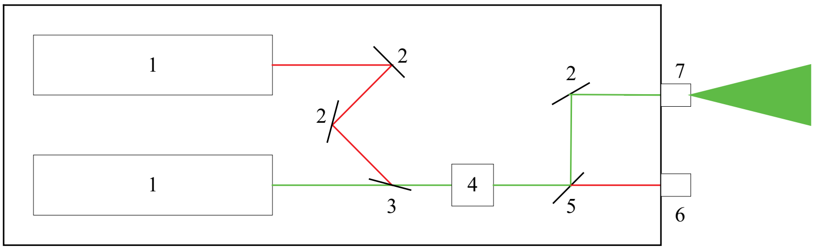

Figure 4.6: *Typical laser system for PIV. 1. Nd:YAG lasers, 2. Mirrors, 3. Beam combiner, 4. Second harmonic generator (the frequency of the laser light is doubled and the wavelength is halved), 5. Beam splitter 532/1064 nm, 6. Beam dump, 7. Light sheet optics.*

4.2.3 Light sheet optics

The necessary light sheet optics is usually aligned and ready for use by vendors of PIV systems. Mirrors are often employed to direct the light sheet in the desired direction. The light sheet defines the area in which the particles/tracer particles are illuminated by the laser beam and the measurements are performed. An illustration of a light sheet illuminating the flow can be seen in Figure 4.7.

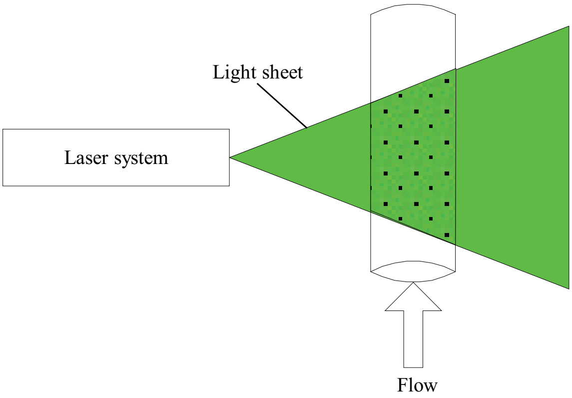

Figure 4.7: *Light sheet illuminating the flow.*

4.2.4 Illumination pulse

In order to avoid blurring of the image the duration of the illumination pulse must be short enough so that the motion of the particles is “frozen” during the pulse exposure. To be able to determine the displacement between the images of the particles with sufficient resolution, the time delay between the illumination pulses must be long enough, but also short enough to avoid particles with an out-of-plane velocity component leaving the light sheet between subsequent illuminations. Particles can also be lost to in-plane dropout, which will be discussed in more detail later in this chapter.

4.2.5 Image recording

Image recordings give immediate image availability and feedback. The most widely used imagers are the charge coupled device, CCD, and the complementary metal oxide semiconductor, CMOS, cameras. Both sensors have been around since the late 1960s, but CCD dominated for a long time. Only recently has CMOS become a satisfactory alternative. The following information on CCD and CMOS sensors is taken from Litwiller (2001). Both the CCD and CMOS sensors are pixelated metal oxide semiconductors, and the principal of both sensors is to convert light into electric charge and process it into electric signals. The sensors are made up of several individual CCDs and CMOSs respectively, which are generally arranged in a rectangular array. These individual CCDs and CMOSs are called pixels (picture elements). In a CCD sensor every pixel is charged. These charges are converted to voltage, buffered, and sent off-chip as an analogue signal. The whole pixel can be used for light capture, and the outputs uniformity is high. Uniformity is the consistency of response for different pixels under identical illumination conditions. In a CMOS sensor every pixel has its own charge-to-voltage conversion. This leads to a different readout technique which will affect the sensor design, capabilities and limitations. The design complexity is higher for the CMOS sensor and the area used for light capture is reduced. The uniformity is lower than for the CCD sensor since each pixel does its own conversion.

The CCD sensor is more sensitive than the CMOS sensor and the exposures contain less noise, but the CMOS sensor is faster. The camera system used in the present study has a CMOS sensor.

The size of a pixel is generally in the order of, 10 x 10 µm or 100 pixels per millimetre [Raffel et al. (1998)].

4.2.6 Recording techniques

There are two main methods of PIV recording modes,

- methods in which the illuminated flow is captured on to a single frame, single frame/ multi exposure PIV.
- methods which provide a single illuminated image for each illuminated pulse, multi-frame(usually two)/single exposure PIV.

Illustration of single frame techniques and of multiple frame techniques is given in Figure 4.8.

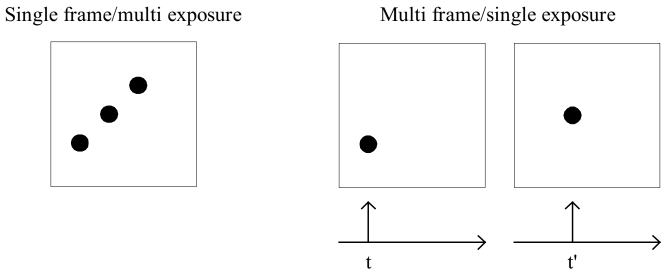

Figure 4.8: Illustration of the single frame/multi exposure and the multi frame/single exposure.

The main difference between the two modes is that a single frame/multi exposure PIV recording gives rise to a directional ambiguity in the recovered displacement vector. The reason for this is that it does not retain information on the temporal order of the illumination pulses. There are ways of solving this but it will not be given here, the reader is referred to Raffel et al. (1998). Directional ambiguity is not a problem in the multi-frame/single exposure PIV recording. Here the temporal order of the particle images is preserved. The evaluation of this approach is easier. The multi frame/single exposure is now the most common recording technique

4.2.7 Tracer particles

When choosing seeding particles it is important to remember that larger particles have better light scattering efficiency, but smaller particles will follow the flow more faithfully. The two fundamental dimensions of the velocity, length and time are determined directly in PIV. But because it is the particle velocity which is determined instead of fluid velocity the technique measures indirectly. In order to avoid significant discrepancies between fluid and particle motion, the fluid mechanical properties of the particles have to be investigated.

The influence of gravitational forces is a primary source of error if the densities of the fluid and the tracer particles do not match. In many practical situations this can be neglected, and a more detailed description is given in Raffel et al. (1998) if the case requires that this needs to be taken into account.

For liquid flows the problem of finding particles with matching densities is usually not difficult. Solid particles with adequate fluid mechanical properties can often be found. In gas flows it is more difficult to find particles that satisfy the criteria. The diameter of the particle should be very small in order to ensure good tracking of the fluid motion, due to the large difference in density between the fluid and the tracer particles. But light scattering properties also need to be taken into account, so the particle diameter should not be too small, and a compromise has to be found. For an overview of seeding particles see Raffel et al. (1998).

4.2.8 Light scattering behaviour

The contrast of the PIV recordings is directly proportional to the intensity of the scattered light based on the obtained particle image intensity. As an alternative to increasing the laser's power, it is often more effective and economical to increase the image intensity by properly choosing the tracer particles. The light scattered by particles is a function of the refractive index of the particles to that of the surrounding medium, the particle size, shape and orientation. The scattered light also depends on polarisation and observation angle. Mie's scattering theory can be applied if the particles are spherical with diameters larger than the wavelength of the incident light. This theory states according to van de Hulst (1981) that the average intensity of the light scattered by a particle is roughly proportional to the square of its diameter. Mie's scattering is also known as Lorenz-Mie scattering theory, explained in Chapter 3.

In Raffel et al. (1998) it is stated that larger particles will increase the scattering efficiency. The negative aspect of using large particles is that the background noise will increase and this will affect the recordings significantly.

4.3 Data analysis

Through data analysis, such as cross and adaptive correlation, the average displacement of all the particles in the interrogation area can be determined. To get reasonable averages it is necessary to have at least 4 – 5 particles present in the interrogation area, ideally it should be 10 – 11 (Dantec Dynamics). Even though this is the recommended quantity, it is possible to perform data analysis on interrogation areas with more or less particles. This average displacement is used in the calculation of the velocity vector.

$$\overline{V} = \frac{\Delta\overline{X}}{\Delta t} \tag{4.1}$$

Here $\overline{V}$ is the average velocity, $\Delta\overline{X}$ the average displacement and Δt is the time between the pulses.

Cross-correlation is the statistical analysis used to find the displacement of the particles captured on image frames. Both image frames are divided into IAs and the corresponding IAs from each of the two image frames are correlated. This is illustrated in Figure 4.9. The IAs from image frame 1 and 2 are called I_1 and I_2 respectively. A control volume is made up of the two corresponding IAs on image frame 1 and 2.

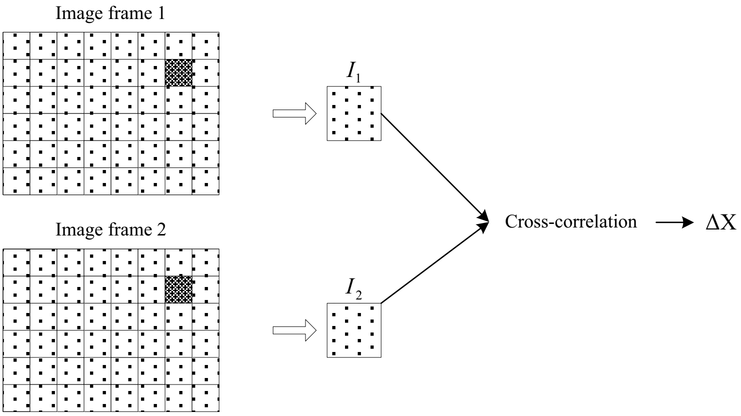

Figure 4.9: An illustration of a cross-correlation between two corresponding IAs on image frame 1 and 2.

The corresponding interrogation areas from image frame 1 and image frame 2 are cross-correlated with each other pixel by pixel.

$$C(s) = \iint_{IA} I_1(X) \cdot I_2(X - s) dX \tag{4.2}$$

A signal peak identifying the common particle displacement, ΔX, is produced for each interrogation area. If the displacement, ΔX, of each of the particles is constant between the two image frames, a prominent peak will be produced. This peak will be significantly higher than the noise peaks, and the height will depend on the number of particle pairs that show the same displacement. The placement of the peak in the plane will correspond to the constant displacement. Sub-pixel interpolation is used to get an accurate measure of the displacement and the resulting velocity vector. This is illustrated in Figure 4.10. When all of the IAs has been cross-correlated the result is a velocity vector map like the one seen in Figure 4.5.

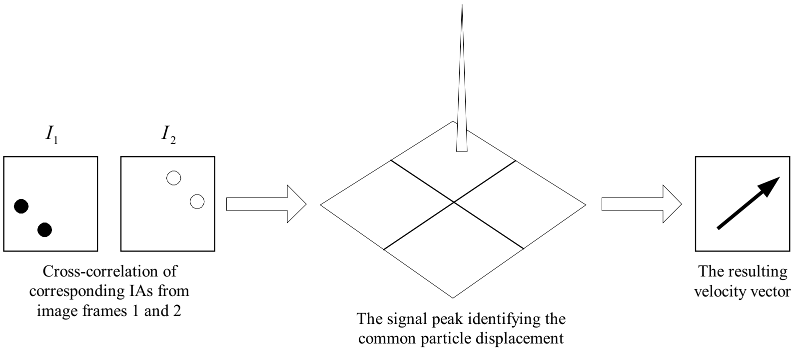

Figure 4.10: An illustration of the signal peak and how its placement relates to the particle movement and the velocity vector.

The latest form of data analysis is adaptive correlation. This is an extension of the cross-correlation analysis and increases the flexibility in capturing the flow characteristics. The principle of adaptive correlation is that it is an iterative procedure. Multiple cross-correlations are performed and the result of the previous pass is used to increase the accuracy of the next calculation. This is illustrated in Figure 4.11.

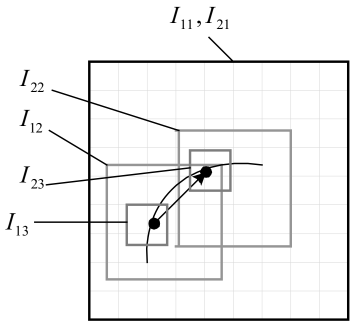

Figure 4.11: Illustration of the iteration process in adaptive correlation. (Dantec Dynamics product information, Adaptive correlation)

The first iteration is a normal cross-correlation calculation. Here the two IAs from the two image frames, represented by I_{11} and I_{21} in Figure 4.11, are identical both in size and placement. The intermediate results are validated before the next iteration. On the second iteration the size of the IAs are reduced and the second image frame are shifted relative to the corresponding IA on the first image frame. These two IAs are represented by I_{12} and I_{22} in Figure 4.11. The shift of the IAs on the second image frame is based on the results from the initial cross-correlation. The results from the second iteration are then validated and based on these results changes are made for the last iteration. The size of the IAs is again reduced and the second set of IAs is shifted relative to the first set of IAs. These IAs can be seen in Figure 4.11 as I_{13} and I_{23}. After this last calculation the final velocity vector map is produced. The number of iterations can be varied depending on the experimental set-up. According to Dantec Dynamics the smallest IA size that will give sensible results is 8 by 8 pixels, but this depends on the flow. A final IA of 32 by 32 is in many cases accurate enough.

The reason for the shift between the first and second IA is to retain more particles. When using the standard cross-correlation particles that leave the IAs between the two laser pulses will be lost. The loss of these particle images are called "in-plane dropout". This loss reduces the signal strength and therefore the number of successful vectors. When using adaptive correlation this loss is reduced because the second IA can be shifted so that most of the particles that left the first IA is captured. Figure 4.12 illustrates the in-plane dropout of particles and how they can be retained when the IA of the second frame is shifted.

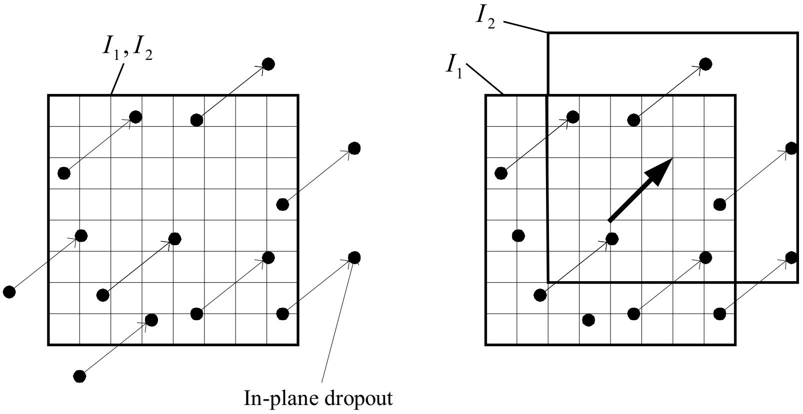

Figure 4.12: Illustration of in-plane dropout and how they can be retained when the second IA is shifted (Dantec Dynamics product information, Adaptive correlation).

4.4 Moments

The particle displacement is scaled by the magnification at imaging (Figure 4.3) and then divided by Δt, the time between the pulses, to give the average velocity of the particle within the control volume. From the correlation the axial (U) and the normal (V) velocities are obtained, Eq. 4.1. The mean velocities are obtained by summation of the instantaneous velocities and dividing them by the number of samples (N). From the instantaneous and mean U and V velocities the U-rms, V-rms and the cross-moments are calculated using the equations below.

The axial and normal mean velocities,

$$\overline{U} = \frac{1}{N}\sum_{i=1}^{N} U_i \qquad \overline{V} = \frac{1}{N}\sum_{i=1}^{N} V_i \tag{4.3}$$

The root mean square, rms, velocities or the velocity fluctuations,

$$U_{rms} = \frac{1}{N-1}\sqrt{\sum_{i=1}^{N}(U_i - \overline{U})^2} \qquad V_{rms} = \frac{1}{N-1}\sqrt{\sum_{i=1}^{N}(V_i - \overline{V})^2} \tag{4.4}$$

The cross-moments are proportional to the Reynolds stresses,

$$\overline{U'V'} = \overline{UV} - \overline{U}\,\overline{V} = \frac{1}{N}\sum_{i=1}^{N}(U_i - \overline{U})(V_i - \overline{V}) \tag{4.5}$$

N is the number of velocity samples.

The cross-moment equation is proportional to the Reynolds stress, but it is important to remember that even though they are equal mathematically, there is one important difference. Classic fluid dynamics operates in an infinitely small fluid element while PIV performs a spatial averaging over an IA. A spatial averaging means that the data obtained from the whole area is averaged.
The visibility of particles in an IA depends on several parameters, for example:

- their scattering properties
- the light intensity at the particle position
- the sensitivity of the recording optics
- the number of particles

4.5 The PIV system

The particle velocity in a gas/particle flow is measured using particle image velocimetry (PIV). The PIV system is a 2d system that enables the measurements of both axial and normal velocities, the set-up is illustrated in Figure 4.13.

The system consists of two 100 Hz 2 x 5 mJ litron lasers and a Nanosense Mkl camera (CMOS sensor) with a 60 mm lens delivered by Dantec Dynamics. The use of a dual laser system makes it possible to fire two pulses within a very short time interval. The two image frames captured on the camera are post-processed through adaptive correlation in a computer program, FlowManager, also delivered by Dantec Dynamics.

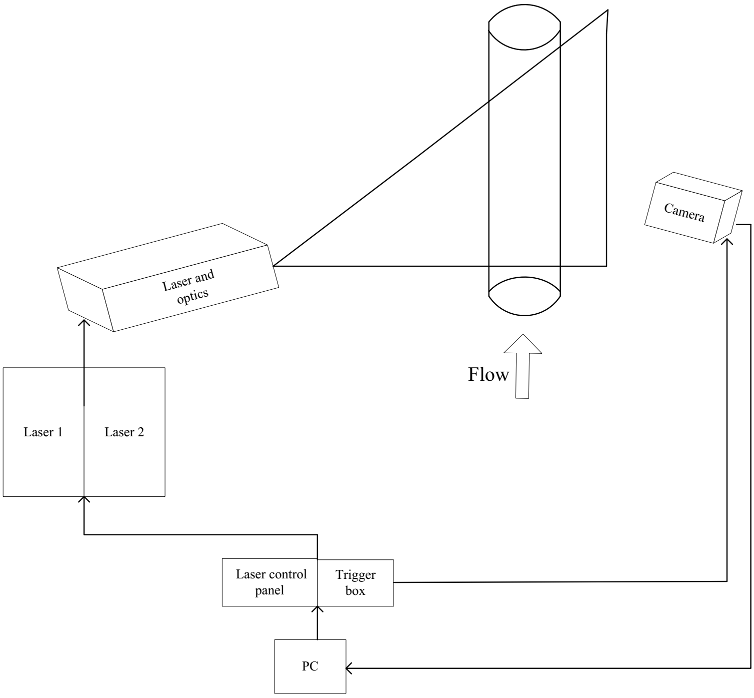

Figure 4.13: The PIV set-up.

In PIV measurements it is vital that the camera takes a picture at the same moment that the laser pulses illuminates the flow. In order to ensure this the lasers and the camera are controlled by a computer with the help of a trigger box. The pictures from one set of measurements are stored temporary in the camera memory. These pictures are transferred to the computer and post-processed in order to obtain velocity information on the flow.

4.6 Performing PIV measurements

Figure 4.14 shows the recipe of the adaptive correlation. Here the number of refinement steps (iterations), the final interrogation area size, overlap and the number of passes/steps can be specified. Three iterations are performed in the adaptive correlation in this thesis. The first IAs has a size of 256 x 256 pixels and the final IAs has a size of 32 x 32 pixels. The velocities of the particles are derived from the displacement of the particles from one frame to the next and the time delay between the two pulses. This time delay is set to 120 µs in these experiments. In order to obtain the correct velocity the magnification at imaging, a scaling factor, is needed. This factor is obtained as illustrated in Figure 4.15. The diameter of the pipe is known and is used to calculate the scaling factor. A picture taken with the camera is opened and the two walls are marked with A and B. The distance between A and B is the diameter of the pipe. This value is entered as the absolute distance and based on this the scale factor is calculated. After the correlation, all the vector maps are transferred to a Matlab script, made by Sondre Vestøl, where the mean axial and normal velocities are used to calculate the fluctuating velocities and the cross-moment. This script can be found in Appendix B. The lasers are operated on a frequency of 50 Hz.

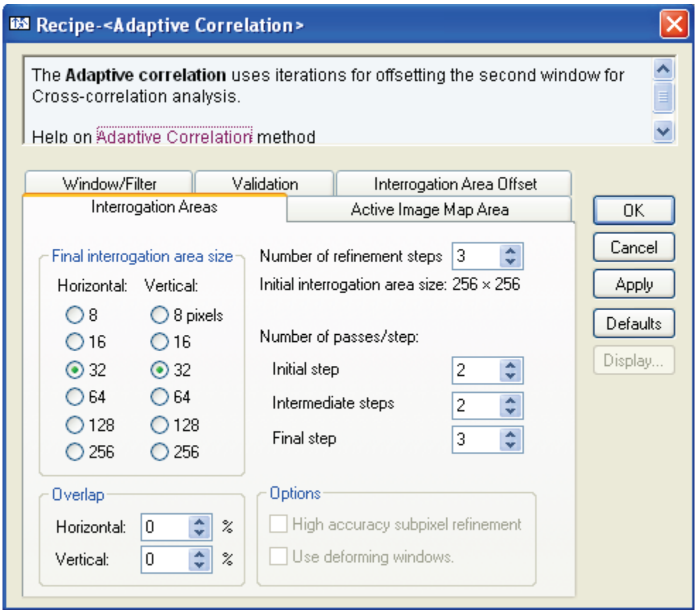

The **Adaptive correlation** uses iterations for offsetting the second window for Cross-correlation analysis.

Help on Adaptive Correlation method

Final interrogation area size
Horizontal: ○ 8 ○ 16 ● 32 ○ 64 ○ 128 ○ 256
Vertical: ○ 8 pixels ○ 16 ● 32 ○ 64 ○ 128 ○ 256

Number of refinement steps: 3
Initial interrogation area size: 256 × 256

Number of passes/step:
Initial step: 2
Intermediate steps: 2
Final step: 3

Overlap
Horizontal: 0 %
Vertical: 0 %

Options
☐ High accuracy subpixel refinement
☐ Use deforming windows.

Figure 4.14: The recipe for the adaptive correlation, interrogation areas.

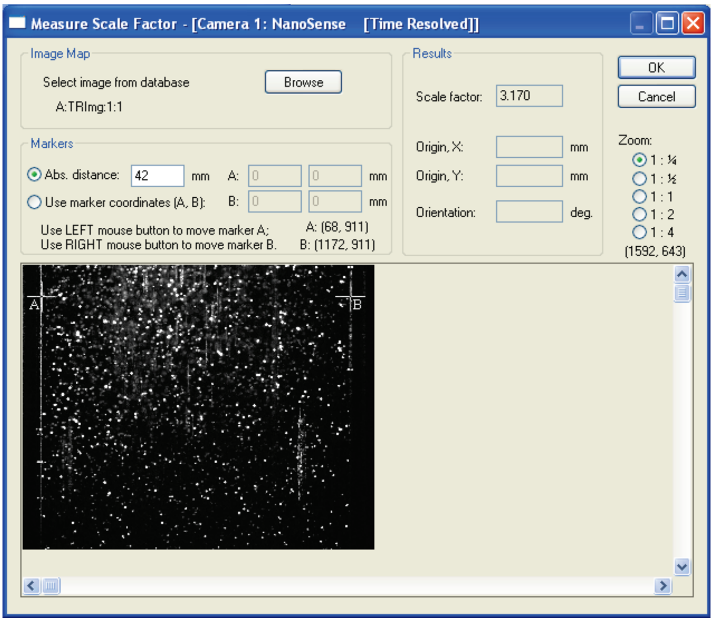

Measure Scale Factor - [Camera 1: NanoSense [Time Resolved]]

Image Map
Select image from database
A:TRImg:1:1

Markers
● Abs. distance: 42 mm
○ Use marker coordinates (A, B):
A: 0 0 mm
B: 0 0 mm
Use LEFT mouse button to move marker A;
Use RIGHT mouse button to move marker B.
A: (68, 911)
B: (1172, 911)

Results
Scale factor: 3.170
Origin, X: mm
Origin, Y: mm
Orientation: deg.

Zoom:
● 1 : ¼
○ 1 : ½
○ 1 : 1
○ 1 : 2
○ 1 : 4
(1592, 643)

Figure 4.15: Measuring of the scaling factor.

]

5. GOVERNING EQUATIONS FOR GAS/PARTICLE FLOW

5.1 Introduction

Multiphase gas/particle flows can be described by two different numerical models. These are the Euler-Euler approach and the Euler-Lagrange approach. In the Euler-Euler model both the fluid and the disperse phase is considered to be interpenetrating continua and are solved by a generalization of the Navier-Stokes equations. While in the Euler-Lagrange model the dispersed phase is solved by tracking and solving the Newtonian equations of motion for each individual particle. The model that best describe the multiphase flow depends on the characteristics of the flow. Due to the difference in modelling the, two approaches are suited for different type of flows. The Euler-Lagrange approach is best suited for dilute flows, where the particle concentration is low. The Euler-Euler approach can be used for both dilute and dense flow. In order to keep computation time down, the Euler-Euler model is often used for modelling pneumatic transport. This is the model that will be the main focus in the numerical simulations. The details of the models are given in Crowe et al. (1998).

Fluent® is one of several commercially available software packages that can be used to model a number of different types of flow. The dilute gas/particle flow is modelled in Fluent® using the Euler-Euler model.

The solids phase is classified by a diameter, density and coefficient of restitution. Each phase is described by a volume fraction, which represent the space occupied by that phase. Three models are available when applying multiphase modelling in Fluent®. The available models are; the VOF (volume of fluid) model, the mixture model and the Eulerian model. Both the VOF and the mixture model use a single fluid approach. This means that a single set of conservation equations for the momentum and the continuity are solved. The difference between the two is that the mixture model allows for the phases to interpenetrate, while the VOF model does not. The Eulerian model is a multiphase model and additional sets of conservation equations are solved. This means that the volume fraction for each phase and mechanisms for exchange of mass and momentum between the phases are introduced. The continuity and momentum equations are solved for each phase. When the kinetic theory of granular flow is enabled, the granular temperature equation is solved for the solids phase. The fluid and the dispersed phase are coupled through the use of the drag force in the momentum equation. The Eulerian model is used to model the dilute gas/particle flow.

The turbulence phenomena in both phases are treated by using the standard k-ε model. There are two other k-ε models available, these are RNG and realizable k-ε model. The standard k-ε model is semi-empirical and is based on model transport equations for k, the turbulence kinetic energy, and ε, the turbulence dissipation rate. While the k model equation is derived from the exact equation, the ε is obtained from physical reasoning. The flow is assumed to be fully turbulent and the effect of the molecular viscosity is negligible in the derived k-ε model. Due to this the standard k-ε model is only valid for fully turbulent flows. The mathematical technique, renormalization group (RNG) methods, is used to derive the RNG k-ε model from the Navier-Stokes equations. When certain mathematical constraints are satisfied the model is called the realizable k-ε model. These constraints are related to the normal stresses. The standard k-ε model is used to model the dilute gas/particle flow. There are three available methods of modelling the turbulence in multiphase flows. These are the mixture, dispersed and the per-phase turbulence models which are extensions of the standard, RNG and the realizable k-ε model. The mixture model can be used when the phases separate and when the density ratio is close to 1. In flows where the continuous phase and the dilute solids phase are clearly defined, the dispersed model can be applied. The turbulence of the continuous phase is the dominant influence on the motion of the particles since the inter-particle collisions are assumed to be negligible. The per-phase model should be applied when the turbulent transfer between the phases plays a dominant role.

5.2 Euler-Euler method

The Eulerian approach is used for both phases. Mass, momentum and turbulence are described by the equations in the following sub-section and the symbols used are listed in the nomenclature section.

5.2.1 Conservation equations of mass and momentum

The mass conservation equations for the gas phase, g, and the solids phase, s, are,

$$\frac{\partial}{\partial t}\left(\alpha_g \rho_g\right)+\frac{\partial}{\partial x_i}\left(\alpha_g \rho_g U_{gi}\right)=0 \tag{5.1}$$

$$\frac{\partial}{\partial t}\left(\alpha_s \rho_s\right)+\frac{\partial}{\partial x_i}\left(\alpha_s \rho_s U_{si}\right)=0 \tag{5.2}$$

With the volume fraction balance equation as a constraint,

$$\alpha_g+\alpha_s=1 \tag{5.3}$$

Here α, ρ and U_i are the volume fraction, density and velocity for each phase respectively. Mass transfer is not allowed between the phases.

The momentum conservation equation for the gas phase and the solids phase in the j direction can be expressed as,

$$\begin{aligned}&\frac{\partial}{\partial t}\left(\alpha_g \rho_g U_{gj}\right)+\frac{\partial}{\partial x_i}\left(\alpha_g \rho_g U_{gi} U_{gj}\right)= \\ &-\alpha_g \frac{\partial P}{\partial x_j}+\frac{\partial \tau_{gij}}{\partial x_j}+\alpha_g \rho_g g_j+K_{sg}\left(U_{sj}-U_{gj}\right)\end{aligned} \tag{5.4}$$

$$\begin{aligned}&\frac{\partial}{\partial t}\left(\alpha_s \rho_s U_{sj}\right)+\frac{\partial}{\partial x_i}\left(\alpha_s \rho_s U_{si} U_{sj}\right)= \\ &-\alpha_s \frac{\partial P}{\partial x_j}-\frac{\partial P_s}{\partial x_j}+\frac{\partial \tau_{sij}}{\partial x_j}+\alpha_s \rho_s g_j+K_{sg}\left(U_{gj}-U_{sj}\right)\end{aligned} \tag{5.5}$$

where P and τ_{ij} are the fluid pressure and the total stress tensor, respectively. G is the gravity, P_s is the solids pressure and $K_{sg} = K_{gs}$ is the drag coefficient between the gas phase and the solids phase. The right hand side terms represent the pressure forces, viscous forces, body forces and drag forces, respectively.

5.2.2 Drag models

There are several drag models available for use in gas/particle flow. The two models presented here are the Gidaspow model, Gidaspow et al. (1992), and the Syamlal-O'Brien model, Syamlal & O'Brien (1989). The Gidaspow model is a correlation which combines the Wen and Yu (1966) model for a dilute system with the Ergun (1952) equation for a dense system.

The Ergun equation (1952),

$$K_{Ergun} = 150\frac{\alpha_s^2 \mu_g}{\alpha_g d_s^2} + 1.75\frac{\rho_g \alpha_s \left|\vec{v}_s - \vec{v}_g\right|}{d_s}, \text{ for } \alpha_g \leq 0.8 \tag{5.6}$$

The Wen and Yu (1966) model,

$$K_{Wen-Yu} = \frac{3}{4} C_D \frac{\alpha_s \alpha_g \rho_g \left|\vec{v}_s - \vec{v}_g\right|}{d_s} \alpha_g^{-2.65}, \text{ for } \alpha_g > 0.8 \tag{5.7}$$

The drag function, C_D, based on the relative Reynolds number,

$$\begin{aligned} C_D &= \frac{24}{\alpha_g \mathrm{Re}_s}\left[1 + 0.15(\alpha_g \mathrm{Re}_s)^{0.687}\right], \quad \mathrm{Re}_s \leq 1000 \\ C_D &= 0.44, \quad \mathrm{Re}_s \geq 1000 \end{aligned} \tag{5.8}$$

The relative Reynolds number,

$$\mathrm{Re}_s = \frac{\rho_g d_s \left|\vec{v}_g - \vec{v}_s\right|}{\mu_g} \tag{5.9}$$

Gidaspow (1994) introduced a switch function to enable rapid transition between the regimes and avoid discontinuity,

$$\varphi_{gs} = \frac{\arctan\left[150 \times 1.75(0.2 - \alpha_s)\right]}{\pi} + 0.5 \tag{5.10}$$

The expression of the Gidaspow drag coefficient is,

$$K_{gs} = (1 - \varphi_{gs})K_{Ergun} + \varphi_{gs} K_{Wen-Yu} \tag{5.11}$$

5.2.3 Kinetic theory of granular flow

The granular temperature is used in the viscosity terms in solving of the solids phase stress needed for closure of the solids phase momentum conservation equation. The granular temperature is proportional to the kinetic energy of the random motion of the particles and defined as,

$$\Theta_s = \tfrac{1}{3}\left\langle U_s'^2 \right\rangle \tag{5.12}$$

Here U_s' is the fluctuating component of the particle velocity. The granular temperature equation is a conservation equation which describes the variation of particle velocity fluctuations. This equation is as follows, Ding and Gidaspow (1990),

$$\begin{aligned} &\frac{3}{2}\left[\frac{\partial}{\partial t}(\alpha_s\rho_s\Theta_s) + \frac{\partial}{\partial x_i}(\alpha_s\rho_s U_{sj}\Theta_s)\right] = \\ &\left(\alpha_s\rho_s\tau_{sij}\frac{\partial U_{sj}}{\partial x_i}\right) + \frac{\partial}{\partial x_i}\left(\alpha_s\rho_s\kappa_{\Theta s}\frac{\partial \Theta_s}{\partial x_i}\right) - \gamma_{\Theta s} - 3K_{gs}\Theta_s \end{aligned} \tag{5.13}$$

The terms on the right hand side is the generation of granular temperature by the solids stress tensor, the diffusion of granular temperature, dissipation due to particle-particle collisions and dissipation due to fluid/particle interaction. An option when simulating kinetic theory of granular flow in Fluent® is to use an algebraic formulation of Eq. 5.13 This algebraic formulation is obtained from the energy equation found in Lun et al. (1984). The convection and diffusion terms are neglected while the generation and dissipation term are kept. This is due to the assumption that the granular energy is dissipated locally. The algebraic equation can be found in Syamlal et al. (1993).

The solids stress tensor has the following form,

$$\tau_{sij} = \alpha_s\mu_s\left(\frac{\partial U_{sj}}{\partial x_i} + \frac{\partial U_{si}}{\partial x_j}\right) + \alpha_s\left(\lambda_s - \frac{2}{3}\mu_s\right)\delta_{ij}\left(\frac{\partial U_{sk}}{\partial x_{sk}}\right) \tag{5.14}$$

The solid phase bulk viscosity, λ_S and the solids shear stress viscosity, μ_s, are derived from the theory of granular flow.

Diffusion of granular temperature, $\kappa_{\Theta s}$, Gidaspow et al. (1992),

$$\kappa_{\Theta s} = \frac{150\rho_s d_s\sqrt{\Theta_s\pi}}{384(1-e)g_0}\left[1 + \frac{6}{5}\alpha_s g_0(1-e)\right]^2 + 2\rho_s d_s\alpha_s^2(1-e)g_0\sqrt{\frac{\Theta_s}{\pi}} \tag{5.15}$$

The dissipation of granular temperature (Eq. 5.13) is due to inelastic collisions between the particles, Lun et al. (1984),

$$\gamma_{\Theta s} = \frac{12(1-e^2)g_0}{d_s\sqrt{\pi}}\rho_s\alpha_s^2\Theta_s^{3/2} \tag{5.16}$$

The solids pressure, P_S, according to Lun et al. (1984),

$$P_s = \alpha_s\rho_s\Theta_s + 2\rho_s(1-e)\alpha_s^2 g_0\Theta_s \tag{5.17}$$

The first term in the solids pressure equation is a kinetic term and the second is due to particle collisions.

When the solids phase becomes dense, the probability of collisions between particles increases, the radial distribution factor is a correction factor that accounts for this. The radial distribution factor, Ogawa et al. (1980),

$$g_0 = \left[1 - \left(\frac{\alpha_s}{\alpha_{s,\max}}\right)^{1/3}\right]^{-1} \tag{5.18}$$

An extension of the above expression by Ogawa et al. (1980) which is enabled if more than one solids phase is present was proposed by Lun et al. (1984).

The solids shear viscosity, μ_s, has a collision and a kinetics viscosity term. The first term represents the collisional contribution and the second term the kinetics part. The contribution due to collisions between particles is taken from kinetic theory of granular flow, Lun et al. (1984). The kinetic term arise from dilute viscosity of gas and is taken from kinetic theory of gasses. A molecule is assumed to be a hard spherical particle and that particles in a dilute region dose not collide. The solids shear viscosity term according to Gidaspow et al. (1992) is,

$$\mu_s = \frac{4}{5}\alpha_s\rho_s d_s g_0(1+e)\left(\frac{\Theta_s}{\pi}\right)^{1/2} + \frac{10\rho_s d_s\sqrt{\Theta_s\pi}}{96\alpha_s(1+e)g_0}\left[1+\frac{4}{5}g_0\alpha_s(1+e)\right]^2 \tag{5.19}$$

The solids bulk viscosity, λ_s, accounts for the resistance of the solids particles to compression and expansion. The expression is given by Lun et al. (1984),

$$\lambda_s = \frac{4}{3}\alpha_s\rho_s d_s g_0(1+e)\left(\frac{\Theta_s}{\pi}\right)^{1/2} \tag{5.20}$$

5.2.4 Turbulence model

The turbulence in the gas phase is modelled using the standard k-ε model modified with extra terms for interphase turbulent momentum transfer. The turbulence quantities for the solid phase are predicted using Tchen theory (Hinze, 1975 and Simonin & Viollet, 1990).

The Reynolds stress tensor τ for the gas phases, g, is,

$$\tau_{gij} = \mu_g^t\left(\frac{\partial U_{gi}}{\partial x_j} + \frac{\partial U_{gj}}{\partial x_i}\right) - \frac{2}{3}\delta_{ij}\left(\rho_g k_g + \mu_g^t\frac{\partial U_{gk}}{\partial x_k}\right) \tag{5.21}$$

here $\mu_g{}^t$ is the gas phase turbulent viscosity and is given in terms of the turbulent kinetic energy of the gas phase,

$$\mu_g^t = \rho_g C_\mu \frac{k_g^2}{\varepsilon_g} \tag{5.22}$$

The turbulence predictions of the gas phase are obtained from the following equations for k and ε. The turbulent kinetic energy for the gas phase is,

$$\frac{\partial}{\partial t}\left(\alpha_g \rho_g k_g\right) + \frac{\partial}{\partial x_j}\left(\alpha_g \rho_g U_{gj} k_g\right) = \frac{\partial}{\partial x_j}\left(\alpha_g \frac{\mu_g^t}{\sigma_k} \frac{\partial k_g}{\partial x_j}\right) + \alpha_g \tau_{gij} \frac{\partial U_i}{\partial x_j} - \alpha_g \rho_g \varepsilon_g + \alpha_g \rho_g \Pi_{kg} \tag{5.23}$$

The first term on the right hand side is the diffusion of turbulent kinetic energy, the second term is the generation of turbulent kinetic energy and the third term is the dissipation rate of kinetic energy.

The dissipation of turbulent kinetic energy for the gas phase is,

$$\frac{\partial}{\partial t}\left(\alpha_g \rho_g \varepsilon_g\right) + \frac{\partial}{\partial x}\left(\alpha_g \rho_g U_{gj} \varepsilon_g\right) = \frac{\partial}{\partial x_j}\left(\alpha_g \frac{\mu_g^t}{\sigma_\varepsilon} \frac{\partial \varepsilon_g}{\partial x_j}\right) + \alpha_g \frac{\varepsilon_g}{k_g}\left(C_{1\varepsilon} \tau_{gij} - C_{2\varepsilon} \rho_g \varepsilon_g\right) + \alpha_g \rho_g \Pi_{\varepsilon g} \tag{5.24}$$

The turbulence interaction term Π_{kg} is derived from the instantaneous equation of the gas phase and simplified, while $\Pi_{\varepsilon g}$ is modelled according to Elgobashi & Abou-Arab (1983). The equation for Π_{kg} is,

$$\Pi_{kg} = K_{sg}\left(k_{sg} - 2k_g + U_{sg} \cdot U_{sg}^{dr}\right) \tag{5.25}$$

Here U_{sg} is the relative velocity and U_{sg}^{dr} is the drift velocity. $\Pi_{\varepsilon g}$ is expressed as follows,

$$\Pi_{\varepsilon g} = C_{3\varepsilon} \frac{\varepsilon_s}{k_s} \Pi_{kg} \tag{5.26}$$

The constants $C_{1\varepsilon}$, $C_{2\varepsilon}$, σ_k and σ_ε have been determined from experiments with air and water and have been found to be applicable for a wide range of flows, Launder & Spalding (1972). The value of the constant $C_{3\varepsilon}$ was determined by Simonin (1996) through fitting model predictions to experimental data in turbulent particle laden jets. The value of the constants can be found in Table 5.1.

U_{sg}^{dr} is the drift velocity of the solids phase and is derived from turbulent fluctuations in the volume fraction.

$$U_{sg}^{dr} = -\left(\frac{D_s}{\sigma_{sg}\alpha_s} \frac{\partial \alpha_s}{\partial x_i} - \frac{D_g}{\sigma_{sg}\alpha_g} \frac{\partial \alpha_g}{\partial x_i}\right) \tag{5.27}$$

σ_{sg} is the dispersion Prandtl number with a value of 0.75. D_g and D_s are diffusivities and when using Tchen theory (Simonin & Viollet, 1990) the following equality is assumed,

$$D_s = D_g \tag{5.28}$$

The turbulence modelling of the solid phase is based on the modelling of the gas phase using algebraic relations. Two central parameters used in the characterisation of the solid phase is the particle relaxation time, τ_{sg}^{F}, which is connected with the inertial effects acting on the solids phase, and the Lagrangian integral time scale, τ_{sg}^{t}, based on the particle trajectories and their crossing in space. The parameters are calculated as follows,

$$\tau_{sg}^{F} = \alpha_s \rho_s K_{sg}^{-1} \left(\frac{\rho_s}{\rho_g} + C_V \right) \tag{5.29}$$

$$\tau_{sg}^{t} = \frac{\tau_g^t}{\sqrt{1 + C_\beta \xi^2}} \tag{5.30}$$

here,

$$\xi = \frac{\left|\vec{v}_{sg}\right| \tau_g^t}{L_g^t} \tag{5.31}$$

$$C_\beta = 1.8 - 1.35 \cos^2(\theta) \tag{5.32}$$

θ is the angle between the mean particle velocity and the mean relative velocity. τ_g^t and L_g^t are the characteristic time of the energetic turbulent eddies and the length scale of the turbulent eddies for the gas phase, respectively and are expressed as follows,

$$\tau_g^t = \frac{3}{2} C_\mu \frac{k_g}{\varepsilon_g} \tag{5.33}$$

$$L_g^t = \sqrt{\frac{3}{2}} C_\mu \frac{k_g^{3/2}}{\varepsilon_g} \tag{5.34}$$

The constant C_μ is also derived from the same air and water experiments mentioned above, Launder & Spalding (1972), and the value is found in Table 5.1.

The ratio between the Lagrangian integral time scale and the characteristic particle relaxation time, η_{sg},

$$\eta_{sg} = \frac{\tau_{sg}^t}{\tau_{sg}^F} \tag{5.35}$$

$$k_s = k_g \left(\frac{b^2 + \eta_{sg}}{1 + \eta_{sg}} \right) \tag{5.36}$$

$$k_{sg} = 2 k_g \left(\frac{b + \eta_{sg}}{1 + \eta_{sg}} \right) \tag{5.37}$$

$$D_s = \frac{1}{3} k_{sg} \tau_{sg}^t + \left(\frac{2}{3} k_s - b \frac{1}{3} k_{sg} \right) \tau_{sg}^F \tag{5.38}$$

where,

$$b = (1 + C_V)\left(\frac{\rho_p}{\rho_q} + C_V\right)^{-1} \tag{5.39}$$

C_V is the added-mass coefficient and has a value of 0.5.

The values of the constants used in the k-ε model are given in Table 5.1.

Table 5.1: Model constants in k-ε turbulence modelling, Launder & Spalding (1972) and Simonin (1996).

$C_{1\varepsilon}$	$C_{2\varepsilon}$	$C_{3\varepsilon}$	C_μ	σ_k	σ_ε
1.44	1.92	1.2	0.09	1	1.3

5.3 Euler – Lagrangian method

The Euler – Lagrangian method is described in the introduction of this chapter. The gas phase is solved through the use of the appropriate equations described in Section 5.2, while the particle phase equations are solved within the Lagrangian reference frame by tracking a number of particles. In this type of modelling the assumption that the discrete phase occupies a low volume fraction is fundamental. It is also assumed that the particle-particle interaction and that the influence of the particle volume fraction on the continuous phase is negligible. The trajectory of a single particle is described by solving the force balance on the particle. This force balance is written as:

$$\frac{dU_p}{dt} = F_D\left(U_g - U_p\right) + \frac{g\left(\rho_p - \rho_g\right)}{\rho_p} \tag{5.40}$$

Here U_g, U_p, ρ_g, ρ_p are the gas velocity, the particle velocity, the gas density and the particle density respectively. $F_D(U_g - U_p)$ is the drag force particle per mass unit.

$$F_D = \frac{18\mu_g}{\rho_p d_p^2}\frac{C_D \mathrm{Re}}{24} \tag{5.41}$$

$$\mathrm{Re} = \frac{\rho_g d_p \left|U_p - U_g\right|}{\mu_g} \tag{5.42}$$

The drag coefficient, C_D, can be expressed either by Morsi & Alexander (1972) or by Haider & Levenspiel (1989). The expression of C_D according to Morsi & Alexander (1972) is,

$$C_D = a_1 + \frac{a_2}{\mathrm{Re}} + \frac{a_3}{\mathrm{Re}^2} \tag{5.43}$$

Here the constants a_1, a_2 and a_3 are given by Morsi & Alexander (1972) for smooth spherical particles over different ranges of Re.

An alternative to the above expression of C_D is the equation proposed by Haider & Levenspiel (1989), which is as follows,

$$C_D = \frac{24}{\mathrm{Re}_{sph}}\left(1 + b_1\,\mathrm{Re}_{sph}^{b_2}\right) + \frac{b_3\,\mathrm{Re}_{sph}}{b_4 - \mathrm{Re}_{sph}} \tag{5.44}$$

where,

$$b_1 = \exp\left(2.3288 - 6.4581\phi + 2.4486\,\phi^2\right) \tag{5.45}$$

$$b_2 = 0.0964 + 0.5565\,\phi \tag{5.46}$$

$$b_3 = \exp\left(4.905 - 13.8944\phi + 18.4222\phi^2 - 10.2599\phi^3\right) \tag{5.47}$$

$$b_4 = \exp\left(1.4681 + 12.2584\,\phi - 20.7322\,\phi^2 + 15.8855\,\phi^3\right) \tag{5.48}$$

Here ϕ is the shape factor defined as,

$$\phi = \frac{s}{S} \tag{5.49}$$

Here s is the surface area of a sphere that has the same volume as the particle while S is the surface area of the particle. In the expression of Re_{sph} the diameter of the particle is exchanged with the diameter of a sphere that has the same volume as the particle.

5.3.1 Turbulent dispersion of particles

The stochastic tracking model can be used to predict the dispersion of particles due to gas phase turbulence. The effect of instantaneous turbulent viscosity fluctuations on the particle trajectories is included when using the stochastic tracking (random walk) model. The turbulent dispersion of the particles is predicted by integration of Equation 5.40 for the individual particles. In the integration the instantaneous gas velocity is expressed as, $\overline{U} + U'(t)$, along the particle path.

The integral time scale, T, is used to predict the particle dispersion. T describes the time spent in turbulent motion along the particle path, ds,

$$T = \int_0^\infty \frac{U_p'(t)U_p'(t+s)}{\overline{U_p'^2}}\,ds \tag{5.50}$$

T is proportional to the particle dispersion rate, where large values indicating more turbulence in the flow.

When using the discrete random walk (DRW) model the interaction between successions of discrete stylized gas phase turbulence and a particle is simulated. Each of the eddies are characterized by Gaussian distributed random velocity fluctuations, U' and V', and a time scale, τ_e. The values U' and V' that prevail during the lifetime of the turbulent eddy are sampled assuming that they follow the Gaussian probability distribution.

$$U' = \zeta\sqrt{\overline{U'^2}} \tag{5.51}$$

Here ζ is the Gaussian random number, $\sqrt{\overline{U'^2}}$ is the local rms (root mean square) value of the velocity fluctuations. The DRW model correlated the particle turbulent dispersion with the turbulent kinetic energy, k, of the flow. The k value is known for each point in the flow and the rms fluctuating velocities are defined as follows for the k-ε model,

$$\sqrt{\overline{U'^2}} = \sqrt{\overline{V'^2}} = \sqrt{2k/3} \tag{5.52}$$

The τ_e (the characteristic lifetime of the eddy) is defined as the constant,

$$\tau_e = 2T_L \tag{5.53}$$

T_L is not well known, but for the k-ε model it is approximated to,

$$T_L \approx 0.15\frac{k}{\varepsilon} \tag{5.54}$$

5.4 Constant viscosity model

When modelling a multiphase flow in where one or more of the phases are solids the kinetic theory of granular flow (KTGF) is used to provide closure for the solid phase. An alternative to the KTGF is to use the constant viscosity model (CVM), Kuipers (1990) and Patil et al. (2005). This means that the solid phase is modelled in the same way as the continuous (gas) phase. The solid phase stress tensor equation (Eq. 5.14) is substituted with the gas phase stress tensor (Eq. 5.21). In the equation it is assumed that the viscosity, μ_g^t, is for the solid and is assumed constant.

6. LDA MEASUREMENTS OF VELOCITY AND TURBULENCE IN A VERTICAL LIFTER

6.1 Introduction

In this chapter the mean particle velocities in axial and normal direction, U-rms and V-rms and cross-moments in a vertical gas/particle flow are measured using laser Doppler anemometry, LDA. The aim of these measurements is to investigate the effect of superficial gas velocity (U_g) and the effect of solid loading (α_s). The solid loading is measured in particle volume fraction. In Chapter 8, the results from the LDA measurements will be compared with the results from the PIV measurements presented in Chapter 7. In Chapter 9, the experimental results from both the LDA and the PIV experiments will be compared to numerical simulations performed in Fluent®.

6.2 Experimental set-up

An overview of the vertical lifter used during the experiments is presented in Section 2.1. The set-up of the laser system can be seen in Figure 6.1. The principle of LDA is given in Chapter 3.

Figure 6.1: The vertical lifter with the LDA set-up.

The laser system is delivered by Dantec Dynamics. A 3 W laser source is used. The laser system is two-dimensional, which means that two velocity components can be measured simultaneously. The wavelength of the laser lights is 488 nm (blue light) and 514.5 nm (green light) for the two velocity components, respectively. The off-axis backscatter mode was used during all of the experiments. The transmitting and receiving lenses had focal lengths of 400 and 310 mm, respectively. The LDA can only measure one point at a time and is therefore dependent on some type of traversing system. The traversing system is able to move in x, y and z direction. It follows a set of pre-determined coordinates and moves to the next specified point when the measurements in the previous point are finished. Points along the cross-section of a pipe can be measured and this will result in a profile. Table 6.1 gives a summary of the most important LDA optics.

Table 6.1: LDA specifications.

Specification	Beam system – U1	Beam system – U2
Wavelengths	514.5 nm (green light)	488 nm (blue light)
Number of fringes	35	33
Fringe spacing (μm)	5.422	5.422
Beam half-angle (deg)	2.720	2.720
Probe volume – dx (mm)	0.194	0.184
Probe volume – dy (mm)	0.194	0.184
Probe volume – dz (mm)	4.091	3.880

The measurements were performed at a height of approximately 1.3 m above the inlet of the transport pipe, at 15 or 17 different radial positions over the cross-section of the transport pipe depending on the particle types. See Figure 2.1 in Chapter 2. The first measurement point is located 1 mm from the wall and the reason for this is that it is difficult to get exact values close to the wall. It is not easy to capture the wall effect when using LDA since it is difficult to perform measurements close to the wall especially if a circular pipe is used with high refractions in the area with a small angle between the light and tangential vector of the glass surface.

The size of the particles will also influence the measurements close to the wall. According to Lee & Durst (1982) there is a particle free region near the wall, the size of this region increases with the particle diameter. A personal computer was used on-line for data acquisition and processing. The velocities measured are the axial and normal velocities. All of the experiments were performed with the same measurement conditions and acceptance criteria. The number of accepted and validated samples collected in each measuring point depends on the size of the particles. It takes a lot longer to obtain enough samples for the larger particles than it does for the smaller particles. The maximum number of samples in each point is set to 50000 for the smallest particles and 30000 for the largest particles or a sampling time of 16 min.

One important and at times difficult aspect of the LDA measurements is finding the walls of the transport pipe. The distance measured by the laser should be the same as the actual diameter of the pipe. According to Wilde et al. (2004) the LDA technique limited is to dilute gas/particle flows. The data rate decreases considerably at solid volume fractions above 1 %.

6.3 LDA-measurements

LDA measurements are performed on several types of particles and the results from these measurements are presented in this chapter. The particle properties can be seen in Table 2.1.

Moments are a form of statistics and with the help of the measured instantaneous axial, U, and normal, V, velocities they can be calculated. This calculation is automatically taken care of in the post-processing. The moments used in the LDA measurements in this thesis can be found in Section 3.4. The particle rms velocity is also referred to as fluctuations.

An outline of the experiments performed for each particle type can be seen in Table 6.2. In the first set, the superficial gas velocity is constant while the particle volume fractions are varied. In the second set, the particle volume fraction is constant while the superficial gas velocity is varied. Not all of the measurements shown in the table are performed on all of the particle types, due to varying difficulty with the measurements and time constraints. The exact measurements that are performed on each particle type are specified when the results are presented. A selection of the measurements is presented in the main part of this thesis, the rest can be found in Appendix C.

Table 6.2: Measurement matrix.

Superficial gas velocity, U_g [m/s]	Particle volume fraction, α_s [%]			
6	0.15	0.20	0.25	0.30
7	0.15	0.20	0.25	0.30
8	0.15	0.20	0.25	0.30
9	0.15	0.20	0.25	0.30
Particle volume fraction, α_s [%]	Superficial gas velocity, U_g [m/s]			
0.15	6	7	8	9

The particle volume fractions are varied from 0.15 – 0.30 % and the effect is investigated. In these investigations the superficial gas velocity is kept constant. Also the effect of superficial gas velocity is investigated. The measurements are performed at the superficial gas velocities 6 to 9 m/s at a constant particle volume fraction of approximately 0.15 %. The superficial gas velocity is the velocity of the air in the transport pipe. Due to the low concentration of particles in the pipe, it is assumed that the presence of particles will have little influence on the air velocity. The air velocity is not measured in this thesis, but calculated based on volume flow measurements.

6.3.1 Zirconium oxide, 260 μm

The measurements which are performed on zirconium oxide (ZrO_2) with a volume averaged mean diameter of 260 μm and a density of 3800 kg/m^3 are listed below:

- constant superficial gas velocity of 7 and 8 m/s and varying particle volume fractions
- constant particle volume fraction of 0.15 % with varying superficial gas velocities

The measurements are performed with a superficial gas velocity of 8 m/s and the measurements performed with a constant particle volume fraction of 0.15 % are presented in this chapter, the rest can be found in Appendix C.

Effect of particle volume fraction
In the following experiments, the superficial gas velocity is constant at 8 m/s and the particle volume fraction is varied between 0.15 – 0.30 %. Figure 6.2a show the mean axial particle velocity profiles at different particle volume fractions. The particle velocity is reduced slightly with increasing particle volume fraction. The axial velocity profiles are flat as expected for turbulent flows. The profiles have the highest value in the centre of the pipe and are reduced when approaching the wall.

The mean normal particle velocity profiles are seen in Figure 6.2b. The value of the mean normal velocity can be used as a measure of the accuracy of the LDA set-up. The value is expected to be as close to zero as possible. This criterion is met in Figure 6.2b and also for the rest of the LDA experiments. The figures containing the mean normal particle velocity profiles for the other experiments are not presented in the main part of this thesis, and are found in Appendix C.

Figure 6.2c shows the axial particle rms profiles. It can be seen from the figure that the fluctuating velocity is lowest in the centre of the pipe and increases towards the wall. No difference in the value can be observed with the increase of particle volume fraction.

The profiles in Figure 6.2d show the normal particle rms profiles. The fluctuations are expected to increase towards the wall, but it is shown in the figure to be almost constant over the cross-section. No changes can be seen from the figure with increasing particle volume fraction.

The particle cross-moments can be seen in Figure 6.2e. The profiles of the cross-moments increase towards zero at the centre of the pipe from the left hand side and then increase from zero at the right hand side. Maximum absolute values are reached near the walls, before they are expected to reach a value of zero at the wall. This tendency can be seen in the figure for all the profiles. No clear differences can be observed in the value of the profiles when the particle volume fraction increases.

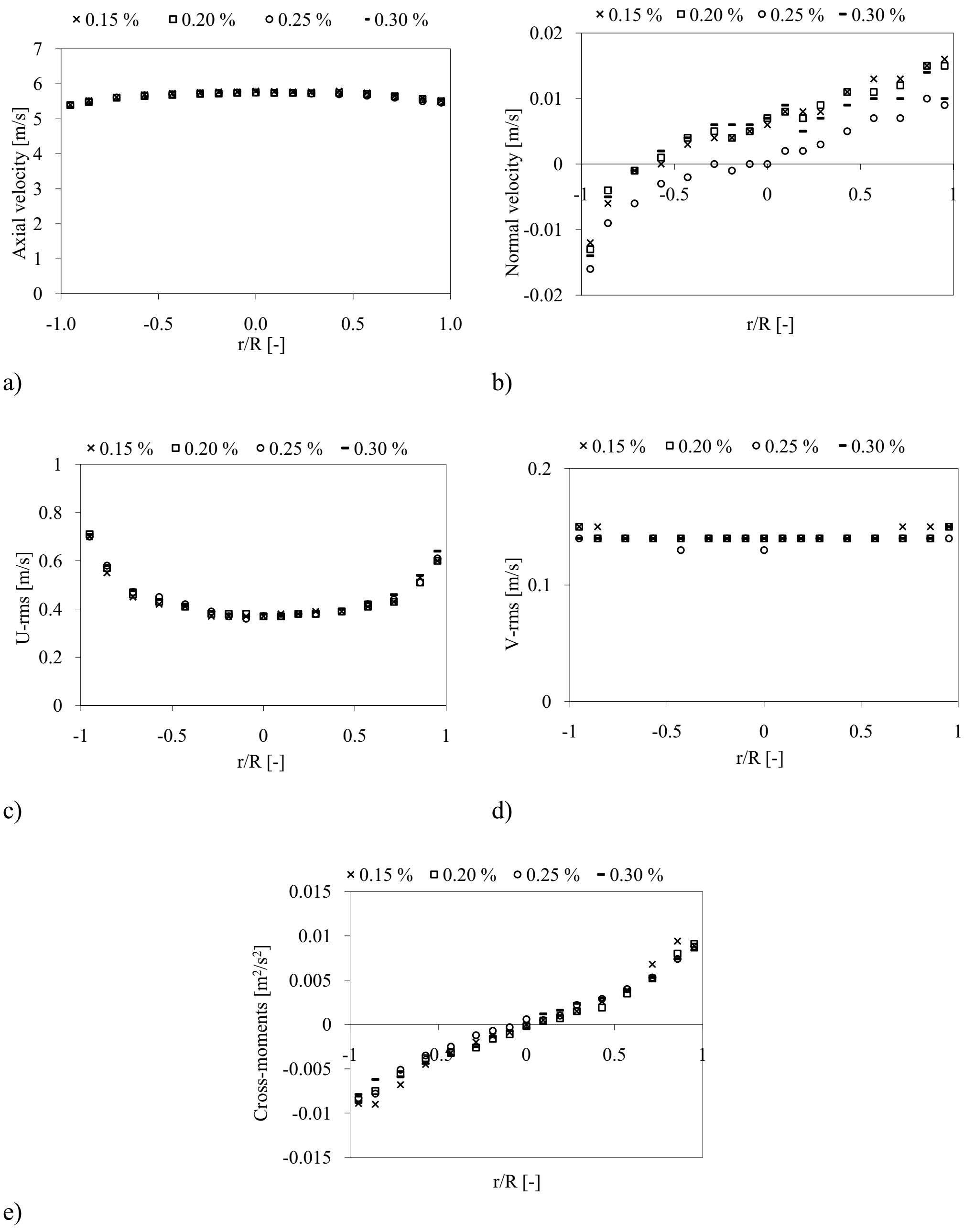

Figure 6.2: *The mean axial and normal particle velocity profiles, the axial and normal rms profiles and the cross-moment profiles for ZrO_2 particles with a diameter of 260 μm at a constant superficial gas velocity of 8 m/s and different particle volume fractions.*

Effect of superficial gas velocity

The superficial gas velocity is varied between 6 – 9 m/s while the particle volume fraction is kept constant at 0.15 %. Figure 6.3a shows the mean axial particle velocity profiles. The profiles are flat in the centre of the pipe and decrease slightly towards the wall as expected for a turbulent flow. The superficial gas velocity is increased with 1 m/s for each experiment while the particle velocity is increased with 0.6 – 0.65 m/s.

Figure 6.3b shows the axial particle rms profiles. It can be seen from the profiles that the fluctuations are lowest in the centre of the pipe. The fluctuations increase towards the wall where they reach the maximum value. The fluctuations increase with increasing superficial gas velocity.

The normal particle rms profiles can be seen in Figure 6.3c. No clear tendency can be observed from the profiles, but it can be seen that there are some differences in the centre of the pipe. Here the profiles show that the lowest fluctuations occur at the lowest superficial gas velocity and that the highest fluctuations occur for the highest. The normal fluctuating velocities are shown to be almost flat across the pipe.

The particle cross-moment profiles are shown in Figure 6.3d. The profiles are as expected with the highest values close to the wall and then an increase/decrease towards the centre of the pipe. The value of the cross-moments is zero as expected in the centre of the pipe. No change can be seen in the profiles when the superficial gas velocity is increased.

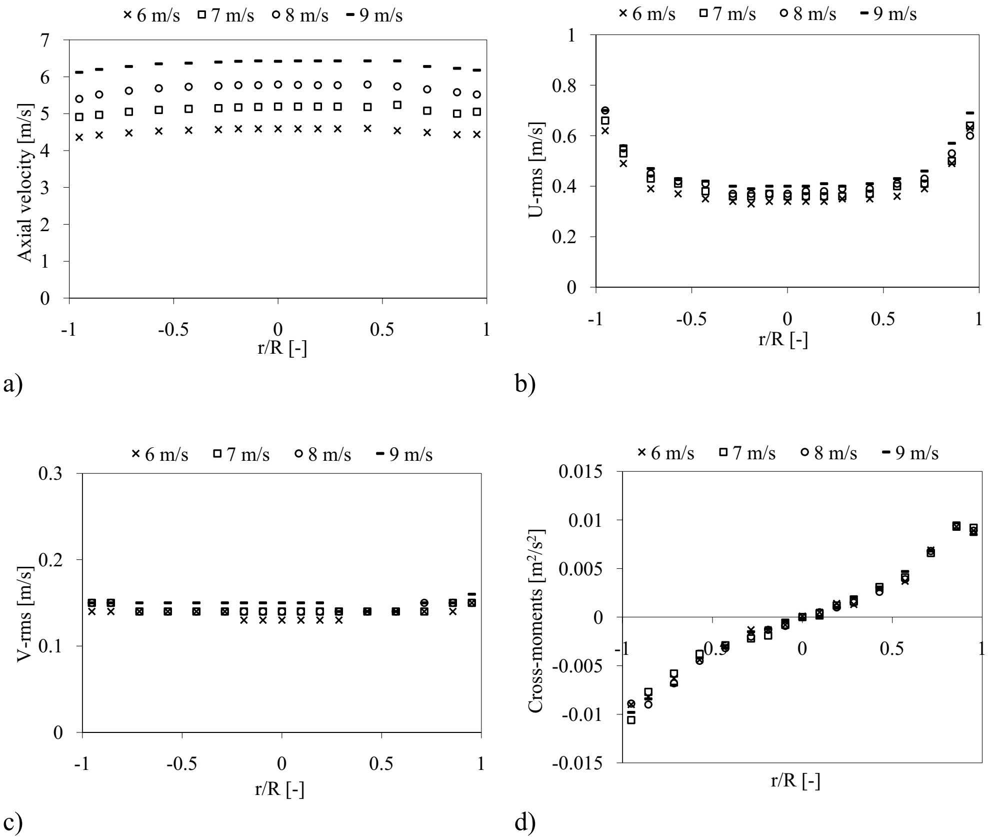

Figure 6.3: *The mean axial particle velocity profiles, the axial and normal rms profiles and the cross-moment profiles for ZrO_2 particles with a diameter of 260 µm at a constant particle volume fraction of approximately 0.15 % at different superficial gas velocities.*

6.3.2 Zirconium oxide, 530 µm

The measurements performed on zirconium oxide (ZrO_2) with a volume averaged mean diameter of 530 µm and a density of 3800 kg/m^3 are listed below:

- constant superficial gas velocity of 8 m/s and varying particle volume fractions
- constant particle volume fraction of 0.15 % with varying superficial gas velocities

The measurements presented in this chapter are performed with a constant superficial gas velocity of 8 m/s or measurements performed with a constant particle volume fraction of 0.15 %. The rest can be found in Appendix C.

Effect of particle volume fraction

In the experiments presented below the particle volume fractions are varied from 0.15 to 0.30 % at a constant superficial gas velocity of 8 m/s. The mean axial particle velocity profiles can be seen in Figure 6.4a. The velocity profiles show that the particle velocities have an apparent increase with increasing particle volume fraction. All of the profiles are flat, with a slight decrease towards the walls.

The axial particle rms velocity profiles can be seen in Figure 6.4b. The profiles show that the fluctuations decrease with increasing particle volume fraction. The fluctuations seem to be slightly varying in value in the centre of the pipe. The point closest to the right wall has been removed because of inaccuracy in the measuring of this point.

The profiles in Figure 6.4c represent the normal particle rms velocity. The measured fluctuations are constant across the pipe, with no increase towards the walls. No effect of the particle volume fraction are observed.

The particle cross-moment profiles are presented in Figure 6.4d. No clear effect of the particle volume fractions can be seen from the profiles in the figure. The shape of the cross-moment profiles is as expected with the highest value close to the wall and a value of zero in the centre of the pipe.

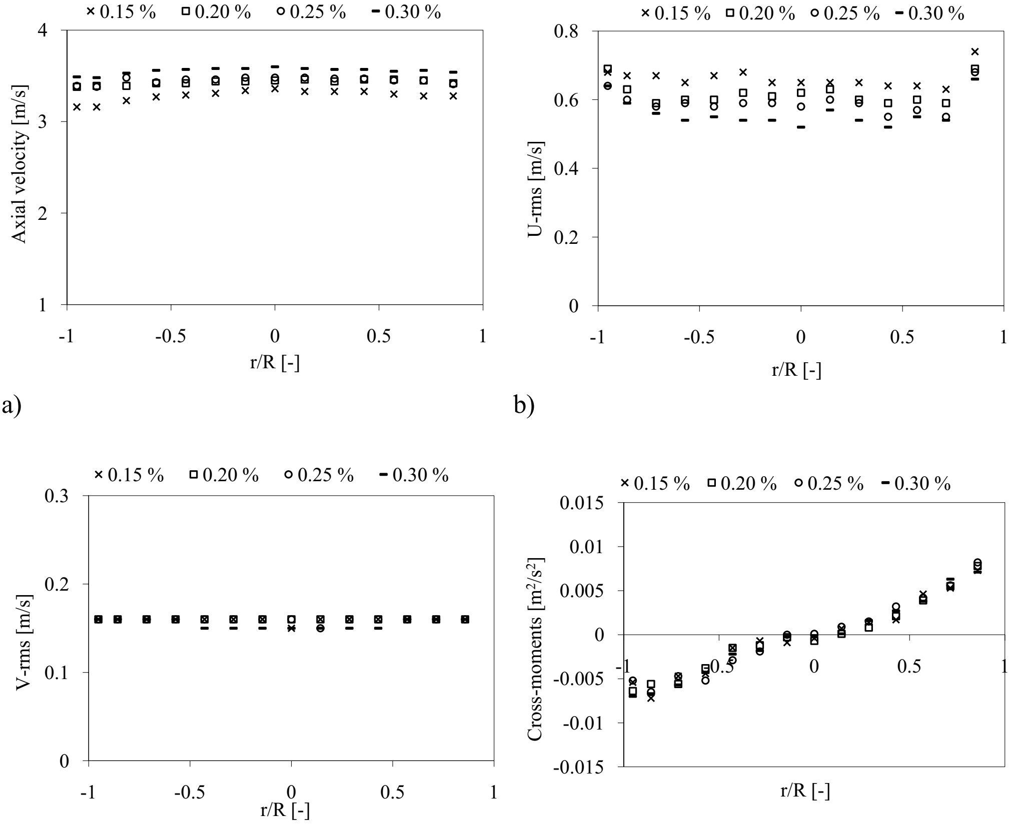

a)

b)

c)

d)

Figure 6.4: The mean axial particle velocity profiles, the axial and normal rms profiles and the cross-moment profiles for ZrO_2 particles with a diameter of 530 μm at a constant superficial gas velocity of 8 m/s and different particle volume fractions.

Effect of superficial gas velocity

In the following measurements, the particle volume fraction is kept constant at 0.15 %, while the superficial gas velocity is varied between 6 – 9 m/s. Figure 6.5a shows the mean axial particle velocity profiles. The profiles are flat over nearly the whole cross-section of the pipe, but a slight decrease can be observed close to the wall. The superficial gas velocity is increased with 1 m/s for each experiment while the particle velocity is increased with 0.42 – 0.79 m/s. It can be seen from this difference that the increments decrease with increasing superficial gas velocity. The reason for this might be that since these are the heavier particles, a superficial gas velocity of 6 – 7 m/s is not high enough to effectively transport the particles. Numerical simulations were performed, which confirmed that the increments decrease with increasing superficial gas velocity. A problem that was observed in these experiments, the same as mentioned above, is that there is a problem in measuring the point closest to the right hand wall.

The axial particle rms velocities can be seen in Figure 6.5b. The profiles in the figure show that the fluctuations increase with the increase in superficial gas velocity. It can also be seen that the fluctuations increase towards the wall.

In Figure 6.5c the normal particle rms velocity profiles are presented. No dependency on the superficial gas velocity is seen. The profiles are flat across the cross-section.

In Figure 6.5d the particle cross-moment profiles are shown. The measured cross-moments show no dependence on the superficial gas velocity.

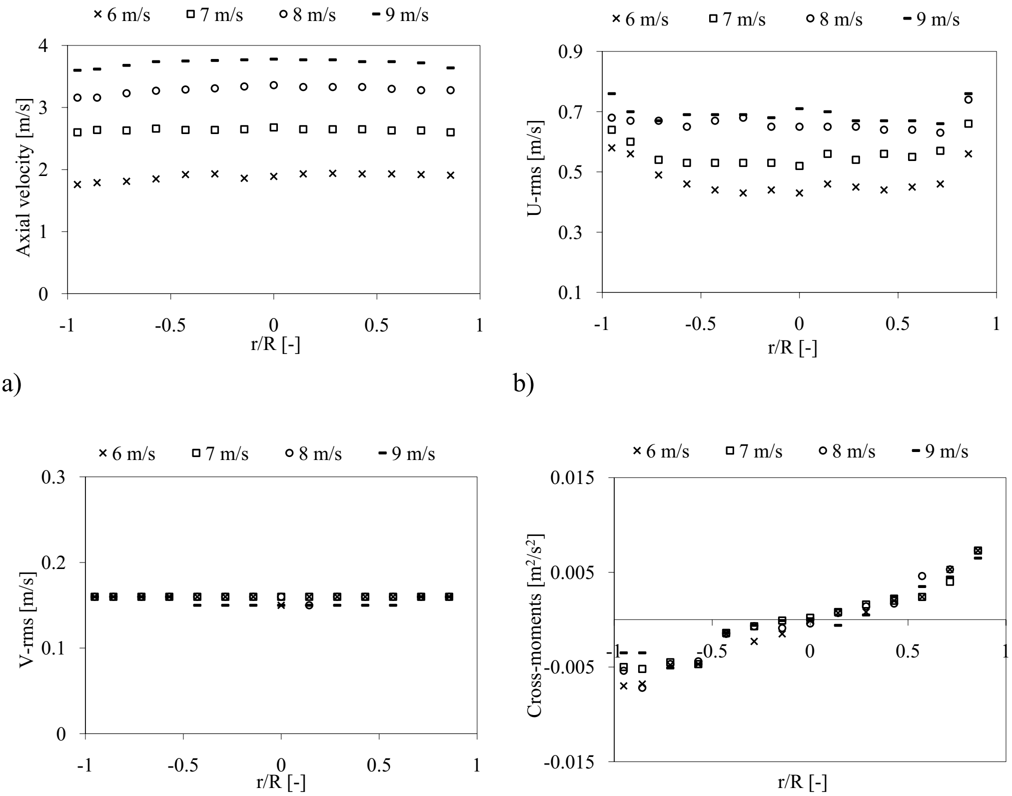

a) b)

c) d)

Figure 6.5: The mean axial particle velocity profiles, the axial and normal rms profiles and the cross-moment profiles for ZrO_2 particles with a diameter of 530 µm at a constant particle volume fraction of approximately 0.15 % at different superficial gas velocities.

6.3.3 Glass, 120 µm

The measurements performed on glass particles with a volume averaged mean diameter of 120 µm and a density of 2500 kg/m^3 are listed below:

- constant superficial gas velocity of 6, 7, 8 and 9 m/s and varying particle volume fractions
- constant particle volume fraction of 0.15 % with varying superficial gas velocity

The measurements performed with a constant superficial gas velocity of 8 m/s and the measurements performed with a constant particle volume fraction of 0.15 % are presented in this chapter. The rest can be found in Appendix C.

Effect of particle volume fraction

In the following experiments, the superficial gas velocity is constant at 8 m/s and the particle volume fraction is varied between 0.15 – 0.30 %. The mean axial particle velocity profiles are presented in Figure 6.6a. It can be seen from the figure that these profiles are not as flat as the ones that have previously been shown for ZrO_2. The profiles shown here have a more parabolic profile. All the profiles have the same value at the wall but they begin to differ when approaching the centre of the pipe. It can be seen that the profiles representing the two lowest particle volume fractions have a lower velocity than the two profiles representing the highest fractions. When looking closely at the profiles, it can be observed that the axial mean particle velocity increases with increasing particle volume fraction.

The axial particle rms velocity profiles can be seen in Figure 6.6b. All of the profiles in the figure show that the fluctuations are lowest in the centre of the pipe, and increase when approaching the wall. It can clearly be seen that the fluctuations increase with increasing particle volume fraction.

The profiles in Figure 6.6c represent the normal particle rms velocities. No clear tendencies can be seen with the increasing particle volume fraction. All of the profiles show almost the same value through the cross-section of the pipe, but a slight increase can be seen near the wall.

The particle cross-moment profiles are presented in Figure 6.6d. These profiles have a typical cross-moment shape and have a value of zero near the centre of the pipe. No clear dependence on the particle volume fraction can be observed, but in certain points it seems that the cross-moments increase with increasing particle volume fraction.

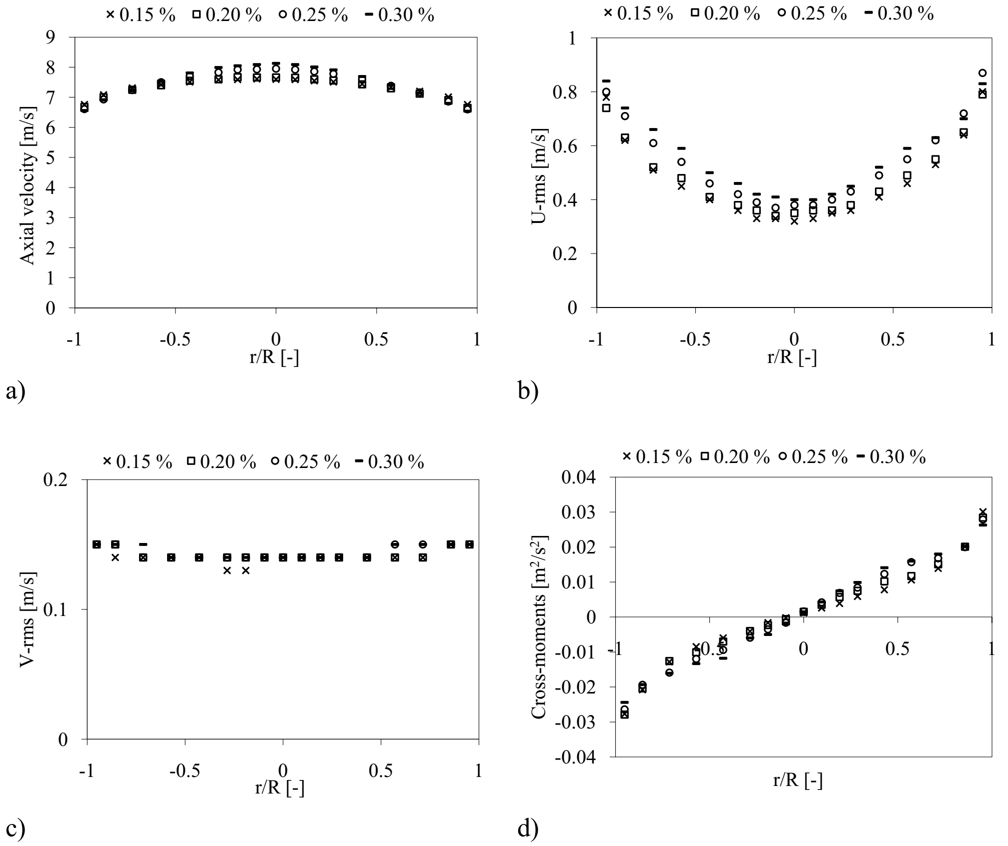

a) b) c) d)

Figure 6.6: The mean axial particle velocity profiles, the axial and normal rms profiles and the cross-moment profiles for glass particles with a diameter of 120 μm at a constant superficial gas velocity of 8 m/s and different particle volume fractions.

Effect of superficial gas velocity

For these experiments, the particle volume fraction is kept constant at approximately 0.15 % while the superficial gas velocity is varied between 6 – 9 m/s. The velocity profiles of the mean axial particle velocity can be seen in Figure 6.7a. The velocity profiles are highest in the centre of the pipe and are gradually reduced towards the walls. The superficial gas velocity increases with 1 m/s for each measurement while the axial particle velocity increases with a value of 0.77 – 1 m/s.

Figure 6.7b show the axial particle rms velocity profiles. The fluctuations are lowest in the centre of the pipe and increase towards the walls. It can be seen from the figure that the fluctuations increase with increasing superficial gas velocity in the centre of the pipe. This is not so clear closer to the wall.

The normal particle rms velocity profiles are presented in Figure 6.7c. No clear tendency can be seen in the profiles with increasing superficial gas velocity. It can be seen from the figure that the fluctuations increase slightly towards the walls, but they are still quite flat.

In Figure 6.7d the particle cross-moment profiles are presented. The figure shows that the profiles reach zero near the centre of the pipe and that the absolute value increases gradually towards the walls. No clear dependency can be seen with increasing superficial gas velocity.

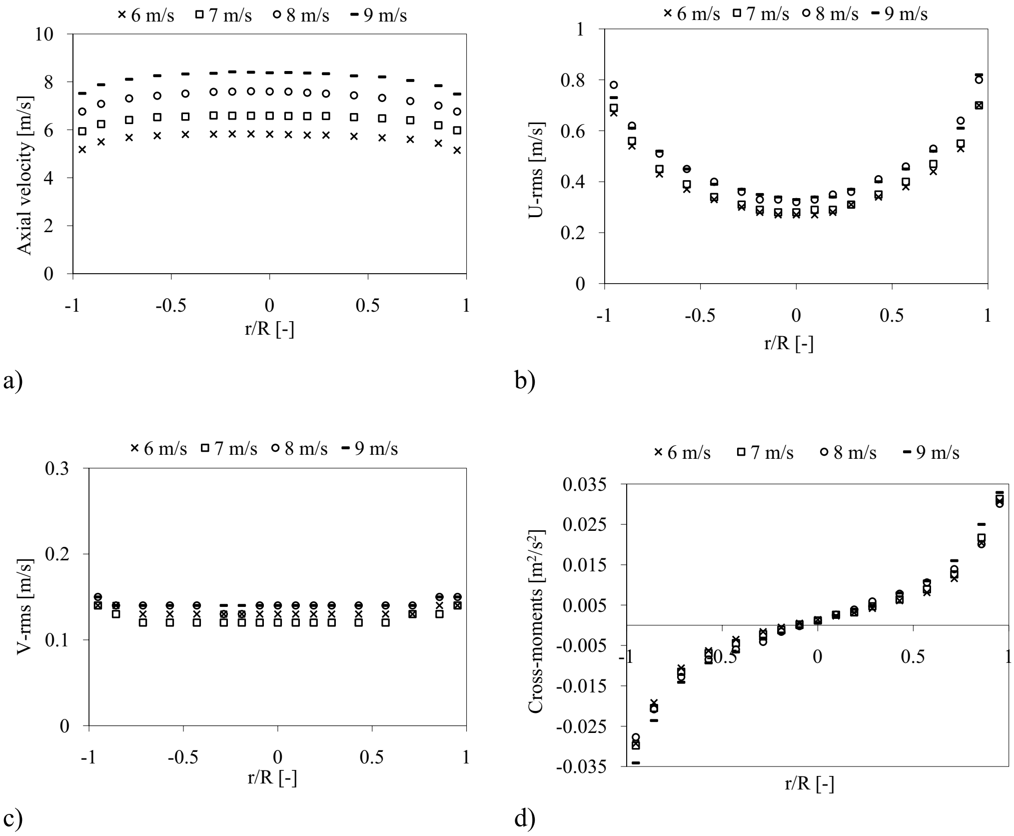

a) b)

c) d)

Figure 6.7: The mean axial particle velocity profiles, the axial and normal rms profiles and the cross-moment profiles for glass particles with a diameter of 120 μm at a constant particle volume fraction of approximately 0.15 % at different superficial gas velocities.

6.3.4 Glass, 518 μm

The measurements performed on glass particles with a volume averaged mean diameter of 518 μm and a density of 2500 kg/m^3 are listed below:

- constant superficial gas velocity of 7 and 8 m/s and varying particle volume fractions
- constant particle volume fraction of 0.15 % with varying superficial gas velocity

The measurements performed with a constant superficial gas velocity of 8 m/s and the measurements performed with a constant particle volume fraction of 0.15 % are presented in this chapter, the rest can be found in Appendix C.

Effect of particle volume fraction

The particle volume fraction is varied between 0.15 and 0.30 % and with a constant superficial gas velocity of 8 m/s. From Figure 6.8a it can be seen that there is no obvious difference in mean axial particle velocity with increasing particle volume fraction. The figure also shows that the velocity profiles are almost flat. The velocity reaches its maximum as expected in the centre of the pipe.

Figure 6.8b shows the particle U-rms velocity profiles. The fluctuations are lowest in the centre of the pipe and then increase towards the walls. The tendency is that the fluctuations are reduced when the particle volume fraction increases.

The normal particle rms velocity profiles can be seen in Figure 6.8c. The normal fluctuations seem to be constant over the whole cross-section. No dependence on the particle volume fraction is observed.

The particle cross-moment profiles are presented in Figure 6.8d. The profiles show a value of zero in the centre of the pipe and the value of the cross-moments has an absolute increase in value when approaching the wall. On the left-hand side of the pipe, the profiles reach a turning point close to the wall. The maximum value has been reached and the value decrease towards the wall. No effect of the particle volume fraction can be observed.

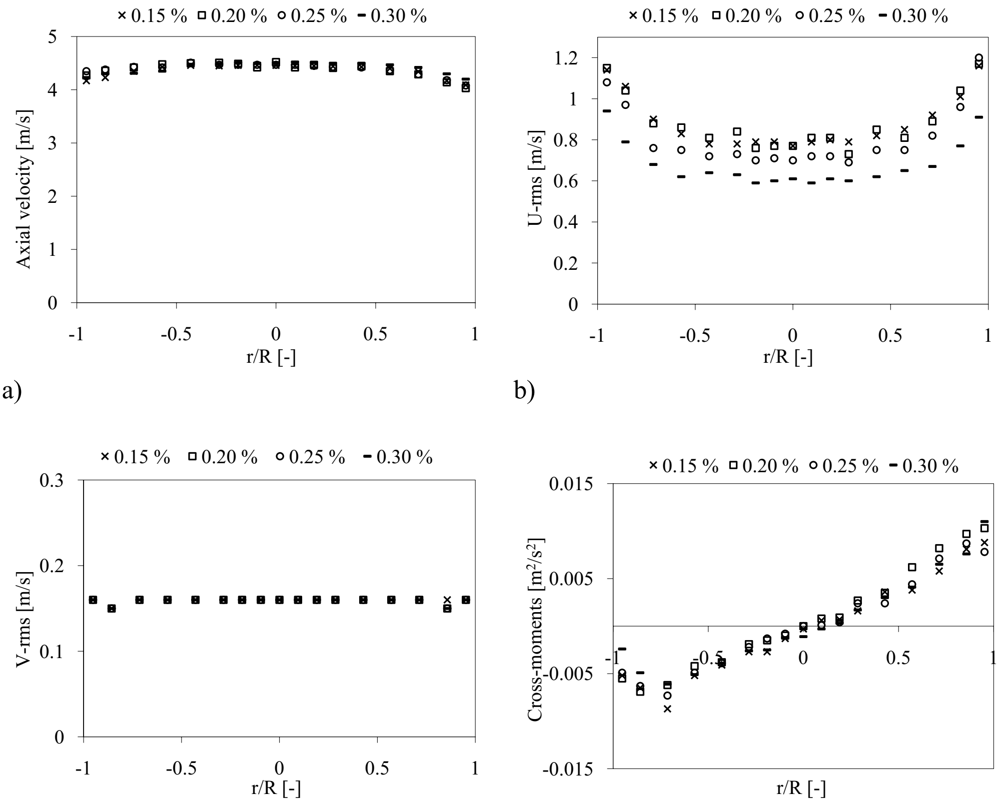

a) b)

c) d)

Figure 6.8: *The mean axial particle velocity profiles, the axial and normal rms profiles and the cross-moment profiles for glass particles with a diameter of 518 µm at a constant superficial gas velocity of 8 m/s and different particle volume fractions.*

Effect of superficial gas velocity

The superficial gas velocity is varied between 6 and 9 m/s and the particle volume fraction is kept constant at approximately 0.15 %. The mean axial particle velocity is seen in Figure 6.9a. The profiles show an increase of 0.52 – 0.75 m/s for a 1 m/s increase in superficial gas velocity. Numerical simulations were performed, which confirmed that the increments decrease with increasing superficial gas velocity. The mean axial particle velocity profiles are almost flat. The highest value can be found in the centre of the pipe with a slight decrease towards the wall. The increase in particle velocity decreases with increasing superficial gas velocity. The reason for this might be because the effect of the superficial gas velocity on the particle velocity decreases with increasing superficial gas velocity.

Figure 6.9b shows the particle U-rms velocity profiles. The fluctuations are lowest in the centre of the pipe and increase when approaching the wall. The fluctuations increase with increasing superficial gas velocity.

The particle V-rms velocity profiles are presented in Figure 6.9c. The profiles are flat across the pipe diameter. Increased superficial gas velocity does not seem to have any influence on the V-rms value.

The graph in Figure 6.9d shows the particle cross-moment profiles. The profiles have a value of zero in the centre of the pipe from which they increase towards the walls. On the right-hand side, the maximum value is reached close to the wall. On the left-hand side, this maximum is found further from the wall. An effect of an increase in superficial gas velocity can only be observed on the right hand side of the profile. Here the cross-moments decrease with increasing superficial gas velocity.

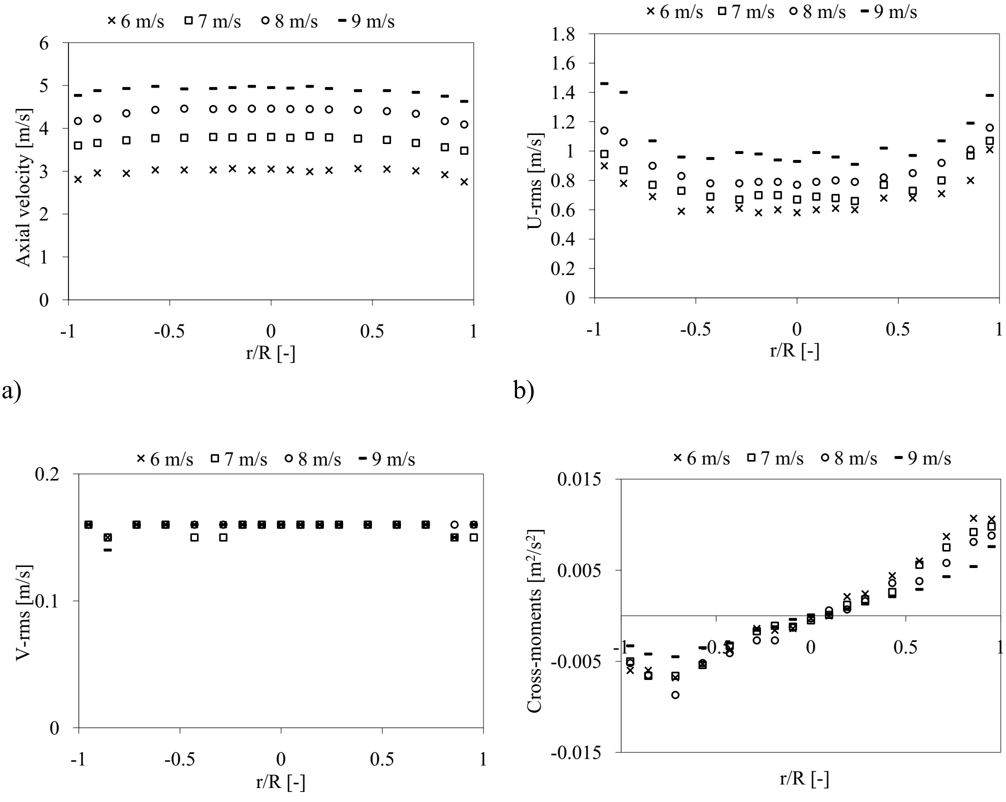

a)

b)

c)

d)

Figure 6.9: *The mean axial particle velocity profiles, the axial and normal rms profiles and the cross-moment profiles for glass particles with a diameter of 518 μm at a constant particle volume fraction of approximately 0.15 % at different superficial gas velocities.*

6.4 Summary and discussion

In this section the results from the experiments in Section 6.3 will be summarized and discussed.

Mean axial particle velocity

The measured mean axial particle velocities for the 260 μm ZrO_2 (Figure 6.2a) and 518 μm glass particles (Figure 6.8a) do not show any clear dependence on the particle volume fraction.

An increase in velocity with increasing particle volume fraction is observed for both 530 µm ZrO_2 (Figure 6.4a) and 120 µm glass (Figure 6.6a). This increase is visible over the whole cross-section for the ZrO_2 particles, but only in the centre of the pipe for the glass particles. All of the velocity profiles have the same value when approaching the wall. The reason for the increase in mean particle velocity for some of the particle types is unknown and has also been observed in Mierka and Timar (1997). According to Bolio et al. (1995) the measurements of Tsuji et al. (1984) showed that increases in particle concentration flatten the gas velocity profile in the centre of the pipe and increase the gradient near the wall.

As expected, all of the particle types show an increase in mean axial particle velocity when the superficial gas velocity increases. For the larger particles (Figure 6.5a and 6.9a) it can be observed that the increase in particle velocity decrease with increase in superficial gas velocity. The smallest increase is found when the superficial gas velocity increases from 8 to 9 m/s. The smallest ZrO_2 particles (Figure 6.3a) show an even increase in velocity with increase in superficial gas velocity. For the smallest glass particles (Figure 6.7a) the increase in particle velocity with increasing superficial gas velocity varies. The increase is the same for the increase from 6 to 7 m/s and from 8 to 9 m/.

The mean axial particle velocity profiles for 260 µm ZrO_2 at a superficial gas velocity of 7 m/s did not show any dependence on the particle volume fraction (Figure C.3a). For the measurements with 120 µm glass particles at superficial gas velocities of 6, 7 and 9 m/s it was observed that the mean axial particle velocity profiles were dependent on the particle volume fraction (Figure C.4a, C.5a and C.6a). The profiles showed that the velocity in the centre of the pipe increased with increased particle volume fraction. The measurements at a superficial gas velocity of 7 m/s for 518 µm glass showed that the two highest particle volume fractions had the highest measured velocity over the whole cross-section of the pipe (C.7a).

Mean normal particle velocity
No dependence on either the particle volume fraction or the superficial gas velocity can be seen from the measured mean normal particle velocity profiles (Figures 6.2b, C.1, C.2 and C.3b – C.7b). The profiles all show values close to zero.

Axial particle rms velocity
The axial fluctuations increase for the lightest particles, 120 µm glass particles (Figure 6.6b), when the particle volume fraction increases. No dependence can be observed for the 260 µm ZrO_2 particles (Figure 6.2c) and hence the axial fluctuations do not change when the particle volume fraction is increased. For the two heaviest particles, 530 µm ZrO2 and 518 µm glass particles (Figures 6.4b and 6.8b), the fluctuations decrease with increasing particle volume fraction.

When the superficial gas velocity increases, the axial particle rms velocity increases for all particle types (Figures 6.3b, 6.5b, 6.7b, and 6.9b).

Measurements with a superficial gas velocity of 7 m/s for 260 µm ZrO_2 particles showed no dependence on the particle volume fraction (Figure C.3c). For 120 µm glass particles with a superficial gas velocity of 6, 7 and 9 m/s an increase was observed for increased particle volume fraction (Figures C.4c, C.5c and C.6c). A dependence on the particle volume fraction was observed for the measurements of 7 m/s on 518 µm glass particles (Figure C.7c). These fluctuations generally decreased with increasing particle volume fraction.

Normal particle rms velocity

For the normal fluctuations, no dependence was found for any of the particle types on neither the superficial gas velocity nor the particle volume fraction. The measured fluctuations were almost constant in all of the experiments (Figures 6.2d, 6.3c, 6.4c, 6.5c, 6.6c, 6.7c, 6.8c, and 6.9c). In Bolio et al. (1995) results from previously unpublished data from Tsuji et al. (1984) are presented. The profiles show the normal particle fluctuating profiles at four different solid loadings and Reynolds numbers. The fluctuations seem to decrease with increasing solid loading. The profiles with the highest solid loadings show increased fluctuations when approaching the wall, while the profiles showing the lowest solid loadings have flatter profiles with no clear tendency.

None of the measurements; superficial gas velocity 7 m/s on 260 μm ZrO_2 particles, superficial gas velocity 6, 7, and 9 m/s on 120 μm glass particles, superficial gas velocity 7 m/s 518 μm glass particles, show any dependence on the particle volume fraction (Figures C.3d, C.4d, C.5d, C.6d, C.7d).

Particle cross-moment

The increase in superficial gas velocity or particle volume fraction does not have any visible effect on the cross-moment for the two types of ZrO_2 particles (Figures 6.2e, 6.3d, 6.4d and 6.5d). For the largest glass particles an increase is observed on the right hand side of the profile with increasing superficial gas velocity (Figure 6.9d) No dependence is observed for increased particle volume fraction (Figure 6.8d). An increase is observed for the smallest glass particles for increase in superficial gas velocity (Figure 6.7d), while no dependence is found for the particle volume fraction (Figures 6.6d).

None of the measurements; superficial gas velocity 7 m/s on 260 μm ZrO_2 particles, superficial gas velocity 6, 7, and 9 m/s on 120 μm glass particles and superficial gas velocity 7 m/s on 518 μm glass particles, show any dependence on the particle volume fraction (Figures C.3e, C.4e, C.5e, C.6e, C.7e).

6.5 Comparison between the particle types

In the previous part of this chapter, the results from the LDA measurements are presented and discussed. In this part, the different particle types are compared. Figure 6.10 displays the profiles of the mean axial particle velocities, particle U-rms and particle V-rms and the particle cross-moments.

All of the measurements shown in this section are performed at 8 m/s superficial gas velocity and a particle volume fraction of approximately 0.15 %. The measurement specifications given in the LDA program have been the same for all of the experiments. The only difference is the number of samples obtained from the different measurements. The size of the particles is an important factor regarding the number of samples obtained. When setting a maximum sample time that is the same for all of the experiments, the larger particles will not be able to reach the same number of samples as the smaller ones within the same time interval. This means that the number of samples that the measured values are averaged over varies from 20000 to 50000 depending on the particles. The maximum sample time is set to 16 minutes or 50000 samples whichever comes first. In experiments with the smallest particles, the limit of 50000 measurements was usually reached before the 16 minutes was up. This was not the case for the larger particles, here it is rare to reach 30000 samples.

In Figure 6.10a, the mean axial particle velocity profiles are shown. It can clearly be seen that the value of the measured particle velocities depend on the particle weight. The smallest and lightest particle type reaches a velocity close to the superficial gas velocity. The other particles have lower velocities depending on their size and density, and hence weight. The weight of the particles can be found in Table 6.3.

Table 6.3: Weight of particles.

Particle	Density [kg/m^3]	Diameter [m]	Volume [m^3]	Weight [kg]
ZrO_2	3800	260 x 10^{-6}	9.2 x 10^{-12}	3.5 x 10^{-8}
ZrO_2	3800	530 x 10^{-6}	7.8 x 10^{-11}	3.0 x 10^{-7}
Glass	2500	120 x 10^{-6}	9.0 x 10^{-13}	2.3 x 10^{-9}
Glass	2500	518 x 10^{-6}	7.3 x 10^{-11}	1.8 x 10^{-7}

From the table above it can be seen that if the particle types are arranged after increasing weight the following sequence is found:

1. Glass particles with a diameter of 120 x 10^{-6} m
2. ZrO_2 particles with a diameter of 260 x 10^{-6} m
3. Glass particles with a diameter of 518 x 10^{-6} m
4. ZrO_2 particles with a diameter of 530 x 10^{-6} m

For the largest particle size of both ZrO_2 (530 µm) and glass (518 µm), the major dissimilarity is probably due to the difference in density, 3800 kg/m^3 for ZrO_2 and 2500 kg/m^3 for the glass. The velocity difference between the air velocity and the measured particle velocity is called the slip velocity which is shown in Eq. 2.2. Larger and heavier particles have a higher slip velocity than smaller and lighter particles.

It can also be seen from Figure 6.10a that the profiles are flat. Only the profile of the smallest and lightest particle shows a clear reduction in velocity when approaching the wall. The last point closest to the wall is removed due to some difficulty in the measurements for the largest ZrO_2 particles. Lee & Durst (1982) reported that from their experiments with 800 µm particles, the axial gas velocity profiles become flatter and that the axial fluctuating velocity increases. They also report that the opposite has been observed for small particles. Tsuji et al. (1984) measured the axial mean and fluctuating velocities on 200 µm and 500 µm polystyrene spheres with a density of 1020 kg/m^3. They report that mean axial velocity profiles seem to flatten with increasing particle size.

Figure 6.10b shows the particle U-rms velocity profiles Generally the largest particles have higher fluctuations. From the figure, it can be seen that the largest glass particles have the highest fluctuations, followed by the largest ZrO_2 particles. The smallest particles have the lowest fluctuations followed by the smallest ZrO_2 particles. These show almost the same fluctuations in the centre of the pipe, but the fluctuations are highest for the glass particles when approaching the wall. The largest ZrO_2 particles have the flattest profile, while the others show a clearer increase towards the walls. It is difficult to draw clear conclusions on the particle fluctuation depending on particle diameter and particle density based on the above observations.

According to Pakhomov el al. (2007), the addition of particle into a turbulent carrier flow decrease the level of turbulence because of particles involvement into fluctuation motion. In Littman et al. (1993) the experimental findings of Lee and Durst (1982) and Tsuji et al. (1984) where discussed. From these studies, it is found that large particles increase the level of gas phase turbulence and that smaller particles reduce the level of gas phase turbulence. Littman et al. (1993) also found that when comparing these sets of data it is indicated that the gas phase turbulence level increase with particle density. The enhanced gas phase turbulence because of large particles is according to Hetsroni (1989) due to the vortex shedding from their wakes. The profiles in Figure 6.10c show the particle V-rms velocity profiles. The figure shows that the measured fluctuations in the current experimental data follow the above reported tendencies, the fluctuations are higher for the larger particles than for the smaller particles.

The graph in Figure 6.10d shows the particle cross-moment profiles. Only the profile for the smallest glass particles differ from the rest, all the others have similar shapes and values.

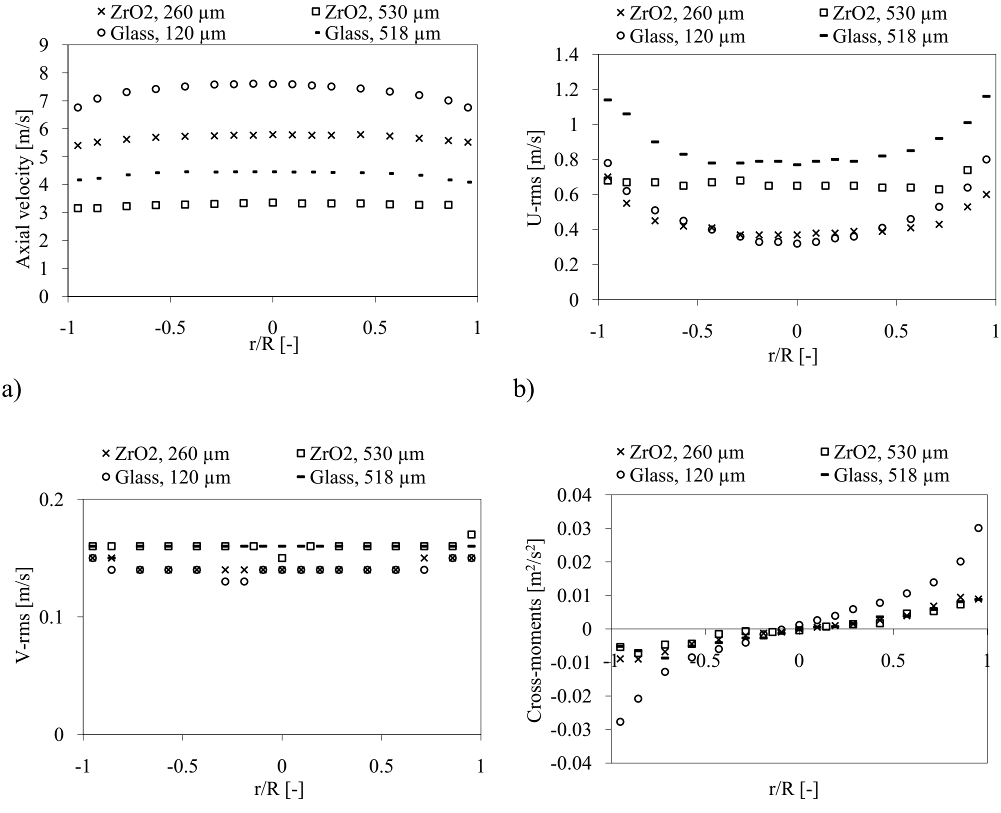

a)

b)

c)

d)

Figure 6.10: The mean axial particle velocity profiles, the axial and normal rms profiles and the cross-moment profiles at a constant particle volume fraction of approximately 0.15 % and a superficial gas velocity of 8 m/s.

6.6 Conclusion

In Chapter 6 and Appendix C the results from the experimental investigation with LDA are presented. Here the effects of particle volume fraction and superficial gas velocity on the mean axial and normal particle velocity, particle U-rms and V-rms, and the particle cross-moment are found. The effect of the particle volume fraction on the aforementioned parameters varies depending on the particle type. The particles used are 260 and 530 μm ZrO_2 and 120 and 518 μm glass particles.

When comparing the different particle types, the results are as expected and the largest and heaviest particles have the lowest axial velocity when the results from the experiments at a constant superficial gas velocity of 8 m/s and a constant particle volume fraction of 0.15% are compared. The axial and normal fluctuations are greatest for the largest particles. The cross-moment profiles had the expected shape for all of the particle types. The smallest and lightest particle type have the highest cross-moment value.

120 μm glass particles and 530 μm ZrO_2 particles show an increase in particle velocity when the particle volume fraction is increased. For the two other particle types, 518 μm glass and 260 μm ZrO_2, no dependence on the particle velocity is found for the particle volume fraction. All of the particle types showed an increase in axial particle velocity with increasing superficial gas velocity. None of the particle types showed any change in the measured normal particle velocity when varying the superficial gas velocity or the particle volume fraction.

The axial particle rms velocity increases for 120 μm glass particles with increasing superficial gas velocity. The opposite is observed for 518 μm glass and 530 μm ZrO_2 particles. No dependence of the particle volume fraction for the axial particle rms is found for 260 μm ZrO_2 particles. Fluctuations increased for all particle types with increase in superficial gas velocity. No dependence of the particle volume fraction and the superficial gas velocity is found on the normal particle velocity of any of the particle types.

The cross-moment increased with increasing superficial gas velocity for 120 μm glass particles. None of the other particle types showed any clear dependence on neither the particle volume fraction nor the superficial gas velocity.

The LDA technique can be used to study the solids phase in a two phase flow. There are some difficulties with measuring the flow close to the wall due to the curvature of the pipe wall. Another limitation with the technique is also observed. The number of particles in the system have a great influence on the effectiveness of the technique. In order to achieve information that correctly describes the flow, a minimum number of particles must be measured. Since one particle is registered and evaluated at a time, a low particle number density in the system means that the experiments can be time consuming. Large particles only enhance this problem, because there are fewer particles in the system. This investigation shows that the use of LDA on the two smaller particle types for all of the solid loadings is very effective.

6.7 Sources of error

Below is a discussion of possible sources of error identified during the experimental investigation with LDA.

- Flow meter. Some error is expected in adjustment of the flow meter for the superficial gas velocity and small variations can occur during the experimental investigations.
- Air flow from compressor. During the course of an experiment no variation in the superficial gas velocity is observed, but small deviations might occur.
- Electrostatic charging. It is obvious from the measurements when electrostatic charging affected the flow, but it is difficult to remove all of the charging. Measures are taken to reduce the problem and the measurements are performed when no apparent charging is observed.

- Fluidizing air. The amount of fluidization air varied from measurement to measurement depending on the particle volume fraction. No apparent influence from the addition of fluidization air is observed in the experiments. Variation in the fluidization air can lead to variation in the particle number density in the transport pipe during experiments.
- Segregation in the fluidization silo. The particles had a particle size distribution and segregation can have occurred. No measures are taken to investigate this and the problem is assumed to be of little importance.
- Near wall measurements. When the laser light travel through the pipe wall it changes direction slightly due to the curvature of the wall. This distortion increases as the measurements along the cross-section approaches the wall. This can affect the measurements, especially for LDA where the control volume is made up of four laser beams. Both the position and the orientation of the fringes are affected by the curvature of the wall. Errors corresponding with the position will be attributed to the measured velocity, Lu et al. (2009). The use of a channel instead of a circular pipe would reduce this problem.
- Yang and Kuan (2006) performed an extensive investigation of errors on parameters measured by LDA using a TSI –Aerometrics 2d back-scattering set-up.
- Accuracy of the traversing system for LDA. Very good accuracy is reported, but very small inconsistencies in the movement can have some small affect on the measurements.
- Alignment of the LDA experimental set-up. It is difficult to achieve a 100% accurate aligned set-up. The traversing system is used to find the centre of the transport pipe, and the normal velocity can be used as a measure of accuracy. A value for the normal velocity close to zero represents an aligned laser set-up.

7. PIV MEASUREMENTS OF VELOCITY AND TURBULENCE IN A VERTICAL LIFTER

7.1 Introduction

In this chapter the measurement technique PIV, particle image velocimetry, is used to measure the mean and fluctuating velocities in axial and normal direction together with the particle cross-moment in a vertical gas/particle flow. The aim of these measurements is to investigate the effect of superficial gas velocity (U_g) and the effect of solid loading (α_s) on the particle velocity when using this technique. The same experiments are measured with both LDA and PIV, the results from the investigation with LDA can be found in Chapter 6. In Chapter 8, the results from the PIV measurements are compared to the LDA results and the main difference between the two techniques are discussed. In Chapter 9, the experimental results from both the LDA and the PIV experiments are compared to numerical simulations performed in Fluent®.

7.2 Experimental set-up

An overview of the vertical lifter used in the experiments is presented in Section 2.1. The arrangement of the laser system is the same for all the experiments. The general set-up of the laser system is illustrated in Figure 4.6.

The PIV system delivered by Dantec Dynamics consists of two 100 Hz 2 x 5 mJ litron lasers and a Nanosense Mkl camera (CMOS sensor) with a 60 mm lens. The use of a dual laser system makes it possible to fire two pulses within a very short time interval. The two image frames captured on the camera are post-processed through adaptive correlation in a computer program, FlowMangager, delivered by Dantec Dynamics. This correlation is described in Chapter 4. Table 7.1 gives a summary of the most important PIV specifications.

Table 7.1: PIV specifications.

Wavelength	532 nm
Time delay between pulses	120 µs
Trigger frequency	50 Hz
IA (final)	32 x 32 pixels
Camera sensor	CMOS
Camera resolution	1260 x 1024 pixels

The measurements are performed at a height of approximately 1.3 m above the inlet of the transport pipe. The result of the adaptive correlation is a vector map. The vectors that are immediately accepted are blue, while vectors that have been substituted are green. The substituted vectors are vectors that have been calculated based on the value of their neighbouring vectors since they are originally rejected. Figure 7.1 shows the picture taken by the camera with the calculated vectors on top. From this figure, it can be seen that most of the substituted vectors are found outside of the pipe wall where there are no particles.

It is important to notice that for any experimental investigation problems will arise when doing measurements close to a wall. One reason why it is difficult to get good measurements close to the wall can be because the measurement volume is not small enough. Another problem occurs when the measurements are performed on a circular pipe. Here the thickness of the wall will be an issue. To reduce this problem a channel can be used when possible. For PIV measurements there are several uncertainties linked to the wall vectors. Parts of the interrogation area can cover both the outside of the wall and the wall itself. In these areas, there are no particles and the vectors are most likely substituted. In the results presented later in this chapter the vectors closest to the wall is often rejected and left out of the graph. In addition, other problems will arise when doing measurements. The most common is unwanted reflection either from the particles or from the glass pipe. The reflection from the glass wall can be removed by coating the inside of the pipe with black paint where the laser beam intersects the glass wall on the way out of the measurement section. This has not been tried during these experiments because of difficulties coating the right area. The flow is gas/particle and will therefore have a sand blowing effect on the coating.

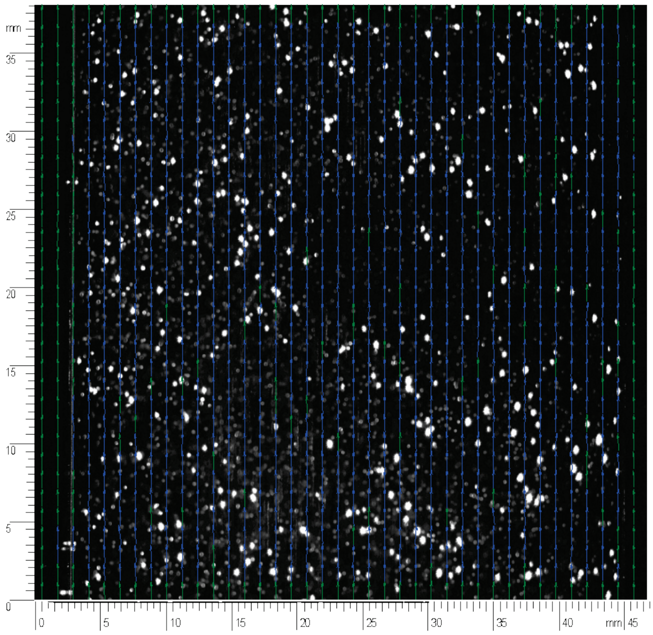

Figure 7.1: The instantaneous vector map placed on top of a picture of the flow.

The final vector map is averaged over approximately 5000 measurements and can be seen in Figure 7.2. In order to see them more clearly only every second vector is shown and their size is increased.

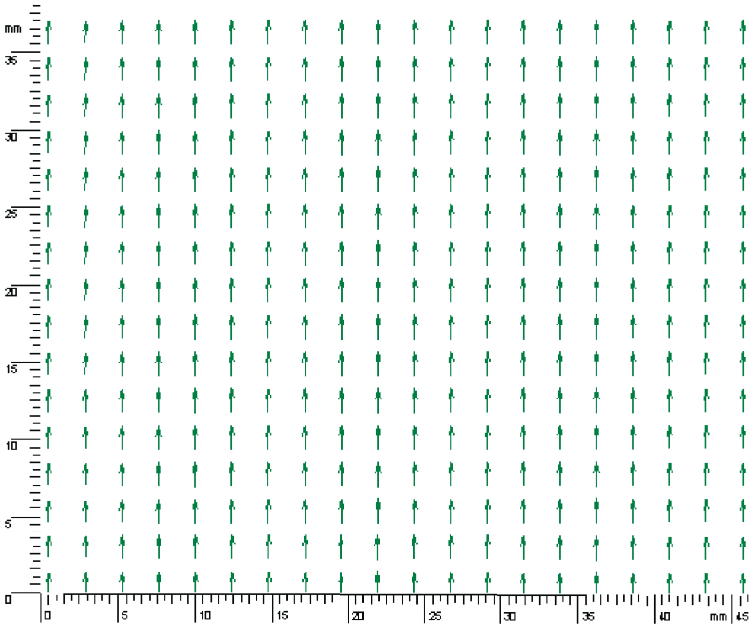

Figure 7.2: The average vector map.

7.3 PIV-measurements

PIV measurements are performed with several types of particles and the results from these measurements are presented in this chapter. The particle mean diameter and density are given in Table 2.1 in Section 2.2. A description of how the size distribution of the particles can be found is presented in Appendix A. The values of the axial and normal velocities are transferred to a Matlab script made by Sondre Vestøl. In this script, the axial and normal mean and fluctuating velocities and the cross-moment can be calculated from the measured axial and normal velocities using Equations 4.3 – 4.5 found in Chapter 4. The Matlab script can be found in Appendix B.

An outline of the experiments performed for each particle type can be seen in Table 6.2. In the first set, the superficial gas velocity is constant while the particle volume fractions are varied. In the second set, the particle volume fraction is constant while the superficial gas velocity is varied. The results from the measurements performed with a superficial gas velocity of 8 m/s and the measurements performed with a constant particle volume fraction of 0.15 % are presented in the following sections, and the rest can be found in Appendix D

7.3.1 Zirconium oxide, 260 μm

An overview of the measurements performed on zirconium oxide (ZrO_2) with a mass averaged mean diameter of 260 μm and a density of 3800 kg/m^3 is given in Table 6.2.

Effect of particle volume fraction

In the following experiments, the superficial gas velocity is constant at 8 m/s and the particle volume fraction is varied between 0.15 – 0.30 %. Figure 7.3a shows the axial mean particle velocity profiles at different particle volume fractions. It can be seen from the figure that there are some differences between the velocities on the left and the right hand side of the transport pipe. On the left hand side, there is a difference in velocity between the measurements. It can be observed that the particle velocity is reduced with increasing particle volume fraction. On the right hand side, it is difficult to distinguish between the measurements. By observing the pictures of the flow, it can be seen that the flow is quite dense for PIV. This may lead to differences in illumination of the flow and can be observed by looking at the pictures. In areas where the illumination is good, more particles are visible. Another problem that can be seen is that some particles reflect more light than other particles. These particles will often look larger than their actual size and may have different illumination intensity between the two correlated images. This can also lead to overshadowing of the surrounding particles. The asymmetry of the profile can also be due to electrostatic charging of the flow. The axial velocity profiles are flat as expected for turbulent flows. The profiles have the highest value in the centre of the pipe and falls somewhat towards the wall.

The normal mean particle velocity profiles are shown in Figure 7.3b. It is desirable that the value of the normal velocity is as close to zero as possible. For this type of flow, there should be no net normal particle movement if averaged over a long time. The measured values in Figure 7.3b are all inside this criteria.

Figure 7.3c shows the axial particle rms profiles. It can be seen from the figure that the fluctuating velocity is lowest in the centre of the pipe and increases towards the wall.

The graph in Figure 7.3d shows the normal particle rms profiles. The fluctuations are expected to increase towards the wall. No clear tendencies can be seen from the figure except that the lowest particle volume fraction has a slightly higher normal fluctuating velocity than the rest.

The particle cross-moments can be seen in Figure 7.3e. The profiles of the cross-moments usually increase towards zero at the centre of the pipe from the left hand side and then increases from zero at the right hand side. A maximum absolute value is reached close to the wall. This tendency can only be observed by the profile with the lowest particle volume fraction. The other profiles do not follow this tendency. Several experiments are performed not only with a superficial gas velocity of 8 m/s, but also for the other velocities, 6, 7 and 9. All of these give the same result.

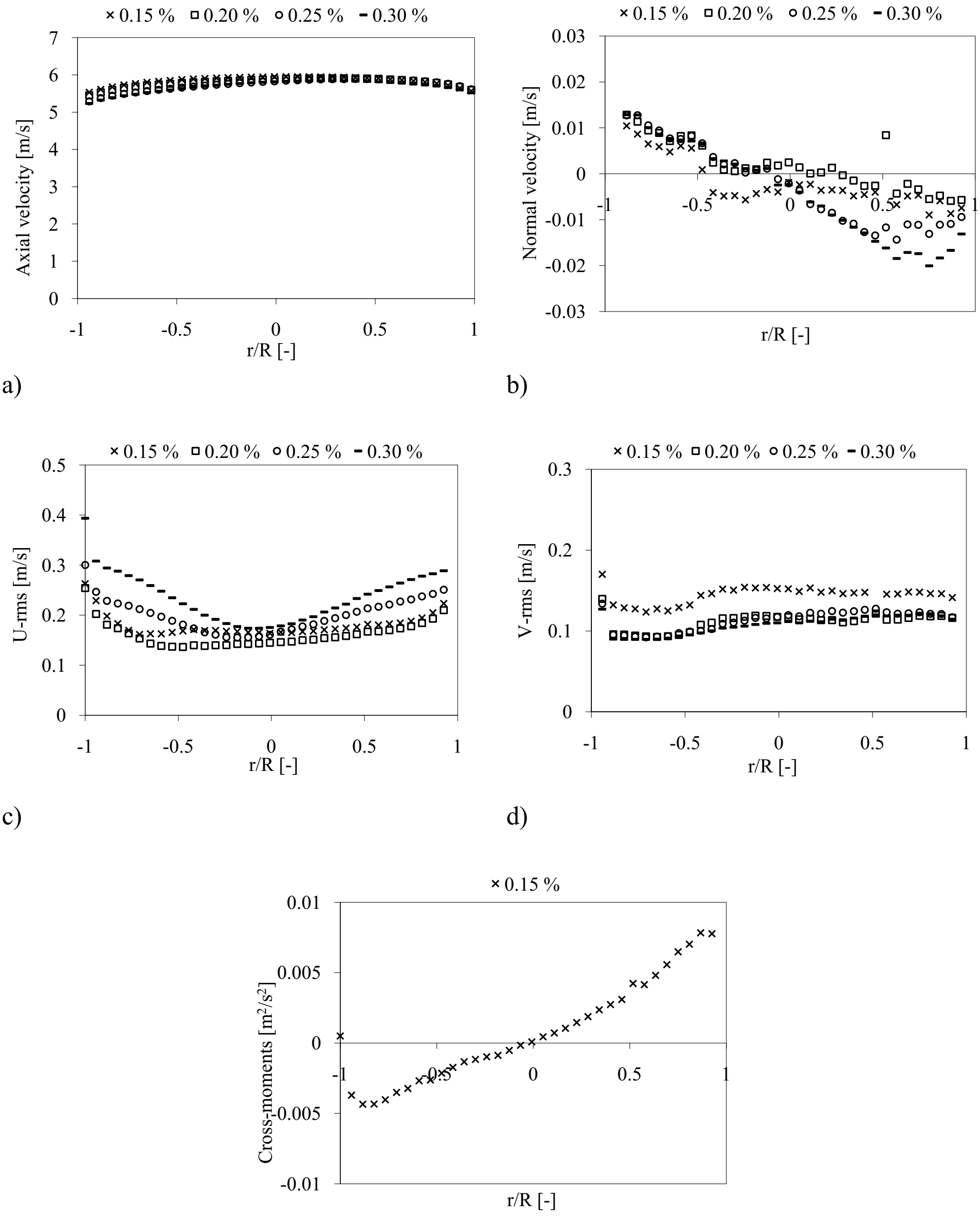

a)

b)

c)

d)

e)

Figure 7.3: *The mean axial and normal particle velocity profiles, the axial and normal rms profiles and the cross-moment profiles for ZrO_2 particles with a diameter of 260 µm at a constant superficial gas velocity of 8 m/s and different particle volume fractions.*

Effect of superficial gas velocity

The superficial gas velocity is varied between 6 – 9 m/s while the particle volume fraction is kept constant at 0.15 %. Figure 7.4a shows the axial mean particle velocity profiles. The profiles are flat in the centre of the pipe and decrease slightly towards the wall as expected for a turbulent flow. The superficial gas velocity is increased with 1 m/s for each experiment while the particle velocity is increased with 0.6 – 0.7 m/s.

Figure 7.4b shows the axial particle rms profiles. It can be seen from the figure that there are less fluctuations at the centre of the pipe. The highest fluctuations are located close to the wall. The profiles in the figure show a fall in the fluctuations when approaching the left wall before the fluctuations increase again when approaching the wall. This drop in fluctuations may be due to reflections captured by the camera which would cause some problem in the raw data. On the right hand side of the pipe, the fluctuations increase gradually towards the wall. The fluctuations increase with increasing superficial gas velocity.

The normal particle rms profiles can be seen in Figure 7.4c. The normal fluctuating velocity increases with increasing superficial gas velocity. One point in each profile stands out from the rest, and this is probably due to some measurement problems for this point in the raw data. Since the fluctuating velocities are derived from the normal velocities, problems that occur there will affect the value of both the V-rms and the cross-moments.

The particle cross-moments are presented in Figure 7.4d. The value should have been zero in the centre of the pipe, instead it intersects a little to the left. The reason for this can be that the flow is pulled slightly to the left. Static charging can have an effect on the flow pattern. It can be seen from the figure that the cross-moments increase with increasing superficial gas velocity.

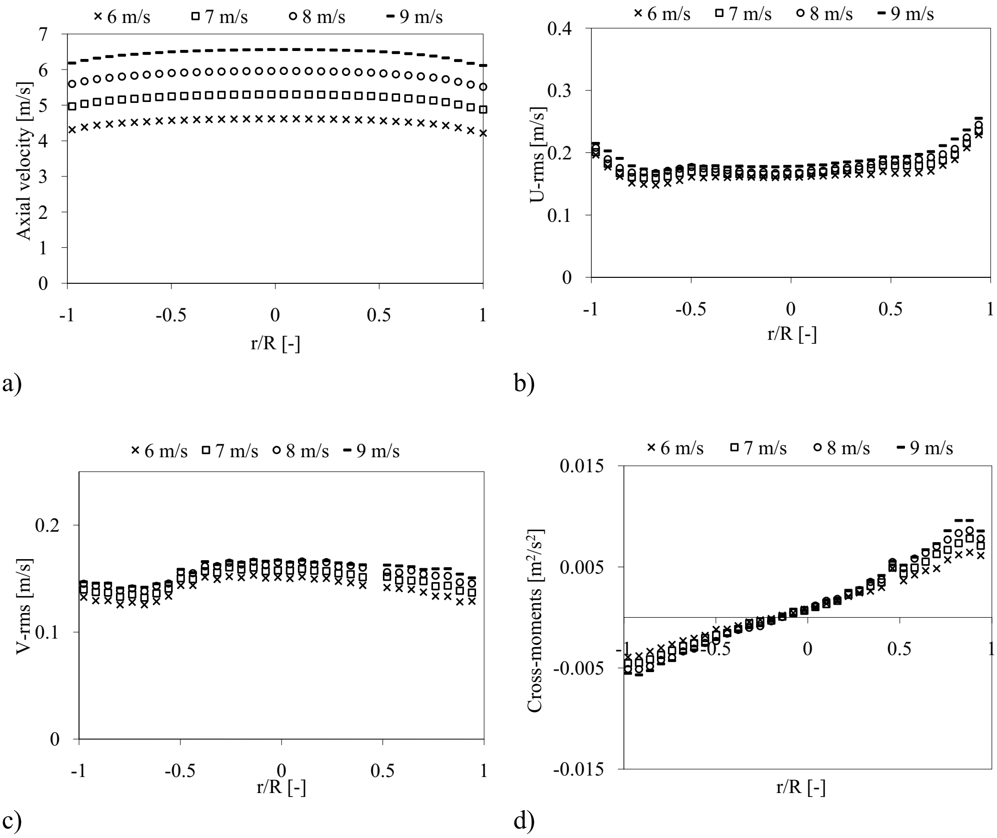

a)
b)
c)
d)

Figure 7.4: *The mean axial particle velocity profiles, the axial and normal rms profiles and the cross-moment profiles for ZrO_2 particles with a diameter of 260 µm at a constant particle volume fraction of approximately 0.15 % at different superficial gas velocities.*

7.3.2 Zirconium oxide, 530 µm

An overview of the measurements performed on zirconium oxide (ZrO_2) with a volume averaged mean diameter of 530 µm and a density of 3800 kg/m^3 is given in Table 6.2. These particles lie on the B/D border in Geldart's classification, but are group D particles according to the mean diameter.

Effect of particle volume fraction

In the experiments below the superficial gas velocity is kept constant at 8 m/s while the particle volume fraction is varied between 0.15 – 0.30 %. Figure 7.5a shows the axial mean particle velocity. It can be seen from the figure that the velocity is highest in the centre of the pipe. The velocities decrease slightly towards the walls. By looking closely at the profiles it can be seen that the velocity is lowest for the smallest particle volume fraction.

The axial particle rms profiles are presented in Figure 7.5b. The fluctuations are expected to increase towards the wall and this tendency can be seen in the figure. It can also be seen that the fluctuations increase with decreasing particle volume fraction.

The graph in Figure 7.5c shows the normal particle rms profiles. The fluctuations are expected to increase towards the wall. The profiles in the figure are quite flat and do not show the expected increase near the wall. The fluctuations are again observed to be increasing with decreasing particle volume fraction. In one point on the right hand side of the pipe the value for all the different particle volume fractions stand out from the rest. The reason for this can be some problem with the measuring in this point, possibly due to reflections.

Figure 7.5d shows the particle cross-moment profiles. They have the expected shape even though they reach zero value a bit right of the centre point. This might be because the flow is pulled to the right, maybe due to static charging. The figure shows that the cross-moments increase with decreasing particle volume fraction.

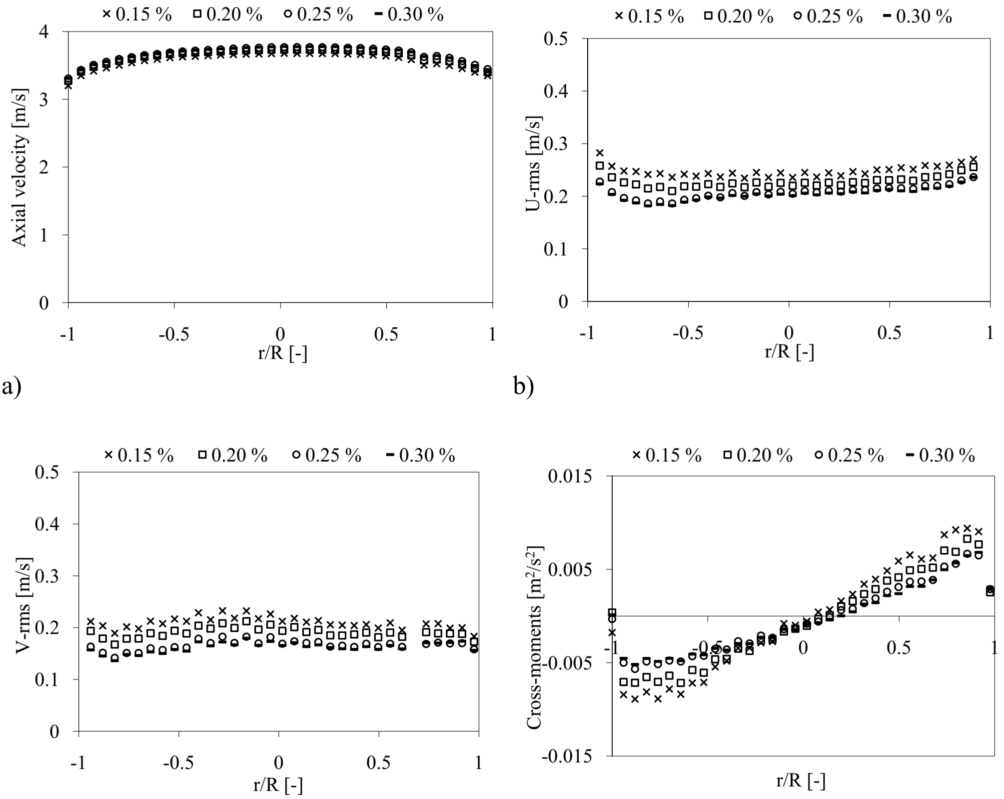

a)

b)

c)

d)

Figure 7.5: *The mean axial and normal particle velocity profiles, the axial and normal rms profiles and the cross-moment profiles for ZrO_2 particles with a diameter of 530 µm at a constant superficial gas velocity of 8 m/s and different particle volume fractions.*

Effect of superficial gas velocity

Figure 7.6a shows the axial mean particle profiles for superficial gas velocities ranging from 6 – 9 m/s. The superficial gas velocity is increased with 1 m/s for each experiment while the particle velocity increased with 0.56 – 0.75 m/s. The relative increase in particle velocity decreases with increasing superficial gas velocity. Numerical simulations were performed, which confirmed that the increments decrease with increasing superficial gas velocity. This can also be seen in the LDA experiments. All the profiles reach their highest value in the centre of the pipe and decrease slightly towards the wall.

The axial particle rms profiles are presented in Figure 7.6b. The profiles show that the fluctuations are lowest in the centre of the pipe and that they increase when approaching the wall. The fluctuations also increase with increasing superficial gas velocity.

Figure 7.6c displays the normal particle rms profiles. The fluctuations are expected to increase towards the wall, but the figure shows that the profiles are fairly flat. There is also a problem with one of the measured values in all of the profiles. The profiles show that the fluctuations increase with increasing superficial gas velocity.

The particle cross-moment profiles are shown in Figure 7.6d. It can be seen from the figure that they have a value of zero in the centre of the pipe and that the cross-moments increase with increasing superficial gas velocity.

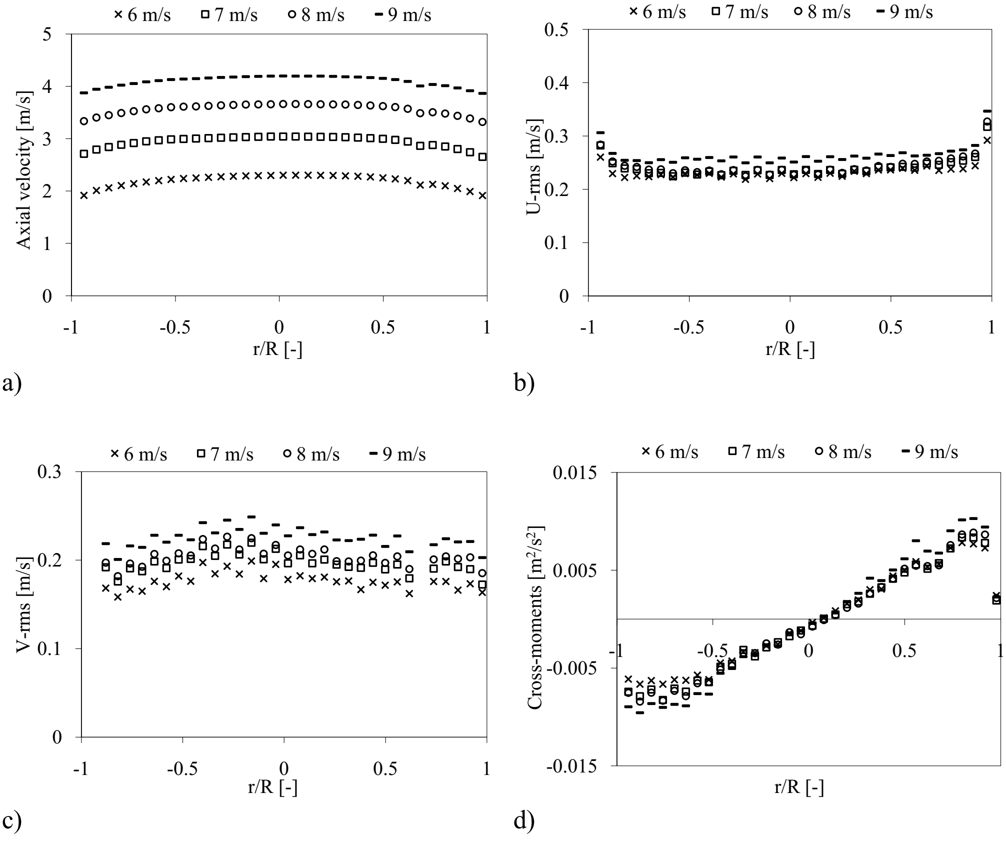

Figure 7.6: The mean axial particle velocity profiles, the axial and normal rms profiles and the cross-moment profiles for ZrO_2 particles with a diameter of 530 µm at a constant particle volume fraction of approximately 0.15 % at different superficial gas velocities.

7.3.3 Glass, 120 μm

The glass particles have a lower density than zirconium oxide, 2500 kg/m^3. An overview of the measurements performed on glass is given in Table 6.2

Effect of particle volume fraction
The mean diameter of the glass particles is smaller than the mean diameter of the ZrO_2 particles and consequently more particles are present in the system. The number of particles seems to have an influence on all the measured values for the glass particles. The particles reflect a lot of light. In certain areas in the frame, it is difficult to obtain enough light without flooding other areas. When particle concentration is high, it is difficult to separate one particle from the other. In the following experiments, the superficial gas velocity is constant at 8 m/s and the particle volume fraction is varied between 0.15 – 0.30 %. The particle mean axial velocity profiles are presented in Figure 7.7a. All the profiles have the same value in the centre of the pipe but they begin to differ when approaching the walls. It can also be observed that the shapes of some of the profiles are not as expected. The velocity profiles should increase gradually towards the centre of the pipe from the walls. On the right hand side the profiles have a slight dip before it starts to increase again. This is especially visible for the profile of the highest particle volume fraction.

The axial particle rms velocity profiles are presented in Figure 7.7b. It can be seen from the graph that only the lowest particle volume fraction profile is shown. The reason is because the profiles for the other particle volume fractions are not as expected. This is due to the number of particles in the system and the difficulty in separating the particles during measurements.

The V-rms or particle velocity is presented in Figure 7.7c. The same problem that is observed in the U-rms profiles can be seen here. No clear tendencies can be seen and only the profile for the lowest particle volume fraction is as expected and therefore shown.

The particle cross-moments are presented in Figure 7.7d. Since the cross-moments are derived from the mean axial and normal velocities, these profiles will not make any sense except for the one with the lowest particle volume fraction. This profile has a recognisable cross-moment shape and has a value of zero near the centre of the pipe.

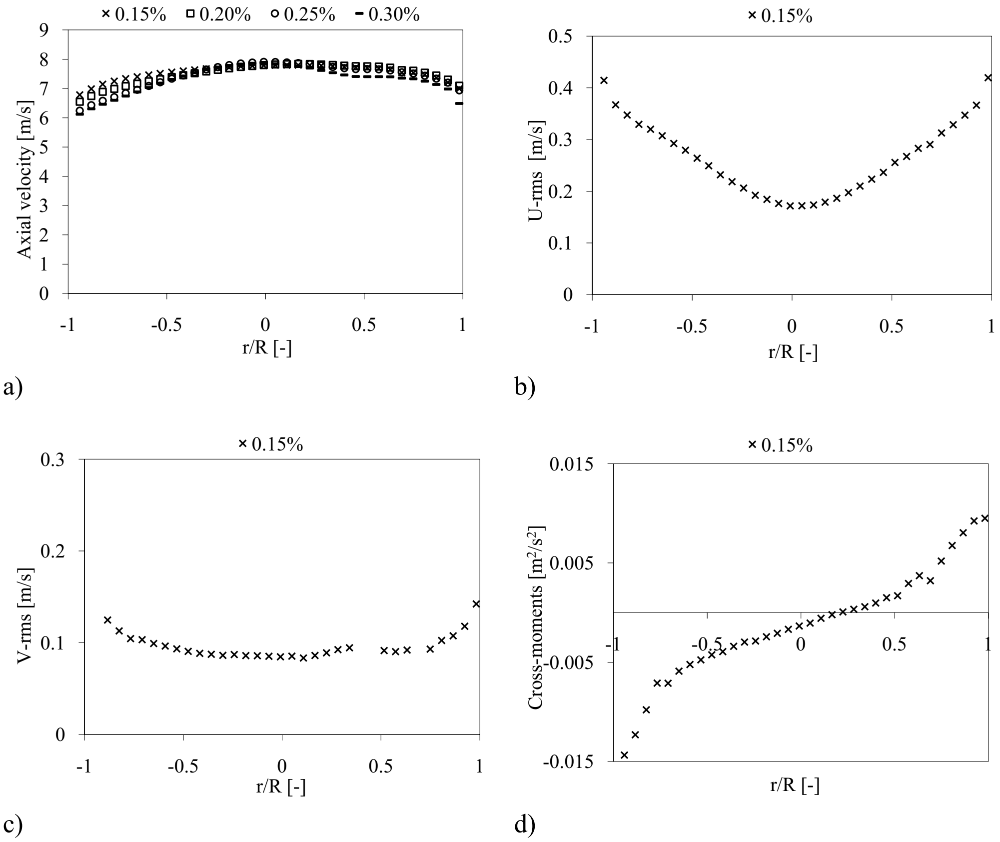

Figure 7.7: The mean axial and normal particle velocity profiles, the axial and normal rms profiles and the cross-moment profiles for glass particles with a diameter of 120 µm at a constant superficial gas velocity of 8 m/s and different particle volume fractions.

Effect of superficial gas velocity
For the following experiments, the particle volume fraction is kept constant at approximately 0.15 % while the superficial gas velocity is varied between 6 – 9 m/s.

There have been some problems with the experimental measurements performed with these glass particles at higher particle volume fractions. The results from the experiments performed with the lowest volume fraction is seen in Figure 7.8. The velocity profiles of the axial particle velocity can be seen in Figure 7.8a. The velocity is at its highest in the centre of the pipe and is gradually reduced towards the walls. The superficial gas velocity is increased with 1 m/s for each measurement while the axial particle velocity increases with a value of 0.68 – 0.77 m/s.

From Figure 7.8b it can be observed that an increase in superficial gas velocity gives an increase in the axial particle rms velocity. The fluctuations are lowest in the centre of the pipe and increase towards the walls.

The normal particle rms velocity profiles are presented in Figure 7.8c. The fluctuations increase with increasing superficial gas velocity. It can be seen from the figure that the fluctuations increase towards the walls. There are some discrepancies on the right hand side of the pipe.

In Figure 7.8d the particle cross-moment profiles are presented. The figure shows that the profiles have a value of zero near the centre of the pipe and that the absolute value increases gradually towards the walls. It can also be observed that the cross-moments increase with increasing superficial gas velocity.

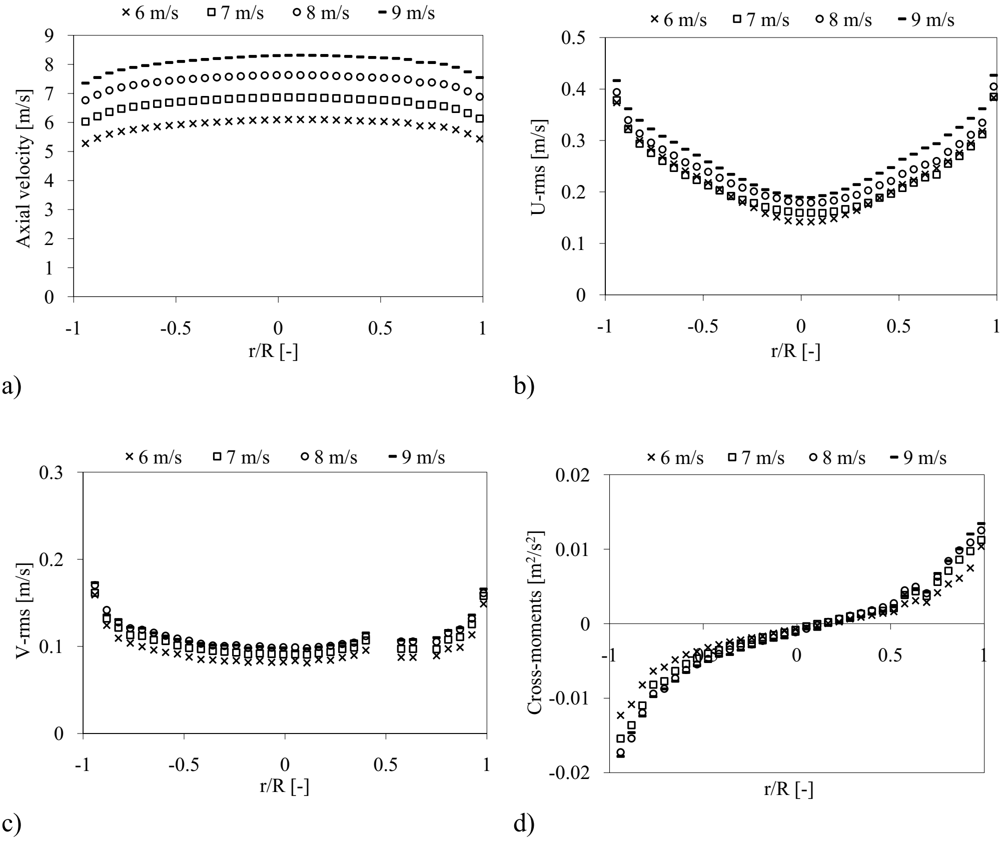

a) b) c) d)

Figure 7.8: The mean axial particle velocity profiles, the axial and normal rms profiles and the cross-moment profiles for glass particles with a diameter of 120 μm at a constant particle volume fraction of approximately 0.15 % at different superficial gas velocities.

7.3.4 Glass, 518 μm

An overview of the measurements performed on glass with a volume averaged mean diameter of 518 μm and a density of 2500 kg/m^3 is given in Table 6.2.

Effect of volume fraction

In the following experiments, the superficial gas velocity is kept constant at 8 m/s and the particle volume fraction is varied between 0.15 – 0.30 %. Figure 7.9a shows that the axial mean particle velocity increases slightly with increasing particle volume fraction. The figure also shows that the velocity profiles are fairly flat, but with the highest velocity as expected in the centre of the pipe.

Figure 7.9b shows the particle U-rms profiles. Again, it can be seen that the profiles are almost flat as they are for the axial velocity. The fluctuations are lowest in the centre of the pipe and then increase towards the walls. It can also be seen from the figure that the fluctuations decrease with increasing particle volume fraction.

The particle V-rms velocity profiles are presented in Figure 7.9c. There are some problems with the profiles on the right hand side of the pipe. This can also be seen in Figure 7.9b, but to a lesser extent. It is most likely due to concentrated reflections from the glass particles, from the glass wall or a combination. It can be seen form Figure 7.9c that the normal fluctuations decrease with increasing particle volume fraction.

The particle cross-moment profiles are presented in Figure 7.9d. The profiles show a value of zero in the centre of the pipe and increase when approaching the walls. The same deviation from the expected profiles as is seen for the normal fluctuating velocity can be observed. The cross-moments decrease with increasing particle volume fraction.

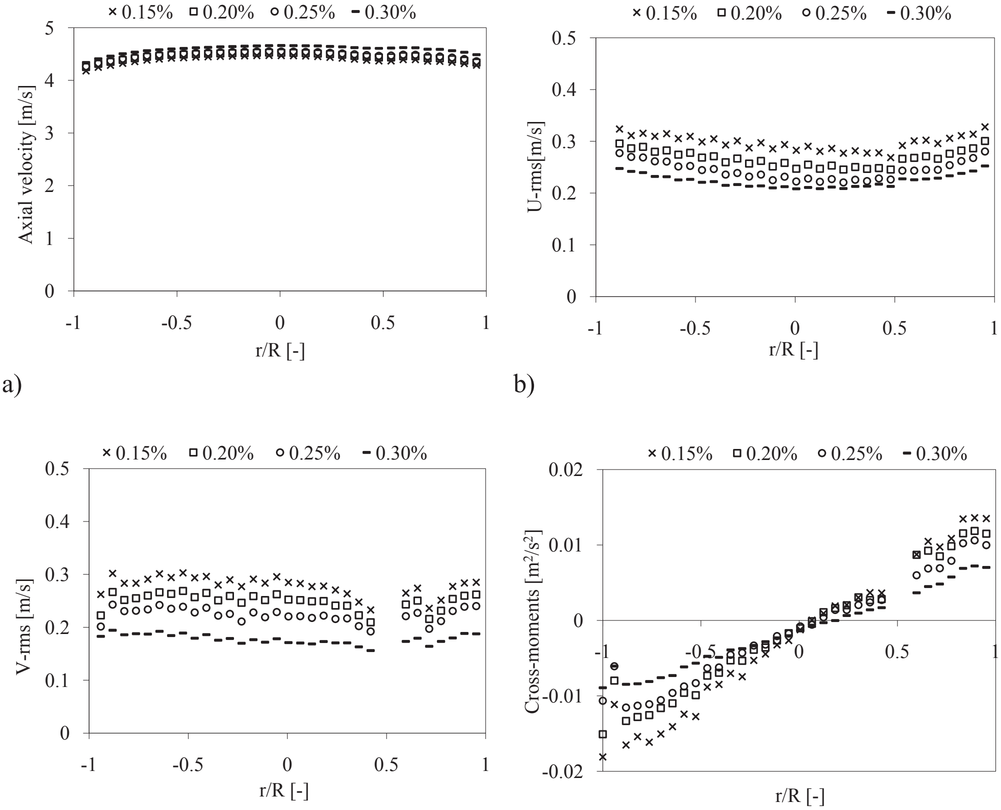

a) b)

c) d)

Figure 7.9: *The mean axial particle velocity profiles, the axial and normal rms profiles and the cross-moment profiles for glass particles with a diameter of 518 µm at a constant superficial gas velocity of 8 m/s and different particle volume fractions.*

The reflections causing the disturbance in the measurements can be seen in Figure 7.10. The distortions makes it difficult to separate the different particles and will therefore influence the measurements.

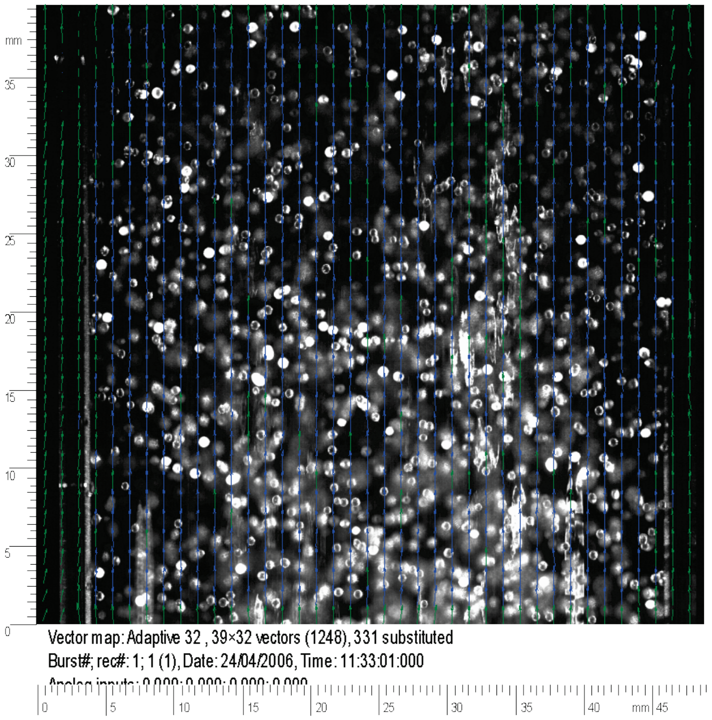

Figure 7.10: An example of the picture and the resulting vector map taken for the experimental investigation of 518 µm glass particles.

Effect of superficial gas velocity

The superficial gas velocity is varied between 6 – 9 m/s while the particle volume fraction is kept constant at approximately 0.15 %. Figure 7.11a shows the profiles of the axial mean particle velocity. The superficial gas velocity is increased with 1 m/s for each experiment while the particle velocity is increased with 0.59 – 0.84 m/s. The relative increase in particle velocity decreases with increased superficial gas velocity. This is also observed in the LDA experiments and confirmed through numerical simulations. The same tendency can also be seen for the largest ZrO_2 particles. The axial mean particle velocity profiles are quite flat. The profiles still have their highest value in the centre of the pipe with a slight decrease towards the wall.

Figure 7.11b shows the particle U-rms velocity profiles. The fluctuations are smallest in the centre of the pipe and increase towards the wall. It can also be observed that the fluctuations increase with increasing superficial gas velocity.

The particle V-rms velocity profiles are presented in Figure 7.11c. The profiles are flat, but a slight increase in fluctuations can be observed near the wall. The figure also shows that there are some inconsistencies for all the profiles on the right hand side. The fluctuations increase with increasing superficial gas velocity.

The particle cross-moment profiles are shown in Figure 7.11d. The profiles cross zero in the centre of the pipe. An increase in superficial gas velocity increases the cross-moment.

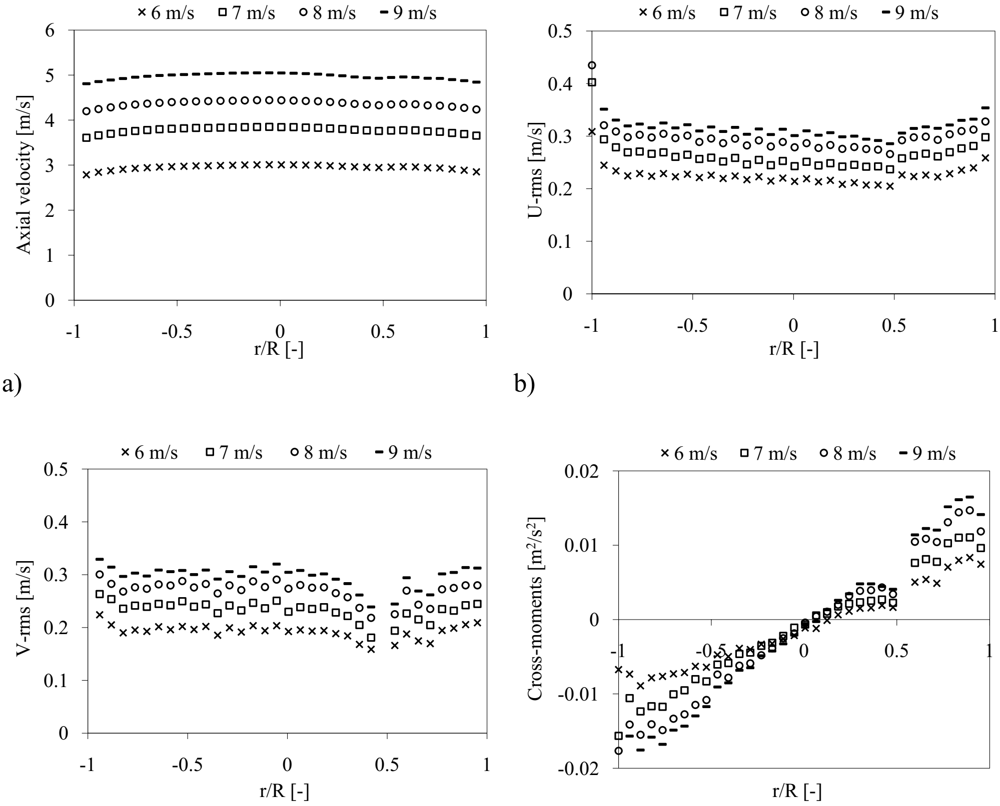

a)

b)

c)

d)

Figure 7.11: The mean axial particle velocity profiles, the axial and normal rms profiles and the cross-moment profiles for glass particles with a diameter of 518 μm at a constant particle volume fraction of approximately 0.15 % at different superficial gas velocities.

7.4 Summary and discussion

In this section the results from the experiments presented in Section 7.3 are summarized and discussed.

Mean axial particle velocity

The measurements performed show that in the case of ZrO_2 260 μm particles (Figure 7.3a) at a superficial gas velocity of 8 m/s there is a dependence on the particle volume fraction. This can only be seen on the left hand side of the pipe, here the velocity decreases with increasing particle volume fraction. The same is observed for the 120 μm glass particles (Figure 7.7a) at the same superficial gas velocity. The experiments for both the 530 μm ZrO_2 and 518 μm glass show that the velocity increases with increasing particle volume fraction (Figure 7.5a and 7.9a). The results from the measurements of ZrO_2 260 μm particles found in Appendix D at a superficial gas velocity of 6, 7 and 9 m/s show that a tendency for a decrease in particle velocity for increases in the particle volume fraction, but this is not clear for the whole cross-section of the pipe (Figures D.3a, D.4a and D.5a). Investigations at superficial gas velocities of 6, 7 and 9 m/s for 530 μm ZrO_2 (Figures D.6a, D.7a and D.8a) and 518 μm glass particles (Figures D.9a, D.10a and D.11a) show that the velocity increases with increasing particle volume fraction. For the measurements at superficial gas velocities of 6, 7 and 9 m/s for the 120 μm glass particles show the same as the measurements at 8 m/s (Figures D.12a, D.13a and D.14a). On the left hand side of the pipe the velocity decrease with increasing particle volume fraction, while for the rest of the cross-section this is not clear. The measurements of the highest particle volume fraction is disregarded because of difficulties in obtaining results due to high particle number density, which leads to distortion of the images.

The measurements performed with different superficial gas velocities show that the particle velocity increases with increase in superficial gas velocity for all of the particle types (Figures 7. 4a, 7.6a, 7.8a and 7.11a). The largest increase in particle velocity is the increase from 6 – 7 m/s superficial gas velocity.

Mean normal particle velocity
No dependence on the particle volume fraction or the superficial gas velocity (6, 7, 8 and 9 m/s) is observed for any of the particle types (Figures 7.3b, D.1, D.2, D.3b, D.4b, D.5b ,D.6b, D.7b, D.8b, D.9b, D.10b, D.11b, D.12b, D.13b, D.14b).

Axial particle rms velocity
The axial rms velocity generally increase with increasing particle volume fraction for the 260 μm ZrO_2 particles (Figure 7.3c) at a superficial gas velocity of 8 m/s. Some discrepancies are observed for the lowest particle volume fraction. For the 120 μm glass only the measurements for the particle volume fraction of 0.15 % are presented since it is not possible to obtain any results from the other particle volume fractions (Figure 7.7b) at a superficial gas velocity of 8 m/s. Both the 530 μm ZrO_2 and 518 μm glass particles show a dependence on the particle volume fraction. A decrease with increasing particle volume fraction is observed (Figures 7.5b and 7.9b) for a superficial gas velocity of 8 m/s. For measurements performed at superficial gas velocities of 6, 7 and 9 m/s for 260 μm ZrO_2 the axial particle rms velocity generally increase with increasing particle volume fraction (Figures D.3c, D.4c and D.5c). The same is observed for the measurement at 8 m/s is also observed for the other superficial gas velocities. The results from the measurements at a superficial gas velocity of 6, 7 and 9 m/s for 530 μm ZrO_2 and 518 μm glass particles show that the axial particle rms velocities decrease with increasing particle volume fraction (Figures D.6c, D.7c, D.8c, D.12c, D.13c and D.14c). Only the measurement at a particle volume fraction of 0.15 % is accepted for 120 μm glass particles at a superficial gas velocity of 6 m/s (Figure D.9c). At a superficial gas velocity of 7 and 9 m/s the two lowest particle volume fraction measurements are accepted (Figure D.10c and D.11c). These results show that the axial particle rms velocities increase with increasing particle volume fraction.

All of the particle types show a dependence on the superficial gas velocity, the axial particle rms velocity increases with increasing superficial gas velocity (Figures 7.4b, 7.6b, 7.8b and 7.11b).

Normal particle rms velocity
For the 260 μm ZrO_2, 530 μm ZrO_2 and 518 μm glass particles a dependence on the particle volume fraction is observed at a superficial gas velocity of 8 m/s. The normal particle rms velocity decrease with increasing particle volume fraction (Figures 7.3d, 7.5c and 7.9c). Only

the measurements at 0.15 % particle volume fraction are accepted for the 120 μm glass particles at a superficial gas velocity of 8 m/s (Figure 7.7c). The measurements performed for the 260 μm ZrO_2 at 6 and 9 m/s show that the normal particle rms velocity decrease for increasing particle volume fraction (Figures D.3d and D.5d), while no clear dependence is observed for 7 m/s (Figure D.4d). The dependence for the 7 m/s measurements of 530 μm ZrO_2 particles is not clear (Figure D.7d). For 6 and 9 m/s it is observed that the normal particle rms velocity decreased with increasing superficial gas velocity (Figures D.6d and D.8d). The same is observed for all of the superficial gas velocities for the 518 μm glass particles (Figures D.12d, D.13d and D.14d). Only the results for the lowest particle volume fraction are accepted for the 6 m/s measurements of 120 μm glass particles (Figure D.9d). For 7 and 9 m/s superficial gas velocity the two lowest particle volume fractions are accepted and here it can be observed that the normal particle rms velocity decrease with increasing particle volume fraction (Figures D.10d and D.11d.)

An increase in normal particle rms velocity is observed for all of the particle types with increasing superficial gas velocity (Figures 7.4c, 7.6c, 7.8c and 7.11c).

Particle cross-moment
Only the results from a particle volume fraction of 0.15 % are accepted for the measurements with 260 μm ZrO_2 and 120 μm glass particles at a superficial gas velocity of 8 m/s (Figures 7.3e and 7.7d). Both the 530 μm ZrO_2 and 518 μm glass particles show a decrease with an increase in particle volume fraction at a superficial gas velocity of 8 m/s (Figures 7.5d and 7.9d). For 260 μm ZrO_2 measurements at 6 and 7 m/s only the result from the 0.15 % are accepted (Figures D.3e and D.4e). No dependence is found for the 9 m/s measurements (Figure D.5e). The measurements at 6 and 9 m/s for 530 μm ZrO_2 showed that the cross-moment deceases with increasing superficial gas velocity (Figures D.6e and D.8e). A dependence is not as clear for the 7 m/s measurements (Figure D.7e). For 120 μm glass particles only the 0.15 % particle volume fraction is accepted for the measurements at 6 and 7 m/s (Figures D.9e and D.10e). The measurements at both 0.15 % and 0.20 % are accepted for the 9 m/s and the results show that the cross-moments decrease with increasing particle volume fraction (Figure D.11e). For all measured superficial gas velocity for 518 μm glass particles the cross-moments are found to decrease with increasing particle volume fraction (Figures D.12e D.13e and D.14e).

A dependence on the superficial gas velocity is observed for all of the particle types. The value of the cross-moments increased with increasing superficial gas velocity (Figures 7.4d, 7.6d, 7.8d and 7.11d).

7.5 Comparison between the particle types

In the previous part of this chapter, the results from the PIV measurements are presented and discussed. In this part, the different particle types are compared. Figure 7.12 displays the profiles of the mean axial particle velocities, axial and normal fluctuation velocities and the cross-moments.

The results presented below are measurements performed at a superficial gas velocity of 8 m/s and a particle volume fraction of approximately 0.15 %. The PIV specifications are the same for all of the measurements and the number of samples is around 5000 for all of the particle types. The alignment of the camera may have varied some-what. This is because every time the particles are changed the camera needs to be taken down. Another problem can be the light reflections, which is more common for the glass particles than the ZrO_2 particles.

The mean axial particle velocity profiles are presented together in Figure 7.12a. The lightest particle, the smallest glass particle, has the highest velocity. These particles are small and light and they will follow the flow better than the other particle types. Their slip velocity will be the smallest. The heaviest particles will have the lowest velocity. The largest ZrO_2 and glass particles have almost the same size, but the density of ZrO_2 is higher than the glass density. The smallest ZrO_2 particles have the second highest velocity. In Table 6.3 the weight of the particles are shown.

Figure 7.12b shows the particle U-rms velocity profiles. All of the profiles, except the one for the smallest glass particles are flat in the centre of the pipe with a slight increase near the walls. The last profile has a more pronounced shape. The lowest fluctuations are found in the centre of the pipe with a marked increase towards the walls. The largest glass particles have the highest fluctuations, followed by the largest ZrO_2 particles. This was also observed in the LDA simulations, Figure 6.10b. The two smallest particle types have almost the same fluctuations in the centre of the pipe, but differ closer to the wall, where the ZrO_2 particles have the lowest fluctuation. The figure show that it is not the largest and heaviest particles that have the highest fluctuation. The smallest particles have the lowest fluctuations in the centre of the pipe, but this increases towards the walls. It is difficult to draw a clear conclusion on the particle fluctuation depending on particle diameter and particle density, but generally the theory given in Section 6.5 is supported. Here it is stated that larger particles tend to increase the turbulence while smaller particles has the opposite effect and decrease the turbulence.

The profiles in Figure 7.12c show the particle V-rms velocity profiles. The largest glass particles have the highest normal fluctuations, followed by the largest ZrO_2 particles, the smallest ZrO_2 particles and finally the smallest glass particles. All of the profiles are flat over the cross-section of the pipe. There are some problems with the fluctuation profile for the largest glass particles and from the raw data this seems to be due to light reflections from the particles.

Figure 7.12d shows the particle cross-moment profiles. The cross-moment values are lowest for the smallest ZrO_2 particles and the smallest glass particles. The largest glass particles have the highest value followed by the largest ZrO_2 particles.

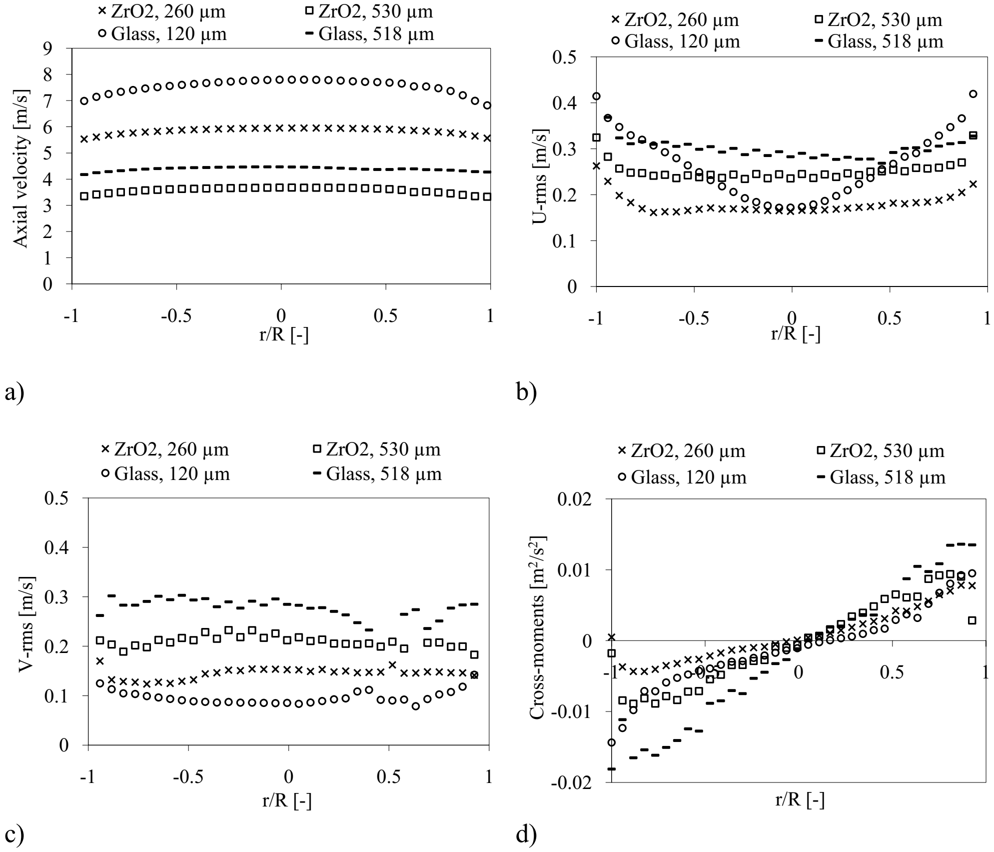

a)

b)

c)

d)

Figure 7.12: *The mean axial particle velocity profiles, the axial and normal rms profiles and the cross-moment profiles for glass particles at a constant particle volume fraction of approximately 0.15 % and a superficial gas velocity of 8 m/s.*

7.6 Conclusion

The results from the PIV experimental investigation is presented in Chapter 7 and in Appendix D. The effect of particle volume fraction and superficial gas velocity on the mean axial and normal particle velocity, particle U-rms and V-rms, and the particle cross-moment is studied. As shown from the LDA experiments presented in Chapter 6 and Appendix C the effect of the particle volume fraction on these parameters varies depending on the particle type.

It is observed from the experiments with varying superficial gas velocity that the axial particle velocity and the particle U-rms and V-rms and the particle cross-moment increase with increasing superficial gas velocity for all of the particle types.

The comparison between the particle types show that the largest and heaviest particles have the lowest axial particle velocity as expected. The fluctuations are highest for the largest particles.

120 µm glass and 260 µm ZrO_2 particles show a slight dependence on the particle volume

fraction, a decrease in axial particle velocity can be observed with increasing particle volume fraction. An increase in axial particle velocity with increasing particle volume fraction is found for 530 µm ZrO_2 and 518 µm glass particles. No dependence for any of the particle types where found for particle volume fraction on the normal particle velocity.

For 260 µm ZrO_2, the axial particle rms velocity particles generally increased with increasing particle volume fraction. Insufficient data makes it difficult to find how the axial particle rms velocity changes with the particle volume fraction for 120 µm glass particles. Both 530 µm ZrO_2 and 518 µm glass particles showed that the axial particle rms velocity decreases with increasing particle volume fraction. Generally a decrease in normal particle rms velocity with increasing particle volume fraction is found for 260 µm ZrO_2, 530 µm ZrO_2 and 518 µm glass particles.

A decrease in particle cross-moment is observed for 530 µm ZrO_2 and 518 µm glass particles when the particle volume fraction increases. From the data accepted for 120 µm glass and 260 µm ZrO_2 particles a decrease in particle cross-moment is observed with increasing particle volume fraction.

The PIV technique can be used to study the solids phase in a two phase flow. There are some difficulties with measuring the flow close to the wall due to the curvature of the pipe wall, the same is observed for LDA. Generally, PIV measures the particles effectively. The measurement time is the same regardless of particle size and number density. The time consuming part when using PIV is the post-processing, but this can be performed afterwards and will not have an effect on the actual measurement time. There are some challenges concerning the use of PIV for smaller particles and high particle number density. Under these conditions it is difficult for the post-processing program to separate the different particles due to reflections. The reflections obscure the particles and they are no longer visible.

7.7 Sources of error

Below is a discussion of possible sources of error identified during the experimental investigation with PIV. Sources of error that are common for both LDA and PIV experiments can be found in Section 6.7.

- Near wall measurements. When the laser light travel through the pipe wall it changes direction slightly due to the curvature of the wall. This distortion increases as the measurements along the cross-section approaches the wall. The use of a channel instead of a circular pipe would reduce this problem.
- Particles present in the interrogation area during PIV experiments. Few particles in the interrogation area. At least 4 – 5 particles should be present and ideally it should be 10 – 11 to get a good average.
- Alignment of the PIV experimental set-up. It is difficult to achieve a 100% accurate aligned set-up. The light sheet of the PIV lasers should pass through the centre of the transport pipe and finding this exact can be time consuming.
- Reflection from pipe wall and particles for PIV measurements. These reflections distort the pictures and are difficult to remove. A solution that is found to work well on another experimental set-up is coating the inside of the pipe wall with a black substance, but this cannot be used here due to the sandblasting effect of the particles. Interrogation areas that give a result that differ from the neighbouring ones are rejected and consequently substituted.

8. COMPARISON BETWEEN LDA AND PIV

In Chapters 6 and 7 the results from the experimental investigation of the dilute vertical gas/particle flow by LDA and PIV respectively are presented and discussed. In this chapter, the results from the two methods are compared and the differences are discussed. There are few comparisons between LDA and PIV in literature. Ibsen (2002) performed PIV experiments on a circulating fluidized bed (CFB) and evaluated these results against LDA measurements. The tracer particles used in this study are 60 μm glass particles with a density of 2400 kg/m^3. Deen et al. (2000) compared the PIV and LDA results for a gas-liquid flow in a bubble column. The liquid is seeded with 50 μm polystyrene particles. The results from these investigations will be discussed at the end of this chapter.

8.1 Difference in the measurement technique between LDA and PIV

The differences between the measurements are most likely due to the differences between the two techniques;

- There is a difference between the control volumes.
- The measurement set-ups differ.
- The criteria used for evaluation and post-processing are different.
- The temporal resolution is higher for LDA than for PIV.

It is also important to remember that the LDA and PIV experiments are not performed under the exact same conditions, but as close as possible.

8.1.1 Difference in acquiring and analysing data

In the PIV software users guide (2000) the differences between the LDA and PIV techniques are discussed. FFT (Fast Fourier Transformation)-processing is used to speed up the calculation of correlations in the post-processing of the PIV data. Whether the input is meaningful or not, the FFT-processing will always yield an outcome. In LDA the signal conditioners are mainly used to ensure that there is a meaningful input. LDA is a time based measurement technique, and so we can wait for the input. PIV on the other hand is an instantaneous measurement technique and all spatial information is sampled at the same time. Because of this there might be regions where there is no meaningful input and so it is essential to subsequently validate the PIV vector map. Erroneous vectors will be detected, removed and replaced when the validation algorithms are applied to the raw data.

The measurements of both LDA and PIV are possible because of the light scattered by the particles. PIV is based on the light scattered sideways, while the LDA usually measure the backward and sometimes also forward scattering (in this thesis off-axis backscattering mode is used). Small particles scatter most light in forward direction, some light will be scattered backwards and very little will be scattered sideways. This means that the intensity of laser light used for LDA might not be enough for the PIV measurements. Photomultipliers are used to amplify the light scattered by the particles in the LDA measurements, and this enables measurements on even very faint signals. A CCD-camera or a CMOS camera with much lower sensitivity than a multiplier captures the scattered light in PIV. The camera used in this investigation is a CMOS camera, and more on both of these cameras can be found in Section 4.2.5. The sensitivity of the camera can be further reduced with short duration of the exposure due to less light.

In LDA only the values that fall inside the pre-set criteria are accepted during the measurements. The post-processing is performed on all of the accepted data. If an adjustment of the criteria is needed, all of the measurements have to be performed again. In PIV the time interval between the double frames and the sampling rate are chosen prior to the measurements. This raw data is then used in post-processing. The post-processing criteria can be changed without having to perform the measurements again.

8.1.2 Difference in control volume

The resolution of the picture taken with the CMOS camera is 1260 x 1024 pixels. The length scale is 46 x 38 mm. From this, it is possible to calculate the mm to pixel ratio. The calculation gives 0.0365 x 0.0371 mm/pixel. The control volume is 32 x 32 pixels. This means that the control volume has a width of 1.168 mm and a height of 1.1872 mm, where both the axial and normal velocities are measured. In the LDA measurements, there are two control volumes one for the measurements of the axial velocity, with a volume of 0.194 mm x 0.194 mm x 4.091mm, and one for the measurements of the normal velocity, with a volume of 0.184 mm x 0.184 mm x 3.880 mm. The control volume has an ellipsoidal shape.

8.1.3 Difference in number of measurements

The number of measurements performed for the PIV investigation are approximately 5000 for all of the particle types. For the LDA investigation the number of measurements varies depending on the particle size. In this thesis the number of measurements performed in each point in the LDA investigation lies between 20000 – 50000. In Deen et al. (2000) they conclude that PIV has an advantage over LDA when many points are to be measured. In every image pair recorded, the order of 10^3 measure points (interrogation areas/control volumes) is acquired. Also every interrogation area contains multiple particles so fewer images are needed. The value of the vector is calculated from several particle pairs. In this thesis 5000 image pairs are averaged. Additional averaging is performed on the control volumes in vertical direction on the average vector map. The control volumes found in a length of approximately 2 cm are averaged. For the LDA, it can be observed from performing the experiments that more than 20000 measurements are needed for each point, this is especially clear when measuring the cross-moment.

8.1.4 Difference in temporal resolution

The low temporal resolution of the PIV technique is considered to be one of its major disadvantages when compared to LDA. In this thesis the frequency of the PIV is 50 Hz, while the frequency of LDA typically is in the order of 1 kHz.

8.1.5 Difference in area measured in the flow

The flow in the vertical pipe is assumed to be axis symmetric. This means that it should not matter on which side the pipe the measurements are performed. In this thesis the LDA and PIV measurements are performed over different cross-section directions of the pipe due to space restrictions around the experimental set-up. This is illustrated in Figure 8.1. The measurements are performed at the same height.

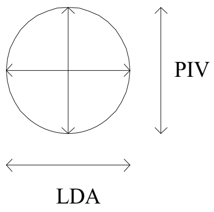

Figure 8.1: *The vertical pipe seen from above to show which cross-section of the pipe the experiments are performed on.*

The effect of this is only clear when comparing the mean normal particle velocity profiles where it is possible to see the difference. For the other measured values it is difficult to see any effect on the profiles because of the different cross-sections measured.

8.2 The results from the comparison between LDA and PIV

In this chapter the experimental findings from the LDA and PIV measurements performed on 260 μm and 530 μm ZrO_2 particles and 120 μm and 518 μm glass particles are compared. In the rest of this chapter, the axial and normal mean particle velocity, the U-rms and V-rms and the particle cross-moments are measured by the LDA and PIV are compared. The particle rms velocity is also referred to as fluctuations.

8.2.1 Zirconium oxide, 260 μm

Below, a comparison between the results from the LDA and PIV measurements for ZrO_2 particles with a diameter of 260 μm is presented.

Effect of particle volume fraction
In Figure 8.2 the superficial gas velocity is kept constant at 8 m/s while the particle volume fraction is varied. It can be seen from Figure 8.2a that the results from the LDA measurements give in general a slightly lower mean axial particle velocity than the PIV measurements. This is most likely due to uncertainties in adjusting of the superficial gas velocity.

The mean normal particle velocity profiles can be seen in Figure 8.2b. The profiles all have values close to zero. This is used to investigate the alignment of the experimental set-up. A value close to zero represents a good alignment. A measurement of the normal particle velocity is performed for all of the particle types, but will not be presented in the main part of this thesis. It can be found in Appendix E.

Figure 8.2c shows the axial particle rms profiles. It can be seen from the figure that the LDA measures higher fluctuations. The results also show that the PIV experiments give flatter fluctuation profiles. The difference between the fluctuations in the centre of the pipe and the wall are small for PIV. The increase in fluctuations when approaching the wall is more pronounced for the LDA experiments. Another difference is that the PIV profiles show a clearer difference in fluctuations when the particle volume fraction is changed.

The profiles in Figure 8.2d show the normal particle rms profiles. All the profiles are almost flat over the cross-section of the pipe, and LDA gives for the most part higher values than PIV. There is some more variation over the cross-section in the profiles from the PIV experiments. They also change in value with different particle volume fractions.

The particle cross-moments can be seen in Figure 8.2e. The shape of the profiles from the LDA experiments is as expected. The values of the cross-moments are zero in the centre of the pipe and then the absolute value increases towards the walls. This is not the case for the PIV experiments. Here only the profiles for the two lowest particle volume fractions have a shape that resembles the ones measured by the LDA. The reason for the lack of results for the other particle volume fractions can be due to the particle number density. It might be difficult to separate individual particles and the illumination of the particles can be uneven. This will lead to problems during post-processing.

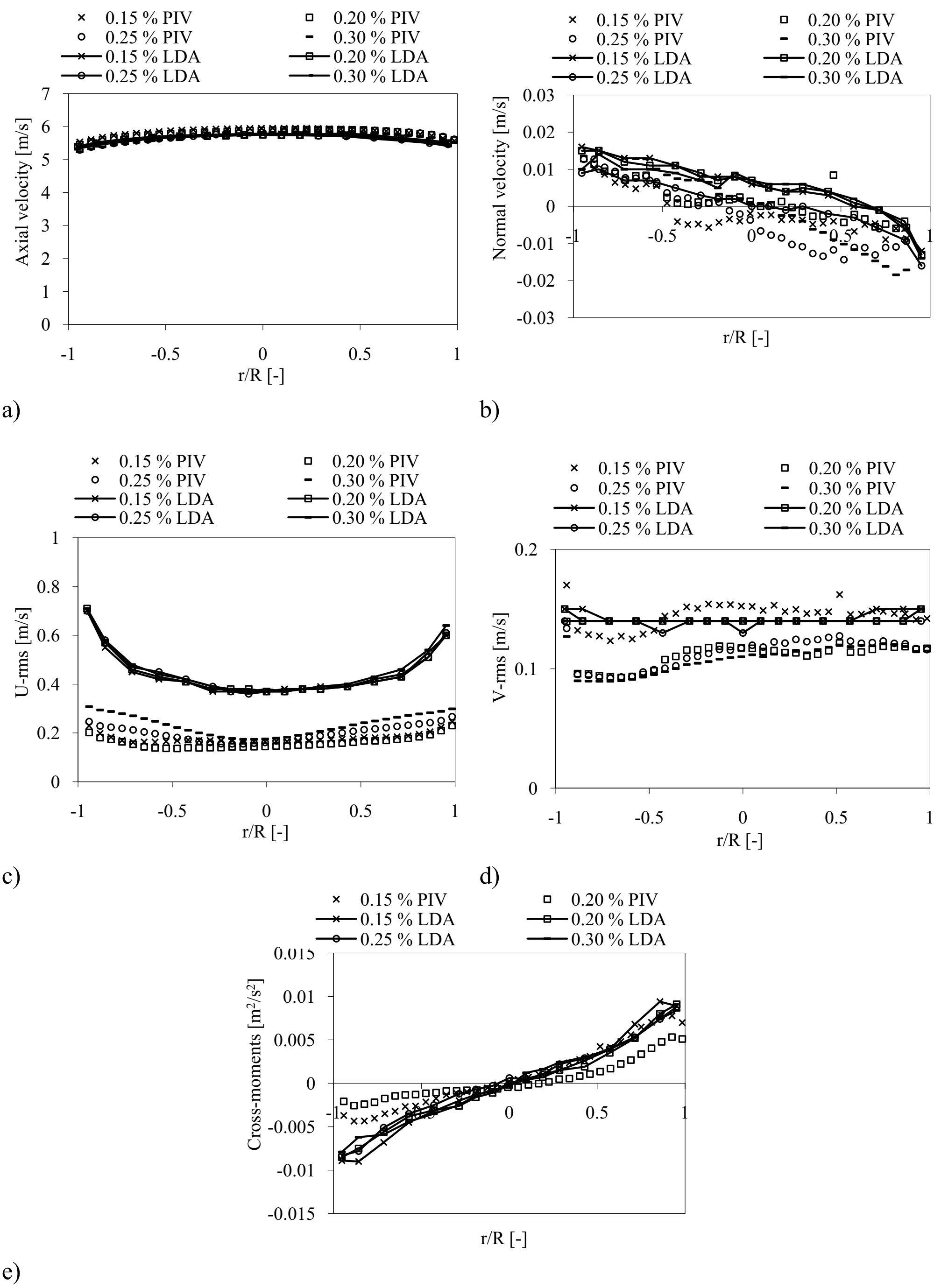

a)

b)

c)

d)

e)

Figure 8.2: The mean axial and normal particle velocity profiles, the axial and normal rms profiles and the cross-moment profiles for ZrO_2 particles with a diameter of 260 µm at a constant superficial gas velocity of 8 m/s and different particle volume fractions for both LDA and PIV.

Effect of superficial gas velocity
The superficial gas velocity is varied between 6 and 9 m/s while the particle volume fraction is kept constant at 0.15 %. Figure 8.3a shows the mean axial particle velocity profiles. There is little difference between PIV and LDA measurements for the lowest superficial gas velocity. The differences are greater for the higher superficial gas velocities.

Figure 8.3b shows the profiles of the axial particle rms velocity or the axial fluctuating velocity. One of the main differences between the results from the two measurement methods is the difference in the degree of fluctuations. The LDA measurements give higher fluctuations than the PIV measurements. It can be seen from the profiles that the fluctuations measured by LDA show a clear increase towards the wall. The fluctuation profiles measured by PIV are flatter, with a slight increase at the wall. A dependence on the superficial gas velocity can be observed from the LDA results, but this can only partly be seen from the PIV results. For LDA the fluctuations increase with increasing superficial gas velocity.

The profiles in Figure 8.3c show the normal particle rms velocity. The profiles for both LDA and PIV are nearly flat and they have almost the same value. From the results from both of the techniques, it is possible to see a weak dependence on the superficial gas velocity. When the superficial gas velocity increases, the fluctuations increase.

The cross-moments profiles can be seen in Figure 8.3d. The figure shows that the absolute value of the PIV profiles increase with increasing superficial gas velocity. The same tendency cannot be seen for the LDA profiles. A value of zero is reached for the LDA profiles in the centre of the pipe, but this is not the case for the PIV profiles.

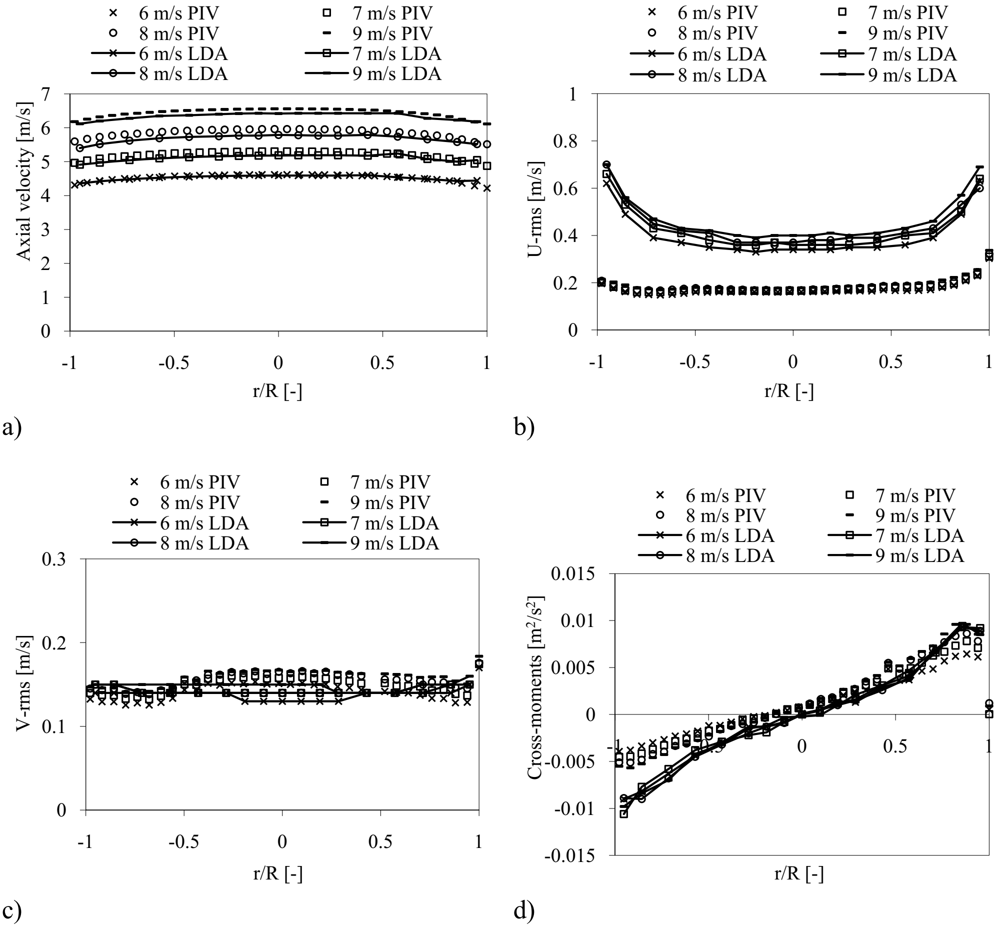

a) b)

c) d)

Figure 8.3: *The mean axial particle velocity profiles, the axial and normal rms profiles and the cross-moment profiles for ZrO_2 particles with a diameter of 260 µm at a constant particle volume fraction of approximately 0.15 % at different superficial gas velocities for both LDA and PIV.*

8.2.2 Zirconium oxide, 530 µm

During the experiments, it became clear that there is some kind of problem when measuring the point closest to the wall on the right hand side when using LDA. Several attempts are made to solve this, but the problem persisted. Hence the value in this point is not included in the following figures. The problem might be due to the size and the type of the particles in combination with the measurement method, which can lead to incorrect measurement of the particles in this region. The measurements are performed with the off-axis backscatter mode.

Effect of particle volume fraction

In Figure 8.4 the superficial gas velocity is kept constant at 8 m/s while the particle volume fraction is varied. It can be seen from Figure 8.4a that the results from the LDA measurements give a lower mean axial particle velocity than the PIV measurements. The main reason for this velocity difference seems to be due to the particle type combined with the measurement method as this difference is not observed for the other particle types. These experiments are performed several times and the results are the same every time. There is a clear difference in measured velocities between the different particle volume fractions for both methods. But this difference is clearer for the LDA measurements. The LDA profiles are also flatter than the PIV profiles.

Figure 8.4b shows the axial particle rms profiles. The axial fluctuations are higher for the LDA measurements than for the PIV measurements. Both of the profiles are flat with a slight increase close to the wall. The fluctuations in the LDA and PIV profiles decrease with increasing particle volume fraction.

The normal particle rms profiles are presented in Figure 8.4c. Here the measured fluctuations are higher for the PIV measurements than for the LDA measurements. It is not possible to see a connection between the normal fluctuations and the particle volume fraction in the LDA profiles. The PIV profiles show that the fluctuations decrease for increasing particle volume fraction.

The graph in Figure 8.4d shows the particle cross-moment profiles. The values of the cross-moments in the figure are close to the same for both the LDA and PIV measurements. It can be seen from the figure that the absolute value of the PIV profiles decrease in value with increasing particle volume fraction, but the same cannot be seen from the LDA profiles.

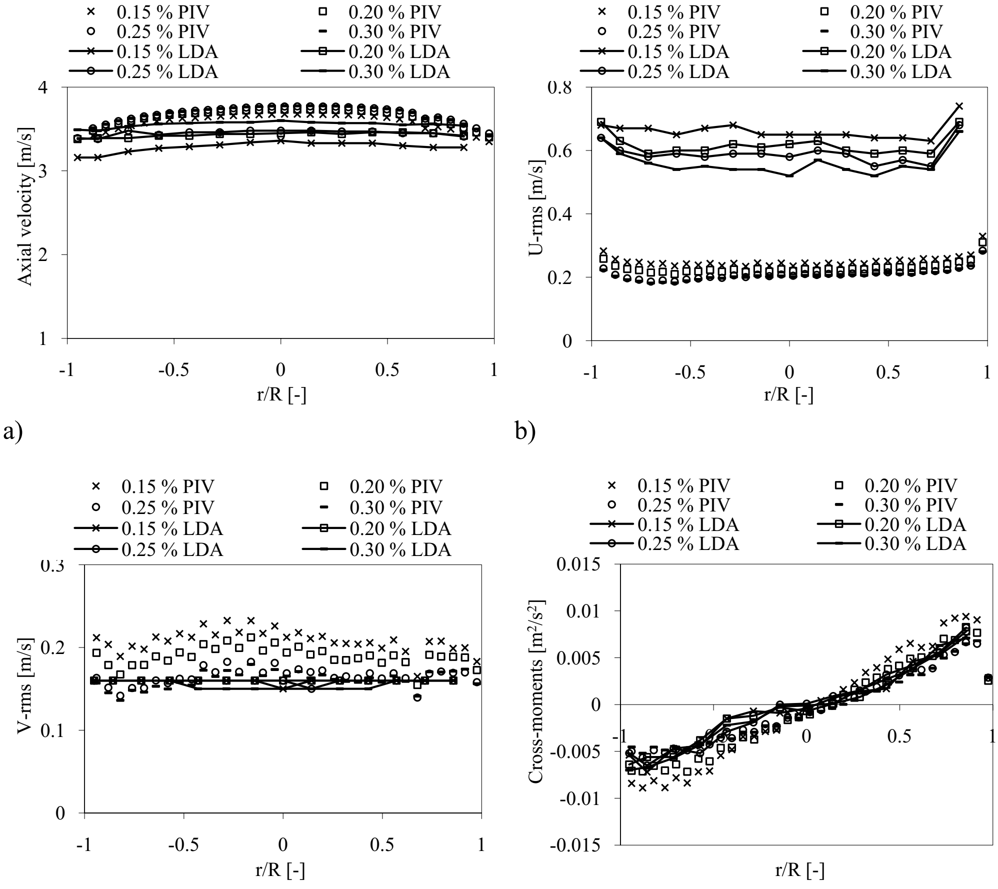

a) b)

c) d)

Figure 8.4: The mean axial particle velocity profiles, the axial and normal rms profiles and the cross-moment profiles for ZrO_2 particles with a diameter of 530 µm at a constant superficial gas velocity of 8 m/s and different particle volume fractions for both LDA and PIV.

Effect of superficial gas velocity

The particle volume fraction is kept constant at approximately 0.15 % while the superficial gas velocity is varied between 6 and 9 m/s in the following experiments. The axial particle velocity profiles are shown in Figure 8.5a. A clear difference can be seen between the measurements in the figure. The LDA values are lower than the PIV values and this difference increases with increasing superficial gas velocity. The same is observed in Figure 8.4a where all of the measured velocities at different particle volume fractions showed a lower velocity for the LDA than for the PIV. Another obvious difference is the shape of the profiles. The LDA profiles are very flat, and there is little change in velocity between the centre of the pipe and close to the wall. The PIV profiles clearly show that the highest velocity is found in the centre of the pipe and that the velocity is reduced towards the wall.

The profiles of the axial particle rms are shown in Figure 8.5b. The axial fluctuations measured are lower for the PIV measurements than for the LDA measurements. The PIV profiles are flat over the cross-section of the pipe with a slight increase near the wall. The fluctuations measured by the LDA are varying more. When the superficial gas velocity increases, both the LDA and PIV fluctuations increases.

In Figure 8.5c the normal particle rms profiles are presented. The measured fluctuations are lower for the LDA measurements than for the PIV measurements. The PIV profiles show that the fluctuations increase for increasing superficial gas velocity, but the same cannot be seen in the LDA profiles.

Figure 8.5d displays the particle cross-moment profiles. The measured cross-moments are lower for LDA than for PIV. It can be seen from the figure that the PIV profiles increase in value with increasing superficial gas velocity, however the same cannot be seen from the LDA profiles.

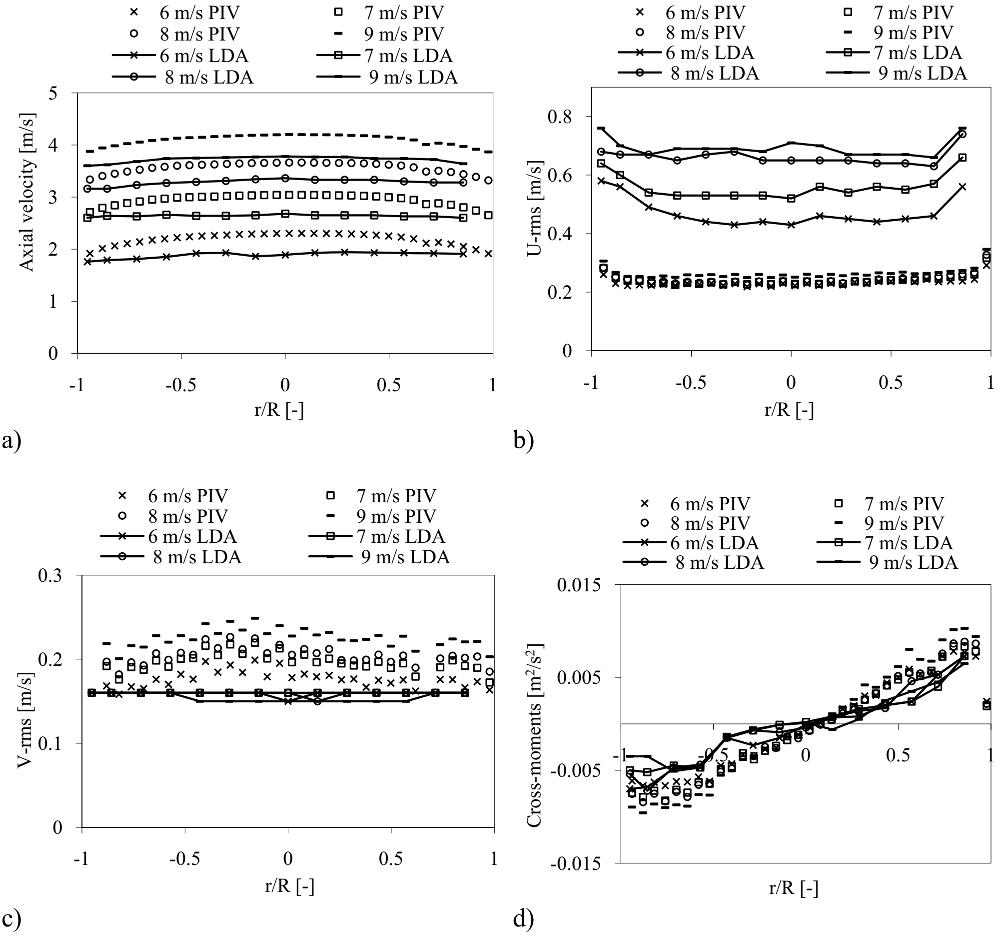

a) b) c) d)

Figure 8.5: The mean axial particle velocity profiles, the axial and normal rms profiles and the cross-moment profiles for ZrO_2 *particles with a diameter of 530 μm at a constant particle volume fraction of approximately 0.15 % at different superficial gas velocities.*

8.2.3 Glass, 120 μm

A comparison between the results from the LDA and PIV measurements shown in Chapters 6 and 7 are presented below for the glass particle with a diameter of 120 μm.

Effect of particle volume fraction
In the following experiments, the superficial gas velocity is constant at 8 m/s and the particle volume fraction is varied between 0.15 and 0.30 %. The mean axial particle velocity profiles are presented in Figure 8.6a. LDA and PIV give generally the same velocity, but there are some differences when approaching the wall. The LDA profiles show that the velocities increase with increasing particle volume fraction. It is more difficult to see any tendency from the PIV profiles, but the velocity seems to be increasing with decreasing particle volume fraction.

The axial particle rms velocity profiles can be seen in Figure 8.6b. Only the PIV profile representing the lowest volume fraction has the expected shape and is included. The LDA profiles increase with increasing particle volume fraction. The fluctuations are higher for the LDA measurements than for the PIV measurements. Problems with the measurements seem to occur for the three highest particle volume fractions and are therefore disregarded in the comparison. This is probably due to difficulties in measuring correctly when the particle concentration is too high and separating the particles becomes difficult in the post-processing.

The profiles in Figure 8.6c represent the normal particle rms velocity. Here the PIV profiles representing the three highest particle volume fractions have unexpected profiles and are not included in the comparison. All the LDA profiles have almost the same fluctuations. The fluctuations are higher for LDA.

The particle cross-moment profiles are presented in Figure 8.6d. Again, the three PIV profiles with the highest particle volume fractions are ignored in the comparison. All the LDA profiles have a higher cross-moment value than the PIV profile. The LDA results also show that the cross-moment increases with increasing particle volume fraction.

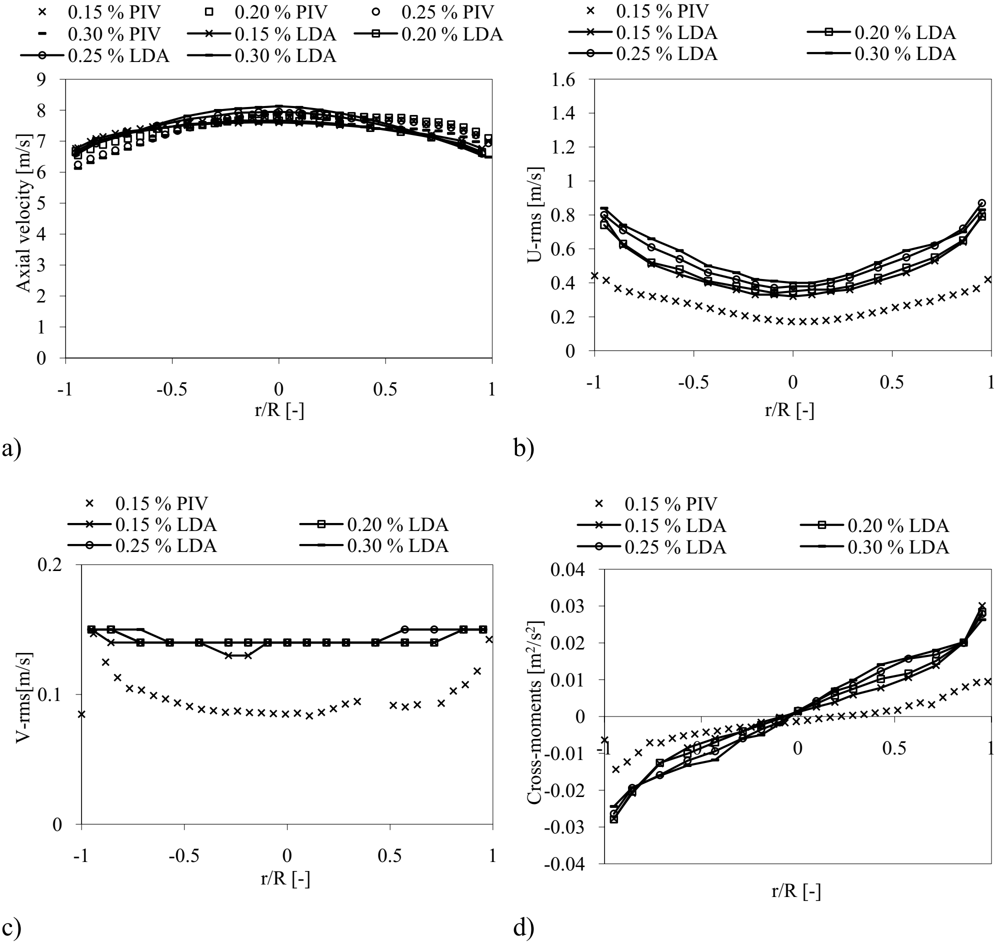

Figure 8.6: *The mean axial particle velocity profiles, the axial and normal rms profiles and the cross-moment profiles for glass particles with a diameter of 120 µm at a constant superficial gas velocity of 8 m/s and different particle volume fractions for both LDA and PIV.*

Effect of superficial gas velocity

For these experiments, the particle volume fraction is kept constant at approximately 0.15 % while the superficial gas velocity is varied between 6 and 9 m/s. The mean axial particle velocity profiles can be seen in Figure 8.7a. The velocity profiles from the LDA and PIV measurements are similar. There are some differences between the profiles for 6 and 7 m/s.

The profiles in Figure 8.7b show the axial particle rms velocity. Both the LDA and PIV profiles show an increase in fluctuations with increasing superficial gas velocity. The figure shows that the LDA measures higher fluctuations. The LDA profiles also show a larger gradient towards the wall than the PIV profiles.

The normal particle rms profiles are presented in Figure 8.7c. The PIV profiles show an increase in fluctuations when approaching the wall, while the LDA profiles are flat. An increase in fluctuations with increased superficial gas velocity can also be observed for the PIV profiles. The fluctuations measured are higher for the LDA measurements.

In Figure 8.7d the particle cross-moment profiles are shown. All of the cross-moment profiles reach a value of zero near the centre of the pipe. The measured LDA cross-moments are the highest. Both the LDA and the PIV profiles increase with increasing superficial gas velocity. The shape of these profiles differs slightly from the ones measured with the other particle types. The profiles increase in absolute value from zero in the centre of the pipe until it reaches its highest value near the wall, and the gradient of the cross-moment profiles increase when approaching the wall.

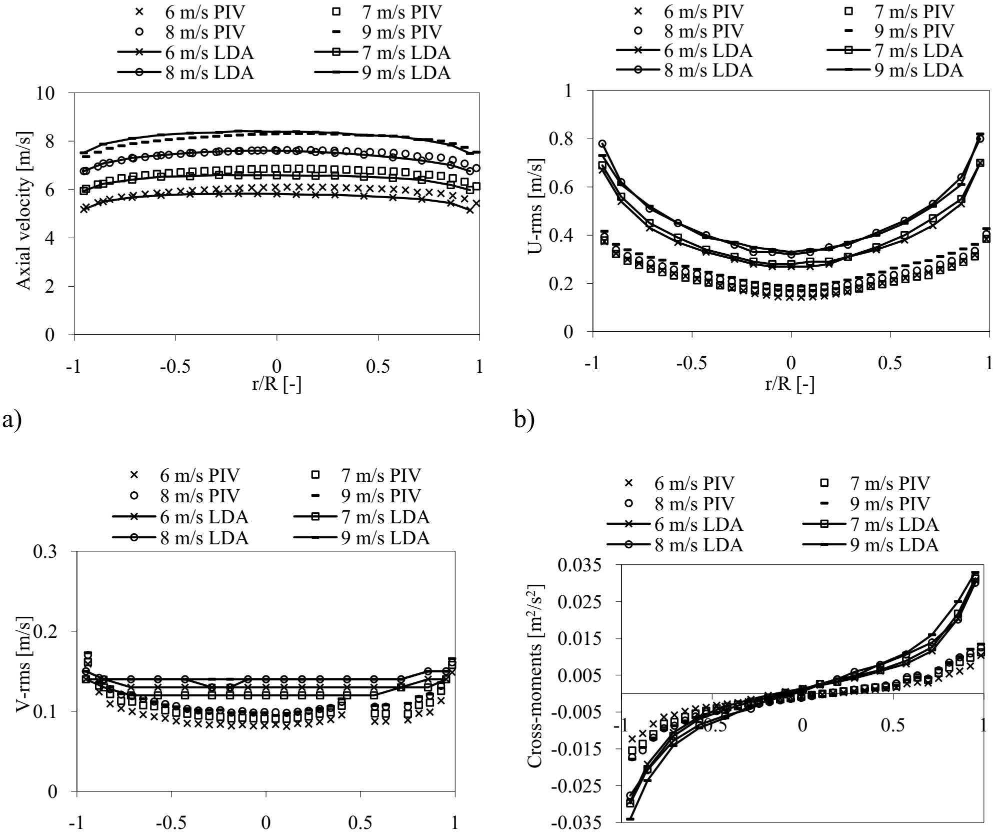

a) b)

c) d)

Figure 8.7: The mean axial particle velocity profiles, the axial and normal rms profiles and the cross-moment profiles for glass particles with a diameter of 120 μm at a constant particle volume fraction of approximately 0.15 % at different superficial gas velocities for both LDA and PIV.

8.2.4 Glass, 518 μm

A comparison between the results from the LDA and PIV measurements shown in Chapters 6 and 7 are presented in this chapter for glass particles with a diameter of 518 μm.

Effect of particle volume fraction

The particle volume fraction is varied between 0.15 and 0.30 % and with a constant superficial gas velocity of 8 m/s. The profiles in Figure 8.8a show the mean axial particle velocity. The profiles from both the LDA and PIV measurements show almost the same velocity except for the PIV profile with the highest particle volume fraction. This discrepancy might be due to the high particle concentration.

Figure 8.8b shows the profiles of the axial particle rms velocity. From the figure, it can be seen that the PIV profiles show a decrease in fluctuations with an increase in particle volume fraction. This can also be observed for the two highest LDA particle volume fraction profiles. The measured fluctuations are higher for LDA than for PIV. The PIV profiles are almost flat compared with the LDA profiles. The LDA profiles show an increase in fluctuations when approaching the wall.

The normal particle rms profiles are presented in Figure 8.8c. All the LDA profiles have close to the same value, while the PIV profiles show a decrease in fluctuations with increasing particle volume fraction. From the figure it can also be seen that the measured fluctuations are lower for LDA than for PIV.

In Figure 8.8d the particle cross-moment profiles are presented. The measured PIV cross-moments decrease with increasing particle volume fraction. The same cannot be observed for the LDA profiles. Here it is difficult to find a clear trend. Both the LDA and the PIV profiles have a value of zero in the centre of the pipe.

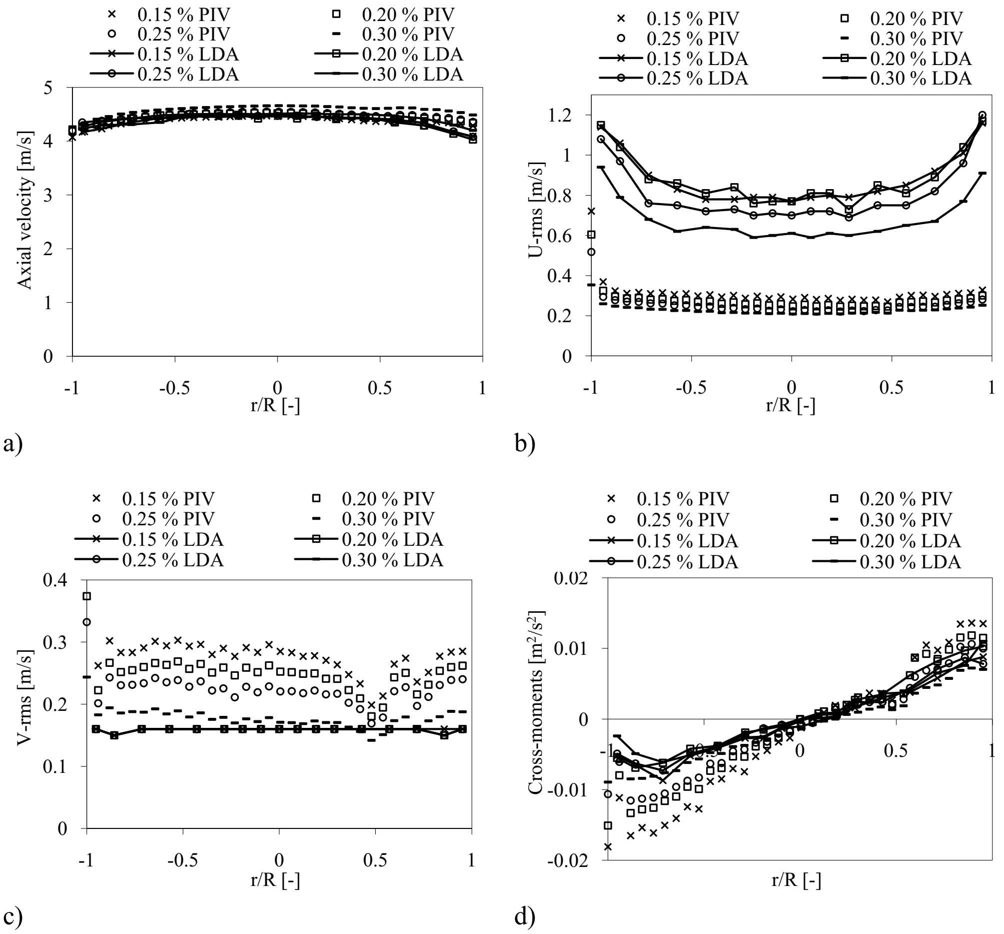

Figure 8.8: *The mean axial particle velocity profiles, the axial and normal rms profiles and the cross-moment profiles for glass particles with a diameter of 518 µm at a constant superficial gas velocity of 8 m/s and different particle volume fractions for both LDA and PIV.*

Effect of superficial gas velocity

The particle volume fraction is kept constant at approximately 0.15 % while the superficial gas velocity is varied between 6 and 9 m/s. From Figure 8.9a it can be seen that there is very good agreement between the mean axial particle velocities measured by LDA and PIV.

Figure 8.9b shows the axial particle rms profiles. The fluctuations increase for increasing superficial gas velocity for both the LDA and PIV results. It can be seen from the figure that the PIV profiles are flatter than the LDA profiles, and the LDA values show a clear increase in fluctuations when approaching the wall. The LDA measures higher fluctuations than the PIV. The figure also shows that the increase in fluctuations between each increase in superficial gas velocity is higher for LDA.

The normal particle rms profiles are presented in Figure 8.9c. It can be seen that there is an increase in normal fluctuations measured by the PIV when the superficial gas velocity increases. The LDA profiles do not show the same dependence. The fluctuations measured by

LDA are lower than the ones measured by PIV and the LDA measurements have no variation.

The cross-moment profiles can be seen in Figure 8.9d. All of the profiles have a value of zero in the centre of the pipe. The cross-moment values measured by PIV are higher than the ones measured by LDA. The PIV cross-moment values increase with increasing superficial gas velocity. This dependence cannot be observed from the LDA profiles.

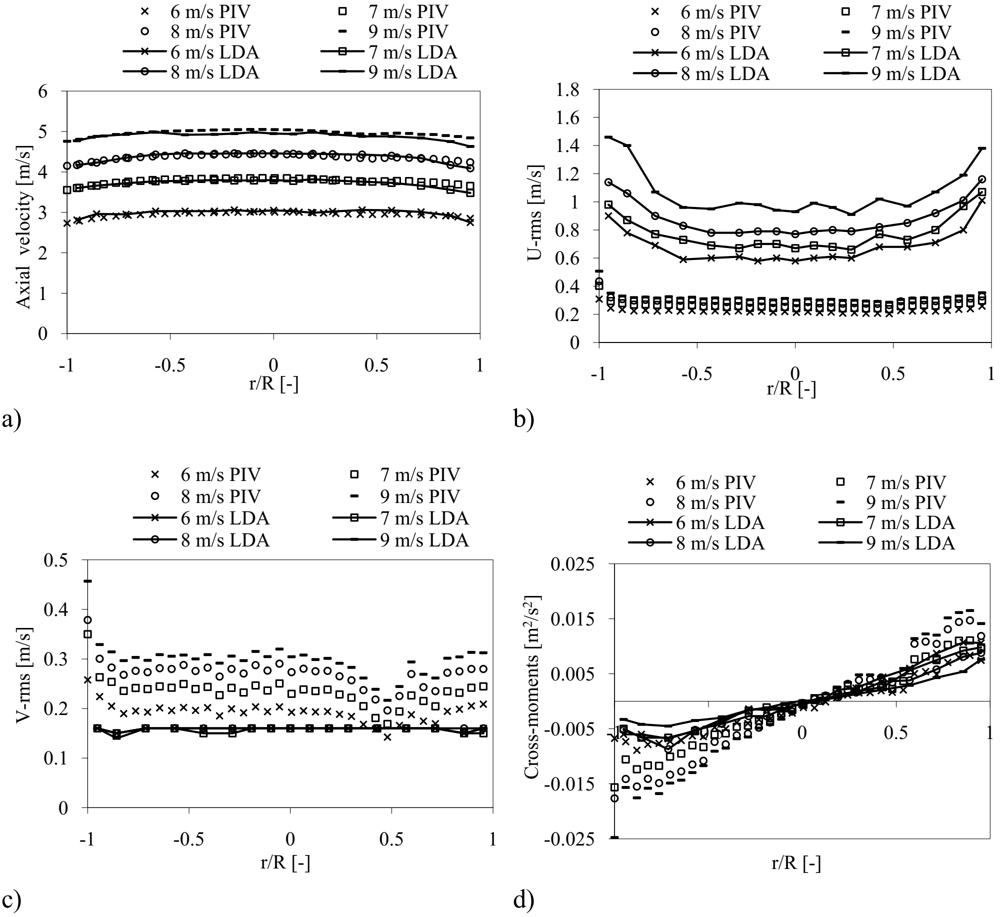

Figure 8.9: *The mean axial particle velocity profiles, the axial and normal rms profiles and the cross-moment profiles for glass particles with a diameter of 518 μm at a constant particle volume fraction of approximately 0.15 % at different superficial gas velocities for both LDA and PIV.*

8.3 Summary and discussion

In Ibsen (2000) PIV experiments are performed on a circulating fluidized bed (CFB) and evaluated against LDA measurements. The particles used in the study are 60 μm glass particles with a density of 2400 kg/m^3. The comparison shows good agreement between the measured PIV and LDA axial particle velocities. In the comparison between the U-rms measurements there is a difference. The fluctuations measured by PIV have a slightly higher value than those measured by LDA. Nomura et al. performed LDA and PIV measurements on in-cylinder flow. The measured axial velocities are the same for both LDA and PIV, while there is a clear difference in the measured fluctuations. The fluctuations measured by PIV are smaller than the ones measured by LDA. The authors explain this by the difference in the control volume.

The flow in a gas/liquid bubble column is studied by using PIV and LDA by Deen et al. (2000). They measured the liquid velocity with both PIV and LDA and found that the mean axial velocity is almost identical. There are differences between the measured axial and normal fluctuating velocities. For both fluctuations the PIV measures smaller fluctuations than the LDA.

When comparing these findings to those found in this thesis, it is clear for the axial velocity measurements that the values measured by PIV and LDA are almost equal. For the fluctuating velocities the PIV technique measures generally lower values than the LDA technique, the exception is the v-rms measurements for the larger particles (530 μm ZrO_2 particles and 518 μm glass particles). The results also show that under certain conditions limited to the PIV investigation, mainly a higher particle number density for the smaller particles, it is difficult to obtain results that give meaning. This is because it is difficult to separate particles from each other during post-processing due to reflections distorting the images. These measurements are excluded, more on this in Chapter 7.

The difference in averaging will influence the compared components. LDA measures on single particles at a time and the averaging is performed over period of time on the particles that passes the control volume. In PIV several particles can be located in the control volume and from the information obtained from the movement of each particle a representative value is given for each control volume. These are again averaged over time and space. This means that the results obtained form the PIV experiments are averaged over more particles than LDA. This will lead to lower values in the PIV experiments since the results are averaged over more particles and any measured extremes will be smoothed out.

Mean axial particle velocity
The results from the measurements of the mean axial particle velocities show generally a good agreement between the LDA and PIV measurements for all measurements for 260 μm ZrO_2, 120 μm and 518 μm glass particles (Figures 8.2a, 8.3a, 8.6a, 8.7a, 8.8a and 8.9a). The exception is the measurements for the 530 μm ZrO_2 particles (Figure 8.4a and 8. 5a). Here the differences between the measured axial velocities are obvious. The LDA measurements at constant superficial gas velocity with varying particle volume fraction show that the particle velocity is highly dependent on the particle volume fraction. This is also observed for the PIV measurements, but to a lesser extent.

Measurements at a superficial gas velocity of 7 m/s for 260 μm ZrO_2 particles with both LDA and PIV show the same axial particle velocity values (Figure E.3a). 120 μm glass particles are measured at a superficial gas velocity of 6, 7 and 9 m/s. Some differences are observed for the particle mean axial velocity when comparing the LDA and PIV measurements (Figures E.4a, E.5a and E.6a). LDA and PIV measurements of 518 μm glass particles are performed at a superficial gas velocity of 7 m/s. Small differences in axial particle velocity measured by LDA and PIV are observed (Figure E.7a).

Mean normal particle velocity
All of the measured mean normal particle velocities have a value close to zero (Figures 8.2b, E.1, E.2, E.3b, E.4b, E.5b, E.6b and E.7b).

Axial particle rms velocity

The U-rms values measured by PIV are lower than the ones measured for LDA for all of the particle types (Figures 8.2c, 8.3b, 8.4b, 8.5b, 8.6b, 8.7b, 8.8b and 8.9b). For 260 µm ZrO_2 particles at varying particle volume fraction it is observed that the fluctuations measured by the PIV varied, while the LDA measurements did not (Figure 8.2c). The opposite is found for the measurements with varying superficial gas velocity (Figure 8.3b). The LDA and PIV measurements for both the 530 µm ZrO_2 and 518 µm glass particles show that the fluctuations decreased with increasing particle volume fraction (Figures 8.4b and 8.8b). When the superficial gas velocity increases the fluctuations increase for both LDA and PIV measurements (Figures 8.5b and 8.9b). For the 120 µm glass particles the LDA measurements show an increase in fluctuations for increased particle volume fraction while the PIV measurements are only performed for a particle volume fraction of 0.15 % (Figure 8.6b). LDA and PIV measurements at varying superficial gas velocity showed that the fluctuations increased with increasing superficial gas velocity (Figure 8.7b).

From the LDA and PIV measurements at a superficial gas velocity of 7 m/s for 260 µm ZrO_2 particles it is observed that the LDA measured higher fluctuations (Figure E.3c). The PIV measurements show an increase in fluctuations with increasing particle volume fraction, the same is not observed for the LDA measurements. The PIV profiles are flatter than the LDA profiles which show a more pronounced increase towards the walls. From the measurements at 6, 7 and 9 m/s superficial gas velocity for 120 µm glass particles it can be observed that the LDA measures higher fluctuations. No dependence on the particle volume fraction can be seen for the LDA measurements for a superficial gas velocity of 6 m/s and only one profile is for the PIV measurements (Figure E.4c). An increase in axial particle rms velocity with increasing particle volume fraction can be observed for both LDA and PIV measurements at a superficial gas velocity of 7 and 9 m/s (Figures E.5c and E.6c). All of the measurements show a clear increase in fluctuations towards the wall. The LDA measures higher fluctuations than PIV for 518 µm glass particles at a superficial gas velocity of 7 m/s (Figure E.7c). The PIV profiles are flatter than the LDA profiles. The fluctuations increase for increasing particle volume fraction for both LDA and PIV measurements, but this is clearer for PIV.

Normal particle rms velocity

The PIV measurements give mostly lower fluctuations for 260 µm ZrO_2 particles (Figures 8.2d and 8.3c) than the LDA measurements. The fluctuations measured by PIV varies depending on the particle volume fraction and superficial gas velocity while the fluctuations measured by LDA only varies for superficial gas velocity. The measured fluctuations are higher for PIV than for LDA for 530 µm ZrO_2 and 518 µm glass particles (Figure 8.4c, 8.5c, 8.8c and 8.9c). For both particle types it is observed that the fluctuations measured by the PIV are reduced with increasing particle volume fraction and increase with increasing superficial gas velocity. No change is observed for the LDA measurements. For 120 µm glass particles the fluctuations measured by PIV are lower than the ones measured with LDA (Figure 8.6c and 8.7c). Little difference in the fluctuations are measured by LDA for both varying particle volume fraction and superficial gas velocity. Only the measurement for the lowest particle volume fraction is presented for the PIV measurements at varying particle volume fraction. When the superficial gas velocity is increased, the fluctuations increase.

The LDA and PIV measurements for 260 µm ZrO_2 particles at a superficial gas velocity of 7 m/s show that the LDA measures the highest fluctuations (Figure E.3d). No clear dependence on the particle volume fraction can be observed. 120 µm glass particles are measured at superficial gas velocities of 6, 7 and 9 m/s (Figures E.4d, E.5d and E.6d). The LDA measures higher fluctuations than the PIV. No dependence on the particle volume fraction is observed for

LDA or PIV. For the LDA and PIV measurements for 518 µm glass particles at a superficial gas velocity of 7 m/s the fluctuations are highest for PIV (Figure E.7d). A dependence on the particle volume fraction is observed for the PIV measurements and the fluctuations decrease with increasing particle volume fraction.

Particle cross-moments
The measured cross-moments for 260 µm ZrO_2 and 120 µm glass particles by LDA and PIV show that the values measured by PIV are generally lower (Figure 8.2e, 8.3d, 8.6d and 8.7d). The cross-moment values measured by PIV for 260 µm ZrO_2 particles at varying particle volume fraction show that the values vary. This is not observed for LDA. The measured cross-moments by LDA and PIV vary when the superficial gas velocity varies. For 120 µm glass particles the cross-moments measured by LDA show an increase with increasing particle volume fraction and superficial gas velocity. The PIV results are only shown for the lowest particle volume fraction, so no tendency is found (Figure 8.6d). The cross-moments increased with increasing superficial gas velocity. The LDA measurements for 530 µm ZrO_2 and 518 µm glass particles are generally lower than the PIV measurements (Figure 8.5d, 8.8d and 8.9d), while in Figure 8.4d this is difficult to see. The measured cross-moments decrease with increasing particle volume fraction, while the cross-moments increase with increasing superficial gas velocity for both the LDA and PIV measurements.

LDA and PIV measurements for 260 µm ZrO_2 particles at a superficial gas velocity of 7 m/s and for 120 µm glass particles at superficial gas velocities of 6, 7 and 9 m/s show that the LDA measures the highest cross-moments (Figures E.3e, E.4e, E.5e and E.6e). No dependence on the particle volume fraction is observed. For 518 µm glass particles the PIV measurements show a dependence on the particle volume fraction (Figure E.7e). The cross-moment decreases with increasing particle volume fraction.

8.4 Conclusion

A comparison between the experimental results from LDA (Chapter 6) and PIV (Chapter 7) are presented in this chapter. Both LDA and PIV measured generally the same mean axial particle velocities. The measured particle fluctuations (axial and normal) and the particle cross-moments are generally measured to be lower with the PIV technique. Both the LDA and PIV technique can be used to measure axial and normal mean particle velocities, particle U-rms and V-rms velocities and particle cross-moments.

There are some limitations concerning the use of PIV when the particle number density is too high. The success of the measurements depend on the post-processing algorithms ability to track individual particles. A high particle number density is preferred for the LDA measurements because this will reduce the measurement time. The number of particles in the system has no influence on the PIV measurement time, but it is recommended that the interrogation area contains a minimum number of particles. The flow velocity is an important factor. If the particles are failed to be recognized in the interrogation area of the next time-step, the information is lost. Under certain conditions unwanted reflections from particles and pipe wall can occur. This can influence the measurements negatively. Both techniques show some difficulty in measuring close to the circular pipe wall. The curvature of the wall is the main reason for this and can be solved by using a rectangular pipe.

9. NUMERICAL SIMULATIONS

9.1 Introduction

Fluent® is a commercially available code that can be used for numerical investigation of many types of flows. It is hoped that in the future numerical codes will be good enough so that the need for experimental investigations will be reduced. This makes it necessary to test the accuracy and flexibility of the available codes. There are many different types of particle flow and a code needs to be able to describe all of these before one can depend entirely on numerical simulations.

In this thesis the focus is on gas/particle flow. Fluent® has been extensively tested for several different particulate flows, including fluidized beds, riser flows and pneumatic transport. The flow in this study is a combination of a dense fluidized bed and a dilute pneumatic transport. But the main focus will be on pneumatic transport in a vertical pipe. In this chapter the experimental investigation performed previously in this thesis is used to evaluate the Fluent® code for this type of flow.

Numerical simulations have been performed on 2d and 3d pipes. The vertical lifter is also simulated. To reduce the simulation time only the strictly necessary parts of the vertical lifter is included. The governing equations used in the simulations are presented in Chapter 5. The boundary conditions will vary and will be described when appropriate.

The solids phase in Fluent® can either be described by the Euler or the Lagrange method. The main difference between these is that the Lagrange method is a simplified particle tracking method. It can be very time consuming and expensive when many particles. It is without a dense flow model and it is therefore only applicable in very dilute flows. When using Euler the solids phase is modelled as a continua. Even though the flow investigated in this thesis is dilute, the Euler model is found to be the best method. It is also necessary to use the Euler model when the whole vertical lifter is simulated since the flow also consists of a fluidized bed which is a dense flow. The Euler–Euler model is the model recommended by the Fluent® User's Manual (2001) for simulations of pneumatic transport. A short summary of the models and solver used in the simulations in this chapter are given in Table 9.1.

Table 9.1: Models and solver used in the simulations with Fluent®.

Multiphase model	Euler-Euler
Solver	Segregated, unsteady
Turbulence model	Standard k-ε
k-ε multiphase model	Dispersed
Near wall treatment	Standard wall function

An important aspect of unsteady (transient) numerical simulations is the length of the computation in time. The simulation time depends on the complexity of the flow and the grid. For transient cases it is important to choose the right time-step size. This time-step must be less than the time for some significant action to occur. One way of finding out if the right time-step size is to investigate the Courant number.

Courant number
The Courant number can be used in any time-marching computer simulation to find the optimal time step. The flow field is divided into control volumes and the time-step needs to be less than the time needed for a fluid flow with a certain velocity to cross one of the control volumes. The

Courant number is written,

$$C_r = \frac{u\Delta t}{\Delta x} \tag{9.1}$$

Where Δt and Δx is the length of the time-step and length of the control volume respectively, and u is a characteristic velocity of the flow.

Due to numerical considerations the Courant number should be less than 1. The optimal time-step size of any case can be found using $C_r = 1$, the length of the control volume and the velocity of the flow. The time-step used is 1.0 x 10^{-4} s.

Average data
The different cases are simulated for different time lengths, depending on the complexity of the flow. It is desirable to investigate how the flow develops along the time-step and also find the time averaged data. The time average values can be found by enabling the "data sampling for time statistics" in Fluent®. It is important to start the data sampling after the flow is stabilised, as there will always be some initial instability.

Report data
Data can be extracted from Fluent® by using the report function and then chose the surface integrals. There are several uses for this report function in Fluent®, but in this case only the value of certain field variables on specified points along the cross-section is of interest. The data needs to be extracted and studied more closely. In order to obtain the data, a report type needs to be chosen. The facet average is one such type. The geometric shape is divided up into facets, which are flat faces. The facet averaged quantity is calculated on the surfaces.

9.2 Preliminary numerical simulations

In the preliminary simulations the gas/particle flow is simulated with the Euler-Euler model. The kinetic theory of granular flow (KTGF) is included, but an alternative, the constant viscosity model (CVM), can also be used. Their function is to provide closure for the internal momentum transfer in the solids phase.

The preliminary simulations are performed on a simple 2d pipe with the geometry displayed in Figure 9.1. The geometry is generated in Gambit®. The pipe has a diameter of 0.042 m and a height of 1.5 m. The grid size is 21 x 300 cells, and boundary conditions based on measurements are used. It is important to note that the inlet configuration will be different from that of the experimental set-up. In the experiments the particles are not present in the air flow when air enters the system. The particles are in a fluidizing silo and packed around the transport pipe. The particles are dragged into the pipe by the air flow when it passes the opening between the bottom of the silo and the beginning of the transport pipe as seen in Figures 2.1 and 2.2. The pipe simulations will later be extended to the vertical lifter presented in Chapter 2, but it is important to test the simplest geometries before starting with the more complex. When the geometry increases in complexity, it follows that the simulations increase in complexity and in simulation time. More complex simulations might also be more difficult to converge.

The initial particle and gas velocities and the particle volume fractions are based on the experimental findings in Chapters 6 and 7. For comparison with the experimental study the results at the height of 1.3 m above the inlet is of most interest, but the whole flow field will be examined.

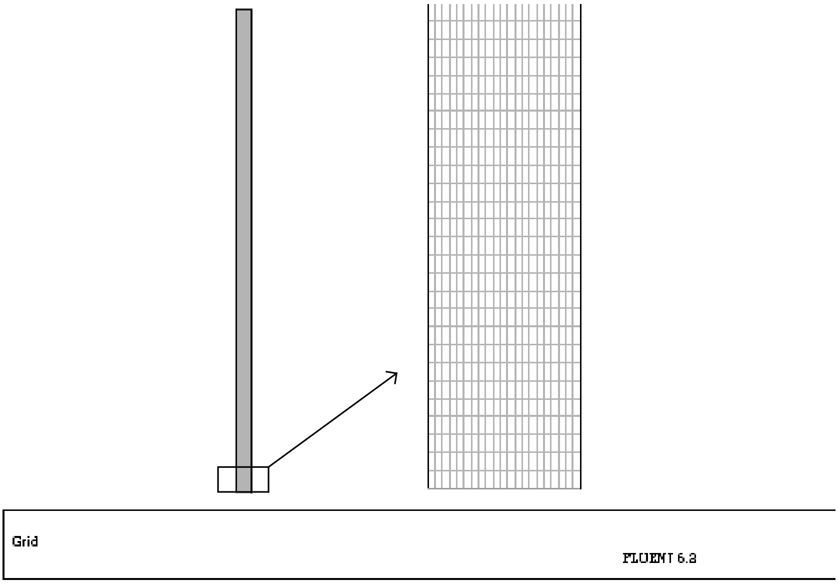

Figure 9.1: 2d-pipe grid generated in Gambit®.

9.2.1 2d simulation of a pipe with kinetic theory of granular flow

The gas/particle flow studied is dilute. This type of flow can usually be simulated in Fluent® by using the Euler–Euler model with kinetic theory of granular flow (KTGF). The simulation based on the specifications given in Table 9.2 gives the particle volume fractions shown in Figure 9.2.

Table 9.2: Specification of the initial simulation, Euler-Euler model with KTGF.

Particle	
Particle diameter (glass) [μm]	518
Glass density [kg/m^3]	2500
Particle viscosity [$Pa \cdot s$]	Not specified when using KTGF
Interactions	
Drag model	Gidaspow (Chapter 5)
Restitution coefficient particle – particle [-]	0.95
Inlet boundary conditions	
Particle volume fraction [-]	0.002
Particle velocity [m/s]	4.3
Granular temperature [m^2/s^2]	0.0001
Air velocity [m/s]	8
Turbulence intensity [%]	5
Hydraulic diameter [m]	0.042
Wall boundary (gas phase)	No slip
Wall boundary (solids phase)	Free slip (zero share)

The Gidaspow drag model is enabled in the simulations, but only the dilute term is enabled due to the dilute flow conditions.

The particle – particle restitution coefficient used in literature varies. Chan et al. (2005) used a restitution coefficient of 0.99 for 76 µm FCC particles. In Tartan & Gidaspow (2004) three different restitution coefficients, 0.89, 0.95 and 0.98, are used for 530 µm glass particles. A particle – particle restitution coefficient of 0.94 is used by Lun & Savage (1986). Samuelsberg & Hjertager (1996) used a value of 0.995 for 75 µm particles. Coefficients of 0.95 and 1 are used by Patil et al. (2005) for particles with a diameter of 285 µm and a density of 3060 kg/m^3. In this thesis a restitution coefficient of 0.95 is selected. A restitution coefficient of 0.9 and 0.98 are tested. No clear differences are observed.

Samuelsberg & Hjertager (1996) used an initial value of zero for the granular temperature. Patil (2005) used a value of 10 m^2/s^2. In a study on horizontal dilute flow Eskin et al. (2004) used an initial granular temperature of 10^{-6}, 10^{-5} and 0.3 m^2/s^2. An initial granular temperature of 0.0001 is used in this thesis.

For the gas phase a no-slip wall boundary condition is used, while a free slip condition is used for the solids phase. The free slip condition is chosen because the particles do not stick to the wall. The no-slip condition models a velocity of zero at the wall while the free-slip model means that the wall has no effect on the particle velocity.

The turbulence boundary conditions are specified by turbulence intensity in percent and the hydraulic diameter. From the experiments a value of 5 % for the turbulent intensity was found to be reasonable, while the hydraulic diameter varies with the simulated geometry.

The simulations are first run for 20 s and then for another 10 s over which the mean value is calculated. In Figure 9.2 the result from the simulation based on the specifications given in Table 9.2 can be seen. The figure shows the mean particle volume fraction in the pipe. The area of interest is found near the top, 1.3 m above the inlet, and this section is enlarged in Figure 9.2.

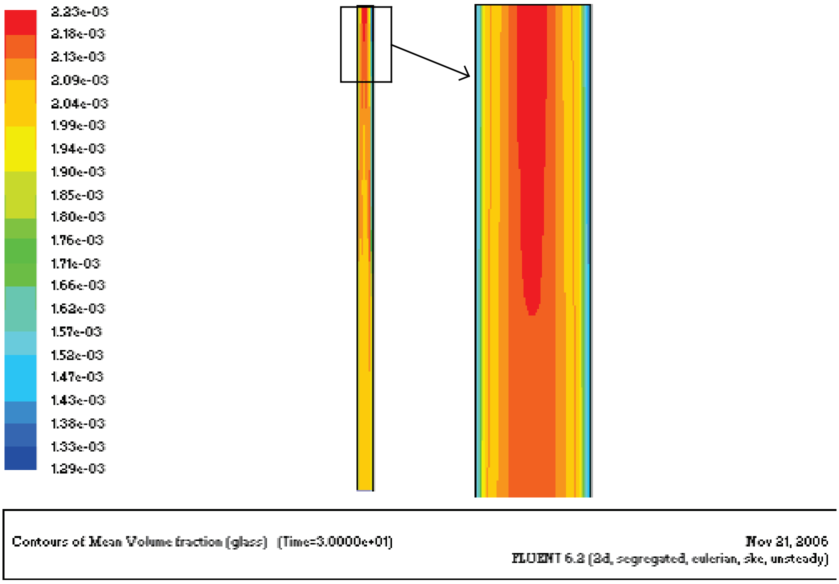

Figure 9.2: The mean particle volume fraction results from the simulation with KTGF in 2d for 518 µm at a superficial gas velocity of 8 m/s.

Figure 9.2 shows that the particle volume fraction is highest in the centre of the pipe. It can be seen that the particle volume fraction varies over the cross-section of the pipe. The highest concentration is found in the centre of the pipe with a drop towards the wall. The figure also shows that particles are gathering in the centre of the pipe as the particles travel up the pipe. This is also observed by Tanaka & Tsuji (1991) who observed this effect for very dilute flows ($\alpha_s = 10^{-4}$). In He & Simonin (1993) it is explained that this is because the solids turbulent energy is highest near the walls which cause the particles to move toward the centre of the pipe.

In Figure 9.4 the particle volume fraction and the particle velocity profiles from the simulation are shown.

9.2.2 2d simulation of a pipe with the constant viscosity model

An alternative to using the KTGF model is the constant viscosity model (CVM). Here a viscosity of the solid phase is specified and kept constant throughout the simulation. Patil et al. (2005) used both KTGF and the CVM to simulate a gas/solid fluidized bed and compared the results. They found that both models gave satisfying results, but that that the KTGF model is the better choice for their system. The solids phase viscosity is assumed to be constant with a value of $1\,Pa \cdot s$, which they found in literature. Both Schügerl et al. (1961) and Grace (1970) performed experiments and found a value of $1\,Pa \cdot s$ for the solid phase viscosity. Gidaspow (1994) used a value of $0.509\,Pa \cdot s$ for transient vertical conveying and a value of $0.724\,Pa \cdot s$ is used in a riser simulation. A value of $0.8\,Pa \cdot s$ is found through simulations to be the best option for the gas/particle flow presented in this thesis. The boundary conditions are given in Table 9.3 and the governing equations are given in Section 5.4.

Table 9.3: Specifications used in the simulation with CVM.

Particle	
Particle diameter (glass) [µm]	518
Glass density [kg/m^3]	2500
Particle viscosity [$Pa \cdot s$]	0.8
Interactions	
Drag model	Schiller-Naumann
Restitution coefficient particle – particle [-]	Not applicable when using CVM
Inlet boundary conditions	
Particle volume fraction [-]	0.002
Particle velocity [m/s]	4.3
Granular temperature [m^2/s^2]	Not applicable when using CVM
Air velocity [m/s]	8
Turbulence intensity [%]	5
Hydraulic diameter [m]	0.042
Wall boundary (gas phase)	No slip
Wall boundary (solids phase)	Free slip (zero share)

When using the CVM model in Fluent®, the Gidaspow drag model is no longer available and the choice of drag models are limited, but a user defined function (UDF) can be implemented. This has been done, but the results are not reported as the Shiller-Naumann drag model (Shiller and Naumann, 1935) gave satisfying results. This drag model is according to Troshko & Mohan (2005) applicable for particles in a dilute mixture (particle volume fraction < 10 %), if they are spherical. This model is based on the relative Reynolds number defined in Equation 5.22. The drag law uses different coefficients for Re > 1000 and for Re < 1000.

Again the simulation is first run for 20 s and then for another 10 s over which the mean value is calculated. Figure 9.3 shows the result from the simulation based on the specifications given in Table 9.3. The figure shows the mean particle volume fraction in the pipe and the main area of interest is enlarged. In Figure 9.4 the particle volume fraction and particle velocity is shown over the cross-section of the pipe at a height of 1.3 m, and compared with results from KTGF calculations.

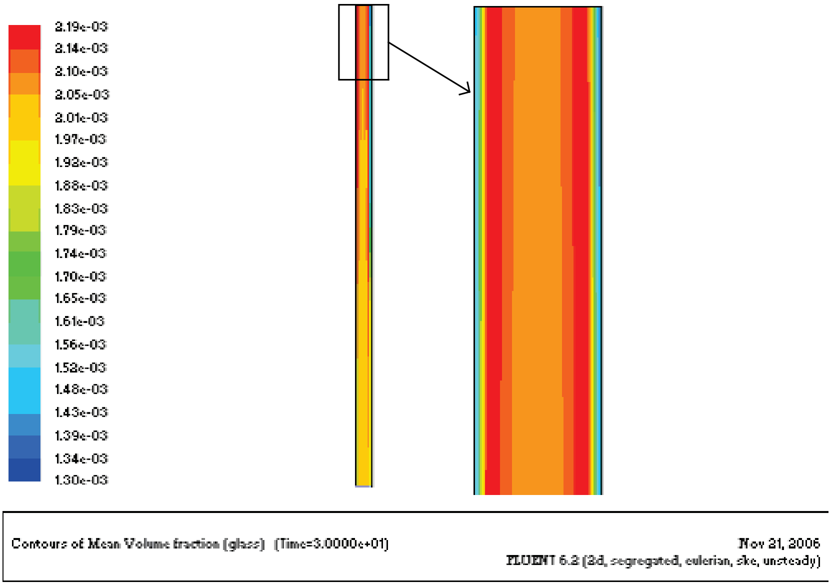

Figure 9.3: *A 2d CVM simulation with a constant solids viscosity of 0.8* $Pa \cdot s$ *for 518 μm at a superficial gas velocity of 8 m/s.*

9.2.3 2d simulation of a pipe, comparison between KTGF and CVM

In Figure 9.4 the graphs from the 2d simulations with KTGF and CVM are presented and compared.

Figure 9.4a shows that there are some small differences between the mean particle volume fraction profiles for the two simulations. The simulations show the same tendency close to the wall. While the CVM simulation gives the highest volume fraction close to the wall, the KTGF model simulation gives the highest value in the centre of the pipe. It can be seen from Figure 9.4b that the two simulations have the same velocity profile. This comparison together with the comparison of the mean particle volume fraction, show that for a simulation of dilute pneumatic transport in a pipe it is not necessary to include KTGF, since the simulation with CVM gives similar results. This is due to the fact that it is the drag and not particle/particle interactions that dominate dilute gas/particle flows. It can be concluded that there is little difference in using the Gidaspow drag model and the Shiller-Naumann drag model when the flow is dilute.

The KTGF model is more flexible according to Patil et al. (2005) since no assumption of solid phase viscosity is involved and it is therefore applicable for a wider variety of flows. The rest of the simulations in this thesis will include the KTGF model.

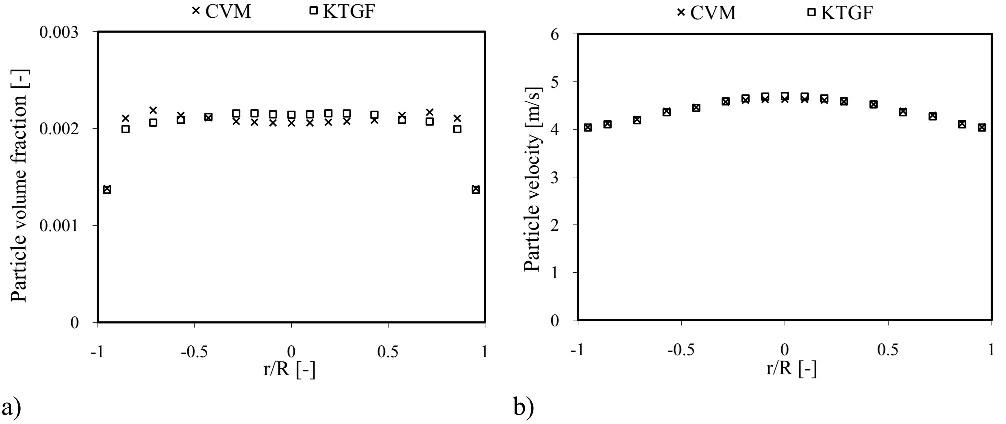

Figure 9.4: The mean particle volume fraction and axial velocity profiles for 2d KTGF and CVM simulation for glass particles with a diameter of 518 μm at a constant superficial gas velocity of 8 m/s and a height of 1.3 m.

9.3 2d and 3d simulations of the transport pipe

In the previous section initial simulations with 518 μm glass particles in a 2d pipe is performed. In this section 2d and 3d pipe simulations are performed with all of the particle types studied in the experimental sections, Chapters 6 and 7.

From the preliminary simulations performed on the 2d pipe it is concluded that the KTGF model and the CVM model can both be used. The governing equations are found in Chapter 5 and the boundary conditions used are found in Table 9.4. The initial particle velocities are based on the experimental findings in Chapters 6 and 7, the mean axial particle velocity in the centre of the pipe. The exact same simulations performed in the 2d pipe are performed for the 3d pipe. Both simulations are run for 20 s, before the data sampling for time statistics is enabled for an additional 10 s.

Table 9.4: Specification for the performed simulations with the different particle types.

Particle type	Glass	Glass	ZrO_2	ZrO_2
Size [μm]	120	518	260	530
Density [kg/m^3]	2500	2500	3800	3800
Particle velocity [m/s]	7.6	4.3	5.8	3.4
Initial granular temperature [m^2/s^2]	0.0001			
Particle volume fraction [-]	0.002			
Air velocity [m/s]	8			
Turbulence intensity [%]	5			
Hydraulic diameter [m]	0.042			
KTGF	Yes			
Drag model	Gidaspow			
Particle-particle restitution coefficient [-]	0.95			
Wall boundary (gas phase)	no slip			
Wall boundary (solids phase)	free slip (zero shear)			

9.3.1 2d transport pipe simulations

The mean particle volume fractions for the 2d simulations seen in Figure 9.5a show a fairly constant value throughout the cross-section of the pipe. All of the profiles show a fall in the volume fraction when approaching the walls.

Figure 9.5b shows the mean particle velocity profiles for the four different particle types. All of the profiles for the 2d simulations are quite flat, but the 120 µm glass particles show a higher gradient when approaching the wall and a more rounded profile. The figure also shows that the two largest particle types have the lowest velocity, which is expected since they are the heaviest particles.

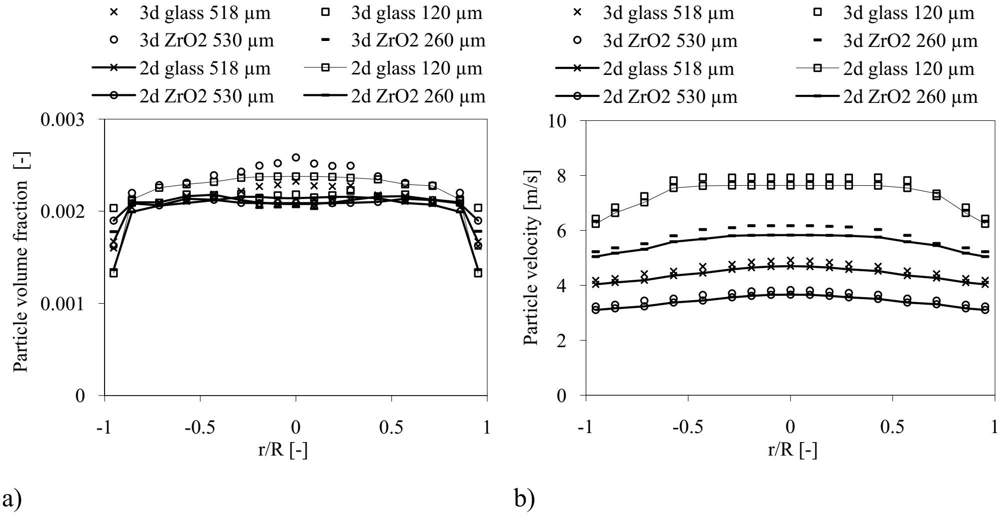

Figure 9.5: The mean particle volume fraction and axial velocity profiles for 2d and 3d KTGF simulations at a superficial gas velocity of 8 m/s at a height of 1.3 m.

9.3.2 3d transport pipe simulations

The grid used in the 3d simulations can be seen in Figure 9.6. The results presented are taken at a height of 1.3 m and at a centre line through the pipe at this height. Figure 9.5 shows the results from the simulations with a 3d geometry.

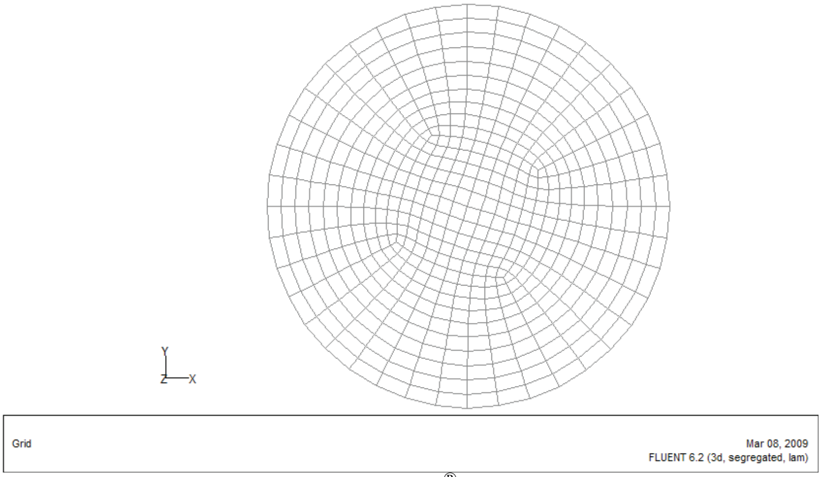

Figure 9.6: 3d pipe grid generated in Gambit$^{®}$.

Figure 9.5a shows that the 3d simulations of the particle volume fraction for the different particle types differ in the centre of the pipe. The profiles for the two largest and heaviest particles show an increase in particle volume fraction towards the centre of the pipe. For the two smallest and lightest particles the profiles show a drop in the particle volume fraction in the centre of the pipe. The particle volume fraction increase towards the centre, reaches a maximum and then is reduced in the centre area.

The particle volume fraction shown for 2d and 3d simulations in Figure 9.5b displays some differences between the simulations. For the 2d and 3d simulations of the two smallest and lightest particles a drop in particle volume fraction in the centre of the pipe is observed. For the largest glass particle type, a slight drop is observed in the centre of the pipe for the 2d simulation, while a slight increase in the centre is shown for the 3d simulation. For the largest ZrO_2 particles an increase in particle volume fraction from the wall and towards the centre of the pipe where a maximum is reached is observed for the 3d simulations, but in 2d the maximum is closer to the wall and one local minimum exists in the centre of the pipe.

From Figure 9.5b it can be seen that all of the particle velocity profiles are fairly flat in the centre of the pipe, but steeper by the wall. The figure shows that the smallest and lightest particles reach the highest velocity and the largest and heaviest particles have the lowest velocity as expected. The results in Figure 9.5b show that the 2d simulations of particle velocity give slightly lower particle velocities than the 3d simulation. The differences are larger for the two smallest and lightest particles.

9.4 Comparison with the experimental investigation

9.4.1 Euler-Euler 2d KTGF transport pipe simulations

Here the results from the 2d pipe simulations with all the different particle types are compared with the experimental LDA and PIV results. In Figure 9.7 the comparison can be seen, both simulations and experiments are performed at a superficial gas velocity of 8 m/s and a particle volume fraction of 0.002. The figure shows that there is generally a good agreement between the simulations for all of the particles and the experimental findings. The largest difference between the simulations and the experiments can be found for the two smallest particle types.

Here a clear difference is observed between the simulated and experimentally measured particle velocities when approaching the wall. The reason for this seems to be that the wall effect is over-predicted for these smaller particles.

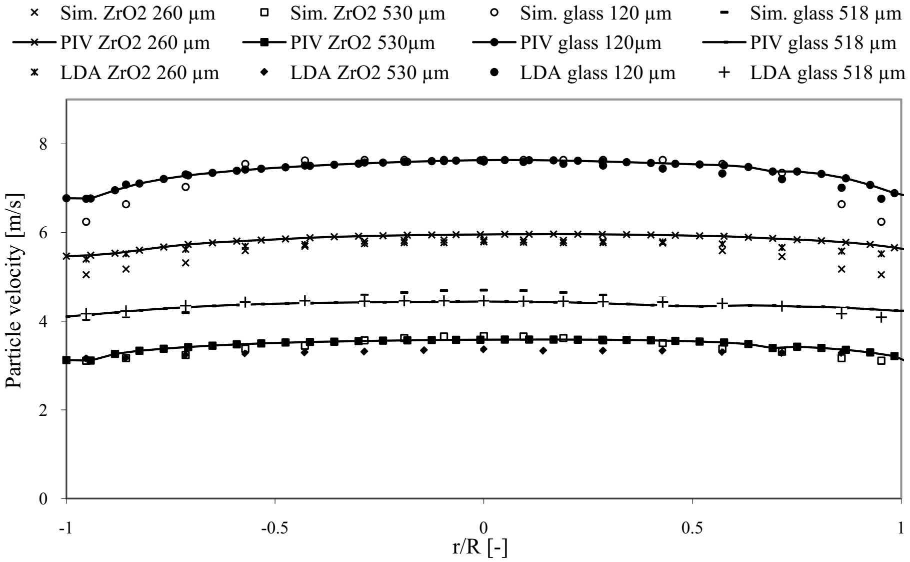

Figure 9.7: *Comparison between the 2d pipe simulations performed in this chapter and the previously measured particle velocities with the experimental techniques LDA and PIV.*

9.4.2 Euler-Lagrange simulations, particle tracking

The mean axial particle velocity in the centre of the pipe from the LDA experimental investigation is compared with the results from a 2d Euler-Lagrange simulation. A brief introduction of the method is given in the beginning of this chapter and the equations used in the Fluent® simulation is presented in Chapter 5. The Euler-Lagrange simulations are performed at a superficial gas velocity of 8 m/s and with the particle velocity given in Table 9.4 (the experimental value). The simulations are performed by tracking 1000 particles and including turbulent flow conditions (k-ε model). The particles are released from the air inlet at the bottom of the transport pipe. Little difference is observed with the increase the number of tracked particles. The particle size distribution and density is given in Table 9.4. The results are presented Figure 9.8 and are compared with the experimental findings (LDA) and Eulerian-Eulerian simulations performed in Section 9.3.1.

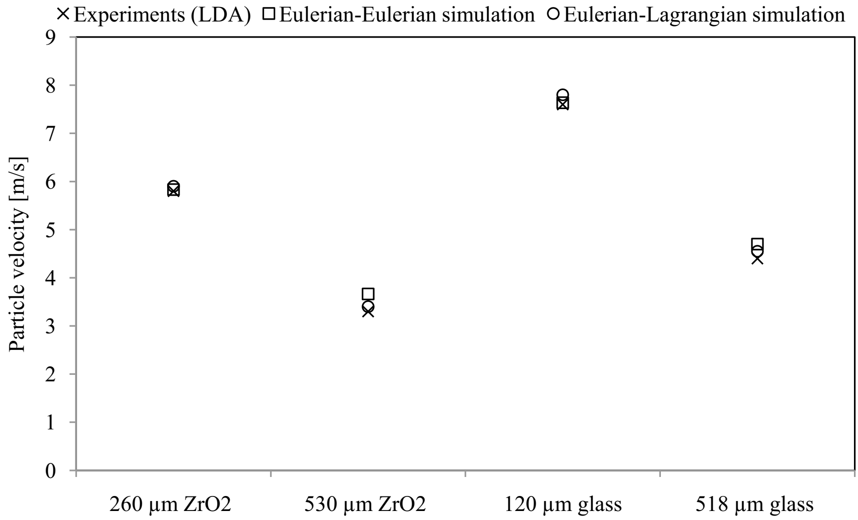

Figure 9.8: The results from the particle tracking simulations and comparison with the experimental results (LDA) at a height of 1.3 m.

The results in Figure 9.8 show that there is good agreement between the Eulerian–Lagrangian simulation, the Eulerian-Eulerian simulations and the experimental results (LDA). The simulations slightly over-predict the particle velocity compared to the experiments. This is clearer for the largest particles.

9.5 2D SIMULATIONS OF THE VERTICAL LIFTER

In order to reduce the computation time only the necessary parts of the lifter is included. This means that the top tank is omitted and that the particles that flow out through the transport pipe leave the system. Initially the bed height is set to 0.3 m and in order to ensure that there are always particles in the bottom silo, particles are continuously fed into the silo from the top. The 2d geometry of the vertical lifter is seen in Figure 9.9.

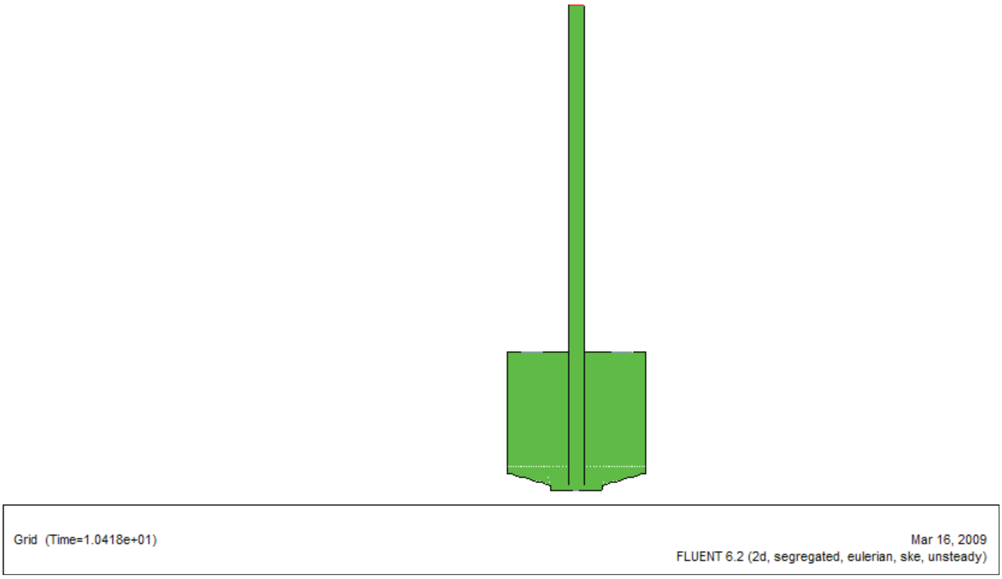

Figure 9.9: The geometry of the 2d vertical lifter without the receiving tank.

The specification used in the 2d simulation of the vertical lifter can be seen in Table 9.5. The particle type chosen for the simulations is 518 µm glass particles.

Table 9.5: Specification of the simulation of the 2d vertical lifter.

Particle	
Particle diameter (glass) [µm]	518
Glass density [kg/m^3]	2500
Particle viscosity [$Pa \cdot s$]	-
Interactions	
Drag model	Gidaspow (Chapter 5)
Restitution coefficient particle – particle [-]	0.95
Inlet boundary conditions	
Particle volume fraction [-]	-
Particle velocity [m/s]	-
Granular temperature [m^2/s^2]	0.0001
Gas velocity [m/s]	22.4 (adjusted for the smaller air inlet diameter, corresponds to 8 m/s in the transport pipe)
Turbulence intensity [%]	5
Hydraulic diameter [m]	0.015
Wall boundary (gas phase)	No slip
Wall boundary (solids phase)	Free slip (zero shear)
Bed packing [-]	0.63
Initial bed height (m)	0.3

The simulated particle volume fraction and particle velocity is presented in Figure 9.10, the profile is taken at a height of 1.3 m. It can be seen from Figure 9.10a that the value of the particle volume fraction from the simulations with the Gidaspow drag model reach a maximum in the centre of the pipe at a value of 0.215. In comparison the experimental investigation is performed at a particle volume fraction between 0.0015 – 0.0030. This means that the particle volume fraction found in the simulations is a factor of 100 higher in the centre of the pipe than the value from the experiments. The distribution of the particle volume fraction is not measured in the LDA or PIV experiments.

The drag model, Gidaspow, used in the simulations gave acceptable results for the particle velocity in the pipe, Figure 9.10b. The simulated particle velocity is close to the velocity found in the experiments. The velocity is the same in the centre of the pipe and at the wall, but the simulation show the highest velocity away from the centre.

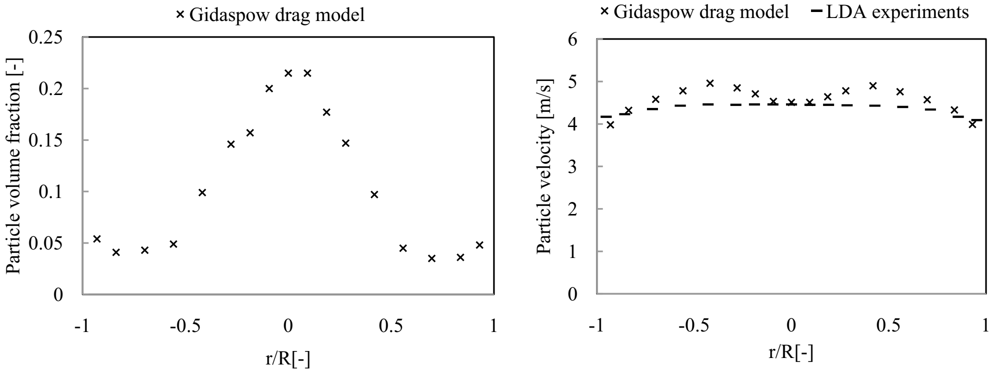

a) b)

Figure 9.10: The simulated particle volume fraction and particle velocity for a 2d vertical lifter for 518 μm glass particles at a height of 1.3 m.

It is clear from the measured particle volume fraction in Figure 9.10a that the current set-up based on the parameters in Table 9.5 did not match the observations from the experiments, performed on 518 μm glass particles at a superficial gas velocity of 8 m/s and a particle volume fraction of 0.002 (0.20%) presented in Chapters 6 and 7. Because of this simulations are performed for the other particle types, but no improvement could be observed. The main problem with the 2d vertical lifter simulations is the concentration of particles in the transport pipe. The experimental set-up is designed so that a dilute flow can be investigated by using lasers. A bleed line connected to the receiving tank are adjusted to control the flow of particles and to give either a dense or dilute flow. This meant that the set-up used in the simulations differed from the experimental set-up and the drag of particle in to the transport pipe is over-predicted compared to the experiments. The forces acting on the particles in the fluidization silo seem to be under-predicted. Measures are taken to increase the forces acting on the particles in the silo, but only very small improvements are observed.

In Figure 9.11 the particle volume fraction distribution in the system is shown.

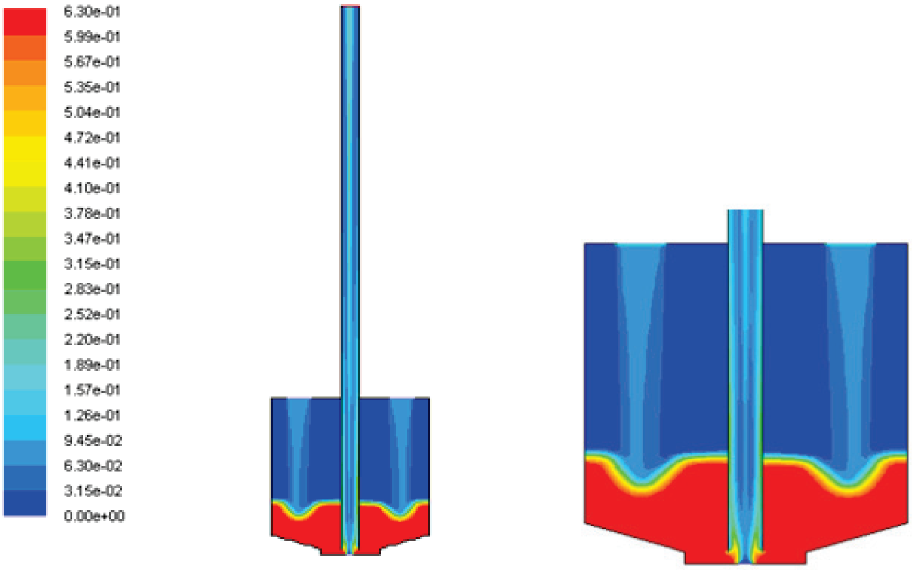

Figure 9.11: The simulated particle volume fraction in the system using the Gidaspow drag model.

9.6 Conclusion

The computational investigation on the gas/particle two phase flow is initially performed using only the transport pipe. The 2d geometry is generated in Gambit®. The simulations are performed using Euler-Euler, here both phases are treated as a continuum. The flow is dilute and as an alternative the Euler-Lagrange (particle tracking) can also be used, but this is not the focus of this investigation. When using Euler to describe the solids phase the kinetic theory of granular flow (KTGF) is usually included. For very dilute flows it can be omitted and the constant viscosity model (CVM) can be applied instead. Simulations with both KTGF using the Gidaspow drag model and CVM with the Shiller-Naumann are performed on 518 µm glass particles and the results are very similar. The 2d Euler-Euler with KTGF is used to simulate on all of the particle types from the experimental investigation. These 2d simulations are extended to 3d and the results are compared. The simulations generally give the same result, but some small differences is observed for the two smallest particle types, 120 µm glass particles and 260 µm ZrO_2, for the particle velocity. When comparing the particle volume fraction, a difference is found for the two largest particle types, 518 µm glass particles and 530 µm ZrO_2. For the two smallest particle types the particle volume fraction is similar.

Good agreement with experimental results (LDA, Chapter 6 and PIV, Chapter 7) for all of the particle types is found for 2d Euler-Euler KTGF simulations. For the two smallest particle types, 120 µm glass particles and 260 µm ZrO_2, a difference between the simulations and the experiments is observed in the vicinity of the wall. The experimental velocity profiles are flatter than the simulated ones. When compared to the experiments the simulations over-predict the wall effect.

The Eulerian-Lagrangian model is also compared with the Eulerian-Eulerian simulation and with experimental findings. A simulation tracking a 1000 particles are performed for all of the particle types and they all showed good agreement with the results from the Eulerian-Eulerian simulations and LDA experiments.

After the good results from the simulations on the single transport pipe in both 2d and 3d, the vertical lifter is simulated. The initial 2d Euler-Euler KTGF simulation on 518 μm glass particles in the vertical lifter show a too high particle volume fraction in the transport pipe. Compared to observations from the experiments the particle volume fraction is over-predicted when using the Gidaspow drag model and. The reason for this discrepancy is that the experimental set-up is modified to give low particle volume fractions in the transport pipe to enable the use of lasers to investigate the flow. The forces acting on the particles seem to be under-predicted in the simulations compared to the experiments, the drag of particles into the transport pipe is over-predicted.

10. CONCLUSIONS AND RECOMMENDATIONS

The aim of this work is to increase the understanding of dilute vertical pneumatic transport of particles. This is achieved through experimental and numerical studies of a vertical gas/particle flow.

10.1 Conclusions

The main part of this study is the experimental investigation of dilute vertical gas/particle flow. Two different laser based techniques are used in the investigation the solids phase of the two phase flow. These are laser Doppler anemometry (LDA) and particle image velocimetry (PIV). The main difference between LDA and PIV is that LDA measures in a single point while PIV is a whole field technique. Another distinction is the difference in measurement time. The PIV measurements are completed in much less time than the LDA measurements, which can take hours for dilute flow. The reason for this is that LDA measures individual particles. Measurements that do not meet the requirements are omitted from the results during sampling. A certain number of measurements are needed to ensure reliable results. For PIV two pictures are taken of the flow and compared. None of the data are omitted during sampling. Data that do not meet the requirements are substituted with accepted data during post-processing. The main advantage of the PIV technique is that it give an instantaneous picture of the whole flow cross-section. Both techniques can be used for studying the solids phase in a two phase flow. There are some limitations using PIV when the particle number density gets too high and it gets difficult to separate the individual particles. Reflections from particles and the pipe wall that obscure the pictures can also be a problem.

The particles used in this investigation are zirconium oxide (ZrO_2) and glass particles. Two particle size distributions of both ZrO_2 particles (260 and 530 μm) and glass particles (120 and 518 μm) are studied. From the density and the size of the particles it is deducted that the largest ZrO_2 particles are the heaviest, closely followed by the largest glass particles, then comes the smallest ZrO_2 particles and the lightest particles are the smallest glass particles. The effect of superficial gas velocity (6, 7, 8 and 9 m/s) solid volume fraction (0.15, 0.20, 0.25 and 0.30%) particle diameter, and particle density on the mean particle velocities, U-rms, V-rms and mean cross-moments are investigated. Both LDA and PIV are used to study the solids phase. A comparison between the measurement techniques LDA and PIV is also carried out.

An extensive study of dilute gas/particle flow in vertical direction by LDA is presented in Chapter 6 and Appendix C. The mean particle velocities, U-rms, V-rms and mean cross-moments are investigated for all of the particle types and at different superficial gas velocities. The effect of the particle volume fraction on the aforementioned parameters varies depending on the particle type, size and density. The following results are obtained from measurements of the solids phase at constant superficial gas velocity, 8 m/s, and varying particle volume fraction.

- When varying the particle volume fraction, the results show that the axial particle velocities increase with increasing particle volume fractions for the largest ZrO_2 particles and for the smallest glass particles. The same cannot be seen for the smallest ZrO_2 or the largest glass particles, for which the particle volume fraction do not seem to have any effect on the particle velocity. The largest and heaviest particle types have the flattest profile. Small glass particles are most influenced by the wall effect.
- Normal velocity profiles for all of the particle types show values close to zero. The ideal is a normal velocity value of zero which would mean that the experimental set-up

is perfectly aligned. Perfect alignment is difficult to attain and might not even be possible. Therefore the experimental set-up is aligned as to give the closest value to zero which can be achieved.
- The particle U-rms is reduced for both the largest glass and ZrO_2 particles with increasing particle volume fractions. For the lightest particles, 120 μm glass particles, the fluctuations increase when the particle volume fraction increases. No dependence on the particle volume fraction is observed for the smallest ZrO_2 particles. This means that the measured particle U-rms dependence on the particle volume fraction is dependent on the particle type (size and density). For the heaviest particles the U-rms is reduced with increasing particle volume fraction, but for the smallest particle it is increased and the particle type in between seems to be in a transitional phase and no clear dependence is observed.
- None of the particle types showed any dependence on the particle volume fraction for the normal fluctuations.
- The cross-moments measured for the smallest glass particles increased with increasing particle volume fraction. No dependence on the particle volume fraction is observed for the other particle types.

When varying the superficial gas velocity and keeping the particle volume fraction constant at 0.15% the following was observed.
- The measured axial particle velocity increases for all particle types.
- The normal velocity is measured to a value close to zero for all particle types.
- When the superficial gas velocity increases the axial particle fluctuations increases for all particle types.
- For the normal fluctuations, no dependence is found for any of the particle types.
- The increase in superficial gas velocity has no visible effect on the cross-moment for the two types of ZrO_2 particles and the largest glass particle. An increase is observed for the smallest glass particles when the superficial gas velocity increases.

The results below are obtained by comparing the measurements of the particle types at a constant superficial gas velocity of 8 m/s and a constant particle volume fraction of 0.15%.
- It is observed that the lightest particles, the smallest glass particles, reach a higher velocity than the heavier particles as expected. The lowest velocity is measured for the largest ZrO_2 particles. The profiles are flat for all particle types, and the largest ZrO_2 particles have the flattest profile. The wall effect is clearly visible for the smallest glass particles.
- The axial and normal particle fluctuations are highest for the largest and heaviest particles, which corresponds with literature.
- The highest cross-moment value is measured for the smallest and lightest particle type.

In Chapter 7 and Appendix D the results from the PIV measurements are presented. During the experimental investigation it is observed that some of the measurements does not give the expected results. This is especially clear for the glass measurements at the higher particle volume fractions. Here the number of glass particles in the measurement area seems to be too high. The theory behind the PIV technique is that when the particles are hit by the laser light the particles reflect light which is captured by a camera. When the concentration of particles is too high, it seems that the camera has difficulties in distinguishing between the individual particles. This makes it difficult to achieve good measurements under these conditions. The first results are obtained from measurements at a constant superficial gas velocity of 8 m/s and a varying particle volume fraction.
- An increase in axial particle velocity with increasing particle volume fraction is found

for 530 μm ZrO_2 and 518 μm glass particles. 120 μm glass and 260 μm ZrO_2 particles show a slight dependence on the particle volume fraction. A decrease in axial particle velocity is observed with increasing particle volume fraction.

- No dependence for any of the particle types are found for particle volume fraction on the normal particle velocity.
- No dependence is found on the axial particle rms velocity for the particle volume fraction for 260 μm ZrO_2 particles. For 120 μm glass particles insufficient data makes it difficult to conclude on any dependence on the axial particle rms velocity for the particle volume fraction. The profiles for 530 μm ZrO_2 and 518 μm glass particles show that the axial particle rms velocity decreases with increasing particle volume fraction.
- Generally a decrease in normal particle rms velocity with increasing particle volume fraction is found for 260 μm ZrO_2, 530 μm ZrO_2 and 518 μm glass particles. For 120 μm glass particles insufficient data makes it difficult to see the effect of particle volume fraction on the normal particle rms velocity.
- A decrease in particle cross-moment is observed for 530 μm ZrO_2 and 518 μm glass particles. From the data accepted for 120 μm glass and 260 μm ZrO_2 particles, a decrease in particle cross-moment is observed.

It is observed from the experiments with varying superficial gas velocities and a constant particle volume fraction of 0.15% that the axial particle velocity and the particle U-rms and V-rms and the particle cross-moment increase with increasing superficial gas velocity for all of the particle types.

The particle types are compared using the experimental findings at a constant superficial gas velocity of 8 m/s and a constant particle volume fraction of 0.15%.

- The comparison between the particle types show that the largest and heaviest particles have the lowest axial particle velocity as expected.
- The fluctuations are highest for the largest particles, which corresponds with literature.

The experimental results of two measurement techniques LDA and PIV are compared in Chapter 8 and Appendix E.

- The results from the measurements of the mean axial particle velocities show generally a good agreement between LDA and PIV measurements. The only exception is the measurements for the largest ZrO_2 particles. Here the difference between the measured velocities is obvious. This might be due to the particle type and the combination with LDA and PIV. It seems that LDA measures this particle differently than PIV.
- All of the measured mean normal particle velocities have values close to zero.
- The U-rms values measured by PIV are lower than the ones measured by LDA for all of the particle types.
- The cross-moment measurements for the two largest particles show that the measured values are generally higher for PIV than for LDA. For the highest particle volume fractions, the value measured by PIV is almost the same as the ones measured by LDA. The PIV measurements for the two smallest particle types show that only the results from the lowest particle volume fraction can be compared to the LDA measurements.

The general findings of the experimental investigations using LDA and PIV are that fluctuations are highest for the larger particles and lower for the smaller particles. The fluctuations decrease with increasing particle volume fraction for the larger particles while it increases for increasing superficial gas velocity for all of the particle types. Both LDA and PIV can be used to investigate a gas/particle flow. There are some challenges when measuring larger particles in dilute flow with LDA in regard to measurement time due to few particles in the system. Smaller particles with a high number density can give problems when using PIV due to reflections and consequently problems separating individual particles.

The commercially available code Fluent® is used in the numerical investigation of the gas/particle flow. In the initial simulations only the flow in the vertical transport pipe is simulated. The boundary conditions, superficial gas velocity, particle velocity and particle volume fraction, are the same as used in the experiments. The numerical simulations are performed for all particle types with a superficial gas velocity of 8 m/s and a particle volume fraction of 0.002 (0.20%). Both 2d and 3d simulations are performed. For the simulations of a dilute gas/particle flow the Euler-Euler model is employed. The flow is transient. The drag model used is Gidaspow, which is a combination of the Wen and Yu model and the Ergun model, where the Ergun model is used for dense phase flow. The particle-particle restitution coefficient used is 0.95.

- The 2d simulations of the simple transport pipe show good results using either the kinetic theory of granular flow (KTGF) or the constant viscosity model (CVM). For the CVM simulations a particle viscosity of 0.8 Pa·s and the Schiller-Naumann drag model is used. According to Troshko & Mohan (2005) this model is applicable for particles in a dilute mixture (particle volume fraction < 10%), if they are spherical. The result of the simulations show that there is very little difference between using the KTGF with the Gidaspow drag model and the CVM with the Schiller-Naumann drag model. For the 3d simulations only Euler-Euler simulations including KTGF are performed.
- The comparison between the 2d and 3d simulations for the four particle types show some small differences in the axial particle velocity. The results show that the simulated velocity is slightly higher for the 3d cases than for the 2d cases for all particle types.
- Comparisons between the numerical simulations and the experimental investigations (both LDA and PIV) show that there is generally a good agreement between the simulations for all of the particles and the experimental findings. The largest difference between the simulations and the experiments is found for the two smallest particle types. Here a clear difference is observed in the simulated and experimental particle velocities when approaching the wall. The reason for this seems to be that the wall effect is over-predicted for these particles in the simulations.
- Simulations using Euler-Lagrange on the simple 2d pipe are compared to the experimental findings for all of the particle types. The simulations are performed with an initial superficial gas velocity of 8 m/s and the initial velocity of the particles are the value of the velocity in the centre of the pipe found in the experiments. The comparison showed good agreement between the Euler-Lagrange simulations, Euler-Euler simulations and the LDA experiments.
- Initial simulations on the 2d vertical lifter using Euler-Euler KTGF with the Gidaspow drag model showed an over-prediction of the particle volume fraction in the pipe compared to the experiments. The reason for this discrepancy is that the experimental set-up is modified to give low particle volume fractions in the transport pipe to enable the use of lasers to investigate the flow.

10.2 Recommendations for further work

The experimental investigation:

- The experimental measurements should be extended to include measurements of the gas phase to achieve a complete understanding of the two phase flow. This includes a further expansion on the experimental techniques LDA and PIV for measurements on the gas and solids phase simultaneously. Measurement of the gas phase must include tracer particles that will be good representatives of the gas flow.

- The study should include further research into denser flows. Both LDA and PIV have limits for measurements of dense flows. PIV as used in this thesis reach its limit before LDA because of difficulties in separating the images of the particles when the particle number density gets too high. Optimisation of the technique will be necessary.
- Measure on particles of other sizes and densities are also wanted. PIV can measure on larger particles, but the accuracy will be reduced because of the lower particle number density in the interrogation area.
- It is also possible to expand the LDA to phase Doppler anemometry (PDA). This technique can be used to measure the particle size distribution over the cross-section of the pipe.
- The curvature of the wall makes it difficult to achieve accurate measurements in the area close to the pipe wall. By using a quadratic transport pipe instead of a circular one more accurate measurements at the wall can be achieved.
- Pressure transducers should be mounted on the test rig to get more information about the flow.

Numerical simulations:

- Further simulation should include deeper investigation into the 2d vertical lifter with focus on the forces acting on the particles in the fluidizing silo and the interface between the silo and the transport pipe.
- Closer investigations into the smaller particles in the near wall region.
- 3d simulations of the vertical lifter should be performed. This will more accurately reflect the real geometry and can be used to verify 2d simulations.
- 2d and 3d simulations on a variation of particle types.

11. ABBREVIATION

2d	Two dimensional
3d	Three dimensional
BSA	Burst spectrum analyser
CCD	Charge coupled device
CFD	Computational fluid dynamics
CMOS	Complementary metal oxide semiconductor
CVM	Constant viscosity model
DEM	Discrete element method
IA	Interrogation area
KTGF	Kinetic theory of granular flow
LDA	Laser Doppler anemometry
LDV	Laser Doppler velocimetry
MFIX	Multiphase flow with interphase exchanges
PC	Personal computer
PDA	Phase Doppler anemometry
PDPA	Phase Doppler particle analyser
PIV	Particle image velocimetry
PM	Photo multiplier
Re	Reynolds
rms	Root mean square
RNG	Renormalization group
St	Stokes
UDF	User defined function
VOF	Volume of fluid

12. NOMENCLATURE

Roman symbols

Ar	Arkimedes number	[-]
A	Pipe cross-section	[m^2]
a_1, a_2, a_3	Constants	[-]
b_1, b_2, b_3, b_4	Constants	[-]
$C_{1\varepsilon}$	Constants in the gas turbulence model with a value of 1.44	[-]
$C_{2\varepsilon}$	Constants in the gas turbulence model with a value of 1.92	[-]
$C_{3\varepsilon}$	Constants in the gas turbulence model with a value of 1.2	[-]
C_D	Friction coefficient	[-]
C_r	Courant number	[-]
C_V	Added-mass coefficient with a value of 0.5	[-]
C_μ	Constants in the gas turbulence model with a value of 0.09	[-]
c	Propagating speed of wave	[m/s]
D	Diffusivity	[m^2/s]
d_0	Beam diameter	[m]
d_f	Fringe spacing	[m]
d_p	Particle diameter	[m]
d_s	Particle diameter	[m]
e	Coefficient of restitution	[-]
e	Mathematical constant equal to 2.71828	[-]
e	Inelasticity factor	[-]
$\vec{e}, \vec{e}_1, \vec{e}_2, \vec{e}_3$	Unit vectors	[-]
f	Frequency	[s^{-1}]
F_D	A part of the expression for the drag force	[-]
f_0	Frequency shift	[Hz]
f_D	Doppler frequency	[s^{-1}]
f_{mr}	Frequency from stationary source recorded by Moving receiver	[s^{-1}]
f_{ms}	Frequency from moving source recorded by stationary receiver	[s^{-1}]
g	Acceleration due to gravity	[m/s^2]
g_j	J-direction of gravity	[m/s^2]
g_0	Radial distribution function of a single solid phase	[-]
L_g^t	Length scale of the turbulent eddies	[m]
K_{gs}	Gas-solid exchange coefficient	[kg/ms^3]
k	Turbulent kinetic energy	[m^2/s^2]
$\dot{m}$	Mass flow rate	[kg/s]
N	Number of samples or number of counts	[-]
N_f	Number of fringes	[-]
$\vec{n}$	Difference vectors between unit vectors	[-]
$\vec{n}_0$	Unit vector in a given direction	[-]
P	Fluid pressure	[Pa]
P_s	Solids pressure	[Pa]
p	Absolute pressure	[N/m^2]
R	Individual gas constant	[J/kg K]
Re	Reynolds number	[-]
Re_s	Relative Reynolds number	[-]
R(z)	Wave front radius	[-]
S	Surface area of a particle	[m^2]

s	Surface area of a sphere with the same volume as the particle with surface area S	[m^2]
St_V	Stokes number	[-]
T	Absolute temperature	[K]
T	Integral time scale	[s]
T(u), T(v)	Turbulence intensities	[%]
T_L	Constant	[-]
t	Time	[s]
U	Flow velocity vector	[m/s]
U	Axial (horizontal) velocity component	[m/s]
U_g	Superficial gas velocity	[m/s]
U_i	Instantaneous axial velocity	[m/s]
U_i, U_j	I and j components of velocity	[m/s]
U_{sg}	Relative velocity	[m/s]
U'	Fluctuating velocity	[m/s]
U'_p	Fluctuating particle velocities in axial direction	[m/s]
U_{rms}	Axial fluctuating velocity	[m/s]
U_{Slip}	Slip velocity	[m/s]
U_{sg}^{dr}	Drift velocity of the solids phase	[m/s]
$\overline{U}$	Mean axial velocity	[m/s]
u	Characteristic velocity of the flow	[m/s]
$\overline{U'V'}$	Cross-moments	[m^2/s^2]
V	Normal (vertical) velocity component	[m/s]
V_i	Instantaneous radial velocity	[m/s]
V_v	Vertical projection of velocity vector	[m/s]
V'_p	Fluctuating particle velocities in normal direction	[m/s]
V_{rms}	Normal fluctuating velocity	[m/s]
$\vec{V}$	Velocity vector	[m/s]
$\overline{V}$	Average velocity	[m/s]
$\overline{V}$	Mean normal velocity	[m/s]
$\vec{V}$	Velocity vector	[m/s]
x, y, z	Axis directions	[-]

Greek symbols

α	Angle difference	[rad]
α	Angel between laser beams	
α	Volume fraction	[-]
α_s	Solid loading	[-]
$\alpha_{s,max}$	Maximum solid volume fraction	[-]
$\gamma_{\Theta s}$	Dissipation of granular temperature due to collisions	[kg/ms^3]
Δf_D	Total frequency shift	[s^{-1}]
Δt	Length of time-step	[s]
Δt	Time between pulses	[s]
Δx	Length of control volume	[m]
$\Delta\overline{X}$	Average displacement	[m]

δ_{ij}	Kroenecker delta	[-]
ε	Dissipation rate of turbulent kinetic energy	[m^2/s^3]
ζ	Gaussian random number	[-]
η	Weighting factor	[-]
η_{sg}	Ratio between the Lagrangian integral time scale and the characteristic particle relaxation time	[-]
Θ_s	Granular temperature	[m^2/s^2]
θ	Angle between the mean particle velocity and the mean relative velocity	[deg,rad]
$\kappa_{\Theta s}$	Diffusion of granular temperature	[kg/ms^3]
λ	Wavelength	[m]
λ_s	Solid phase bulk viscosity	[kg/ms]
μ	Shear viscosity	[kg/ms]
μ^t	Turbulent viscosity	[kg/ms]
Π_{kg}, $\Pi_{\varepsilon g}$	Turbulence exchange terms	[-]
π	Pi	[-]
ρ	Density	[kg/m^3]
σ_k	Constant in gas turbulence model with a value of 1.0	[-]
σ_{sg}	Dispersion Prandtl number	[-]
σ_ε	Constant in gas turbulence model with a value of 1.3	[-]
ϕ	Shape factor	[-]
τ_e	Characteristic life time of the eddy	[s]
τ_{sg}^F	Characteristic particle relaxation time connected with inertial effects	[s]
τ_g^t	Characteristic time of the energetic turbulent eddies	[s]
τ_{sg}^t	Lagrangian integral time scale	[s]
τ_F	Time characteristics of the flow field	[s]
τ_{ij}	Production of turbulent kinetic energy	[Pa]
τ_V	Time characteristics of the particle	[s]
φ_{sg}	Switch function	[-]

Subscripts/superscripts

Mr	Moving receiver
Ms	Moving source
g	Gas phase
i, j, k	i, j and k directions
f	Fluid
p	Particle
s	Solids phase
Slip	Slip velocity
Sph	Spherical
rms	Root mean square
0	Evaluated at the wall
∞	Evaluated at the free stream

13. REFERENCES

Alajbegović A., Assad A., Bonetto F. Lahey R.T., *Phase distribution and turbulence structure for solid/fluid upflow in a pipe*, International Journal of Multiphase Flow, 20(3), pp. 453-479, 1994

Ayrancı I., Pinguet G., Escudié D., Selçuk N., Vaillon R., André F., *Effect of particle polydispersity on particle concentration measurement by using laser Doppler anemometry*, Experimental Thermal and Fluid Science, 31(8), pp. 839-847, 2007

Benyahia S., Arastoopour H., Knowlton T.M., Massah H., *Simulation of particles and gas flow behavior in the riser section of a circulating fluidized bed using the kinetic theory approach for the particulate phase*, Powder Technology, 112(1-2), pp. 24-33, 2000

Benyahia S., Syamlal M., O'Brien T.J., *Evaluation of boundary conditions used to model dilute, turbulent gas/solids flows in a pipe,* Powder Technology, 156(2-3), pp. 62-72, Aug 2005

Besançon R.M., *The Encyclopedia of Physics, Third Edition.* Van Nostrand Reinhold Company, ISBN 0-442-25778-3, 1985

Bolio E.J., Yasuna J.A., Sinclair J.L., *Dilute Turbulent Gas/solid Flow in Risers with Particle – Particle Interactions*, AIChE Journal, 41(6), pp. 1375-1388, 1995

Bolio E.J., Sinclair J.L., *Gas Turbulence Modulation in the Pneumatic Conveying of Massive Particles in Vertical Tubes,* Int. J. Multiphase Flow, 6, pp. 985-1001, 1995

Boree J., Caraman N., *Dilute bidispersed tube flow: Role of interclass collisions at increased loadings*, Phys. Fluids 17, 055108, 2005

Caraman N., Boree J., Simonin O., *Effect of collisions on the dispersed phase fluctuation in a dilute tube flow: Experimental and theoretical analysis,* Physics of Fluids, 15(12), pp. 3602-3612, 2003

Cao J., Ahmadi G., *Gas-Particle Two-Phase Turbulent Flow in a Vertical Duct*, Int. J. Multiphase Flow, 21, pp. 1203-1228, 1995

Chan C.K., Guo Y.C., Lau K.S., *Numerical modelling of gas-particle flow using a comprehensive kinetic theory with turbulence modulation,* Powder Technology, 150(1), pp. 42-55, 2005

Crow C., Sommerfeld M., Tsuji Y., *Multiphase Flows with Droplets and Particles*, CRC Press LLC, 1998

Dantec Reference Guide, 2000

Dantec, FlowManager software and Introduction to PIV Instrumentation, Software Users Guide, 2000

Deen, N.G., Solberg, T., Hjertager, B.H., *Comparison of PIV and LDA Measurements Methods Applied to the Gas-Liquid Flow in a Bubble Column*, 10th Int. Symp. On Appl. of Laser Techniques to Fluid Mech., Lisbon, Portugal, 2000

Deen, N.G., Solberg, T., Hjertager, B.H., *Flow Generated by an Aerated Rushton Impeller: Two-phase PIV Experiments and Numerical Simulations*, The Canadian Journal of Chemical Engineering, 80(4), pp. 638-652, 2003

Deen N.G., Annaland M.V., Kuipers J.A.M., *Detailed computational and experimental fluid dynamics of fluidized beds*, Applied Mathematical Modelling, 30(11), pp. 1459-1471, 2006

de Silva S.R., Datta B.K., *Transport of Particulate Materials, Dilute Phase Pneumatic Transport*, Tel-Tek, Sept 2004

Ding J., Gidaspow D., *A bubbling fluidization model using kinetic theory of granular flow*, AIChE Journal, 36(4), pp. 523-538, 1990

Durst F., Melling A., Whitelaw J.H., *Principles and Practice of Laser Doppler Anemometry*, Second Edition, 1981

Elgobashi S.E., Abou-Arab T.W., *A Two-Equation Turbulence Model for Two-Phase Flows*, Phys. Fluids, 26(4), pp. 931-938, 1983

Elseth G., *An Experimental Study of Oil/Water Flow in Horizontal Pipes,*
Ph.D. Thesis, NTNU, Norway, 2001

Ergun S., *Fluid Flow through Packed Columns*, *Chem. Eng. Prog.*, 48(2), pp. 89-94, 1952.

Eskin D., Leonenko Y., Vinogradov O., *Modelling Nonsteady-State Regimes of Dilute Pneumatic Conveying*, Chemical Engineering & Technology, 27(4), pp. 390-397, 2004

Fan L., Mao Z., Yang C., Wang Y., *Numerical simulation of turbulent solid–liquid two-phase flow and orientation of slender particles in a stirred tank*, Chemical Engineering Science, 60(24), pp. 7045-7056, 2005

Fluent®, Fluent® 6.0 User's Guide, Lebanon, New Hampshire Company, USA, Fluent Incorporated, 2001

Foerster S.F., Lounge M.Y., Chang A.H., et al., *Measurements of the Collision Properties of Small Spheres*, Physics of Fluids, 6(3), pp. 1108-1115, 1994

Geldart D., *Types of Gas Fluidization,* Powder Technology, 7, pp. 285-292, 1973

Gidaspow D., *Multiphase Flow and Fluidization, Continuum and Kinetic Theory Description – Continuum and Kinetic Theory Descriptions*, USA, 1994

Gidaspow D., Bezburuah R., Ding J., *Hydrodynamics of Circulating Fluidized Beds, Kinetic Theory Approach*, *In* Fluidization VII, Proceedings of the 7th Engineering Foundation Conference on Fluidization, pp. 75-82, 1992

Gore R.A., Crowe C.T., *Effect of Particle-size on Modulating Turbulent Intensity*, International Journal of Multiphase Flow, 15(2), pp. 279-285, 1989

Grace J. R., *The Viscosity of Fluidized beds*, Canadian Journal of Chemical Engineering, 48, pp. 30-33, 1970

Grüner C., Kanther W., Götz S., Strauß K., *Identification of regions with inhomogeneous particle behavior in dilute gas-solid flows*, Particle & Particle Systems Characterization, 21(3), pp. 219-227, Oct 2004

Hadinoto K., Curtis J.S., *Effect of interstitial fluid on particle-particle interactions in kinetic theory approach of dilute turbulent fluid-particle flow*, Industrial & Engineering Chemistry Research, 43(14), pp. 3604-3615, 2004

Haider A., Levenspiel O., *Drag Coefficient and Terminal Velocity of Spherical and Nonspherical Particles*, Powder Technology, 58, pp. 63-70, 1989

Hartge E-U., Ratschow L., Wischnewski R., Werther J., *CFD-simulation of a circulating fluidized bed riser*, Particuology, 7(4), pp. 283-296, 2009

He J., Simonin O., *Non-equilibrium prediction of the particle-phase stress tensor in vertical pneumatic conveying*, Fifth International Symposium on Gas-Solid Flows, ASME FED, 166, pp. 253-263, 1993

Hetsroni G., *Particles turbulence interaction*, International Journal of Multiphase Flow, 15(5), pp. 735-746, 1989

Hidayat M., Rasmuson A., *Some aspects on gas-solid flow in a U-bend: Numerical investigation*, Powder Technology, 153 (1), pp. 1-12, May 2005

Hinze J.O., *Turbulence*, New York, McGraw-Hill, 1975

Van De Hulst H.C., *Light Scattering by Small Particles*, Dover Publications, Inc., 1981.

Hjertager B.H., Solberg T., Hansen K.G., *Reactive gas solids flow in circulating fluidized beds,* Fourth International Conference on CFD in the Oil and Gas, Metallurgical & Process Industries SINTEF / NTNU, Trondheim, Norway, 2005

Ibsen C.H., *An Experimental and Computational Study of Gas-Particle Flow in Circulating Fluidized Reactors*, PhD. Thesis, 2002

Ibsen C.H., Onofri F., Solberg T., et al. *Improved particle image velocimetry measurements in gas-particle flows with a dense wall layer,* Measurement Science & Technology, 14(4), pp. N9-N12, 2003

Jakobsen M.L., Easson W.J., Greated C.A., Glass D.H., *Particle image velocimetry: Simultaneous two-phase flow measurements*, Measurement Science & Technology, 7(9), pp. 1270-1280, 1996

Jiradilok V., Gdaspow D., Damronglerd S., et al., *Kinetic theory based CFD simulation of turbulent fluidization of FCC particles in a riser,* Chemical Engineering Science, 61(17), pp. 5544-5559, 2006

Johnson P.C., Jackson R., *Frictional-Collisional Constitutive Relations for Granular Materials, with Application to Plane Shearing*, J. Fluid Mech., 176, pp. 67-93, 1987

Joseph S., Klinzing G.E., *Vertical gas-solid transition flow with electrostatics*, Powder Technology, 36(1), pp. 79-87, 1983

Keane R.D., Adrian R.J., *Optimization of particle image velocimeters*: *I Double pulsed systems,* Meas. Sci. Technol., 1, pp. 1202-1215, 1990

Keane R.D., Adrian R.J., *Optimization of particle image velocimeters: II. Multiple pulsed systems,* Meas. Sci. Technol., 2, pp. 963-974, 1990

Kenning V.M., Crowe C.T., *Brief Communication on the Effect of Particles on Carrier Phase Turbulence in Gas-Particle Flows*, Int. J. Multiphase Flow, 23(2), pp. 403-408, 1996

Kiger K.T., Pan C., *PIV technique for the simultaneous measurement of dilute two-phase flows*, Journal of Fluids Engineering-transactions of the ASME, 122(4), pp. 811-818, 2000

Kuan B., Yang W., Schwarz M.P., *Dilute gas-solid two-phase flows in a curved 90 ° duct bend : CFD simulation with experimental validation*, Chemical engineering science, 62(7), pp. 2068-2088, 2007

Kuipers J.A.M., *A two-fluid micro balance model of fluidized bed.* Ph.D. Thesis, U. Twente, Enschede, The Netherlands 1990

Kussin J., Sommerfeld M., *Investigation of particle behaviour and turbulence modification in particle laden channel flow*, Nuremberg, Germany, 27-29 March 2001. International Congress for Particle Technology

Launder B.E. and Spalding D.B., *Lectures in Mathematical Models of Turbulence*, Academic Press, London, England, 1972

Lee S., Durst F., *On the Motion of Particles in Duct Flows*, Int. J. Multiphase Flow, 8. pp. 125-146, 1982

Li H., Tomita Y., *A numerical simulation of swirling flow pneumatic conveying in a vertical pipeline*, Particulate Science and Technology, 19(4), pp. 355-368, 2001

Littman H., Morgan M.H., Jovanovic S. Dj., Paccione J.D., Grbavcic Z.B., Vukovic D.V., *Effect of particle diameter, particle density and loading ratio on the effective drag coefficient in steady turbulent gas-solids transport*, Powder Technology, 84(1), pp. 49-56, 1995

Littman H., Morgan M.H., Paccione J.D Jovanovic S.Dj., Grbavcic Z., *Modeling and measurement of the effective drag coefficient in decelerating and non-accelerating turbulent gas—solids dilute phase flow of large particles*, Powder Technology, 77(3), pp. 267-283, 1993

Litwiller D., CCD vs. CMOS: *Facts and Fiction*, Photonics Spectra, 2001

Liu Z., Jiao J., Zheng Y., Zhang Q., Jia L., *Investigation of turbulence characteristics in a gas cyclone by stereoscopic PIV*, AIChE Journal, 52(12), pp. 4150-4160, 2006

Lim E.W.C., Wang C, Yu A., *Discrete element simulation for pneumatic conveying of granular material*, AIChE Journal, 52(2), p.p. 496-509, 2006

Louge M.Y., Mastorakos E., Jenkins J.T., *The Role of Particle Collisions in Pneumatic Transport*, Journal of Fluid Mechanics, 231, pp. 345-359, 1991

Lu Y., Glass D. H., Easson W. J., *An investigation of particle behaviour in gas–solid horizontal pipe flow by an extended LDA technique*, Fuel, 88(12), pp. 2520-2531, 2009

Lueptow R.M., Akonur A., Shinbrot T., *PIV for granular flows*, Experiments in Fluids, 28(2), pp. 183-186, 2000

Lun C.K.K., Savage S.B., Jeffrey D., J., Chepurniy N., *Kinetic Theories for Granular Flow: Inelastic Particles in Couette Flow and Slightly Inelastic Particles in a General Flow Field*, Journal of Fluid Mechanics, 140, pp. 223-256, 1984

Maeda M., Hishida K., Furutani T., *Optical Measurements of Local Gas and Particle Velocity in an Upward Flowing Dilute Gas-solids Suspension,* Polyphase Flow and Transport Technology, Century 2-ETC, pp. 211-216, 1980

Martin T.W., Wildman R.D., Hargrave G.K., Huntley J.M, Halliwell N., *Capturing gas and particle motion in an idealised gas-granular flow*, Powder Technology, 155(3), pp. 175-180, 2005

Mathiesen V., *LDA/PDA Measurements in Dispersed Multiphase Flow,* Visit at DETL, 2002

Mathiesen V., Solberg T., *Laser-based flow measurements of dilute vertical pneumatic transport,* Chem. Eng. Commun., 191(3), pp. 414-433, 2004

Mathiesen V., Solberg T., Hjertager B.H., *Predictions of gas/particle flow with an Eulerian model including a realistic particle size distribution*, Powder Technology, 112(1-2), pp. 34-45, 2000

Mierka O., Timár P., Bafrnec M., Stopka J., *Choice of the operating velocity of the carrier gas by means of a mathematical model for pneumatic transport*, Powder Handling & Processing, 6(3), pp. 291 – 294, 1994

Mierka O., Timar P., *Analysis of Results of Modelling of Vertical Pneumatic Transport,* Powder handling and processing, 9(4), pp. 349-354, 1997

Morsi S.A., Alexander A.J., *An Investigation of Particle Trajectories in Two-Phase Flow Systems*, J. Fluid Mech., 55(2), pp.193-208, 1972

Nieuwland J.J., Annaland M.V., Kuipers J.A.M., van Swaaij W.P.M., *Hydrodynamic modelling of gas/particle flows in riser reactors*, AIChE Journal, 42(6), pp. 1569-1582, 1996

Nomura T., Takahashi Y., Ishima T., Obokata T., LDA *and PIV Measurements and Numerical Simulation on In-Cylinder Flow Under Steady State Flow Condition*, 2004

Ogawa S., Umemura A., Oshima N., *On the Equation of Fully Fluidized Granular Materials*, J. Appl. Math. Phys., 31, pp. 483, 1980

Pakhomov M.A., Protasov M.V., Terekhov V.I., Varaksin A.Y., *Experimental and numerical investigation of downward gas-dispersed turbulent pipe flow*, International Journal of Heat and

Mass Transfer, 50(11-12), pp. 2107-2116, 2007

Patil, D.J., *An Experimental and Computational Study of Dense Gas-Solid Fluidized Beds*, Ph.D. Thesis, U. Twente, Enschede, The Netherlands, 2003

Patil D.J., Annaland M.V., Kuipers J.A.M., *Critical comparison of hydrodynamic models for gas-solid fluidized beds - Part I: bubbling gas-solid fluidized beds operated with a jet*, Chemical Engineering Science, 60(1), pp. 57-72, 2005

Pita J.A., Sundaresan S., *Gas-solid Flow in Vertical Tube*, AIChE Journal, 37(7), pp. 1009-1018, 1991

Raffel M., Willert C., Kompenhans J., *Particle Image Velocimetry, A Practical Guide*, Springer-Verlag Berlin Heidelberg, 1998

Ranade V., *Modelling of gas-solid flows in FCC riser reactors: Fully developed flow,* Second International Conference on CFD in Minerals and Process Industries CSIRO, Melbourne, Australia, 1999

Recktenwald I., Alkishriwi N., Schröder W., *PIV-LES analysis of channel flow rotating about the streamwise axis*, European journal of mechanics. B, Fluids, 28(5), pp. 677-688, 2009

Rhodes M.J., *Introduction to particle technology*, Chichester : Wiley, 1998

Rhodes M.J., *Pneumatic transport of powders*, 2010

Rizk, Elghobashi, *A two-equation turbulence model for dispersed dilute confined two-phase flows*, International Journal of Multiphase Flow, 15(1), pp 119-133, 1989

Ruck B., *Distortion of LDA Fringe Pattern by Tracer Particles*, Experiments in Fluids, 10, pp. 349-354, 1991

Rudd M.J., *A New Theoretical Model for the Laser Dopplermeter*, Journal of Scientific Instruments, (Journal of Physics E) Series 2, 2, 1969

Samuelsberg A., Hjertager B.H., *Computational Modelling of Gas/Particle Flow in a Riser*, AIChE Journal, 42(6), pp. 1536-1546, 1996

Scarano F., *Iterative image deformation methods in PIV,* Measurement Science & Technology, 13(1), pp. R1-R19, 2002

Schiller L. and Naumann Z., *Z. Ver. Deutsch. Ing.*, 77, 318, 1935

Schlicke T, *Breaking Waves and the Dispersion of Surface Films,* PhD Thesis, 2001

Schügerl K., Merz M., Fetting F., *Rheologische Eigenschaften von gasdurchströmten Fliessbettsystemen*, Chemical Engineering Science, 15, pp. 1-38, 1961

Shao S., *Study of the Flow Behaviour of Multiphase Flow System Using Laser Doppler Anemometry (LDA),* Thesis, Chicago, Illinois 1996

Shubin A.B. and Shunyaev K.Y., *Average excluded volume and density limit for random close packing of hard spheres,* The Fourth International Conference on Mathematical Modelling and Computer Simulation of Materials Technologies, 2006

Simonin O., *Continuum modelling of dispersed two-phase flows, Combustion and turbulence in two-phase flows*, Von Karman institute of fluid dynamics, Lecture series, pp. 1-47, 1996

Simonin O. and Viollet P.L., *Predictions of an oxygen droplet pulverization in a compressible subsonic coflowing hydrogen flow*, Laboratoire National d'Hydraulique, Chatou, France, 1990

Shah M.K., Agelinchaab M., Tachie M.F., *Influence of PIV interrogation area on turbulent statistics up to 4th order moments in smooth and rough wall turbulent flows*, Experimental Thermal and Fluid Science, 32(3), pp. 725-747, 2007

Slominski C., Niedostatkiewicz M., Tejchman J., *Application of particle image velocimetry (PIV) for deformation measurement during granular silo flow*, Powder Technology, 10, pp. 1-18, 2006

Syamlal M., O'Brien T.J., *Computer Simulation of Bubbles in a Fluidized Bed*, AIChE Symp. Series, 85, pp. 22-31, 1989

Syamlal M., Rogers W., O'Brien T.J, *MFIX Documentation: Volume 1, Theory Guide*, National Technical Information Service, DOE/METC-9411004, NTIS/DE9400087., 1993

Tanaka Y., Oba G., Hagiwara Y., *Experimental study on the interaction between large scale vortices and particles in liquid-solid two-phase flow*, International Journal of Multiphase Flow, 29(3), pp. 361-373, 2003

Tanaka T., Tsuji Y., *Numerical simulation of gas – solid two-phase in a vertical pipe: on the effect of inter-particle collision*, 4th Symposium on Gas – Solid Flows, 121, ASTM FED, pp. 123-128, 1991

Tartan M., Gidaspow D., *Measurement of granular temperature and stresses in risers,* AIChE Journal, 50(8), pp. 1760-1775, 2004

Tartan M., Gidaspow D., *Measurement of granular temperature and stresses in risers*, AIChE Journal, 50(8), pp. 1760-1775, 2004

Triesch O., Bohnet M., *Measurement and CFD prediction of velocity and concentration profiles in a decelerated gas-solids flow,* Powder Technology, 115(2), pp. 103-113, 2001

Troshko A, Mohan S., *Drag Laws 101*, Fluent News, Summer 2005

Tsuji Y., Morikawa Y., Shiomi H., *LDV Measurements of an Air-solid Two-phase Flow in a Vertical Pipe,* J. Fluid Mech. 139, pp. 417-434, 1984

Varaksin A.Y., Zaichik L. I., *Effect of particles on the turbulence intensity of a carrier phase for gas-solid pipe flow,* International Symposium on Multiphase Flow and Transport Phenomena, 05-10 Nov. 2000

Wen C.Y., Yu Y.H., *Mechanics of Fluidization*, Chem. Eng. Prog. Symp. Series*,* 62, pp. 100-111, 1966.

De Wilde J., Van Engelandt G., Hynderickx G.J., *Gas-solids mixing in the inlet zone of a dilute circulating fluidized bed*, Powder Technology, 151(1-3), pp. 96-116, 2005

Woodcock C.R., Mason J.S., *Bulk Solids Handling: An Introduction to the Practice and Technology*, Leonard Hill, 1987

Yang W., Kuan B., *Experimental investigation of dilute turbulent particulate flow inside a curved 90° bend*, Chemical Engineering Science, 61(11), pp. 3593-3601, 2006

Yao J., Zhang Y., Wang C.H., Liang C.Y., *On the Electrostatic Equilibrium of Granular Flow in Pneumatic Conveying Systems*, AIChE Journal, 52(11), pp. 3775-3793, 2006

Zang Z., Eisele K., *On the Overestimation of the Flow Turbulence due to Fringe Distortion in LDA Measurement Volumes*, Experiments in Fluids, 25, pp.371-374, 1998

Zeilstra C.; Collignon J.G.; Hoef van der M.A.; Deen N.G.; Kuipers J.A.M., *Experimental and numerical study of wall-induced granular convection*, Powder Technology, 184, pp.166-176, 2007

Zhang D.Z., VanderHeyden W.B., *High-resolution three-dimensional numerical simulation of a circulating fluidized bed*, Powder Technology, 116(2-3), pp. 133-141, 2001

Zhao X. -L., Li S.-Q., Liu G.-Q., Song Q, Yao Q., *Flow patterns of solids in a two-dimensional spouted bed with draft plates: PIV measurement and DEM simulations*, Powder Technology, 183(1),pp. 79-87, 2008

http://www.storenorskeleksikon.no, 20.02.2004

http://www.sew-lexicon.com, 31.01.2005

14. APPENDIX

A. Size distribution
B. Matlab-script for PIV measurements
C. Additional LDA results
D. Additional PIV results
E. Additional comparisons between LDA and PIV results
F. Articles

A. Size distribution

The particle size distribution of a granular material can be decided through a sieving analysis. The analysis is performed in a laboratory using a proper equipment, see Figure A.1. Sieves with wire mesh cloths are used. The sieve sizes and number used depends on the granular material to be investigated. The selected sieves are placed in order of decreasing size, from top to bottom, on a mechanical shaker. A pan is placed under the bottom sieve to collect the particles that pass through the last sieve. The representative sample of the powder is added to the top sieve and the shaker is turn on. The analysis is usually performed in intervals, usually three, of chosen lengths. After each interval the sieves are weighed and the compared to the weight of the sieve before the analysis. The increase in weight is du to the particles retained by the sieve. After the last interval the finial amount of particles in the sieves are calculated and the size distribution of the powder is found.

Figure A.1: Sieving analysis equipment.

Below is the analysis for the largest glass particles shown. The total weight of the sample is 100.91. In Table A.1 the results from the analysis is presented.

Table A.1: Results from the particle size distribution analysis of the largest glass particles.

Nominal size of sieve (μm)	Weight of sieves (g)				Mass in sieve (g)	% of total mass
	Before	10 min	5 min	5 min		
Bottom	357.690	357.72	357.72	357.72	0.03	0.03 %
355	467.193	471.40	471.80	471.96	4.77	4.73 %
425	421.299	452.25	452.46	471.96	31.28	31.28 %
500	493.706	558.75	558.17	557.93	64.22	64.22 %
630	390.699	391.40	391.33	391.28	0.58	0.58 %
710	502.398	502.39	502.39	502.39	0	0 %

The arithmetic mean particle diameter is calculated to 518 µm by using the following equation:

$$Arithmetic\ mean = \frac{1}{\sum \frac{x_i}{d_i}}$$

Here x_i is the mass fraction and d_i is the mean nominal size between the two sieves on which the particles lie.

B. Matlab-script for PIV measurements

Made by Sondre Vestøl.

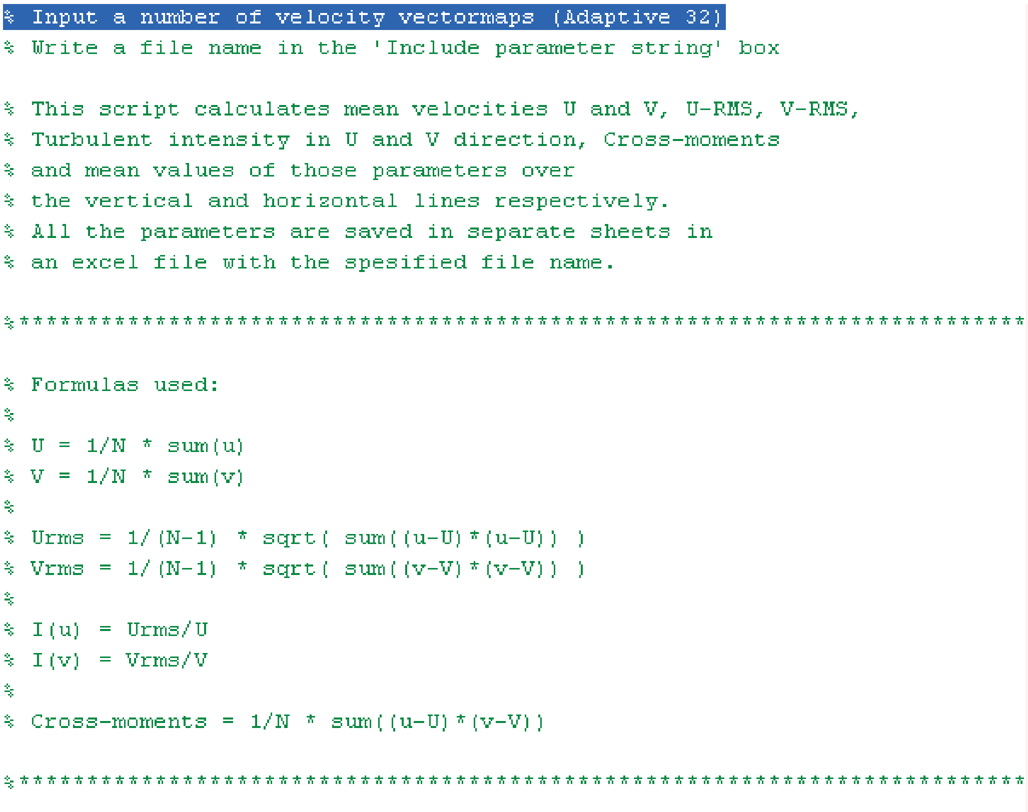

```
% Input a number of velocity vectormaps (Adaptive 32)
% Write a file name in the 'Include parameter string' box

% This script calculates mean velocities U and V, U-RMS, V-RMS,
% Turbulent intensity in U and V direction, Cross-moments
% and mean values of those parameters over
% the vertical and horizontal lines respectively.
% All the parameters are saved in separate sheets in
% an excel file with the spesified file name.

%****************************************************************************

% Formulas used:
%
% U = 1/N * sum(u)
% V = 1/N * sum(v)
%
% Urms = 1/(N-1) * sqrt( sum((u-U)*(u-U)) )
% Vrms = 1/(N-1) * sqrt( sum((v-V)*(v-V)) )
%
% I(u) = Urms/U
% I(v) = Vrms/V
%
% Cross-moments = 1/N * sum((u-U)*(v-V))

%****************************************************************************
```

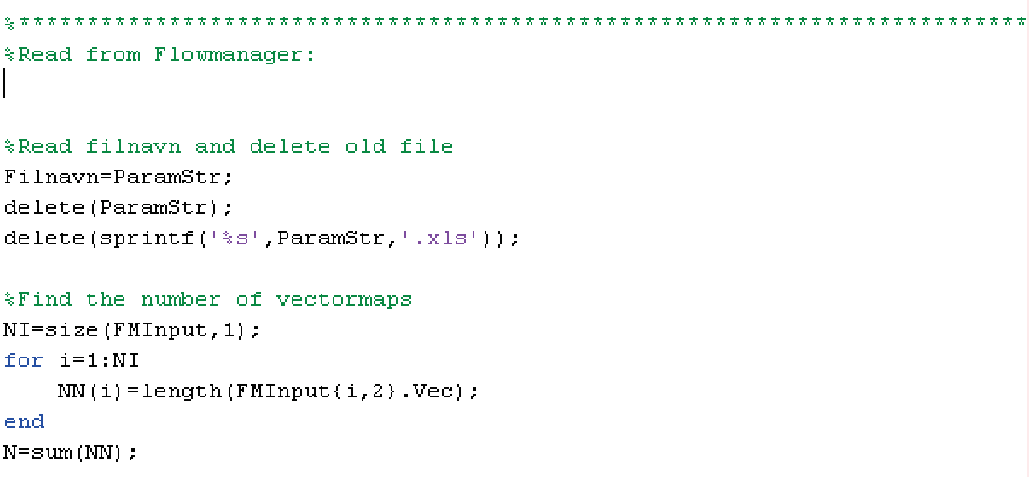

```
%****************************************************************************
%Read from Flowmanager:


%Read filnavn and delete old file
Filnavn=ParamStr;
delete(ParamStr);
delete(sprintf('%s',ParamStr,'.xls'));

%Find the number of vectormaps
NI=size(FMInput,1);
for i=1:NI
    NN(i)=length(FMInput{i,2}.Vec);
end
N=sum(NN);
```

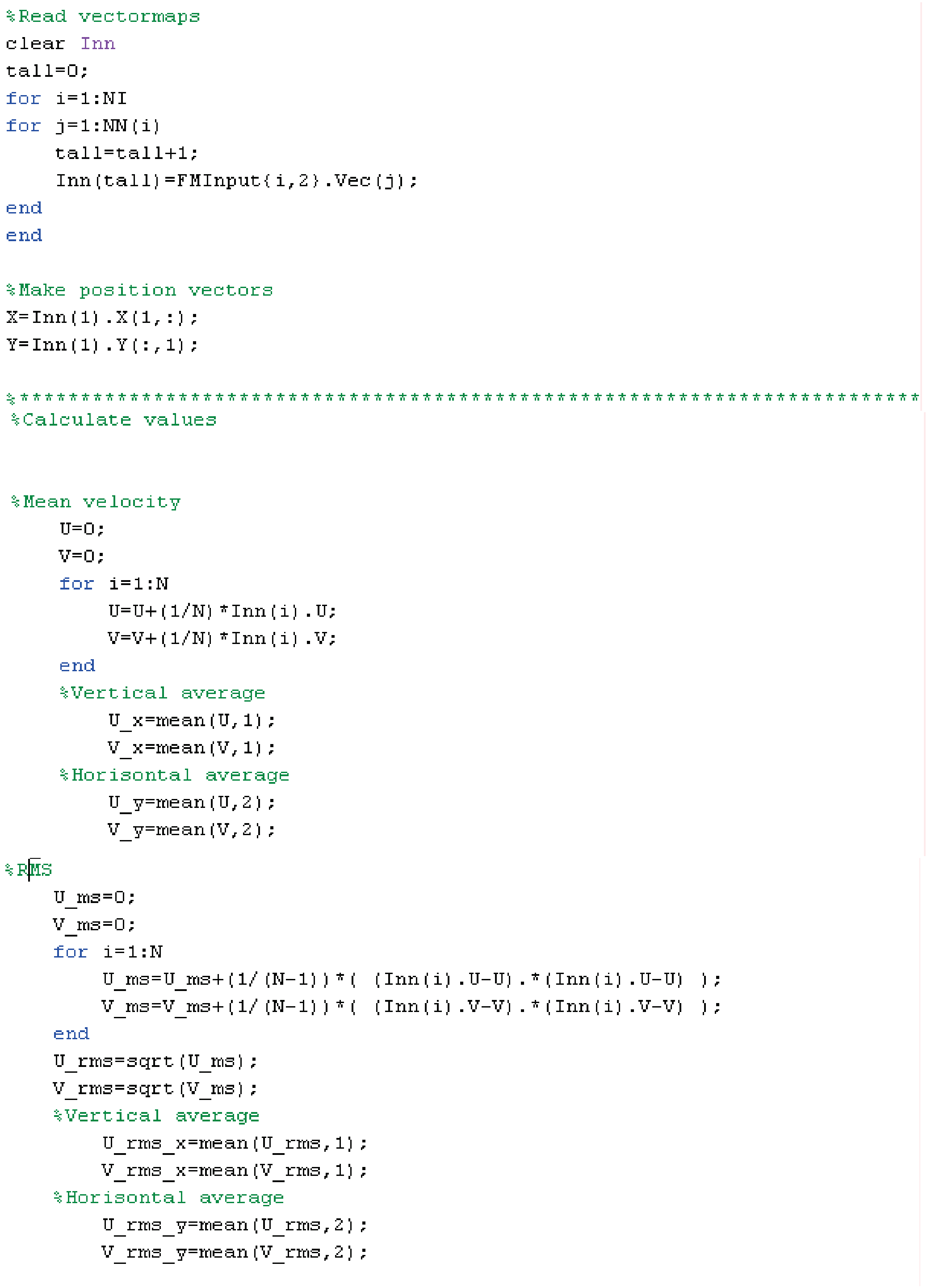

```
%Read vectormaps
clear Inn
tall=0;
for i=1:NI
for j=1:NN(i)
    tall=tall+1;
    Inn(tall)=FMInput(i,2).Vec(j);
end
end

%Make position vectors
X=Inn(1).X(1,:);
Y=Inn(1).Y(:,1);

%************************************************************************
%Calculate values


%Mean velocity
    U=0;
    V=0;
    for i=1:N
        U=U+(1/N)*Inn(i).U;
        V=V+(1/N)*Inn(i).V;
    end
    %Vertical average
        U_x=mean(U,1);
        V_x=mean(V,1);
    %Horisontal average
        U_y=mean(U,2);
        V_y=mean(V,2);

%RMS
    U_ms=0;
    V_ms=0;
    for i=1:N
        U_ms=U_ms+(1/(N-1))*( (Inn(i).U-U).*(Inn(i).U-U) );
        V_ms=V_ms+(1/(N-1))*( (Inn(i).V-V).*(Inn(i).V-V) );
    end
    U_rms=sqrt(U_ms);
    V_rms=sqrt(V_ms);
    %Vertical average
        U_rms_x=mean(U_rms,1);
        V_rms_x=mean(V_rms,1);
    %Horisontal average
        U_rms_y=mean(U_rms,2);
        V_rms_y=mean(V_rms,2);
```

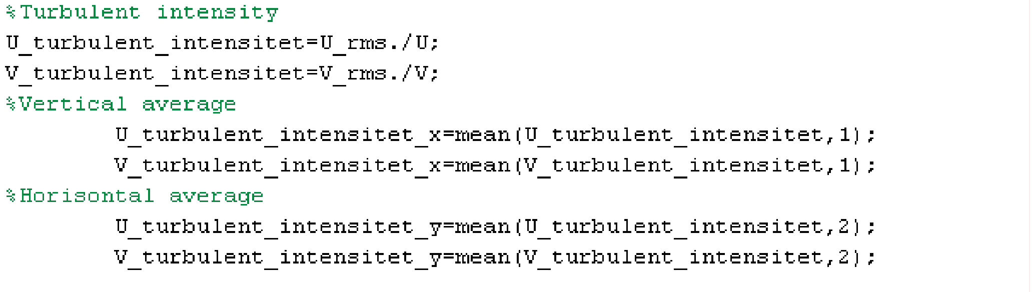

```
%Turbulent intensity
U_turbulent_intensitet=U_rms./U;
V_turbulent_intensitet=V_rms./V;
%Vertical average
        U_turbulent_intensitet_x=mean(U_turbulent_intensitet,1);
        V_turbulent_intensitet_x=mean(V_turbulent_intensitet,1);
%Horisontal average
        U_turbulent_intensitet_y=mean(U_turbulent_intensitet,2);
        V_turbulent_intensitet_y=mean(V_turbulent_intensitet,2);
```

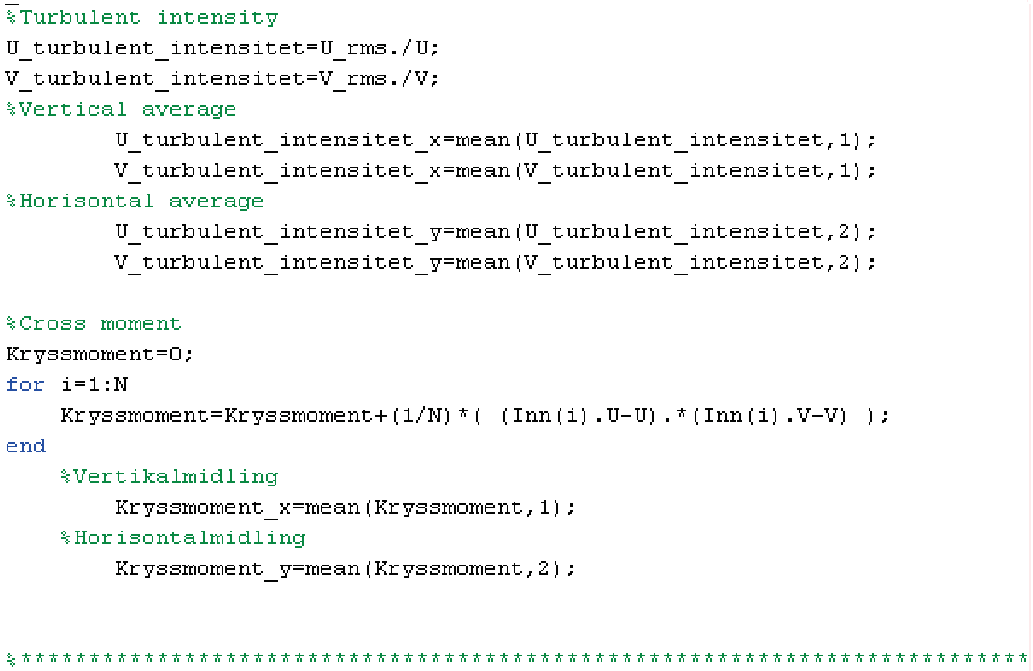

```
%Turbulent intensity
U_turbulent_intensitet=U_rms./U;
V_turbulent_intensitet=V_rms./V;
%Vertical average
        U_turbulent_intensitet_x=mean(U_turbulent_intensitet,1);
        V_turbulent_intensitet_x=mean(V_turbulent_intensitet,1);
%Horisontal average
        U_turbulent_intensitet_y=mean(U_turbulent_intensitet,2);
        V_turbulent_intensitet_y=mean(V_turbulent_intensitet,2);

%Cross moment
Kryssmoment=0;
for i=1:N
    Kryssmoment=Kryssmoment+(1/N)*( (Inn(i).U-U).*(Inn(i).V-V) );
end
    %Vertikalmidling
        Kryssmoment_x=mean(Kryssmoment,1);
    %Horisontalmidling
        Kryssmoment_y=mean(Kryssmoment,2);


%**************************************************************************
```

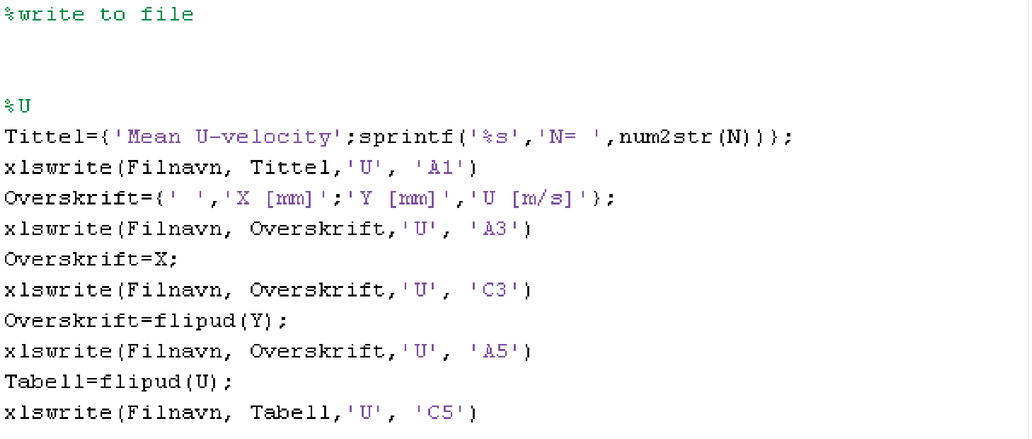

```
%write to file


%U
Tittel={'Mean U-velocity';sprintf('%s','N= ',num2str(N))};
xlswrite(Filnavn, Tittel,'U', 'A1')
Overskrift={' ','X [mm]';'Y [mm]','U [m/s]'};
xlswrite(Filnavn, Overskrift,'U', 'A3')
Overskrift=X;
xlswrite(Filnavn, Overskrift,'U', 'C3')
Overskrift=flipud(Y);
xlswrite(Filnavn, Overskrift,'U', 'A5')
Tabell=flipud(U);
xlswrite(Filnavn, Tabell,'U', 'C5')
```

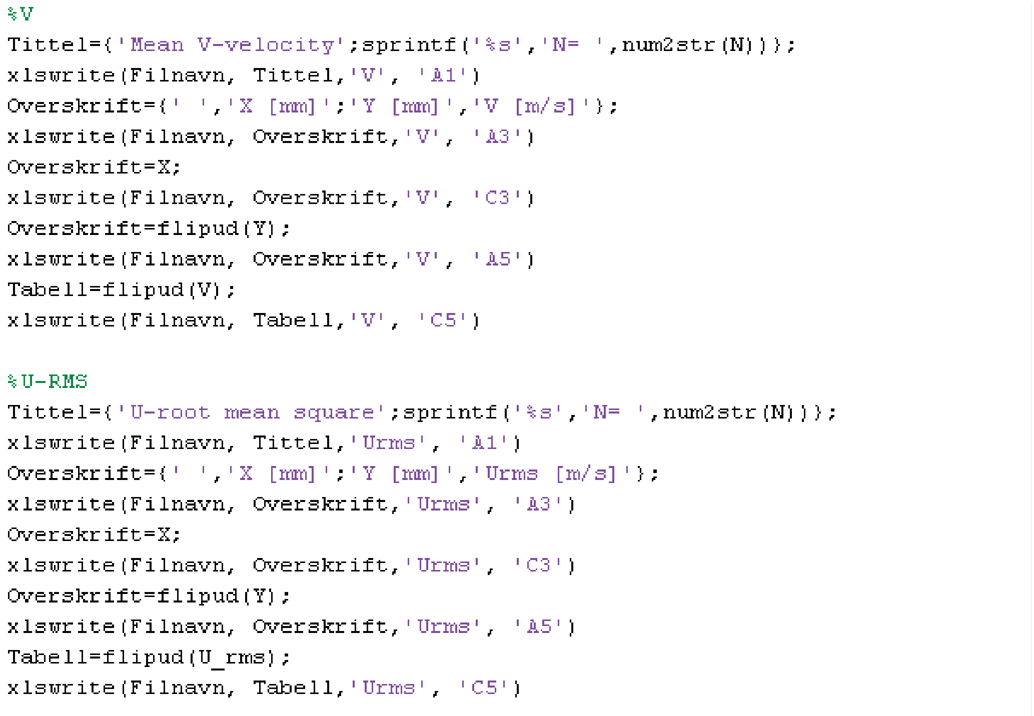

```
%V
Tittel={'Mean V-velocity';sprintf('%s','N= ',num2str(N))};
xlswrite(Filnavn, Tittel,'V', 'A1')
Overskrift={' ','X [mm]';'Y [mm]','V [m/s]'};
xlswrite(Filnavn, Overskrift,'V', 'A3')
Overskrift=X;
xlswrite(Filnavn, Overskrift,'V', 'C3')
Overskrift=flipud(Y);
xlswrite(Filnavn, Overskrift,'V', 'A5')
Tabell=flipud(V);
xlswrite(Filnavn, Tabell,'V', 'C5')

%U-RMS
Tittel={'U-root mean square';sprintf('%s','N= ',num2str(N))};
xlswrite(Filnavn, Tittel,'Urms', 'A1')
Overskrift={' ','X [mm]';'Y [mm]','Urms [m/s]'};
xlswrite(Filnavn, Overskrift,'Urms', 'A3')
Overskrift=X;
xlswrite(Filnavn, Overskrift,'Urms', 'C3')
Overskrift=flipud(Y);
xlswrite(Filnavn, Overskrift,'Urms', 'A5')
Tabell=flipud(U_rms);
xlswrite(Filnavn, Tabell,'Urms', 'C5')
```

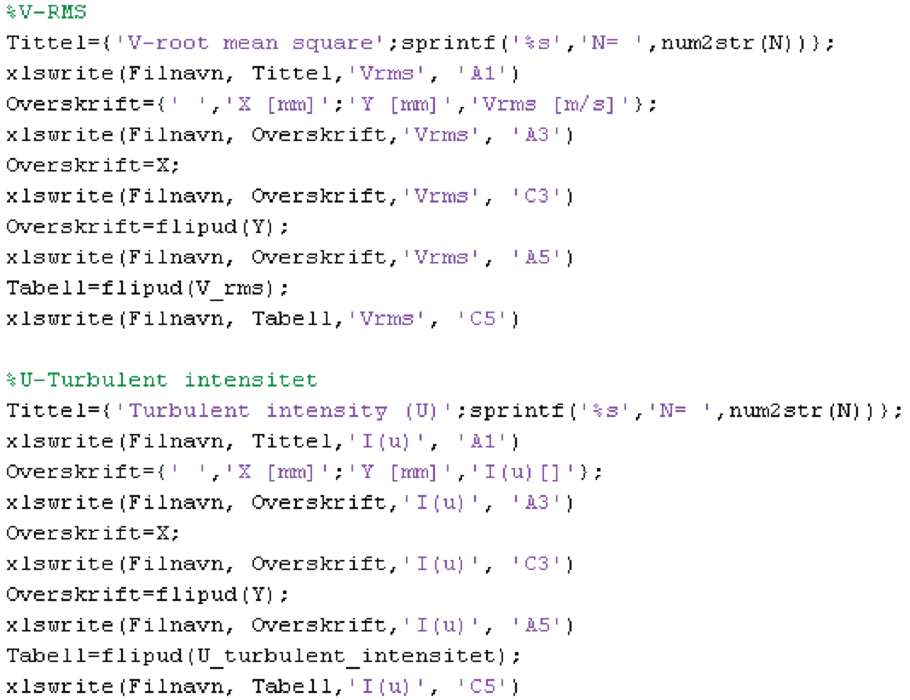

```
%V-RMS
Tittel={'V-root mean square';sprintf('%s','N= ',num2str(N))};
xlswrite(Filnavn, Tittel,'Vrms', 'A1')
Overskrift={' ','X [mm]';'Y [mm]','Vrms [m/s]'};
xlswrite(Filnavn, Overskrift,'Vrms', 'A3')
Overskrift=X;
xlswrite(Filnavn, Overskrift,'Vrms', 'C3')
Overskrift=flipud(Y);
xlswrite(Filnavn, Overskrift,'Vrms', 'A5')
Tabell=flipud(V_rms);
xlswrite(Filnavn, Tabell,'Vrms', 'C5')

%U-Turbulent intensitet
Tittel={'Turbulent intensity (U)';sprintf('%s','N= ',num2str(N))};
xlswrite(Filnavn, Tittel,'I(u)', 'A1')
Overskrift={' ','X [mm]';'Y [mm]','I(u)[]'};
xlswrite(Filnavn, Overskrift,'I(u)', 'A3')
Overskrift=X;
xlswrite(Filnavn, Overskrift,'I(u)', 'C3')
Overskrift=flipud(Y);
xlswrite(Filnavn, Overskrift,'I(u)', 'A5')
Tabell=flipud(U_turbulent_intensitet);
xlswrite(Filnavn, Tabell,'I(u)', 'C5')
```

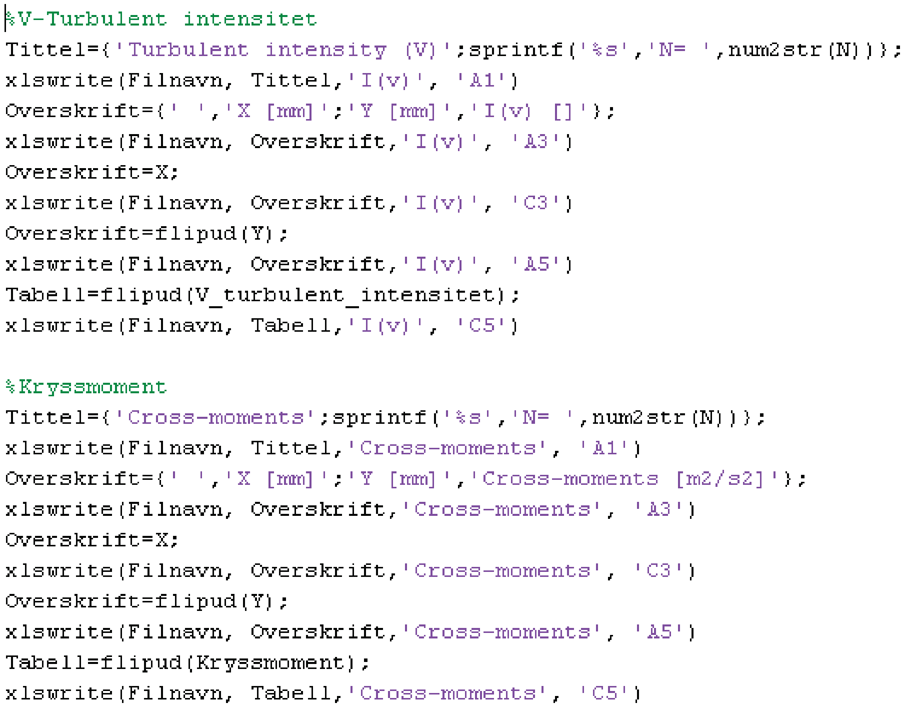

```
%V-Turbulent intensitet
Tittel={'Turbulent intensity (V)';sprintf('%s','N= ',num2str(N))};
xlswrite(Filnavn, Tittel,'I(v)', 'A1')
Overskrift={' ','X [mm]';'Y [mm]','I(v) []'};
xlswrite(Filnavn, Overskrift,'I(v)', 'A3')
Overskrift=X;
xlswrite(Filnavn, Overskrift,'I(v)', 'C3')
Overskrift=flipud(Y);
xlswrite(Filnavn, Overskrift,'I(v)', 'A5')
Tabell=flipud(V_turbulent_intensitet);
xlswrite(Filnavn, Tabell,'I(v)', 'C5')

%Kryssmoment
Tittel={'Cross-moments';sprintf('%s','N= ',num2str(N))};
xlswrite(Filnavn, Tittel,'Cross-moments', 'A1')
Overskrift={' ','X [mm]';'Y [mm]','Cross-moments [m2/s2]'};
xlswrite(Filnavn, Overskrift,'Cross-moments', 'A3')
Overskrift=X;
xlswrite(Filnavn, Overskrift,'Cross-moments', 'C3')
Overskrift=flipud(Y);
xlswrite(Filnavn, Overskrift,'Cross-moments', 'A5')
Tabell=flipud(Kryssmoment);
xlswrite(Filnavn, Tabell,'Cross-moments', 'C5')
```

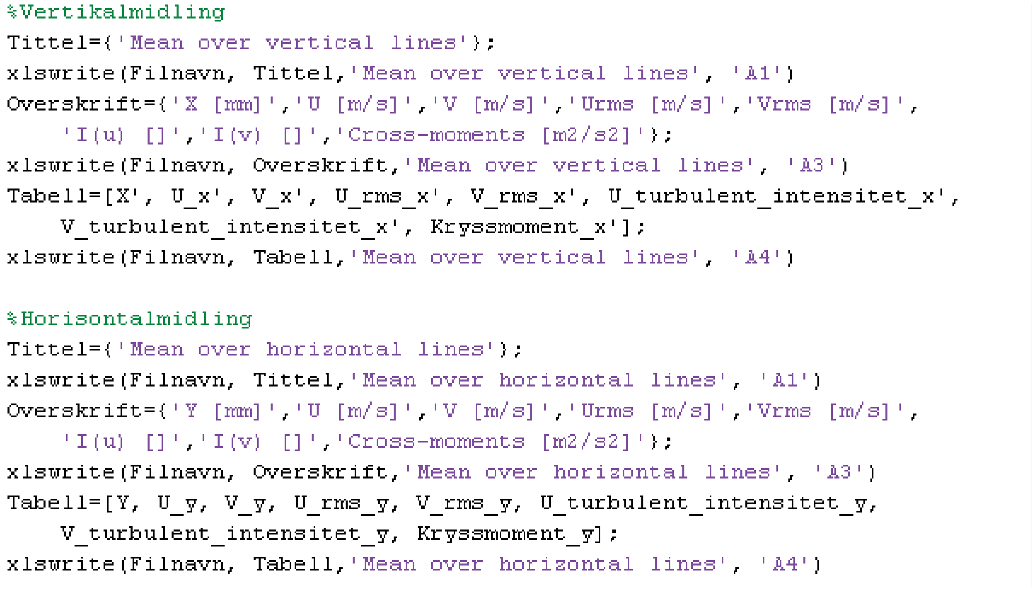

```
%Vertikalmidling
Tittel={'Mean over vertical lines'};
xlswrite(Filnavn, Tittel,'Mean over vertical lines', 'A1')
Overskrift={'X [mm]','U [m/s]','V [m/s]','Urms [m/s]','Vrms [m/s]',
    'I(u) []','I(v) []','Cross-moments [m2/s2]'};
xlswrite(Filnavn, Overskrift,'Mean over vertical lines', 'A3')
Tabell=[X', U_x', V_x', U_rms_x', V_rms_x', U_turbulent_intensitet_x',
    V_turbulent_intensitet_x', Kryssmoment_x'];
xlswrite(Filnavn, Tabell,'Mean over vertical lines', 'A4')

%Horisontalmidling
Tittel={'Mean over horizontal lines'};
xlswrite(Filnavn, Tittel,'Mean over horizontal lines', 'A1')
Overskrift={'Y [mm]','U [m/s]','V [m/s]','Urms [m/s]','Vrms [m/s]',
    'I(u) []','I(v) []','Cross-moments [m2/s2]'};
xlswrite(Filnavn, Overskrift,'Mean over horizontal lines', 'A3')
Tabell=[Y, U_y, V_y, U_rms_y, V_rms_y, U_turbulent_intensitet_y,
    V_turbulent_intensitet_y, Kryssmoment_y];
xlswrite(Filnavn, Tabell,'Mean over horizontal lines', 'A4')
```

C. Additional LDA experiments

The rest of the LDA experiments that are not presented in Chapter 6 in the main part of this thesis can be found in this appendix. Normal mean particle velocities for ZrO_2 260 µm, ZrO_2 530 µm, glass 120 µm and glass 518 µm are presented below. All the values are less than 5 % of the axial mean particle velocity.

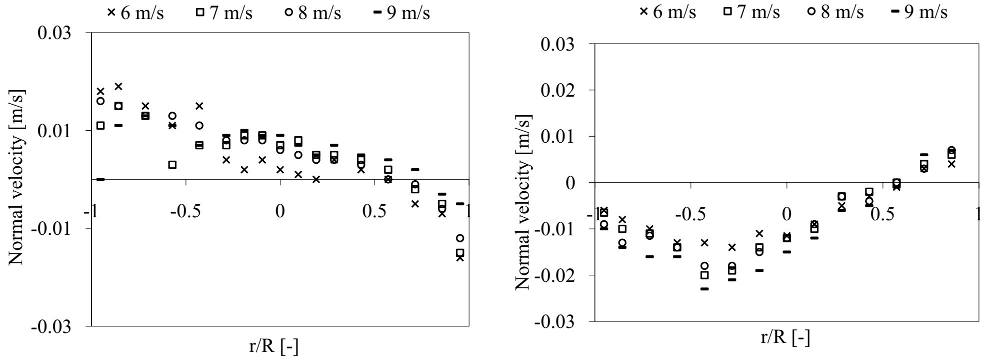

a) ZrO_2 particles with a diameter of 260 µm b) ZrO_2 particles with a diameter of 530 µm

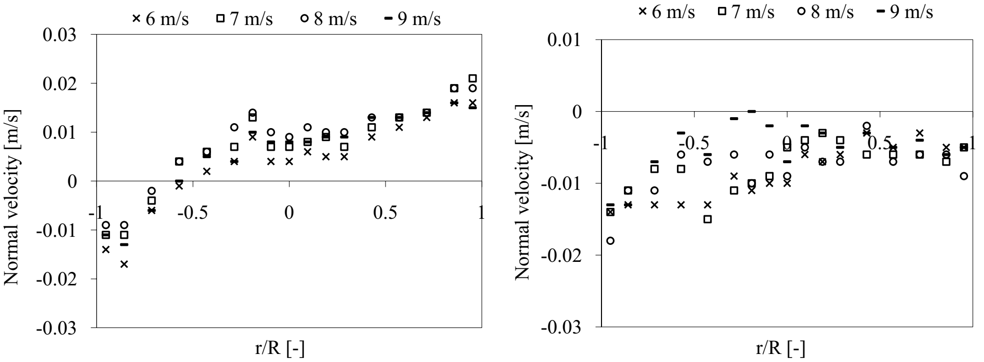

c) Glass particles with a diameter of 120 µm d) Glass particles with a diameter of 518 µm

Figure C.1: *The normal particle velocity profiles for at a constant particle volume fraction of approximately 0.15 % different superficial gas velocities.*

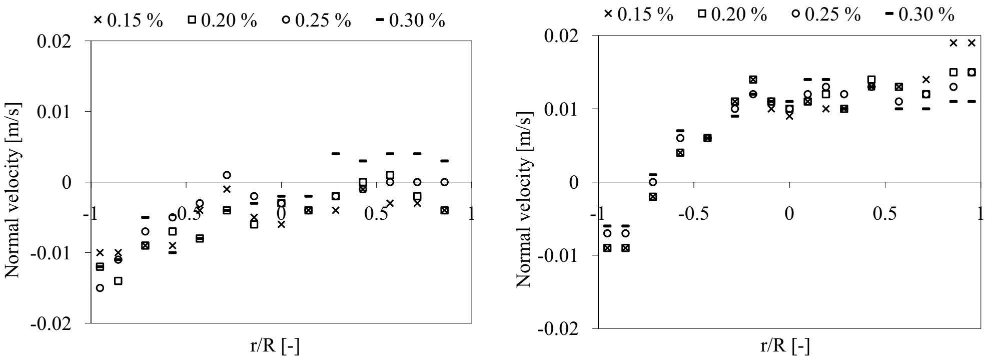

a) ZrO_2 particles with a diameter of 530 µm b) Glass particles with a diameter of 120 µm

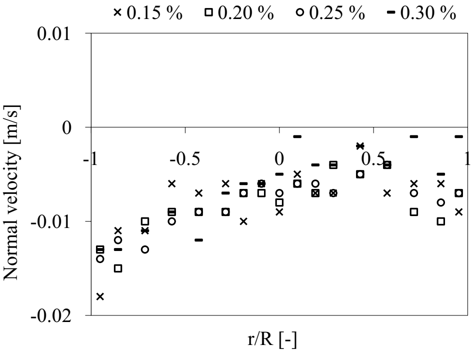

c) Glass particles with a diameter of 518 µm

Figure C.2: The mean normal particle velocity profiles at a constant superficial gas velocity of 8 m/s and different particle volume fractions.

ZrO_2, 260 µm

Results of experiments performed at a superficial gas velocity of 7 m/s with varying particle volume fractions.

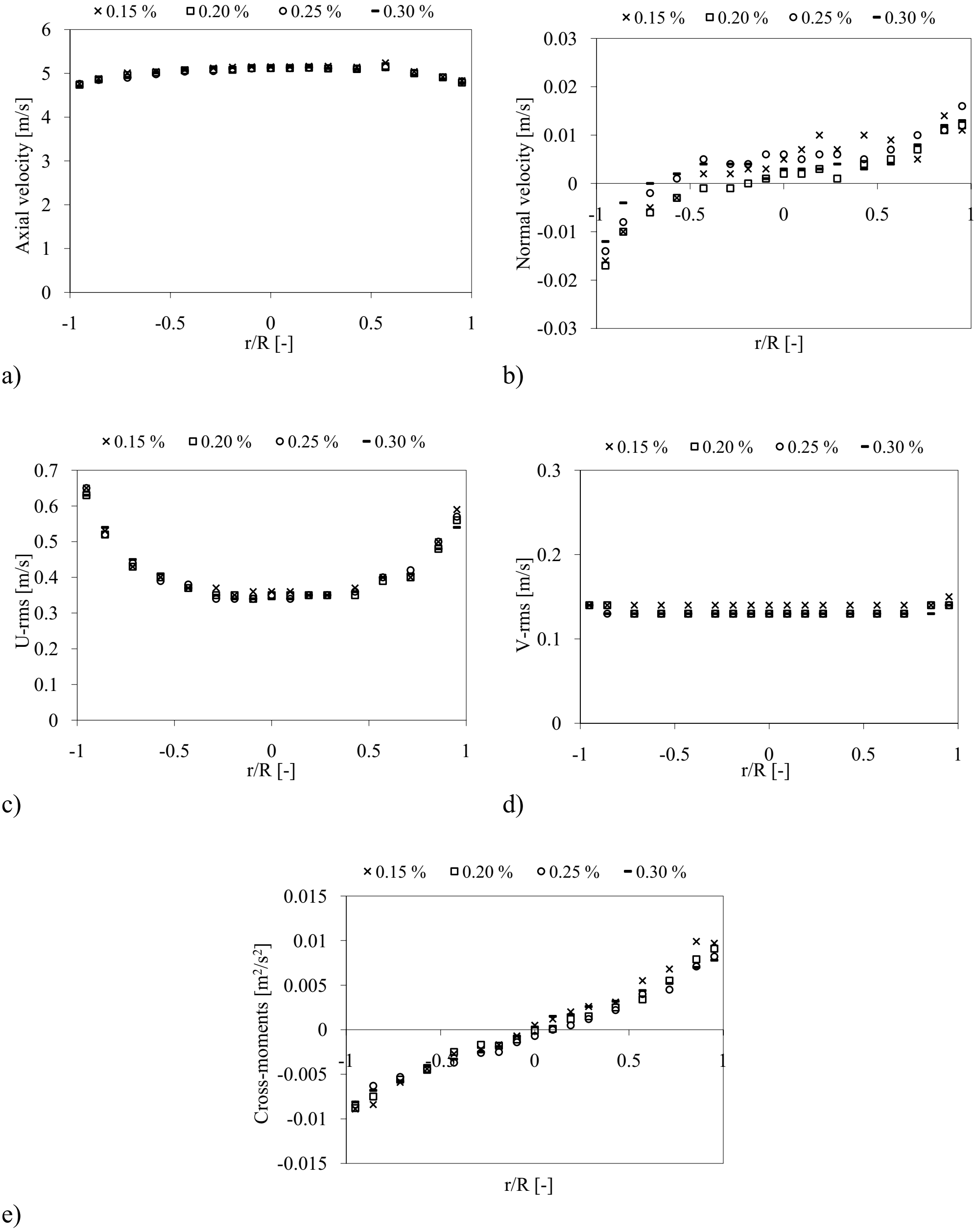

Figure C.3: *The mean axial and normal particle velocity profiles, the axial and normal rms profiles and the cross-moment profiles for ZrO_2 particles with a diameter of 260 µm at a constant superficial gas velocity of 7 m/s and different particle volume fractions*

Glass, 120 µm

Results of experiments performed at a superficial gas velocity of 6 m/s with varying particle volume fractions.

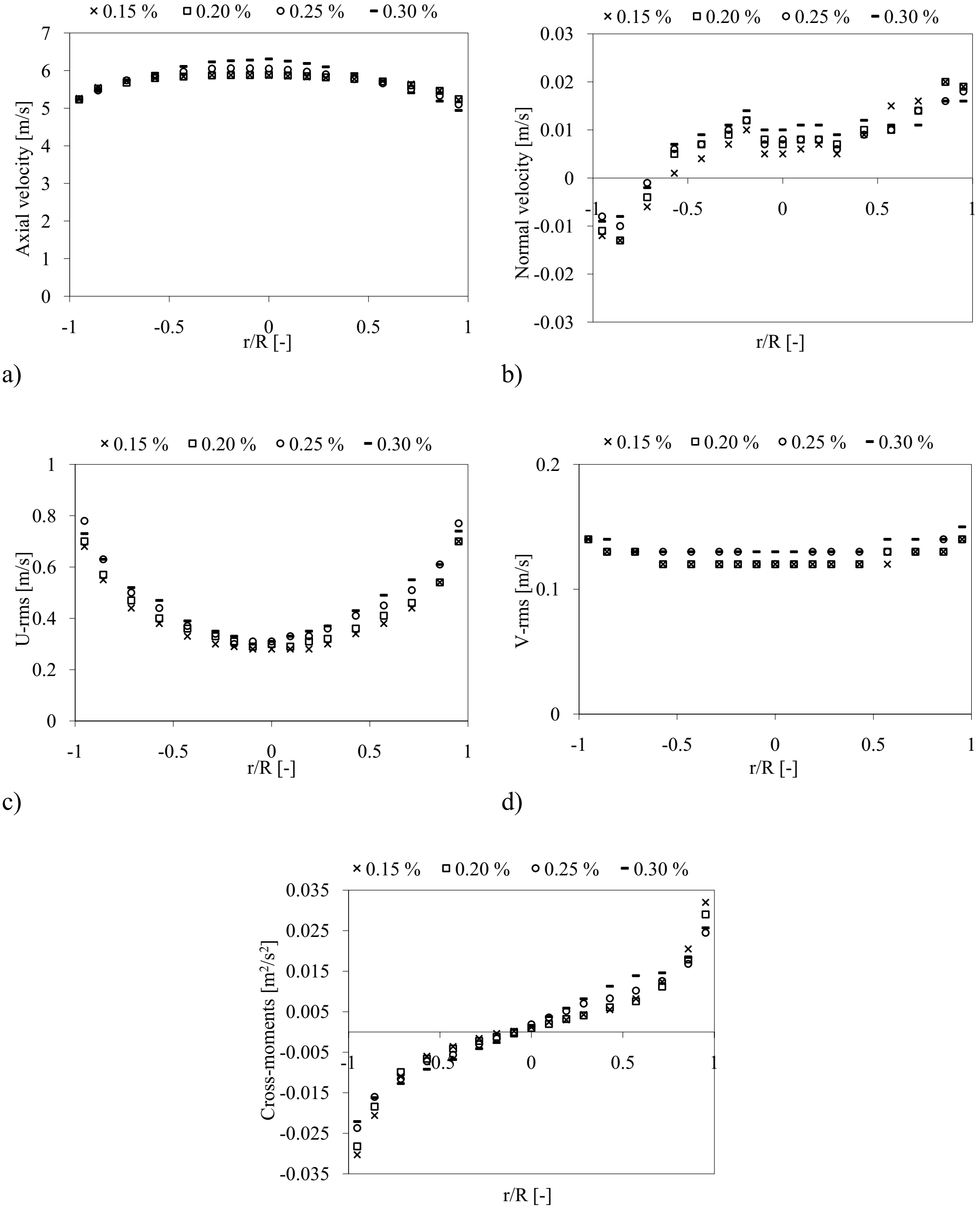

a)

b)

c)

d)

e)

Figure C.4: *The mean axial and normal particle velocity profiles, the axial and normal rms profiles and the cross-moment profiles for glass particles with a diameter of 120 µm at a constant superficial gas velocity of 6 m/s and different particle volume fractions*

Results of experiments performed at a superficial gas velocity of 7 m/s with varying particle volume fractions.

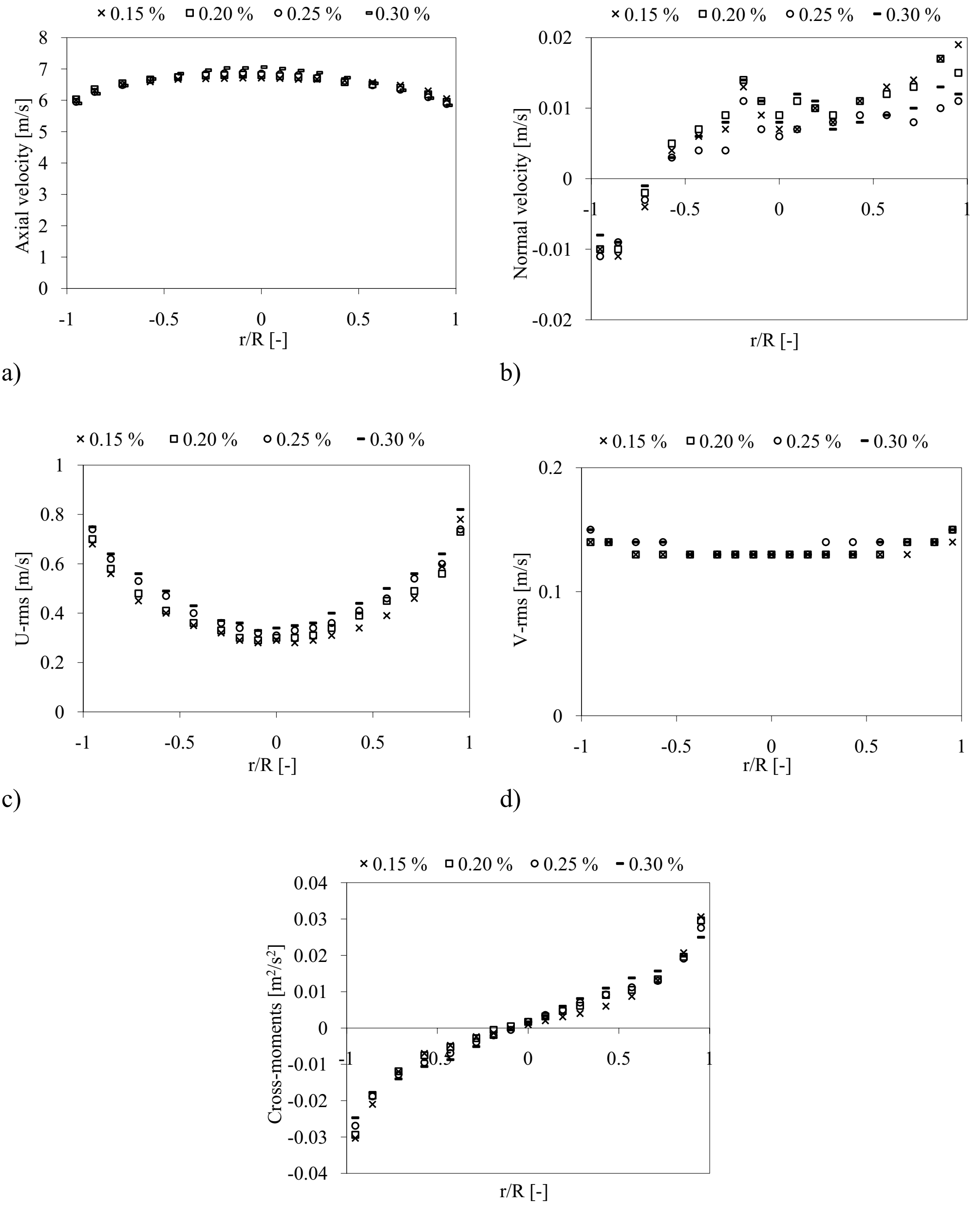

a)

b)

c)

d)

e)

Figure C.5: *The mean axial and normal particle velocity profiles, the axial and normal rms profiles and the cross-moment profiles for glass particles with a diameter of 120 µm at a constant superficial gas velocity of 7 m/s and different particle volume fractions*

Results of experiments performed at a superficial gas velocity of 9 m/s with varying particle volume fractions.

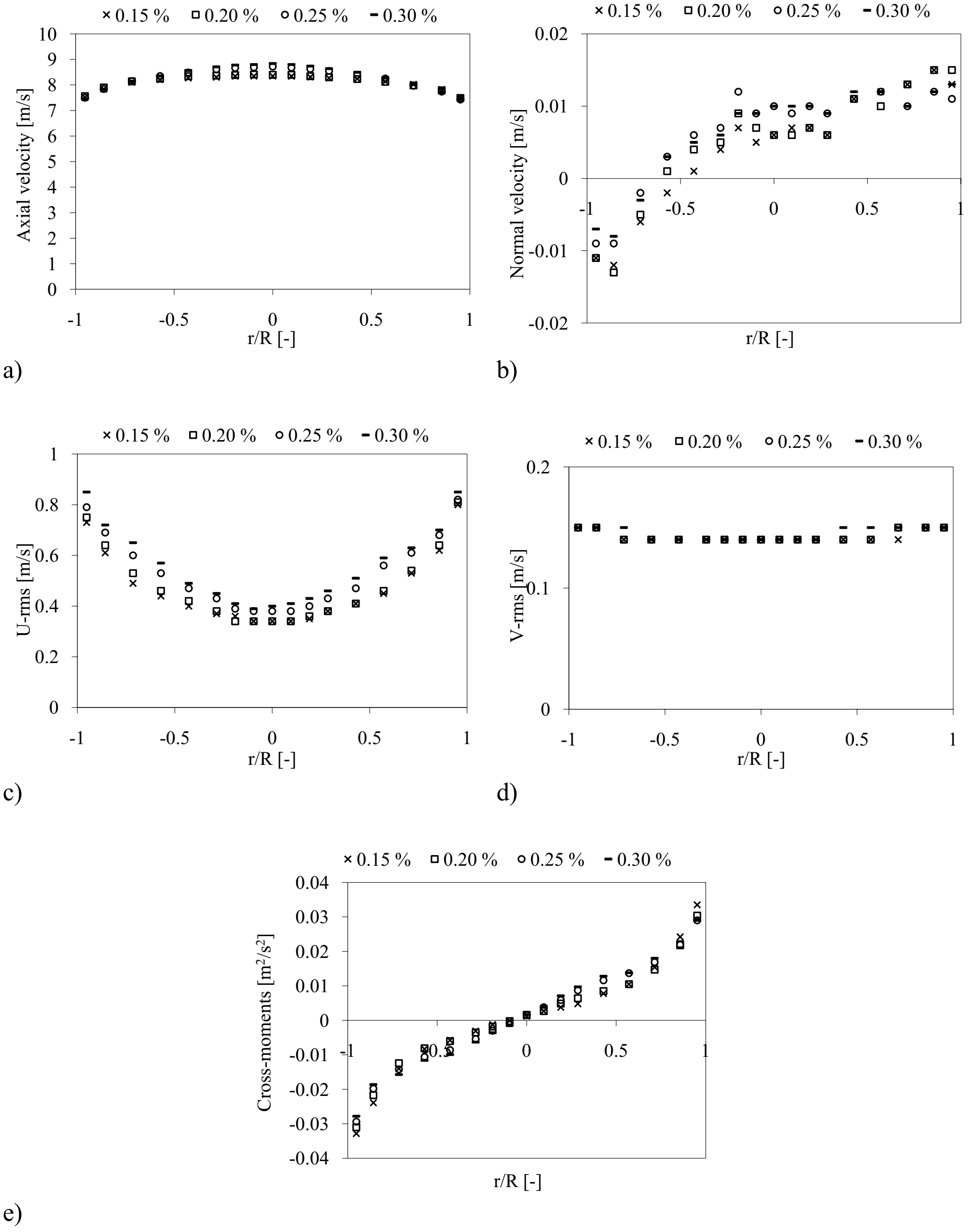

a)

b)

c)

d)

e)

Figure C.6: *The mean axial and normal particle velocity profiles, the axial and normal rms profiles and the cross-moment profiles for glass particles with a diameter of 120 µm at a constant superficial gas velocity of 9 m/s and different particle volume fractions*

Glass, 518 µm

Results of experiments performed at a superficial gas velocity of 7 m/s with varying particle volume fractions.

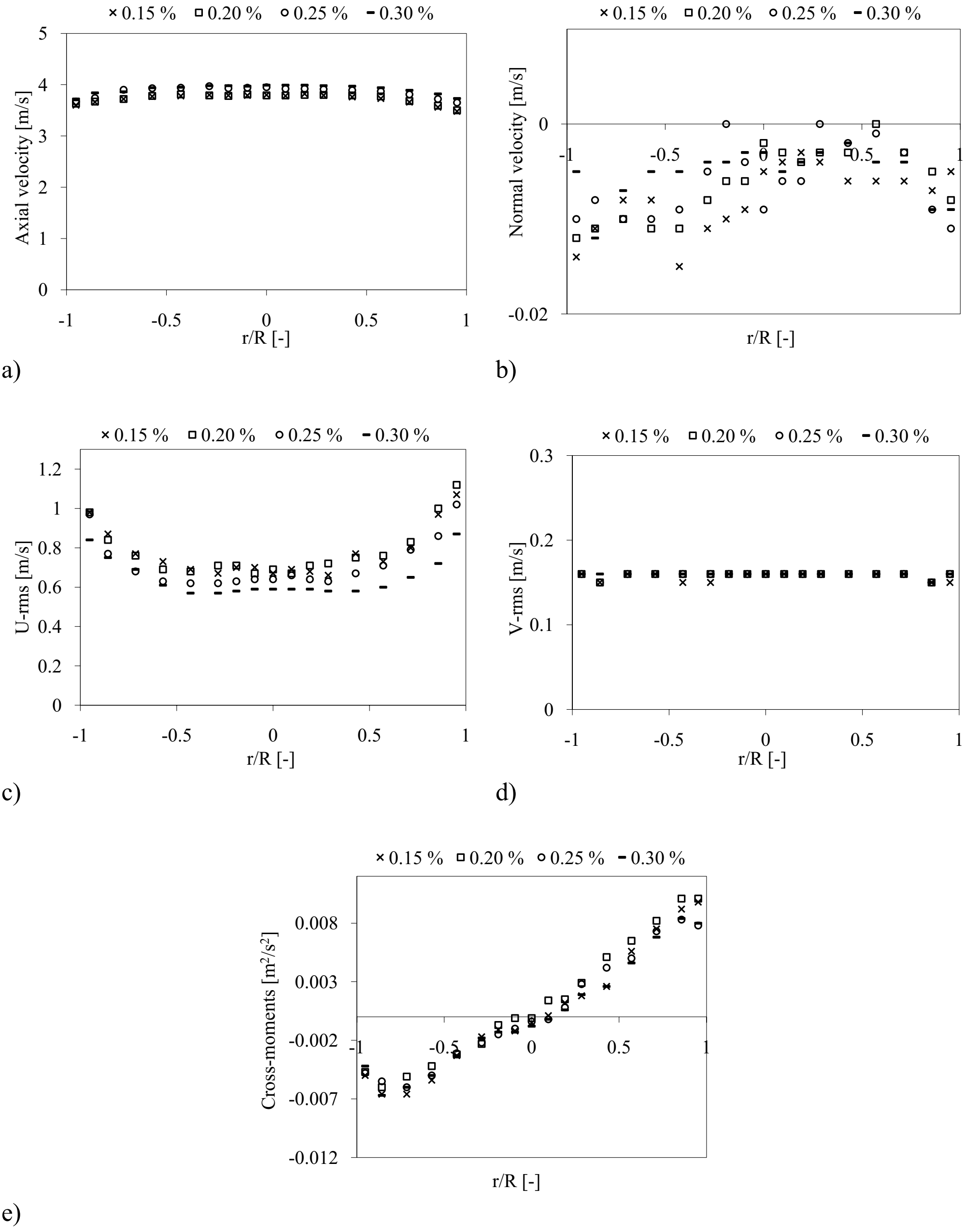

Figure C.7: The mean axial and normal particle velocity profiles, the axial and normal rms profiles and the cross-moment profiles for glass particles with a diameter of 518 µm at a constant superficial gas velocity of 7 m/s and different particle volume fractions

D. Additional PIV experiments

The rest of the PIV experiments that are not presented in Chapter 7 in the main part of this thesis can be found in this appendix.

Normal mean particle velocities for ZrO_2 260 µm, ZrO_2 530 µm, glass 120 µm and glass 518 µm are presented below. All the values are less than 5 % of the axial mean particle velocity.

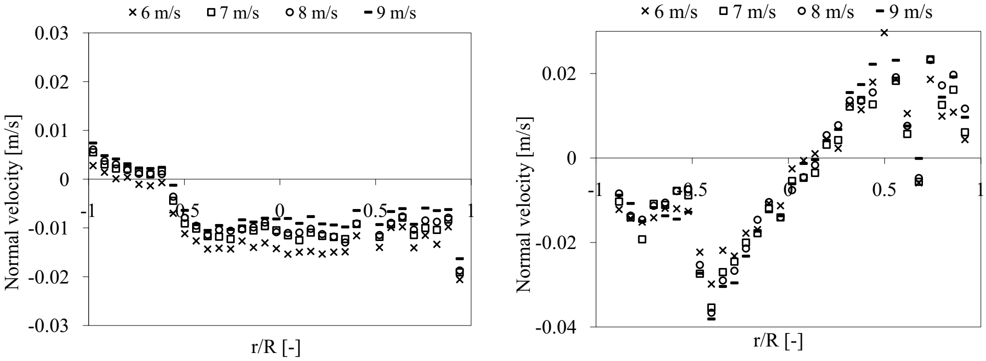

a) ZrO_2 particles with a diameter of 260 µm   b) ZrO_2 particles with a diameter of 530 µm

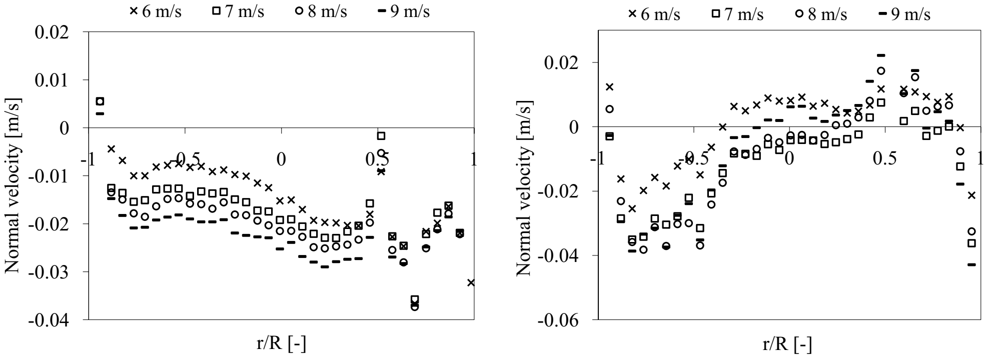

c) Glass particles with a diameter of 120 µm   d) Glass particles with a diameter of 518 µm

Figure D.1: The normal particle velocity profiles for at a constant particle volume fraction of approximately 0.15 % different superficial gas velocities.

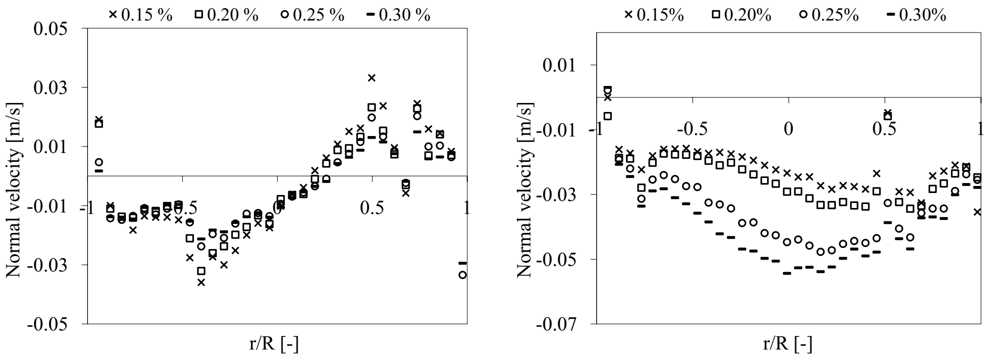

a) ZrO_2 particles with a diameter of 530 µm b) Glass particles with a diameter of 120 µm

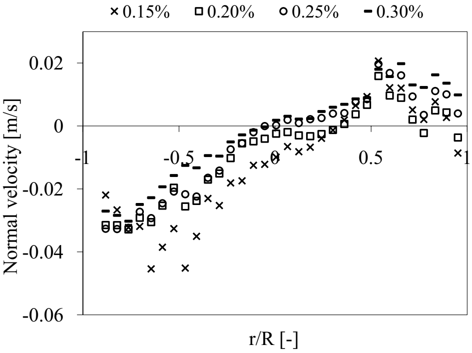

c) Glass particles with a diameter of 518 µm

Figure D.2: *The mean normal particle velocity profiles at a constant superficial gas velocity of 8 m/s and different particle volume fractions.*

ZrO$_2$, 260 µm

Results of experiments performed at a superficial gas velocity of 6 m/s with varying particle volume fractions.

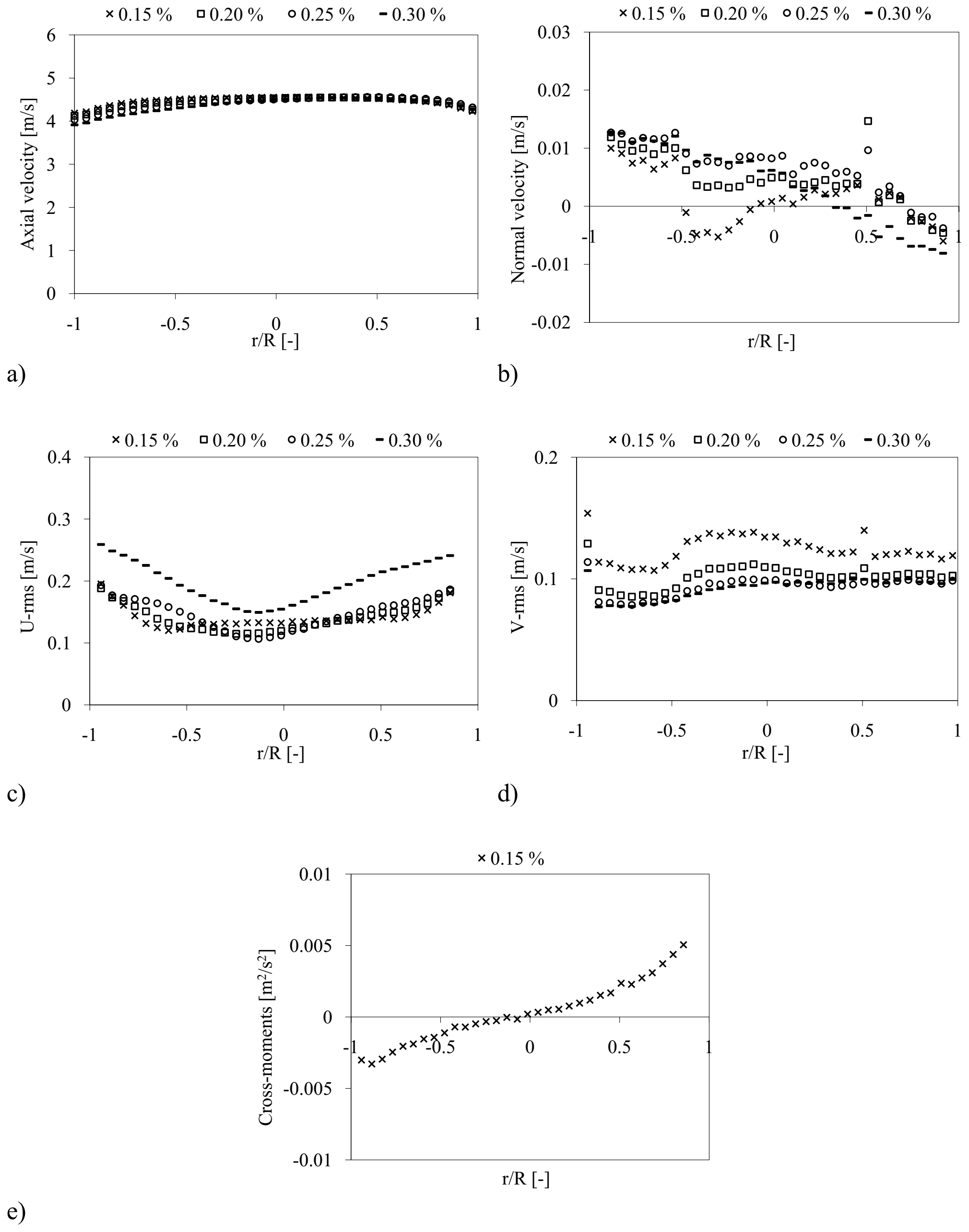

Figure D.3: *The mean axial and normal particle velocity profiles, the axial and normal rms profiles and the cross-moment profiles for ZrO$_2$ particles with a diameter of 260 µm at a constant superficial gas velocity of 6 m/s and different particle volume fractions*

Results of experiments performed at a superficial gas velocity of 7 m/s with varying particle volume fractions.

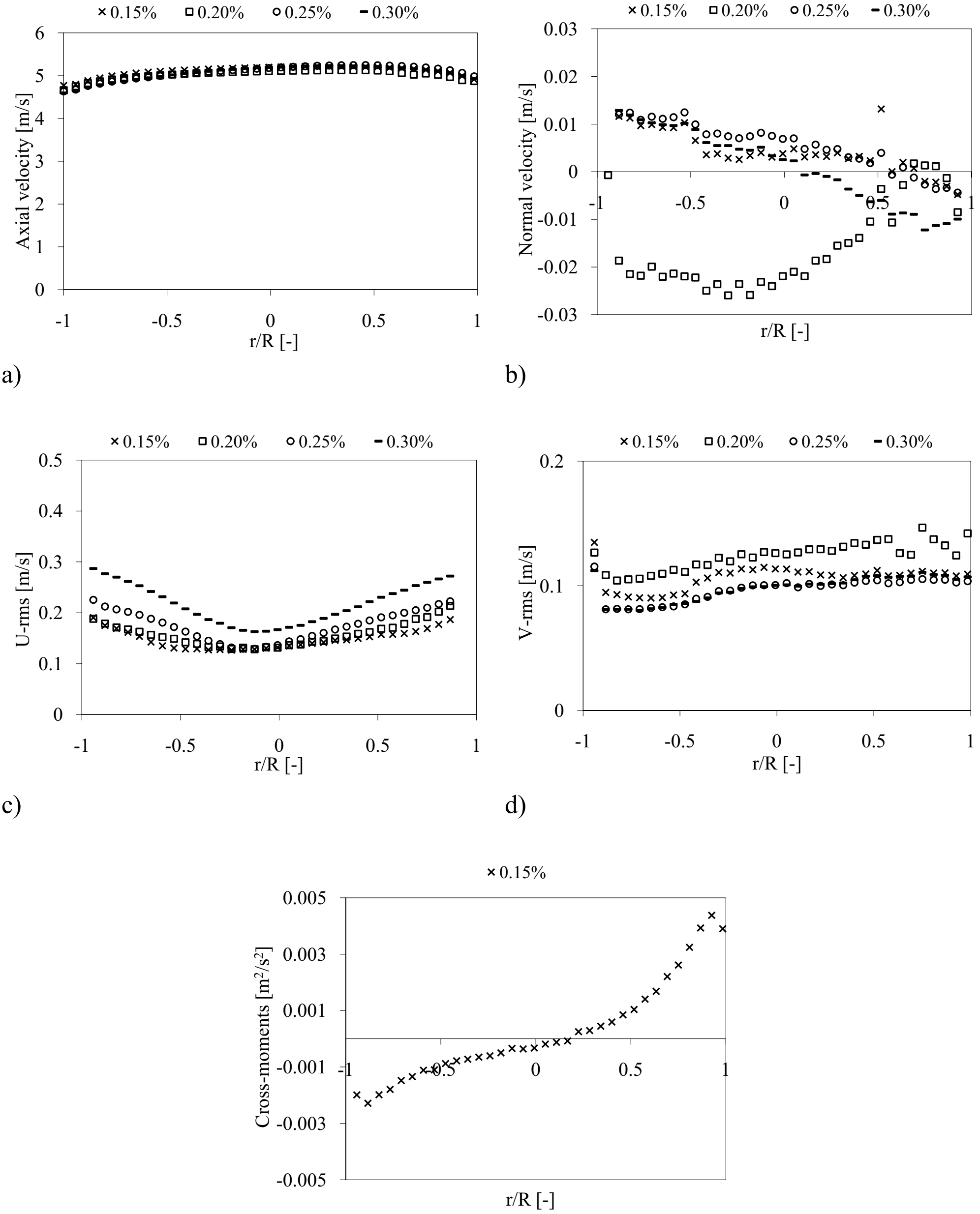

a)

b)

c)

d)

e)

Figure D.4: *The mean axial and normal particle velocity profiles, the axial and normal rms profiles and the cross-moment profiles for ZrO_2 particles with a diameter of 260 µm at a constant superficial gas velocity of 7 m/s and different particle volume fractions*

Results of experiments performed at a superficial gas velocity of 9 m/s with varying particle volume fractions.

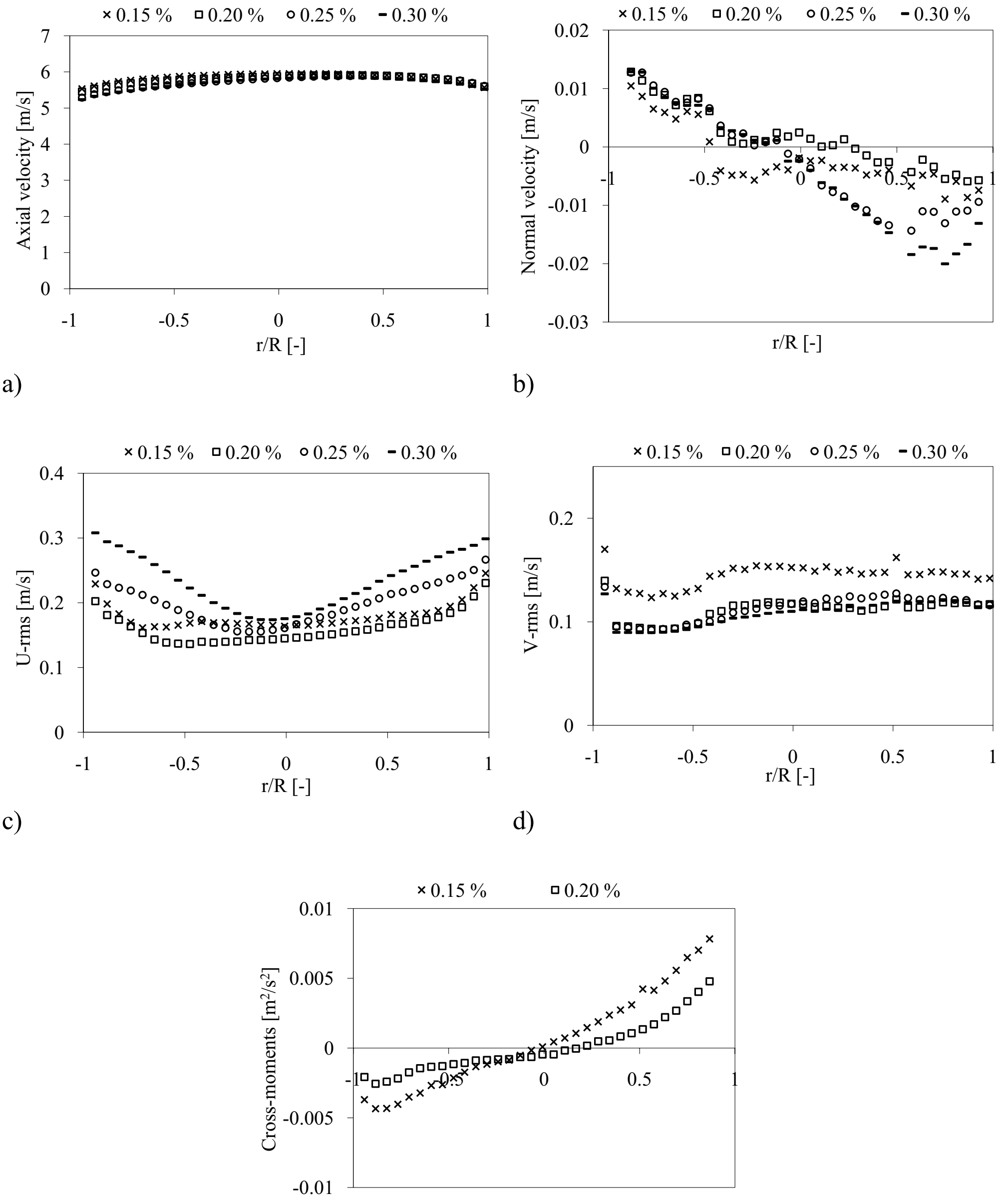

a)

b)

c)

d)

e)

Figure D.5: *The mean axial and normal particle velocity profiles, the axial and normal rms profiles and the cross-moment profiles ZrO_2 particles with a diameter of 260 μm at a constant superficial gas velocity of 9 m/s and different particle volume fractions*

ZrO_2, 530 µm

Results of experiments performed at a superficial gas velocity of 6 m/s with varying particle volume fractions.

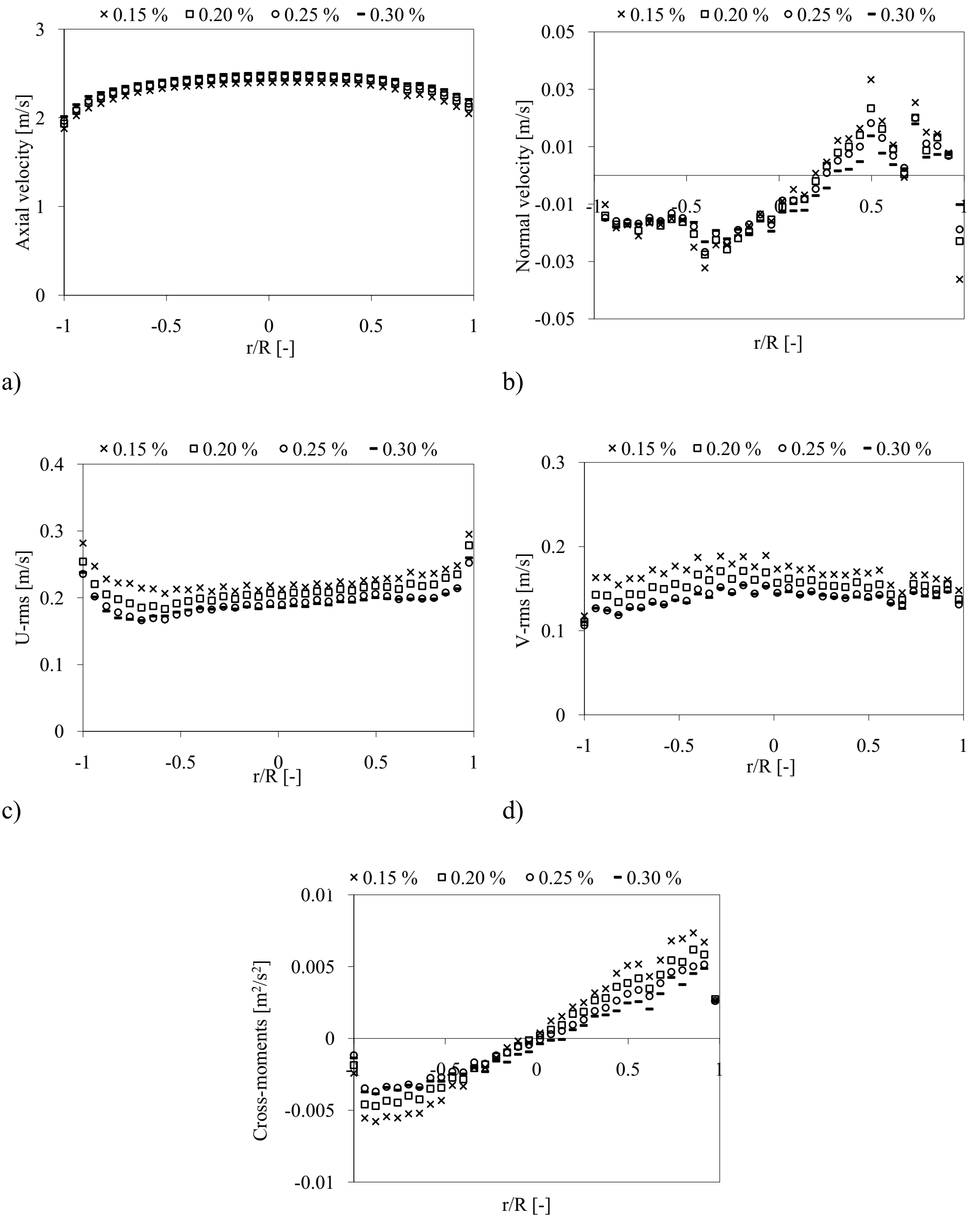

a)

b)

c)

d)

e)

Figure D.6: *The mean axial and normal particle velocity profiles, the axial and normal rms profiles and the cross-moment profiles for ZrO_2 particles with a diameter of 530 µm at a constant superficial gas velocity of 6 m/s and different particle volume fractions*

Results of experiments performed at a superficial gas velocity of 7 m/s with varying particle volume fractions.

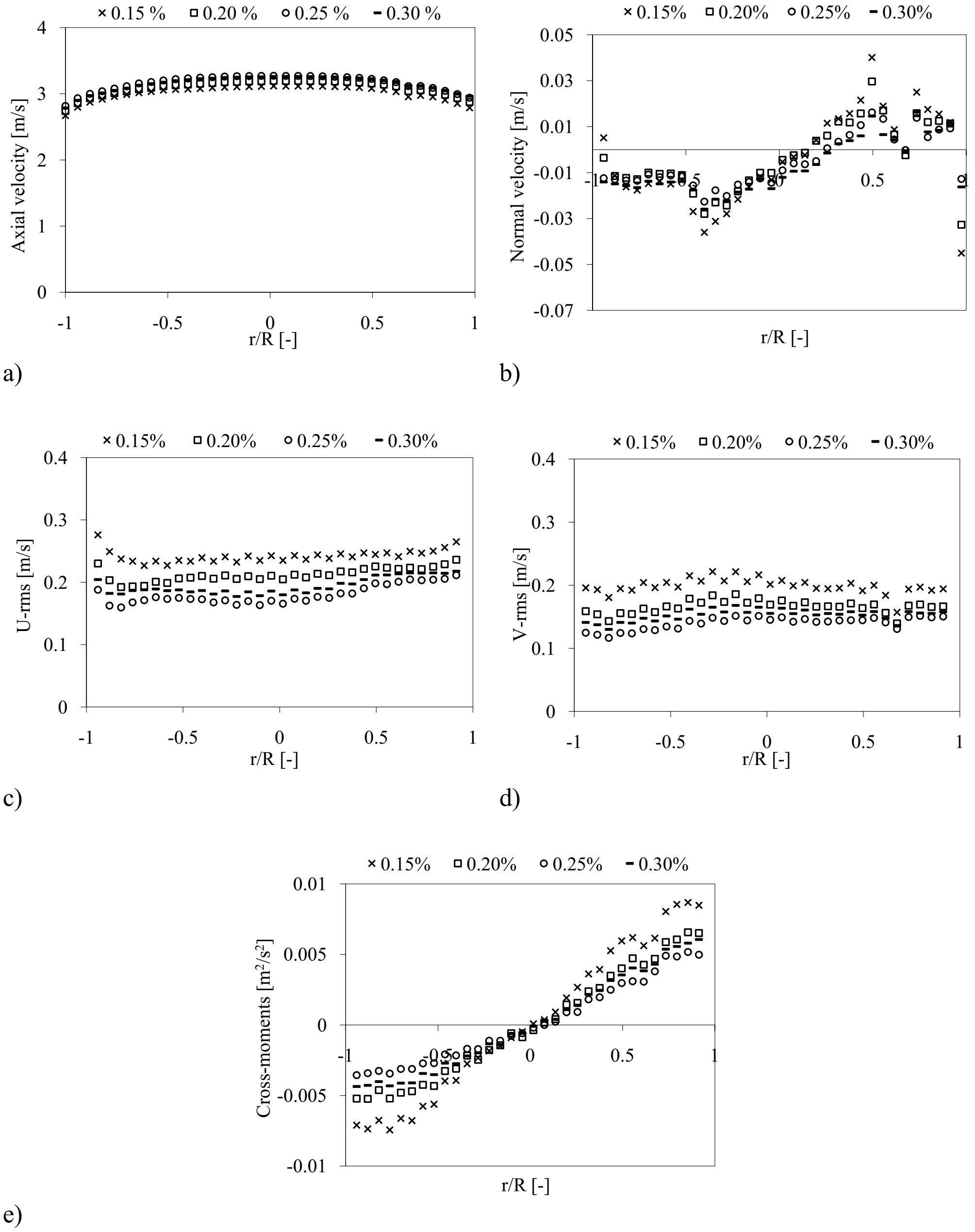

Figure D.7: *The mean axial and normal particle velocity profiles, the axial and normal rms profiles and the cross-moment profiles for ZrO_2 particles with a diameter of 530 μm at a constant superficial gas velocity of 7 m/s and different particle volume fractions*

Results of experiments performed at a superficial gas velocity of 9 m/s with varying particle volume fractions.

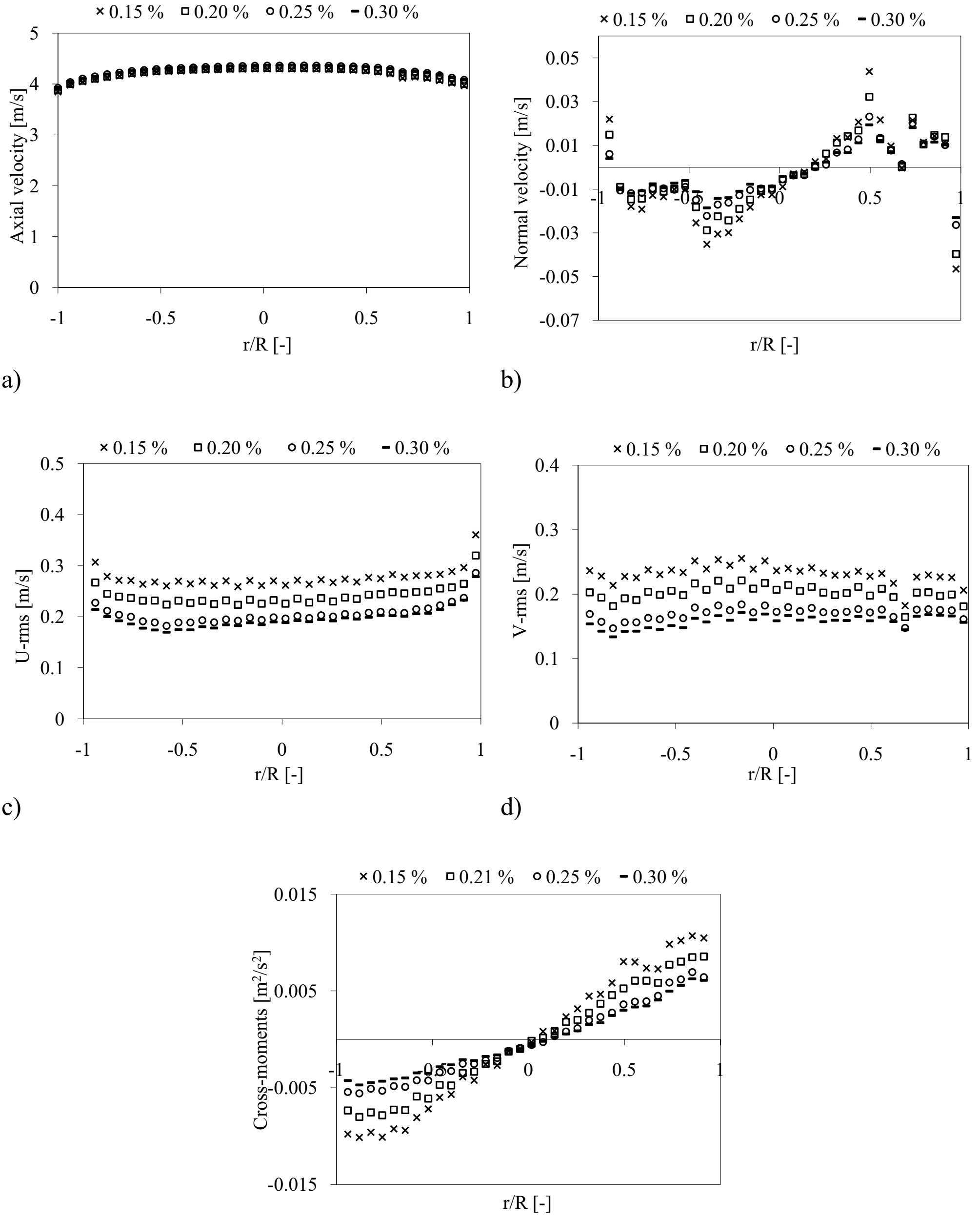

Figure D.8: The mean axial and normal particle velocity profiles, the axial and normal rms profiles and the cross-moment profiles ZrO_2 particles with a diameter of 530 µm at a constant superficial gas velocity of 9 m/s and different particle volume fractions

Glass, 120 µm

Results of experiments performed at a superficial gas velocity of 6 m/s with varying particle volume fractions.

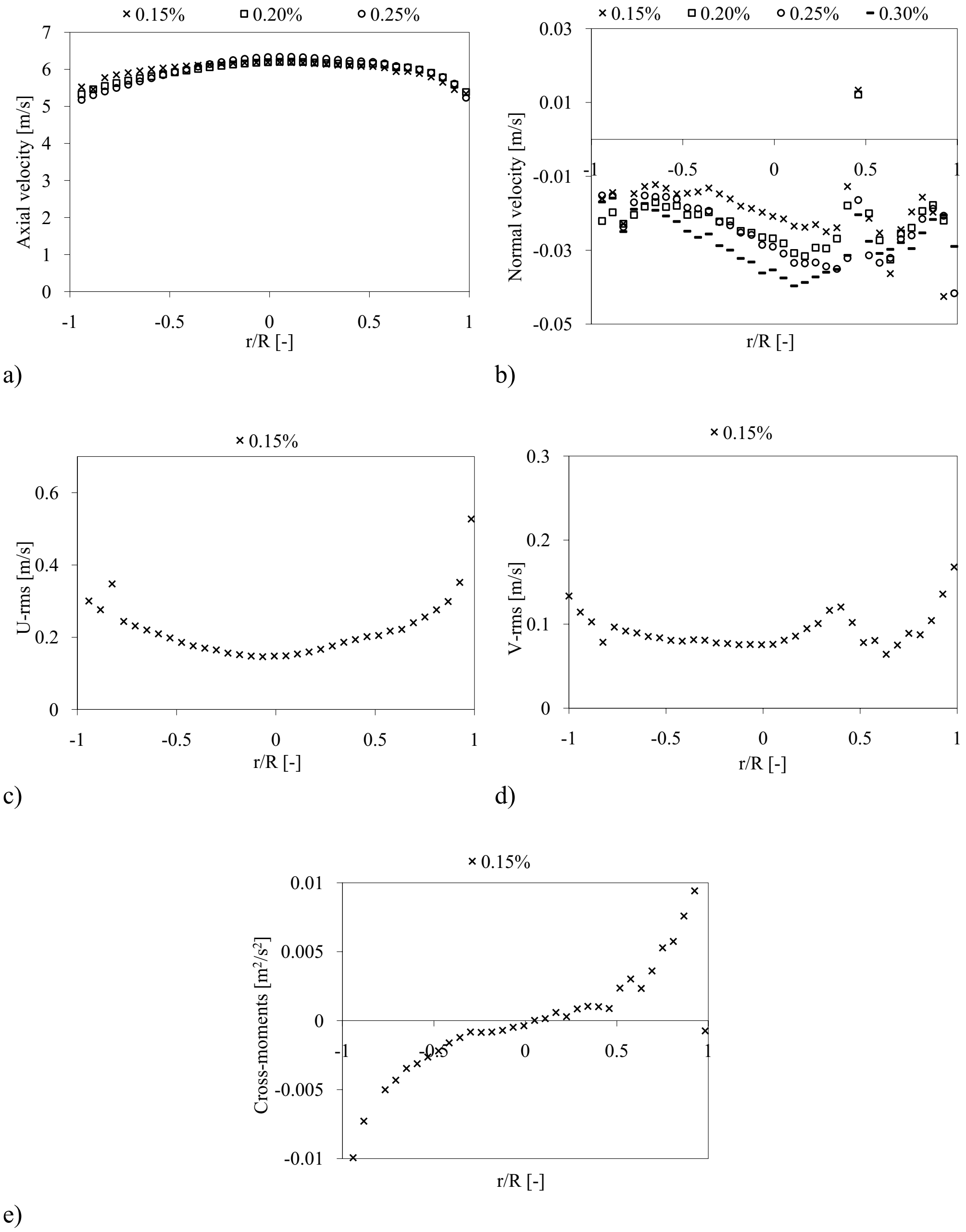

a)

b)

c)

d)

e)

Figure D.9: *The mean axial and normal particle velocity profiles, the axial and normal rms profiles and the cross-moment profiles for glass particles with a diameter of 120 µm at a constant superficial gas velocity of 6 m/s and different particle volume fractions*

Results of experiments performed at a superficial gas velocity of 7 m/s with varying particle volume fractions.

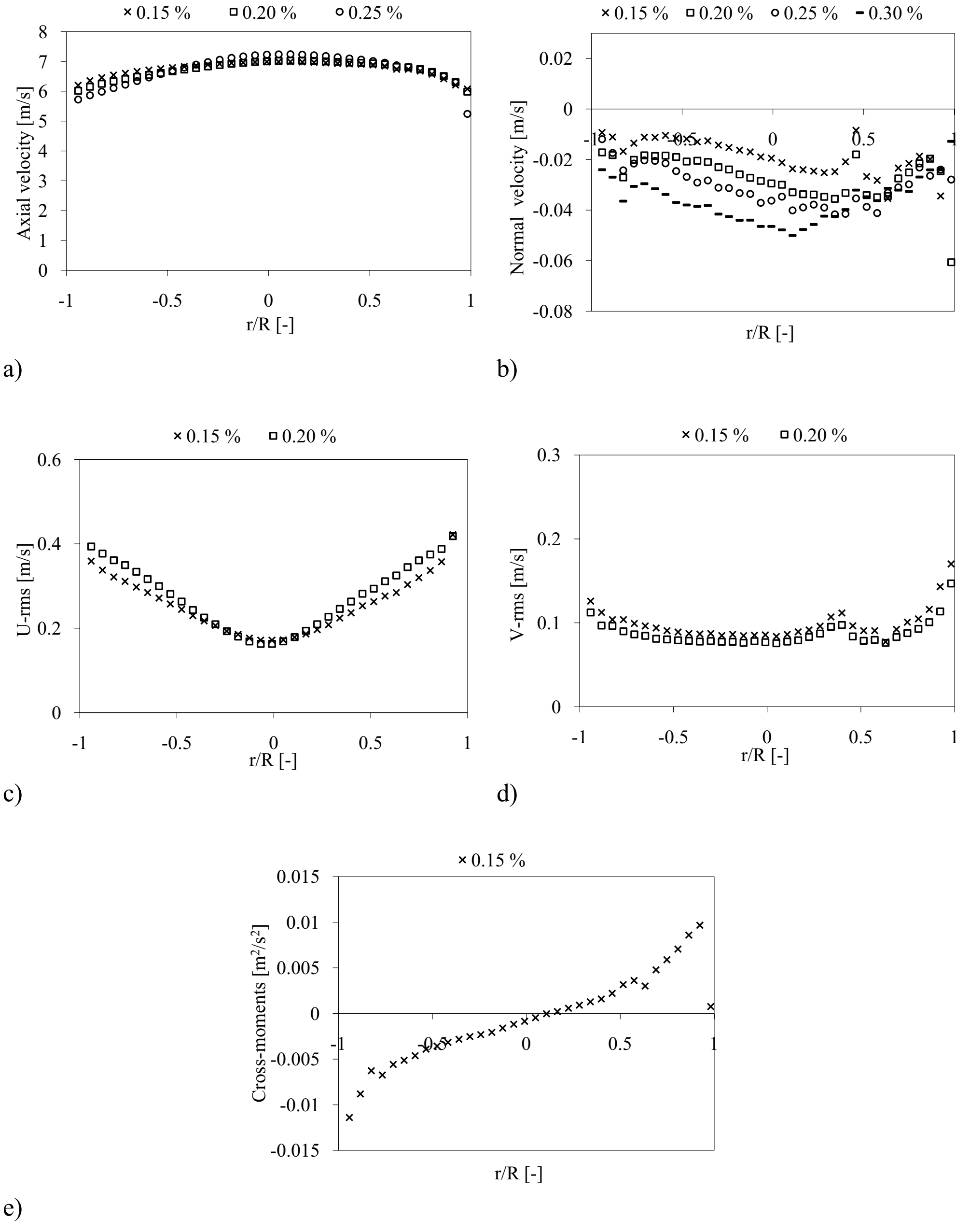

Figure D.10: *The mean axial and normal particle velocity profiles, the axial and normal rms profiles and the cross-moment profiles for glass particles with a diameter of 120 μm at a constant superficial gas velocity of 7 m/s and different particle volume fractions*

Results of experiments performed at a superficial gas velocity of 9 m/s with varying particle volume fractions.

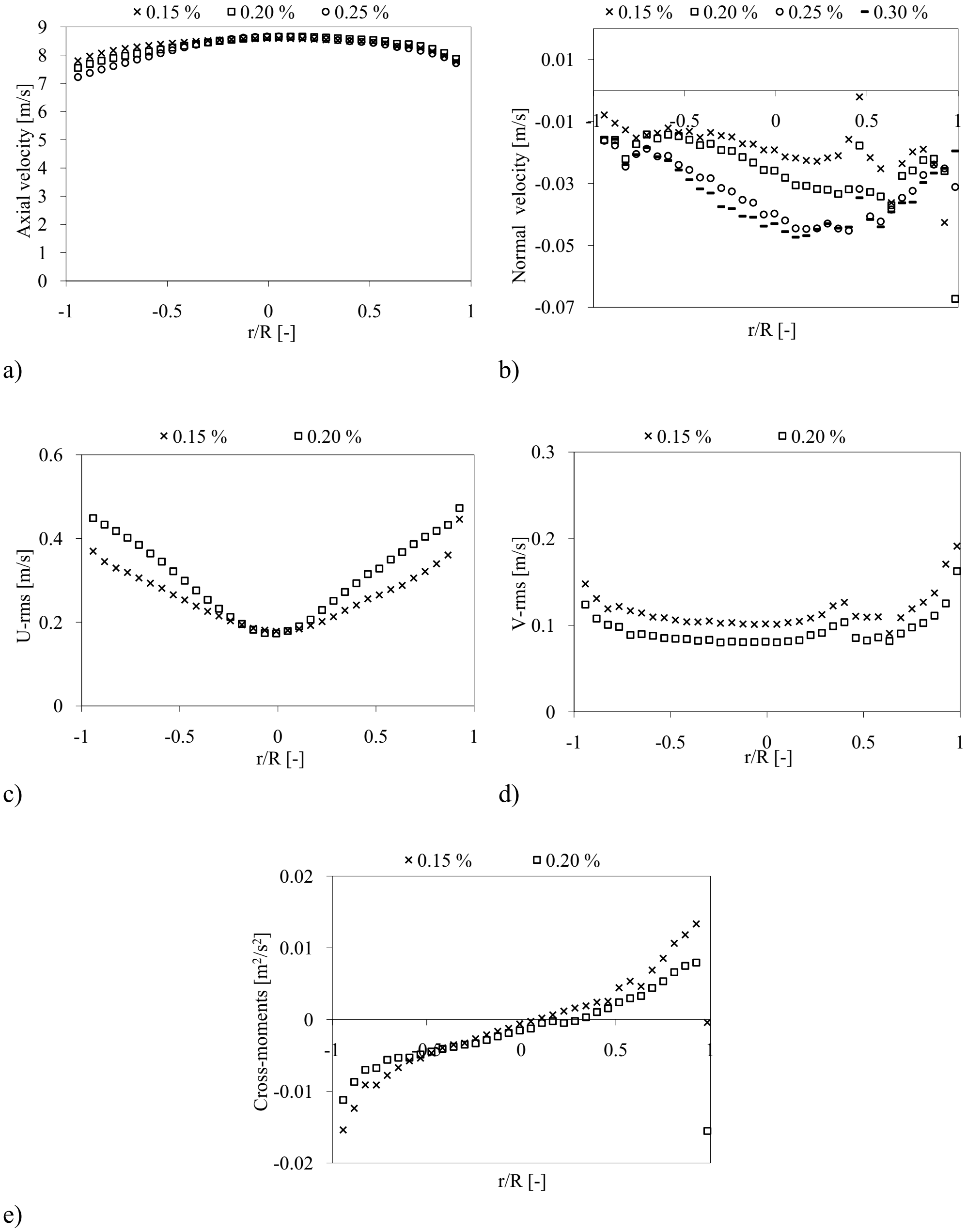

Figure D.11: The mean axial and normal particle velocity profiles, the axial and normal rms profiles and the cross-moment profiles glass particles with a diameter of 120 µm at a constant superficial gas velocity of 9 m/s and different particle volume fractions

Glass, 518 µm

Results of experiments performed at a superficial gas velocity of 6 m/s with varying particle volume fractions.

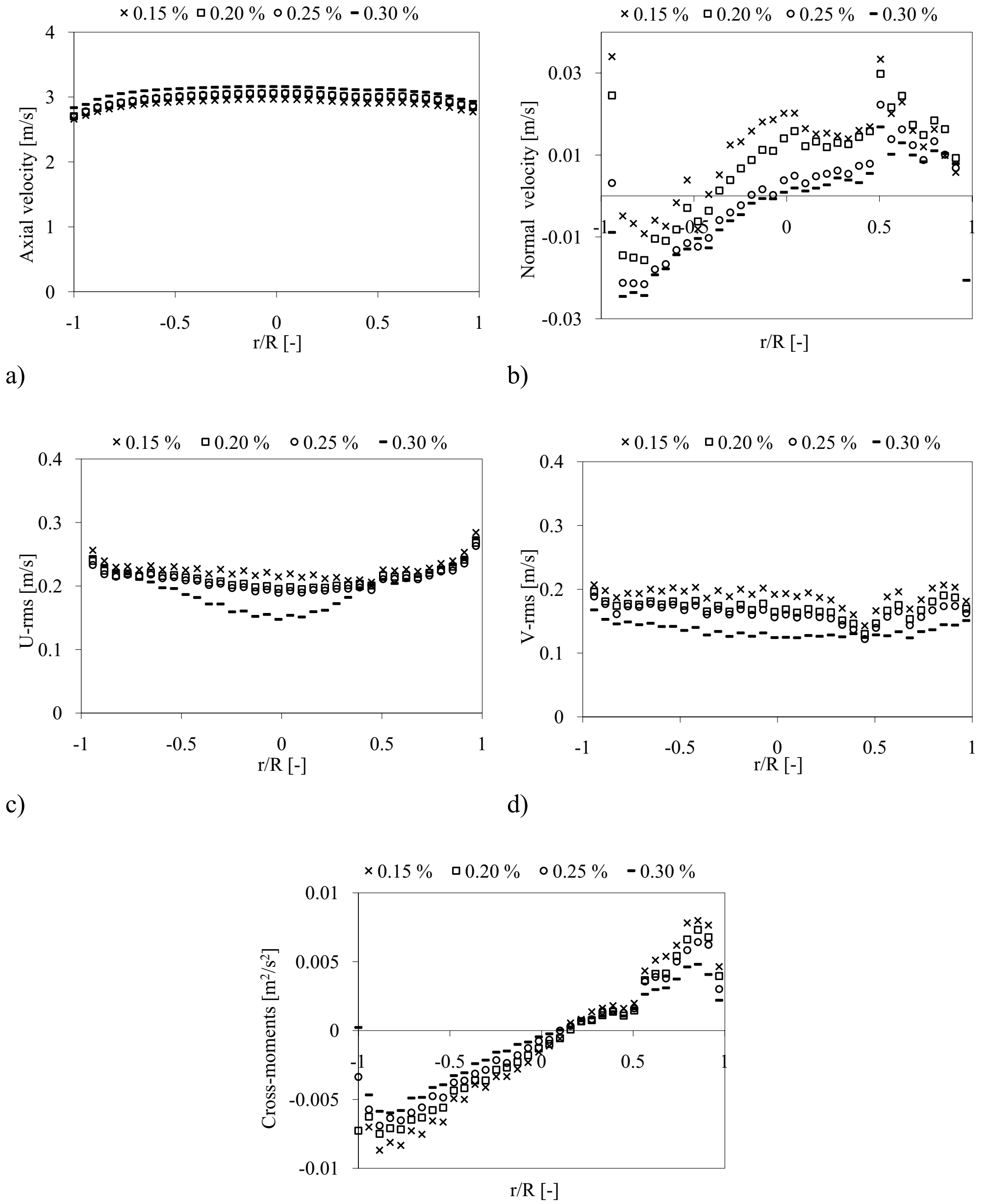

a)

b)

c)

d)

e)

Figure D.12: The mean axial and normal particle velocity profiles, the axial and normal rms profiles and the cross-moment profiles for glass particles with a diameter of 518 µm at a constant superficial gas velocity of 6 m/s and different particle volume fractions

Results of experiments performed at a superficial gas velocity of 7 m/s with varying particle volume fractions.

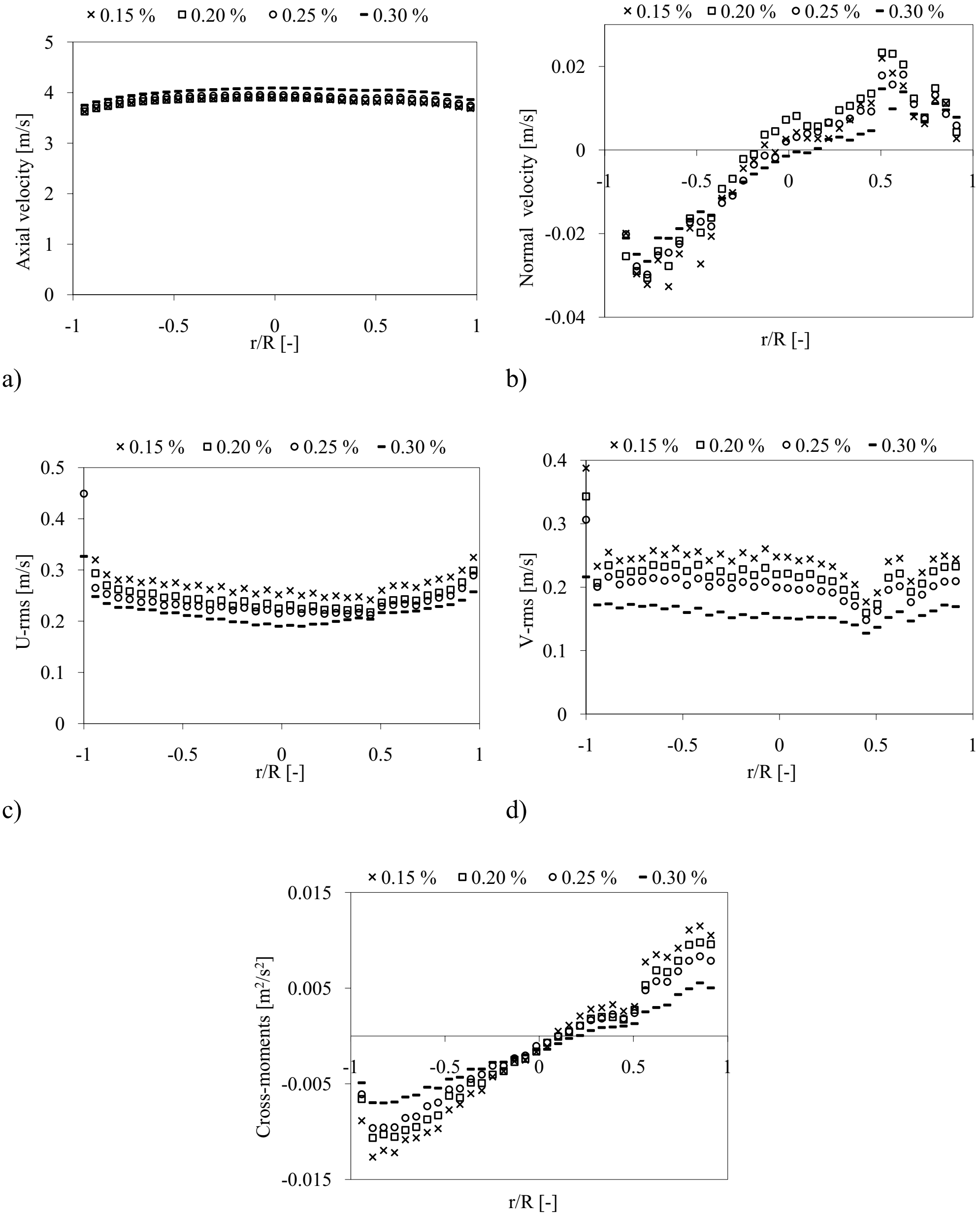

a)

b)

c)

d)

e)

Figure D.13: The mean axial and normal particle velocity profiles, the axial and normal rms profiles and the cross-moment profiles for glass particles with a diameter of 518 µm at a constant superficial gas velocity of 7 m/s and different particle volume fractions

Results of experiments performed at a superficial gas velocity of 9 m/s with varying particle volume fractions.

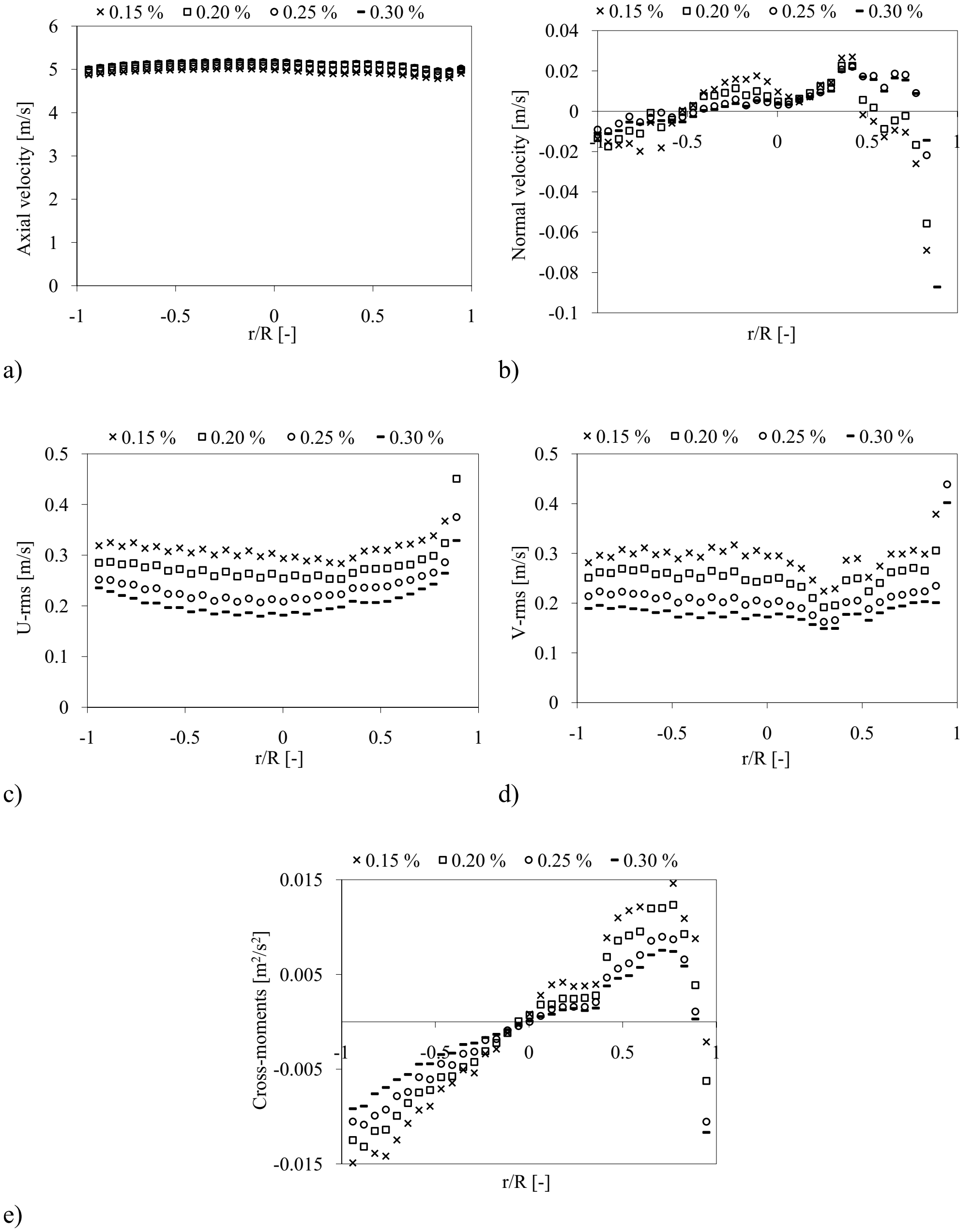

Figure D.14: *The mean axial and normal particle velocity profiles, the axial and normal rms profiles and the cross-moment profiles glass particles with a diameter of 518 μm at a constant superficial gas velocity of 9 m/s and different particle volume fractions*

E. Additional comparisons between LDA and PIV experiments

The rest of the LDA and PIV comparisons that are not presented in Chapter 8 in the main part of this thesis can be found in this appendix. Normal mean particle velocities for ZrO_2 260 μm, ZrO_2 530 μm, glass 120 μm and glass 518 μm are presented below.

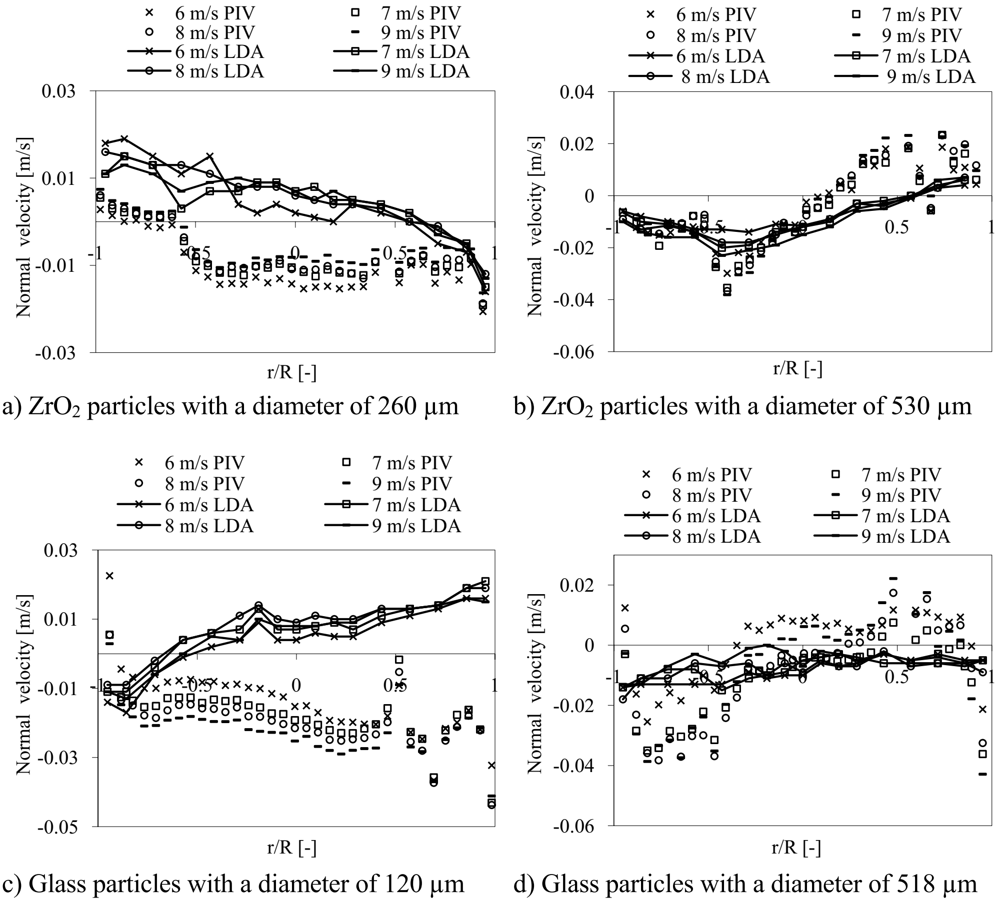

a) ZrO_2 particles with a diameter of 260 μm b) ZrO_2 particles with a diameter of 530 μm

c) Glass particles with a diameter of 120 μm d) Glass particles with a diameter of 518 μm

Figure E.1: The normal particle velocity profiles for at a constant particle volume fraction of approximately 0.15 % different superficial gas velocities.

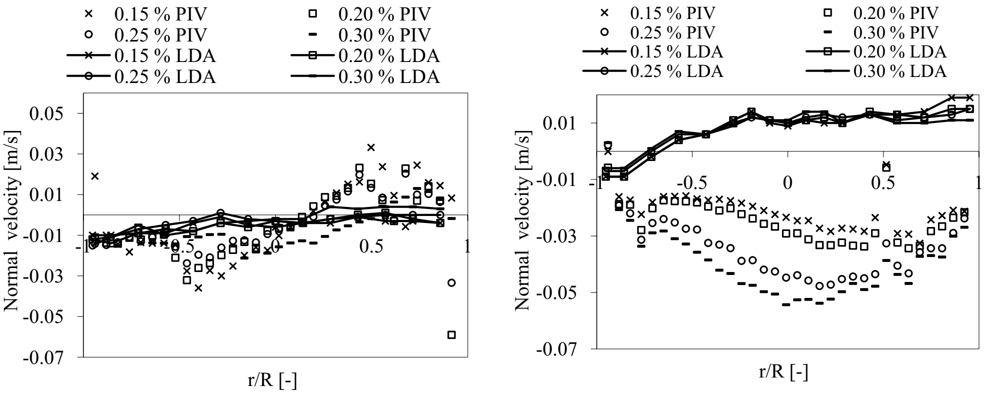

a) ZrO_2 particles with a diameter of 530 µm b) Glass particles with a diameter of 120 µm

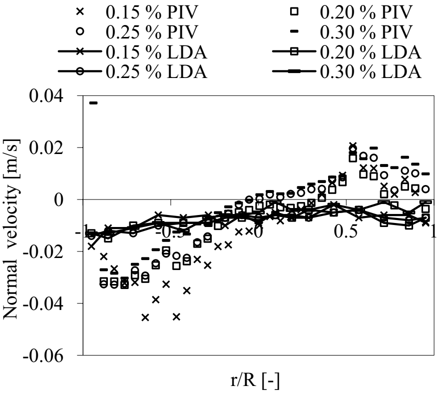

c) Glass particles with a diameter of 518 µm

Figure E.2: *The mean normal particle velocity profiles at a constant superficial gas velocity of 8 m/s and different particle volume fractions.*

ZrO$_2$, 260 µm

Results of experiments performed at a superficial gas velocity of 7 m/s with varying particle volume fractions.

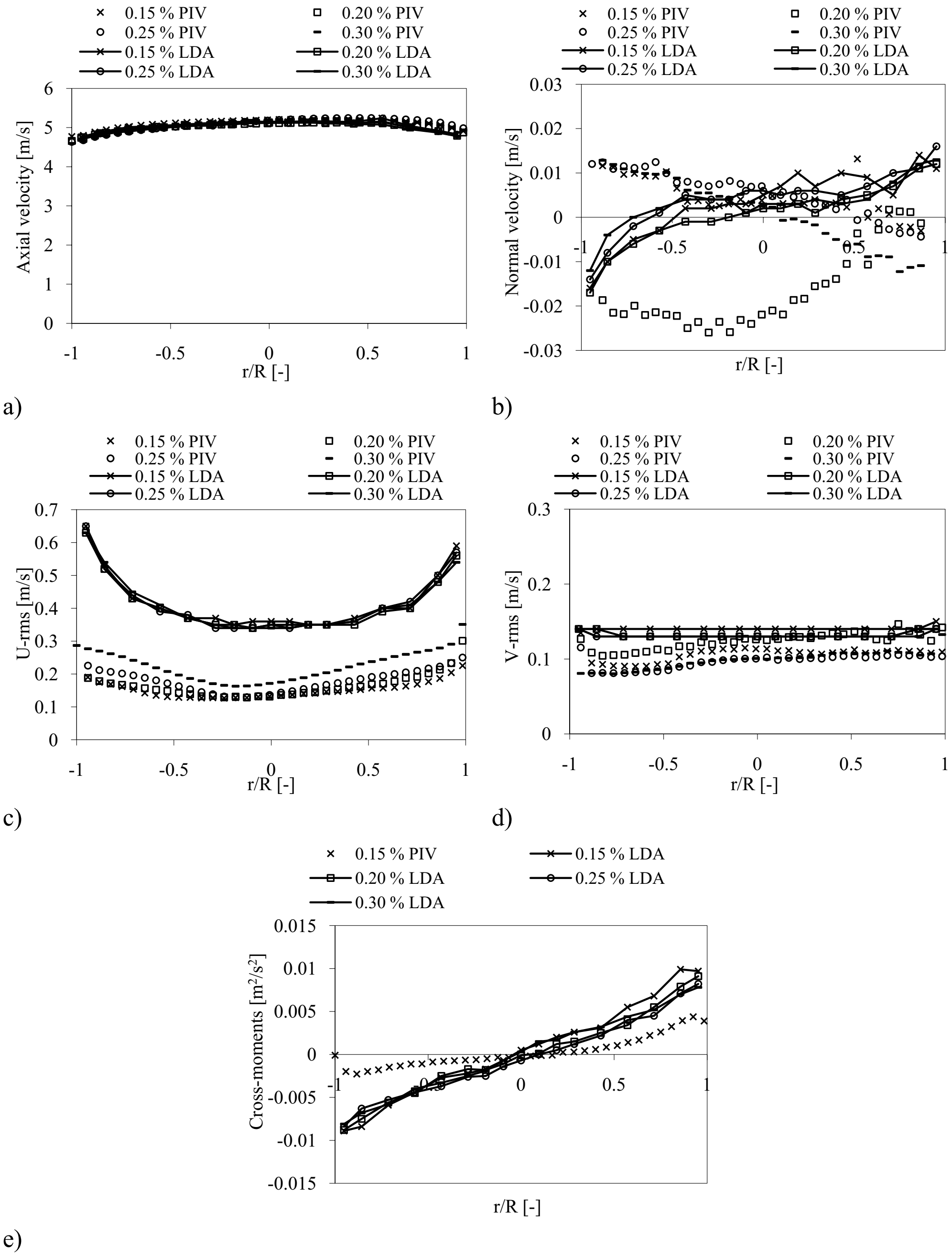

Figure E.3: *The mean axial and normal particle velocity profiles, the axial and normal rms profiles and the cross-moment profiles for ZrO$_2$ particles with a diameter of 260 µm at a constant superficial gas velocity of 7 m/s and different particle volume fractions*

Glass, 120 µm

Results of experiments performed at a superficial gas velocity of 6 m/s with varying particle volume fractions.

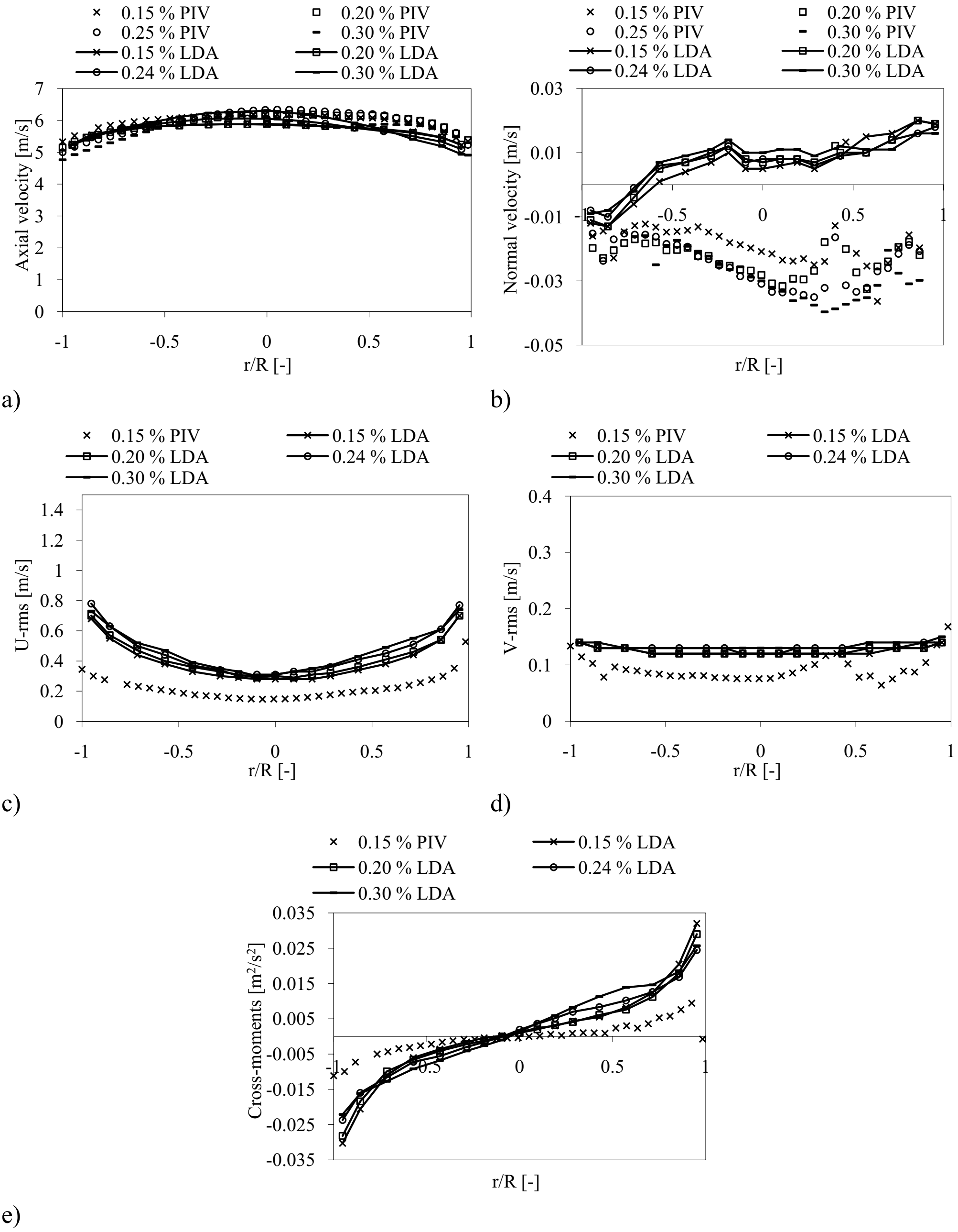

Figure E.4: *The mean axial and normal particle velocity profiles, the axial and normal rms profiles and the cross-moment profiles for glass particles with a diameter of 120 µm at a constant superficial gas velocity of 7 m/s and different particle volume fractions*

Results of experiments performed at a superficial gas velocity of 7 m/s with varying particle volume fractions.

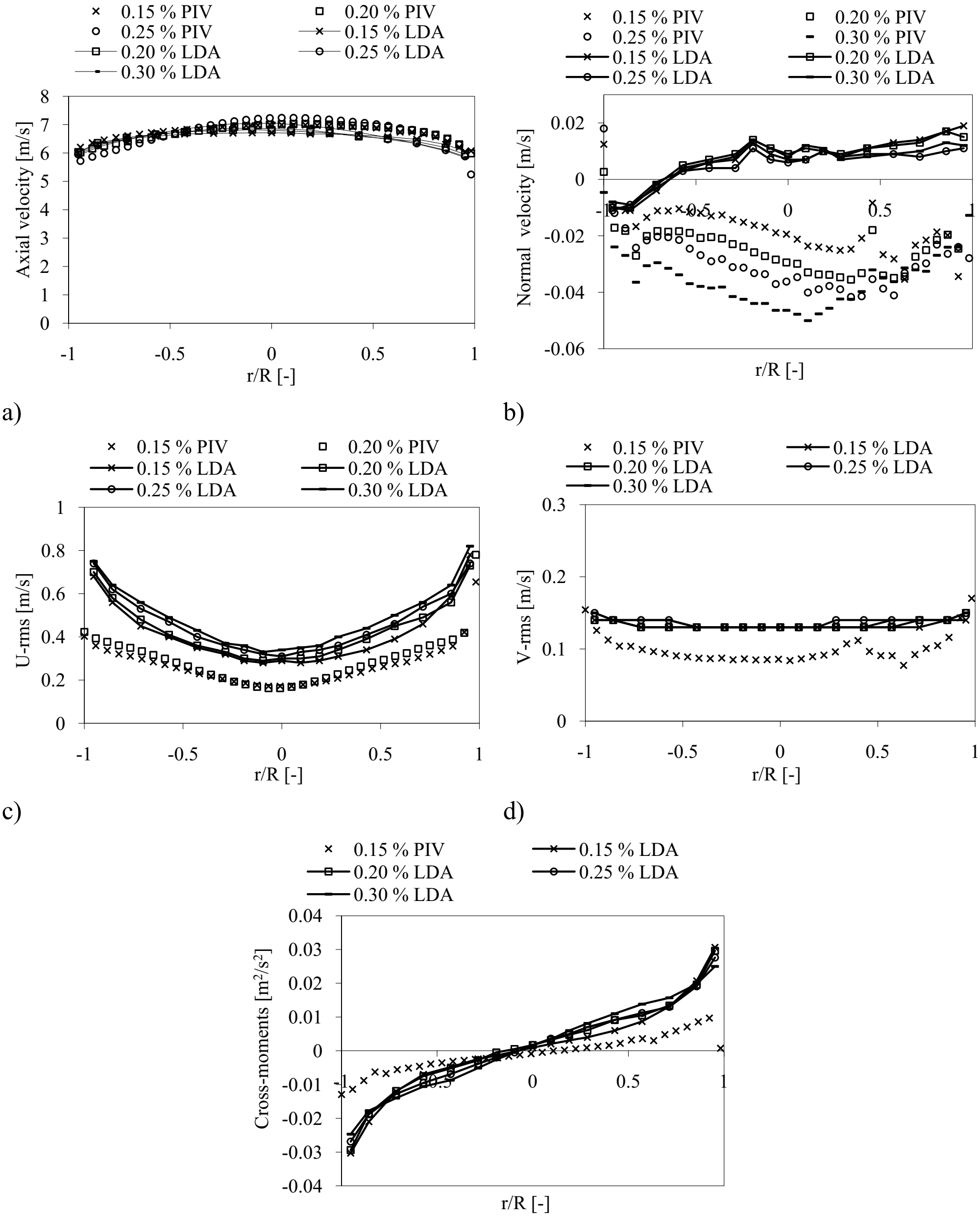

a)

b)

c)

d)

e)

Figure E.5: *The mean axial and normal particle velocity profiles, the axial and normal rms profiles and the cross-moment profiles for glass particles with a diameter of 120 µm at a constant superficial gas velocity of 7 m/s and different particle volume fractions*

Results of experiments performed at a superficial gas velocity of 9 m/s with varying particle volume fractions.

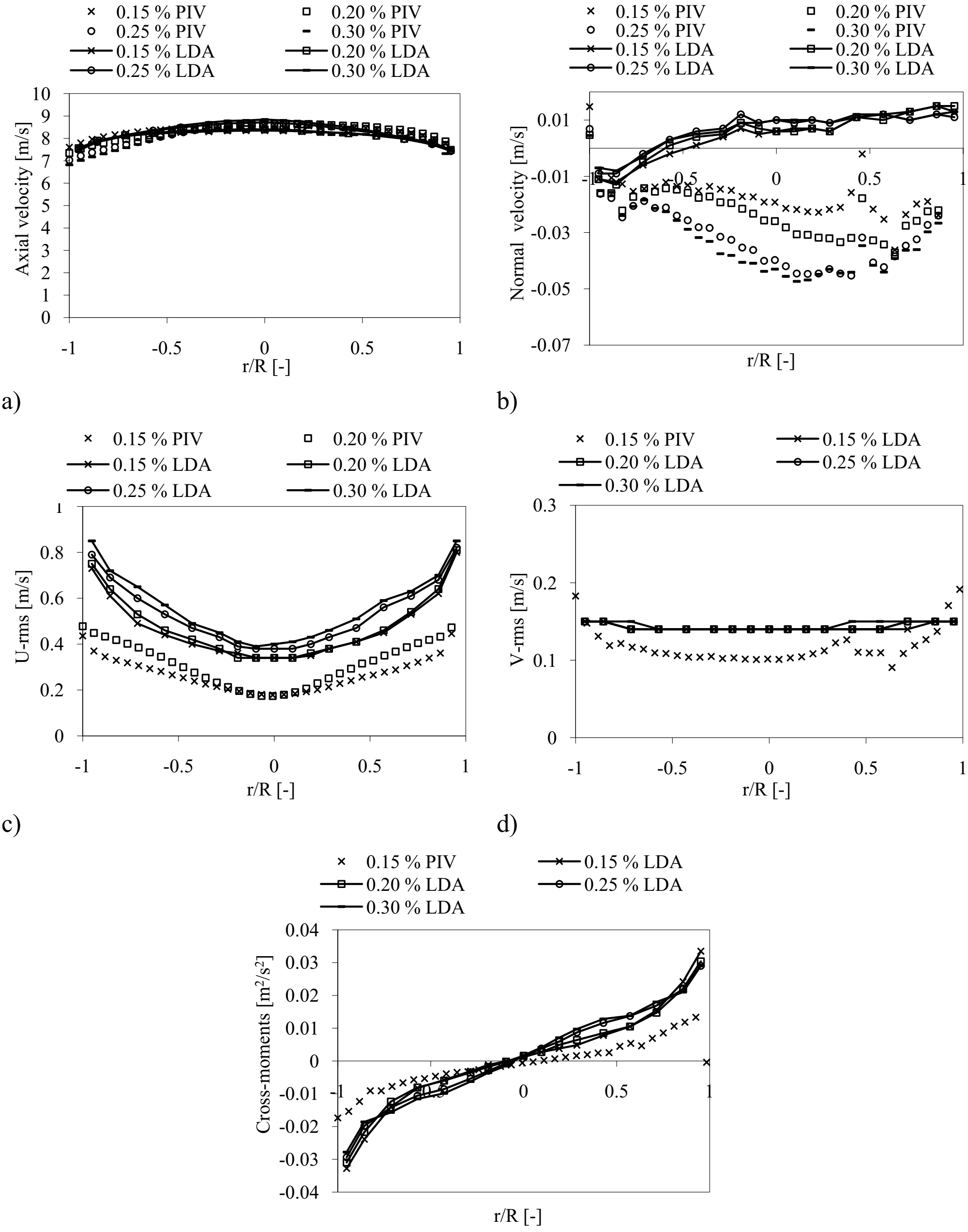

a)

b)

c)

d)

e)

Figure E.6: *The mean axial and normal particle velocity profiles, the axial and normal rms profiles and the cross-moment profiles glass particles with a diameter of 120 µm at a constant superficial gas velocity of 9 m/s and different particle volume fractions*

Glass, 518 µm

Results of experiments performed at a superficial gas velocity of 7 m/s with varying particle volume fractions.

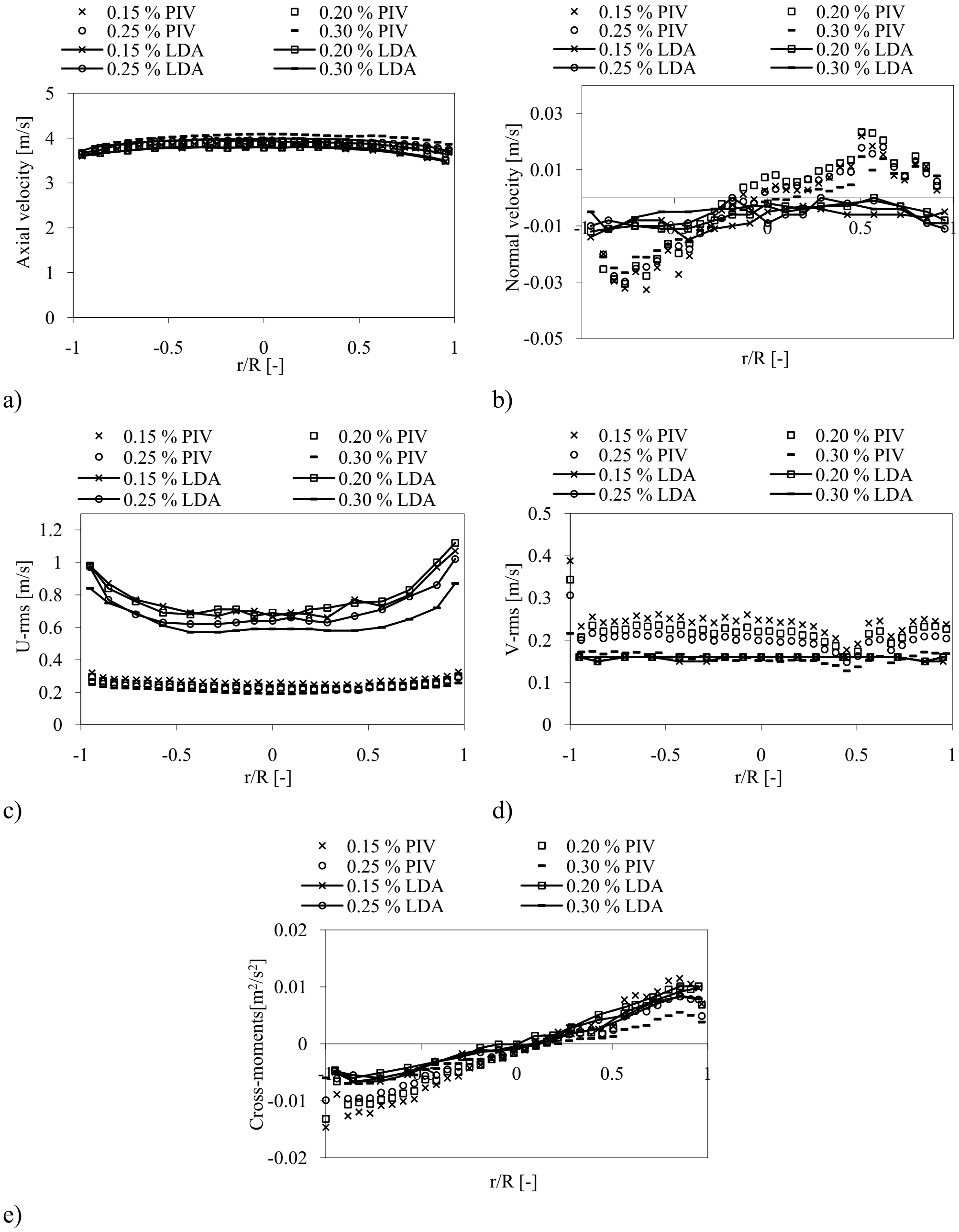

Figure E.7: The mean axial and normal particle velocity profiles, the axial and normal rms profiles and the cross-moment profiles for glass particles with a diameter of 518 µm at a constant superficial gas velocity of 7 m/s and different particle volume fractions

F. Articles

1. Mathisen A., Halvorsen B. and Melaaen, M.C., *Experimental studies of dilute vertical pneumatic transport*, Particulate Science and Technology, 26(3), pp. 235 – 246, 2008 http://www.informaworld.com/smpp/content~db=all~content=a792967560

2. Mathisen A., Halvorsen B. and Melaaen M.C., *Experimental study of dilute vertical pneumatic transport using PIV*, Presented at The 4th International Symposium Reliable Flow of Particulate Solids, 2008.

Experimental Studies of Dilute Vertical Pneumatic Transport

A. MATHISEN, B. HALVORSEN, AND M. C. MELAAEN
Telemark Technological R&D Centre (Tel-Tek)=Telemark University
College, Porsgrunn, Norway

Dilute vertical pneumatic transport has been studied by using the experimental techniques LDA and PIV. LDA and PIV are two different techniques, but they are both common methods used to gain a better understanding of gas=particle multiphase flows. A comparison between the two methods has been performed. The main focus of this study was an experimental LDA investigation of ZrO_2 particles and glass beads. The particles have approximately the same particle size distribution but different densities. The superficial gas velocity and the particle loading have also been varied in the experiments. The effects of superficial gas velocity, particle loading, and particle density on the particle mean velocities, particle u-rms, particle v-rms, and particle cross-moment were investigated. From the experimental investigation it was found that the axial particle velocities showed a dependence on the particle volume fraction for the ZrO_2 particles. It was also observed that the axial fluctuations decreased for both glass and ZrO_2 particles when the particle volume fraction increased. The axial fluctuations measured for the glass beads were higher than the fluctuations measured for the ZrO_2 particles. The mean axial particle velocity measured by LDA and PIV showed good agreement.
Keywords dilute, gas=particle, LDA, PIV, solids loading, vertical flow

EXPERIMENTAL STUDY OF DILUTE VERTICAL PNEUMATIC TRANSPORT USING PIV

Anette Mathisen, Britt Halvorsen and Morten C. Melaaen

Telemark Technological R&D centre (Tel-Tek)/Telemark University College
Porsgrunn, Norway

Abstract - Dilute vertical pneumatic transport is studied using the laser based experimental technique particle image velocimetry (PIV). PIV is a whole field technique and is used to gain a better understanding of the dilute gas/particle multiphase flow. The experimental setup is a vertical lifter. The PIV technique enables the simultaneous measurements of the axial and radial particle mean and fluctuating velocities as well as the cross-moments of the flow in the whole flow field at once. Two types of particles are used in the investigation. They are zirconium oxide (ZrO_2) and glass particles both at two different size distributions. The superficial gas velocity has been varied in the experiments. The effects of superficial gas velocity, particle size and particle density on the particle mean axial velocities, particle u-rms and particle cross-moment were investigated.

1. INTRODUCTION

The pneumatic transportation of particles is a crucial and necessary part of many industrial processes, mainly mining, pharmaceutical, food processing and chemical industries, and also in the oil and gas industry. There are many aspects connected to the transportation of powders. Powders used in manufacturing have a large influence on the quality of the end product and the efficiency of the process. It is also necessary to reduce the energy cost of the process, to keep the production costs low.

In this investigation, the experimental technique Particle Image Velocimetry (PIV) was employed to investigate a dilute vertical gas/particle flow. The aim of this study was to obtain a better understanding of this complex two-phase flow and to investigate the use of PIV in an investigation of this type of flow.

Laser based experimental techniques have a long history when it comes to the investigation of gas/particle multiphase flows. Some of the earliest laser measurements were performed by Maeda et al. [1], Lee and Durst [2] and Tsuji et al. [3]. During the 1990's PIV became a popular method for studying flow. PIV has been used in the study of fluidized beds by Ibsen et al. [4], among others. A method for the simultaneous measurement of both the gas and particulate phase in pneumatic conveying was developed by Jakobsen et al. [5]. The particulate phase in a highly turbulent gas flow in a vertical channel was studied by Grüner et al. [6]. Tartan & Gidaspow [7] used a particle imaging technique on a riser flow to verify CFD models for multiphase flows. The flow in a gas cyclone was studied by stereoscopic PIV (3D-PIV) by Liu et al. [8]. Yao et al. [9] used PIV to measure granular velocities in a study on electrostatic equilibrium in granular flow.

2. EXPERIMENTAL SETUP

A schematic sketch of the lab scale vertical lifter used in the experiments is shown in Figure 1. The particles are pneumatically conveyed from the bottom silo to the top silo through a pipe. The figure also provides a closer view of the bottom of the fluidizing tank. The pipe consists of two sections; a lower section made of glass to enable optical measurements and a top section is made of steel to reduce the build-up of static charging. The internal diameter of the transport pipe was 0.042 m, the total length of the pipe for both the glass and steel sections were approximately 2 m. The bottom tank is a fluidization silo where fluidizing air was used to control the particle loading in the pipe. The transport air entered at the bottom of the fluidization silo through a short steel pipe with an internal diameter of 0.015 m, and the bottom of the transport pipe was placed a distance of 0.015 m directly above this inlet. The measurements were performed at a height of approximately 1.3 m above the air inlet. The flow was assumed to be fully developed, and a previous study performed on this system by Mathiesen and Solberg [10] confirmed this.

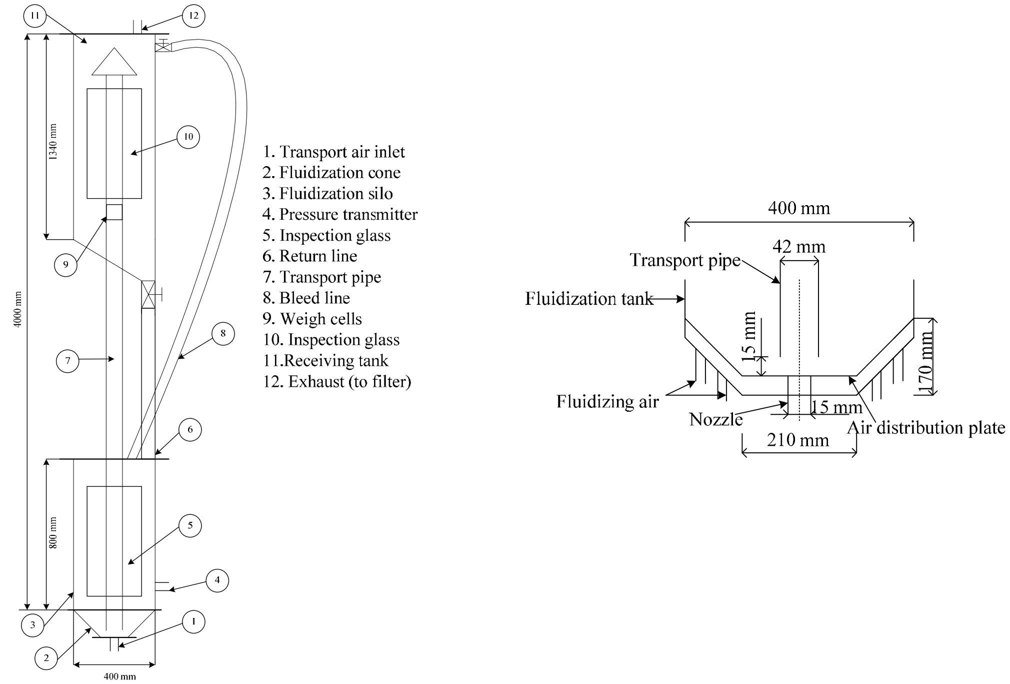

Figure 1: Schematic sketch of the lab scale vertical lifter and a closer view of the bottom of the fluidization tank.

2.1 The PIV experimental technique

A PIV system was used to measure the particles instantaneous axial and radial mean velocities. The fluctuating particle velocities and the cross-moments were calculated from these measured values. The PIV system is delivered by Dantec Dynamics and consists of two 100 Hz 2x5 mJ litron lasers and a Nanosense Mkl camera. The lasers were able to fire two pulses within a very short time interval and produce light sheets. The two light sheets were adjusted so that they illuminated the same section of the transport pipe. They enter the pipe through the centre. Particles which pass through this section of the pipe at the time of the two pulses were also illuminated. The light reflected by these particles was captured by a camera and one frame was produced for each pulse. The camera is placed perpendicular to the light sheets. The two frames were post-processed through adaptive correlation using the computer program, FlowManager, delivered by Dantec Dynamics. The resolution of the picture taken with the camera was 1260x1024 pixels. The direction and value of the particle velocities were derived from the displacement of the particles from one frame to the next and the time delay between the two pulses. This time delay was set to 120 µs and approximately 5000 double frames were taken for each measurement. A summary of the PIV specifications is shown in Table 1.

The post-processed data, axial and radial particle velocities, were transferred to a Matlab script. Based on the instantaneous velocities the u-rms and the mean cross-moments were calculated and then averaged. The u-rms is the root mean square of the fluctuating velocities, while the cross-moment is the Reynolds shear stress divided by the fluid density. The averaging was both temporal and spatial. The parameters and post-processing were the same for all of the experiments. The particles used in PIV measurements need to reflect light, so white or transparent particles are most commonly used. Large particles reflect more light than small particles. More information on PIV can be found in Raffel et al. [11].

Table 1: PIV Specifications.

Wavelength (nm)	532
Time delay between pulses (µs)	120
Trigger frequency (Hz)	50
Camera sensor	C-MOS
Camera resolution (pixels x pixels)	1260 x 1024
Final control volume (pixels x pixels)	32 x 32
Final control volume (mm x mm)	1.168 x 1.187

The particles used in this investigation are given in Table 2. They were zirconium oxide (ZrO_2) particles and glass particles. These particles were chosen because they are robust, spherical and they reflect light.

Table 2: The Particles Used in This Investigation.

Particle	Type	Size distribution (µm)	Average particle diameter (µm)	Particle density (kg/m^3)	Particle weight (kg)
Glass	Glass beads	100-200	120	2500	3.5×10^{-8}
Glass	Glass beads	400-600	518	2500	3.0×10^{-7}
ZrO_2	Zirconium oxide	100-300	260	3800	2.3×10^{-9}
ZrO_2	Zirconium oxide	400-600	530	3800	1.8×10^{-7}

During the investigation it was concluded that the PIV technique can be used to study the gas/particle flow. Some limitations where identified. When too many particles are present in the control volume it is difficult to separate the different particles. Another problem was related to the reflection of the light from the particles which in some instances where directed to a specific part of the cross-section of the pipe making it very difficult to obtain useful results in this area.

3. EXPERIMENTAL RESULTS

The focus in this study was the use of PIV in the investigation of the particulate phase in a gas/particle two-phase flow. The effect of the particle size, particle density and the superficial gas velocity was investigated. The use of PIV for gas/particle multiphase flow was evaluated.

3.1 Effect of particle type

The effect of particle type on the axial particle velocity was investigated through the use of PIV. In Figure 2, the mean axial velocity profiles for the particles presented in Table 2 are shown. From these measurements the effect of particle density and particle size can be seen. The experiments were performed at a superficial gas velocity of 8 m/s, while the solid loading was kept constant at approximately 0.15 %. From the figure, it can be seen that the smallest glass particles achieved the highest velocities. This was expected since these were the lightest of the particle types used and they will follow the gas flow better than the other particle types. The heaviest particles will have the lowest velocity. The largest ZrO_2 and glass particles have almost the same size. The density of ZrO_2 is higher than that of the glass. The smallest ZrO_2 particles have the second highest velocity. The slip velocity increases with the weight of the particle. The slip velocity is the difference between the gas velocity and the particle velocity. The axial particle velocity profiles seen in Figure 2 are almost flat in the centre and decrease in the direction of the wall with a steep gradient very close to the wall. An exemption of this is seen in the more curved profile of the smallest glass particles. It is not easy to capture this wall effect when using PIV since it is difficult to perform measurements close to the wall.

In Figure 3, the mean axial particle fluctuating velocities or the u-rms profiles are presented. The velocity fluctuations of the particles are caused by particle-particle, particle-wall collisions and turbulence in the gas phase. All of the profiles except for the one for the smallest glass particles are flat in the centre of the pipe with a slight increase near the walls. The last profile has a more pronounced shape, the lowest fluctuations are found in the centre of the pipe with a marked increase towards the walls. The largest glass particles have the highest fluctuations, followed by the largest ZrO_2 particles. The two smallest particle types have almost the same fluctuations in the centre of the pipe, but the profile shapes become different when approaching the walls.

In Littman et al. [12] the experimental findings of Lee and Durst [2] and Tsuji et al. [3] were discussed. From these studies, it was found that large particles increase the level of gas phase turbulence and that smaller particles reduce the level of gas phase turbulence. The enhanced gas phase turbulence due to large particles is, according to Hetsroni [13], due to the vortex shedding from their wakes.

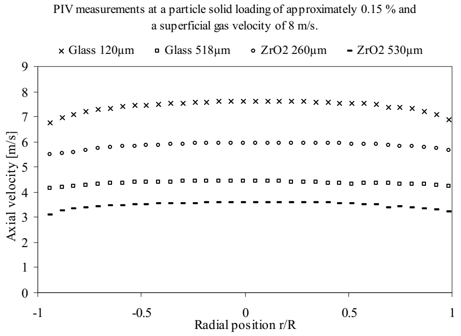

Figure 2: Mean axial particle velocity measured by the PIV for different particle types.

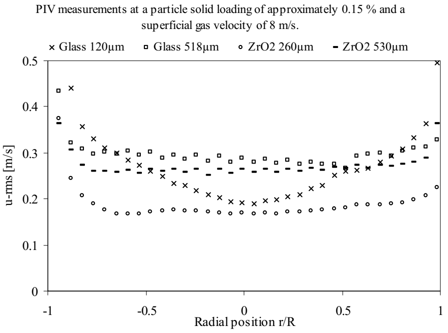

Figure 3: Particle u-rms measured by the PIV for different particle types.

Figure 4 shows the particle cross-moment profiles. The cross-moment values are lowest for the smallest ZrO_2 particles and the smallest glass particles. The largest glass particles have the highest value followed by the largest ZrO_2 particles. The profiles have a value near of zero the centre of the pipe with and increase in absolute value when approaching the walls. It can also be observed that the cross-moment profile shape of the smallest glass particles differ slightly from the rest. This is unexpected since classical theory states that this profile should be linear through the centre of the pipe with a maximum close to the wall and then finally reaching a value of zero at the wall.

3.2 Effect of superficial gas velocity

The effect of the superficial gas velocity was investigated for the smallest glass particles. The solid loading was kept constant at approximately 0.15 % while the superficial gas velocity was varied between 6 – 9 m/s. From Figure 5 the velocity profiles of the particles are shown. The velocity is at its highest in the centre of the pipe and is gradually reduced towards the walls. The superficial gas velocity is increased with 1 m/s for each measurement.

The effect of superficial gas velocity on the mean axial particle fluctuating velocities or the u-rms profiles are presented in Figure 6. It can be seen from the figure that the fluctuations increase with increasing superficial gas velocity for these types of particles. The fluctuations are lowest in the centre of the pipe and increase towards the walls.

In Figure 7 the particle cross-moment profiles are shown. An increase in superficial gas velocity results in an increase in the measured cross-moment for these glass particles. The cross-moment profiles have a value of zero near the centre of the pipe and that the absolute value increases gradually towards the walls.

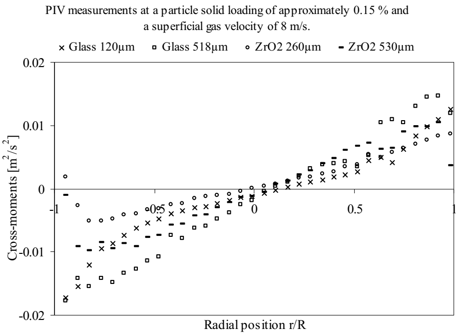

Figure 4: Particle cross-moments measured by the PIV for different particles.

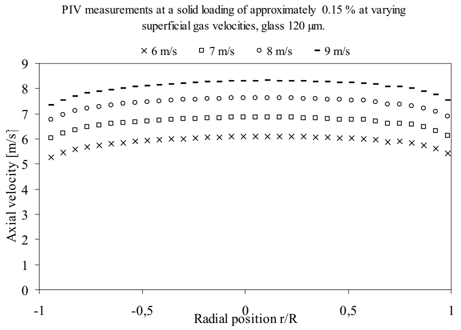

Figure 5: Mean axial particle velocity measured by the PIV at varying superficial gas velocity.

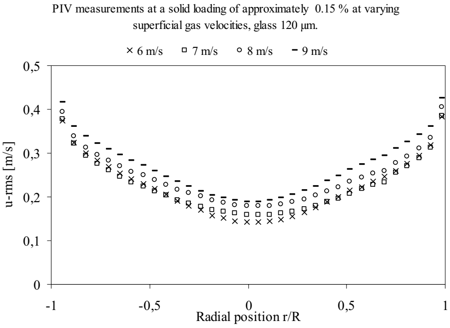

Figure 6: Particle u-rms measured by the PIV at varying superficial gas velocity.

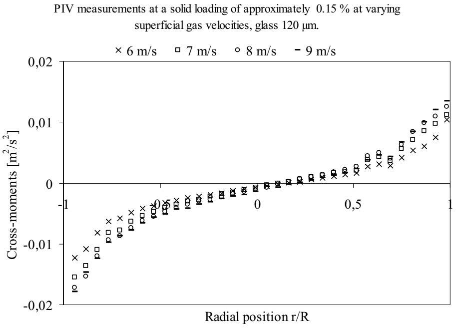

Figure 7: Particle cross-moments measured by the PIV at varying superficial gas velocity.

4. CONCLUSIONS

The laser-based technique PIV has been used to investigate the flow in dilute vertical pneumatic transport of particles. The PIV method was used to study the effect of particle size, particle density and superficial gas velocity on the mean particle velocity, the particle u-rms and the particle cross-moments. From the experimental results and analysis, the following conclusions were drawn.

When performing experiments with the different particle types it was observed that the lightest particles, the smallest glass beads, reached a higher velocity than the heavier particles as expected. The profiles were flat for all particle types, except for the smallest glass beads which have a curvier profile. The measured axial fluctuations were highest for the two largest particle types. The profile for the smallest glass particles differed from the other profiles which were flat over the whole cross-section of the pipe. All of the cross-moment profiles showed a value of zero close to the centre of the pipe with an increase in absolute value when approaching the walls. The measured cross-moments were lowest for the smallest particle types.

The superficial gas velocity was varied during the investigation of the smallest glass particles. All of the measured velocity profiles were flat in the centre of the pipe, with a slight decrease in value when approaching the walls due to the wall effect. The measurement of the axial fluctuating velocity showed that the fluctuations increased with increasing superficial gas velocity. The same was observed for the measured cross-moments.

During the investigation it was concluded that the PIV technique can be used to study the gas/particle flow, but there are some limitations.

5. REFERENCES

1. Maeda, M., Hishida. K. and T. Furutani, Optical Measurements of Local Gas and Particle Velocity in an Upward Flowing Dilute Gas-solids Suspension, *Polyphase Flow and Transport Technology*, Century 2-ETC; pp. 211-216: 1980
2. Lee, S. and F. Durst, On the Motion of Particles in Duct Flows, *International Journal of Multiphase Flow,* Vol. 8, pp. 125-146: 1982
3. Tsuji, Y., Y. Morikawa and H. Shiomi, LDV Measurements of an Air-solid Two-phase Flow in a Vertical Pipe, *J. Fluid Mech,* Vol. 139, pp. 417-434: 1984
4. Ibsen, C. H., F. Onofri, T. Solberg, et al., Improved particle image velocimetry measurements in gas-particle flows with a dense wall layer, *Measurement Science &Technology,* Vol. 14, No. 4, pp. N9-N12: 2003.
5. Jakobsen, M. L., W. J. Easson, C. A. Greated and D. H. Glass, Particle image velocimetry: Simultaneous two-phase flow measurements, *Measurement Science & Technology,* Vol. 7, No. 9, pp. 1270-1280: 1996
6. Grüner, C., W. Kanther, S. Götz, and K. Strauß. Identification of regions with inhomogeneous particle behaviour in dilute gas-solid flows, *Particle & Particle Systems Characterization,* Vol . 21, No. 3, pp. 219-227
7. Tartan. M.and D. Gidaspow, Measurement of granular temperature and stresses in risers, *AIChE Journal,* Vol. 50, No. 8, pp. 1760-1775: 2004
8. Liu, Z., J. Jiao, Y. Zheng, Q. Zhang and L. Jia, Investigation of turbulence characteristics in a gas cyclone by stereoscopic PIV, *AIChE Journal,* Vol. 52, No. 12, pp. 4150-4160: 2006
9. Yao, J., Y. Zhang, C. H. Wang and C. Y. Liang, On the Electrostatic Equilibrium of Granular Flow in Pneumatic Conveying Systems, *AIChE Journal,* Vol. 52, No. 11, pp. 3775-3793:

10. Mathiesen, V. and T. Solberg, Laser-based flow measurements of dilute vertical pneumatic transport, *Chem. Eng. Commun,* Vol. 191, No. 3, pp. 414-433: 2004
11. Raffel, M., C. Willert and J. Kompenhans, *Particle Image Velocimetry, A Practical Guide*, Springer-Verlag Berlin Heidelberg, 1998
12. Littman, H., M. H. Morgan, J. D. Paccione, S. Dj. Jovanovic and Z. B. Grbavcic, Modeling and measurement of the effective drag coefficient in decelerating and non-accelerating turbulent gas-solids dilute phase flow of large particles *Powder Technology*, Vol. 77, No. 3, pp. 267-283: 1993
13. Hetsroni, G., Particles turbulence interaction, *International Journal of Multiphase Flow,* Vol. 15, No. 5 735-746: 1989

6. ACKNOWLEDGMENTS

This study was a part of the strategic research program "Development and Experimental Verification of Numerical Models of Powder Flow" (MODPOWFLO), at Tel-Tek/Telemark University College. The financial support of the Norwegian Research Council is gratefully acknowledged.